Institut für Kernphysik

Cluster-Jet Targets for the $\overline{\text{P}}$ANDA-, MAGIX-, and CryoFlash-Experiments at Hadron-, Lepton-, and Laser-Facilities

Doctoral thesis

Inaugural-Dissertation zur Erlangung des Doktorgrades
der Naturwissenschaften im Fachbereich Physik
der Mathematisch-Naturwissenschaftlichen Fakultät
der Westfälischen Wilhelms-Universität Münster

vorgelegt von

Silke Grieser

aus Troisdorf

- 2018 -

Zusammenfassung

Der Erfolg von Cluster-Jet Targets in der Hadronen-, Lepton- und Laserphysik liegt in ihren hohen Leistungsfähigkeiten begründet. Als Grundlage dafür ist eine genaue Bestimmung der Target- und Clustereigenschaften und sowie das Verständnis des Clusterbildungsprozesses unerlässlich.

Im Rahmen dieser Arbeit wurden Untersuchungen und Entwicklungen für und mit drei verschiedenen Cluster-Jet Targets durchgeführt, dem $\overline{P}$ANDA Cluster-Jet Target Prototypen für das $\overline{P}$ANDA Experiment an FAIR, dem MCT1S für CryoFlash an der Universität Düsseldorf und dem Jet Target MCT-M für MAGIX an MESA.

Lavaldüsen stellen die Schlüsselkomponenten von Jet Targets dar. Besonderes Augenmerk wird im Rahmen dieser Arbeit daher auf Lavaldüsen aus eigener Produktion an der Universität Münster gelegt. Ihre Leistungsfähigkeit wurde untersucht und darauf aufbauend wurden ihre Produktionsprozesse weiter verfeinert und neue andwendungsorientierte Düsenformen entwickelt. Desweiteren führten die Untersuchungen zu einem tieferen Verständnis des komplexen Clusterproduktionsprozesses. Unter anderem konnte eine neue höchste Targetdichte von $(4.85 \pm 0.24) \times 10^{15}$ Atomen/cm^2 in einem Abstand von $2.1\,\mathrm{m}$ mit dem $\overline{P}$ANDA Cluster-Jet Target Prototypen erzielt werden.

Das State-of-the-Art Jet Target MCT-M für MAGIX an MESA wurde konzipiert, aufgebaut und erfolgreich in Betrieb genommen und die Eignung eines Mach-Zehnder-Interferometers zur Untersuchung der Clusterstrahlcharakteristik daran bestätigt. Dies zeigt sich unter anderem durch Aufnahmen eines definierten Clusterstrahls mit einer stabilen Dichte von $(2.1 \pm 0.2) \times 10^{18}$ Atomen/cm^2 und einer Reichweite von mehr als $30\,\mathrm{mm}$ hinter der Düse. Diese und weitere Ergebnisse des Jet Targets wurden bereits publiziert [G$^+$18].

Strahlzeiten am bestehenden MAinz MIcrotron mit diesem Jet Target wurden zur Aufnahme elastischen Elektronen-Protonen-Wirkungsquerschnitten durchgeführt und zeigten die Möglichkeit, präzise Niedrigenergiephysik auf Basis von Elektron-Proton-Streuung durchzuführen, wie z.B. die Bestimmung des Protonenradiuses.

Die Installation und der Betrieb des Cluster-Jet Targets MCT1S am ARCTURUS-Lasersystem der Universität Düsseldorf zeigt im Rahmen dieser Arbeit die Möglichkeit, Protonen und Elektronen zu beschleunigen. Desweiteren wurde gezeigt, dass durch die Cluster-Laser-Wechselwirkung Röntgenstrahlen erzeugt werden. Hervorzuheben ist die Stabilität und Reproduzierbarkeit der Ergebnisse, da dies eine Neuheit im Vergleich zu üblichen Targetquellen der Laser-Plasma-Physik darstellt. Darüber hinaus wurden am U1-Lasersystem Plasmatemperaturen von $1600\,\mathrm{K}$ bis $4500\,\mathrm{K}$ durch die beobachteten Balmer-Spektrallinien bestimmt. Basierend auf diesen erfolgreichen Ergebnissen und den gewonnenen Erfahrungen dieser Arbeit wurde ein neues, leistungsfähiges Cluster-Jet Target entwickelt, um weiterere Messungen mit höheren Targetdichten zu ermöglichen.

Abstract

The success of cluster-jet targets in hadron, lepton, and laser beam physics depends highly on their performance. Therefore, a precise determination and optimisation of the target properties and understanding of the cluster formation process is essential.

Within the work presented in this thesis, investigations and developments for and measurements using three different cluster-jet targets were performed: the $\overline{\text{P}}$ANDA cluster-jet target prototype for the $\overline{\text{P}}$ANDA experiment at FAIR, the MCT1S for CryoFlash at the University of Düsseldorf and the jet target MCT-M for MAGIX at MESA.

Laval nozzles, as key components of jet targets, originating from production processes developed at the University of Münster are reviewed with respect of their performance and based upon that their developed processes were further improved yielding an optimised nozzle geometry, production processes, and a deeper insight into the complex cluster formation process.

A new record hydrogen target thickness of $(4.85 \pm 0.24) \times 10^{15}$ atoms/cm^2 in a distance of $2.1\,\text{m}$ from the nozzle was achieved within this thesis work with the $\overline{\text{P}}$ANDA cluster-jet target prototype.

The high performance, state-of-the-art jet target for MAGIX at MESA was designed, built up, and set into operation. The suitability of a Mach-Zehnder interferometer to investigate the jet beam characteristics was shown and a well defined cluster beam with a high range of constant target thickness of more than $30\,\text{mm}$ and a thickness of $(2.1 \pm 0.2) \times 10^{18}$ atoms/cm^2 directly behind the nozzle was recorded and the results were published [G+18]. Beam times at the MAinz MIcrotron results in elastic electron-proton cross sections and the feasibility to perform precise low energy physics like the determination of the proton radius using the jet target.

The installation of a cluster-jet target at the high intensity ARCTURUS laser system of the University of Düsseldorf resulted in accelerated protons with energies up to $(88.0 \pm 14.5)\,\text{keV}$, accelerated electrons, and X-rays within the framework of this thesis. Novel in this field is the stability and reproducibility of the accelerated particles. Moreover, a plasma temperature in the range of $1600\,\text{K}$ to $4500\,\text{K}$ by the cluster-laser interaction with the U1 laser system was determined by the observation of Balmer spectral lines. Based on these successful results and the gained experience within this thesis, a new powerful cluster-jet target was designed to perform extended measurements.

Contents

1 Introduction

In recent years cluster-jet targets became more and more important in many fields of physics. Prominent examples are accelerator experiments using hadron and lepton beams where cluster beams serve, e.g., as high-quality (quasi-)internal targets. Inspired by this, cluster beams were found to be also highly suited in combination with high-power laser systems. Here cluster-jets can act either as primary target or might be used to produce secondary beams in laser-cluster interactions, such as ultra-short X-rays or relativistic ions. Due to the highly growing interest in powerful cluster-jet sources and due to the need of new innovative technologies meeting the requirements of future facilities, detailed studies and developments on the field of cluster production and preparation have been carried out within the presented thesis. Moreover, the extensive work described here has been performed in imminent connection with the experiments $\overline{P}$ANDA, MAGIX, and CryoFlash, which require state-of-the-art cluster-jet targets. For all of these three experiments using hadron, lepton, and laser beams, new technologies have been developed which will come into operation at the experimental facilities. Moreover, (prototype) cluster-jet targets have been prepared for these installations and have been used for first pilot experiments. In the following, the aims of these three experiments and the filed of research will be presented. Special attention will be laid on the requirements on the desired jet targets.

Todays physics achieved milestones in the explanation of the universe on large scales down to the elementary particles of matter on small scales which is described by the standard model of particles by well established and studied elementary particles of our universe. Nevertheless, this theory leaves some questions unacknowledged in the understanding of the strong interaction e.g. the predicted existence of exotic particles in the frame of Quantum ChromoDynamics (QCD). To face these open questions, the future $\overline{P}$ANDA (antiProton ANnihilation at DArmstadt) experiment at the future Facility for Antiproton and Ion Research (FAIR) at Darmstadt will be performed. Using proton-antiproton annihilations at beam momenta above $2\,\text{GeV}/c$ allows for investigations within the mass region where exotic hadrons and other reactions of interest are predicted or partly observed. The $\overline{P}$ANDA cluster-jet target prototype was designed and therefore built up, and is successfully in operation since years [Kö15]. Based on the experiences gained with this target, a new high performance cluster-jet target, the final cluster-jet target for the $\overline{P}$ANDA experiment, was designed, built up, set into operation, and is currently installed at the COoler SYnchrotron (COSY) in Jülich to study the cluster-accelerator interaction with next to FAIR conditions [Het17, Het18]. In parallel, the $\overline{P}$ANDA cluster-jet target prototype remains at the University of Münster and allows for important analyse of the cluster beam characteristics with respect to further optimise cluster-jet targets.

The strong hint of existence of dark matter in the universe is an evidence for physics beyond the standard model of particles. A proposed dark photon as a dark matter particle, is a promising candidate to strengthen this theory. The upcoming MAGIX (MESA Gas Internal target eXperiment) experiment at MESA will focus on the search for a low mass dark photon as a high precision low energy experiment. This experiment focuses also on the determination of the proton radius. In the past, various experiments were performed to determine the proton radius, but they show discrepancies of up to $7\,\sigma$ [M^{+}14b]. Therefore, new experiments, like MAGIX, are necessary to solve this discrepancies. The MAGIX experiment will consist of the Münster jet target MCT-M and two high resolution spectrometers. Essential for the experiment is the designed high luminosity of $10^{35}\,\mathrm{cm}^{-2}\mathrm{s}^{-1}$ requiring a target thickness in the order of $\mathcal{O}\left(10^{19}\,\mathrm{atoms/cm}^2\right)$ in combination with a minimal background signal due to residual gas.

In the field of plasma physics, mostly foil or gas jet targets are used to generate accelerated particles. An innovative and new idea is the use of a cluster-jet target which allows for a continuous stream of target material and an interaction of the laser with micro-sized particles. By the use of a cluster-jet target, the high repetition rate of the nowadays available terawatt lasers can be used to investigate the cluster-laser interaction. Moreover, the generation of X-rays with such a compact system is feasible as a substitution for large accelerator facilities.

To fulfil these high performance demands on cluster-jet targets, continuous measurements and based on these results, developments and further optimisations were performed. Essential for every Münster cluster source is a Laval nozzle. Their performance is optimised by these studies and the cluster formation process within these nozzles has been further investigated. The fine and complex inner geometry of a Laval nozzle is essential for the cluster production process and determines the characteristics of the cluster beam, e.g., velocity, thickness, size, and shape. At the University of Münster a diversity of nozzle production processes were developed and established to ensure the availability of these nozzles for future experiments and to study the influence of the nozzle geometry on the cluster beam. The produced Laval nozzles were installed at the $\overline{\mathrm{P}}$ANDA cluster-jet target prototype and the jet target MCT-M to study them.
At the $\overline{\mathrm{P}}$ANDA cluster-jet target prototype a variety of diagnostic tools are available to investigate the cluster beam characteristics. Precise measurements on the achievable target thickness, beam structures within the beam, and the velocity distributions in comparison with simulations were performed. Next to the well established measurements, new measurements using a nozzle tilting system were performed. These results lead to an evaluation and further an optimisation of the nozzle production processes. Furthermore, important information within the complex cluster formation process were observed. Within the framework of this thesis, several thesis on cluster-jet targets have been prepared [Hor15, Bö15, Wes16, Har16, Leß16, Bal17, Bra18, Ves18].

The state-of-the-art jet target MCT-M was built up within the bachelor thesis of C. Hargens [Har16] and within this thesis. The operation of the target showed the stability of the target and the feasibility for the MAGIX experiment. Investigations on jet beam thickness profiles using a Mach-Zehnder interferometer in combination with the jet target MCT-M were carried out within the bachelor thesis of C. Westphälinger [Wes16] and master thesis of L. Leßmann [Leß16] and this thesis. The system allows for the study of nozzles with different geometries, which were produced at the University of Münster. Moreover, the visualisation and analysis of the MCT-M jet beam with the interferometer was performed within this thesis and published [G+18]. There, important characteristics of the cluster beam were determined with respect to the later application of the jet target MCT-M at the MAGIX at MESA experiment and the optimisation of the catcher system to minimise the gas flow into the scattering chamber.

While the accelerator MESA is still in preparation, first beam times with the jet target MCT-M at the electron accelerator MAMI at Mainz were performed to study electron-proton interaction. These measurements resulted in first electron-proton scattering data using the final jet target which match the previous determined elastic electron-proton cross sections. Furthermore, target thickness beam profiles were recorded. Moreover, the feasibility to use a jet target for high precision low energy physics was successfully demonstrated.

Additionally, the cluster-jet target MCT1S was installed at the U1 and U2 laser systems of the University of Düsseldorf to investigate the cluster-laser interaction within this thesis. Detailed investigations on the cluster-laser interaction were performed with various diagnostic systems to investigate a wide range of plasma and particle physics. The highly intense U2 laser system in combination with the cluster-jet target allowed for the generation of X-rays, the acceleration of electrons and protons. These results yield a deeper insight into the cluster-laser interaction and based on these experiences a new cluster-jet target was designed and will be used for further studies.

2 Cluster-Jet Targets for Hadron-, Lepton-, and Laser-Experiments

Experiments which investigate the nature of particles and their interactions typically use accelerators to provide particles with high energies to understand the fundamentals of existence. Some experiments, like the BESIII experiment, perform their studies with two accelerated beams contrary to each other, which collide inside a detector to analyse the physics happen. Other experiments, like the upcoming $\overline{\text{P}}$ANDA or MAGIX experiments, perform their investigations with an internal target, which interacts with one accelerated particle beam.

This chapter describes the characteristics of internal targets, especially the different possible kinds of targets with their advantages and disadvantages. Moreover, cluster-jet targets, which are the main focus in this thesis, are discussed in detail, with emphasise on their production process and working principle. Furthermore, the designs of the Münster cluster sources are described.

2.1 Internal Targets

Experiments like the future $\overline{\text{P}}$ANDA (antiProton ANnihilation at DArmstadt) experiment (chapter 4.3) or the upcoming MAGIX (MESA Gas Internal target eXperiment) experiment (chapter 6.3) will use internal fixed targets [PAN12d,Gri]. Thereby, the accelerated particle beam interacts with a target installed directly in the beam line. In comparison to an external target, where the particle beam is extracted from the beam line and dumped after the interaction with the target, the particle beam interacts several times with an internal target. The MAGIX target will be a quasi internal target, because the electron beam of the accelerator MESA only interacts once with the target, afterwards the kinetic electron energy is recovered and is used to accelerate following electron bunches for the next interaction. Therefore, the requirements on the target are the same as for internal targets. In this kind of an internal target, the recovery of the electron beam is suppressed, if the thickness of the target is too high and the next injected electron beam has not enough energy for the interaction wanted.

The CryoFlash experiment (chapter 8.2) does not fit in this terminology of an internal target, because in this experiment not an accelerated particle beam, but a high intensity laser will interact with the target material [Wil17b]. Nevertheless, CryoFlash is an internal fixed target experiment.

Several target types are available for internal target experiments like gas-jet, cluster-jet, pellet or solid state targets (thin fibres, wires, foils). The requirements and the experimental programme determine the best target type for a specific experiment. This

section presents the requirements of the mentioned experiments after explaining the key figure of accelerator physics, the luminosity, and gives an overview of different target types with their specific characteristics.

Luminosity

The luminosity L describing the performance of an accelerator or scattering experiment is an important and significant value [Hin08]

$$L = \frac{\dot{N}_{\mathrm{int}}}{\sigma_{\mathrm{tot}}} \qquad (2.1)$$

with the event rate $\dot{N}_{\mathrm{int}}$ and the cross section σ_{tot} of a given reaction. The cross section is a fixed property of a reaction, therefore, the luminosity $[L] = \mathrm{cm}^{-2}\mathrm{s}^{-1}$ is adjustable via the number of projectiles of the accelerator beam per time unit $\left[\dot{N}_p\right] = \mathrm{s}^{-1}$ or the areal target thickness $[\rho_{\mathrm{areal}}] = \mathrm{cm}^{-2}$ describing the number of target particles per unit of area N_t/A

$$L = \dot{N}_p\, \rho_{\mathrm{areal}}. \qquad (2.2)$$

In the case of an external beam experiment the particle flow $\dot{N}_p$ is defined by the number of extracted particles N_e and the time for beam extraction t_e, so that the luminosity L_{external} is determined by

$$L_{\mathrm{external}} = \frac{N_e}{t_e}\rho_{\mathrm{areal}}. \qquad (2.3)$$

For an internal target experiment the luminosity L_{internal} is given by

$$L_{\mathrm{internal}} = N_b\, N f\, \rho_{\mathrm{areal}}, \qquad (2.4)$$

wherein N_b is the number of bunches, N the number of particles in such a bunch, and f the beam revolution frequency.

Due to accelerator beam losses and interaction with the target material the luminosity is not constant over time. Therefore, the mean luminosity $\overline{L}$

$$\overline{L} = \frac{1}{T}\int\limits_0^T \dot{N}_p\, \rho_{\mathrm{areal}}\, dt \qquad (2.5)$$

is a more suitable figure in most cases.

In experiments studying rare processes the time integrated luminosity $[L_{\mathrm{int}}] = \mathrm{nb}^{-1}$ comes into account

$$L_{\mathrm{int}} = \int\limits_{t=0}^{t_{\mathrm{end}}} L\, dt \qquad (2.6)$$

to describe the total number of events during a beam time.

To maximize the luminosity of an internal beam experiment the number of circulating particles $N_c = N_b N$ should be enlarged, because increasing target thickness leads to increasing beam losses. Whereas in an external beam experiment the areal target thickness

of the target should be as high as possible to have a maximal interaction rate of the extracted beam on the target. Figure 2.1 shows typical areal target thicknesses for internal and external targets and the thereby reachable luminosities. The advantage of internal target experiments is the use of low areal target thicknesses which leads to low background and a good energy and momentum resolution of the ejectiles. Therefore, they are ideally suited for high precision experiments like $\overline{\text{P}}$ANDA and MAGIX.
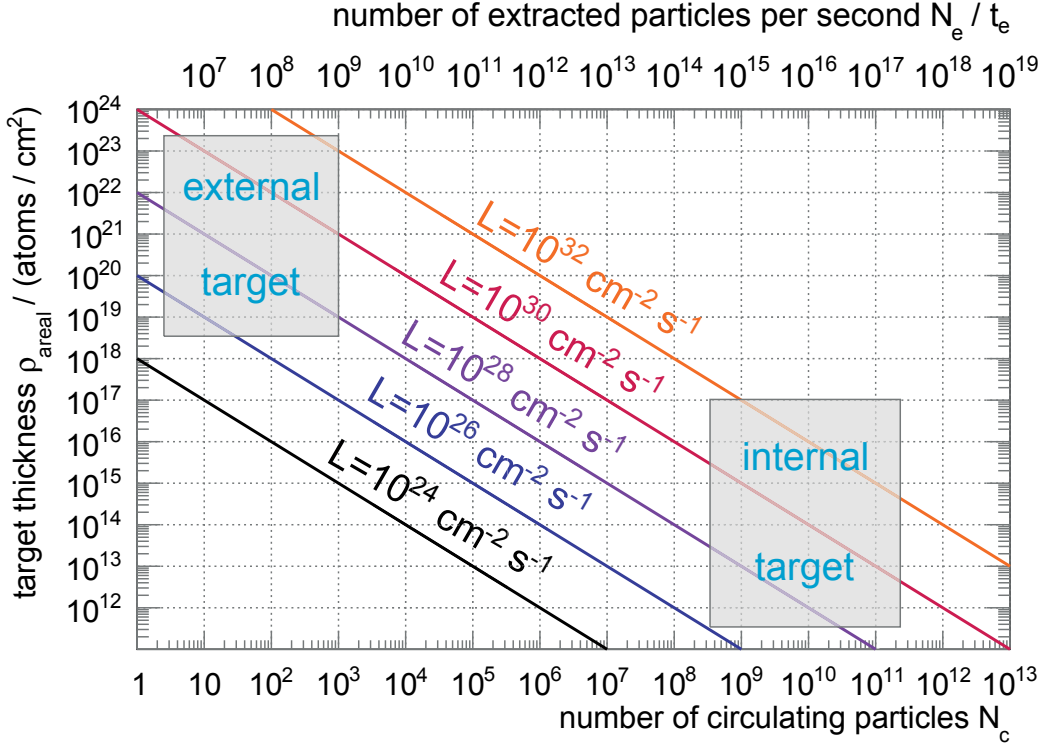
Figure 2.1: The coloured lines indicate constant luminosities between $L = 10^{24}\,\text{cm}^{-2}\text{s}^{-1}$ and $L = 10^{32}\,\text{cm}^{-2}\text{s}^{-1}$. These are feasible with various areal target thicknesses ρ_{areal} and number of circulating particles N_C assuming a revolution frequency of $1\,\text{MHz}$ with an internal beam experiment or number of extracted particles per second N_e/t_e for an external beam experiment. External target experiments work with high areal target thicknesses in comparison to internal target experiments which use lower areal target thicknesses to realise the same luminosity due to the variation of the particle numbers of the corresponding accelerator beam.

The $\overline{\text{P}}$ANDA experiment will be one future experiment which will use proton-antiproton annihilations. The cross section for this annihilation is $\sigma_{\text{tot}} \approx 100\,\text{mb}$ [P+16]. Due to the planned construction of the experiment, an antiproton production rate of $\dot{N}_{\text{int}} = 2 \times 10^7\,\text{s}^{-1}$ is envisaged [GSI06]. Hence, $\overline{\text{P}}$ANDA is aiming for a maximal luminosity of $L_{\text{max}} = 2 \times 10^{32}\,\text{cm}^{-2}\text{s}^{-1}$ (Eq. (2.1)). The desired areal target thickness for an internal target experiment can be calculated via Eq. (2.1) and Eq. (2.4)

$$\rho_{\text{areal}} = \frac{\dot{N}_{\text{int}}}{\sigma_{\text{tot}}\,N_b\,N f}. \tag{2.7}$$

The protons of the $\overline{\text{P}}$ANDA target will interact with the accelerated antiprotons provided by the HESR (High Energy Storage Ring) consisting of 10^{11} antiprotons with a revolution frequency of $443\,\text{kHz}$ [PAN12d]. This results in a needed areal target thickness of $\rho_{\text{areal}} = 4.5 \times 10^{15}\,\text{atoms/cm}^2$ for the $\overline{\text{P}}$ANDA target. A higher target thickness leads to a decrease of the beam lifetime due to extensive beam heating effects, causing beam prticles leaving the acceptance of HESR.

Another high precision experiment will be the upcoming MAGIX experiment located in the energy recovering sector of MESA. The Mainz Energy-Recovering Superconducting Accelerator (MESA) will provide an electron beam current of $\text{I} = 10\,\text{mA}$ in the ERL (energy recovery linac) mode which corresponds to an event rate of $\dot{N}_{\text{int}} = \text{I}/e \approx 6.2 \times 10^{16}\,\text{s}^{-1}$ [H$^+$17b]. The designed luminosity for the MAGIX experiment $L = 10^{35}\,\text{cm}^{-2}\text{s}^{-1}$ leads to a desired areal target thickness of $\rho_{\text{areal}} \approx 1.6 \times 10^{18}\,\text{atoms/cm}^2$ (Eq. (2.2)) for the MAGIX target.

Requirements of Internal Targets

In addition to the desired target thickness, i.e. the designed luminosity, other important requirements on the target have to be considered. On the one hand, the high target thickness should be constant in time and should show no time structure to yield a constant luminosity. On the other hand a continuously adjustable target thickness over several orders of magnitude during the experiment leads to an optimum event rate for every experimental program and compensates the beam consumption caused by the interaction with the target which results in a constant event rate. The possibility to adjust the target thickness to the density of the accelerated particle beam was investigated in the bachelor thesis of F. Hordt [Hor15] and is presented in more detail in chapter 5.1.

Most of the experiments use hydrogen as target material for proton targets with respect to reactions on the elementary nucleon or quarks. The proton-antiproton annihilation at the $\overline{\text{P}}$ANDA experiment will give a deeper insight into the strong interaction and the physics of exotic particles. The MAGIX experiment will investigate the proton radius via electron-proton scattering with high precision. Nevertheless, also other gases as target material are of highest interest, for example oxygen to study the astrophysical S-Factor by the MAGIX experiment [Mer16a]. In the framework of the CryoFlash experiment heavier gases, like argon, are requested for interactions with large mass and atomic number to analyse the interaction of the laser with different target materials.

Every experiment suffers from background reactions next to the desired events. To minimize the background reaction rate, target material of highest purity is used. In the case of hydrogen, purifiers are used to achieve hydrogen with a purity of 9.0 (99.9999999 %). Furthermore, the characteristic of an internal target, the absence of windows or foils between target and the accelerated particles or laser also reduces the background.

Moreover, to reach a high detection acceptance possibly close to 4π, as in the case of the $\overline{\text{P}}$ANDA experiment, the target generator has to be located outside of the detector module or has to be as small as possible if located near the interaction zone.

The influence of the accelerator vacuum conditions by the target should be as low as possible. Therefore, different features were investigated. The $\overline{\text{P}}$ANDA target optimises the

size and shape via specially shaped collimators of the target beam to the geometry of the accelerator beam, so that the target size equals the overlap region [Her13]. Furthermore, a nozzle shutter is installed as an on/off switch of the target beam to optimise the period of introducing gas in the scattering chamber. The MAGIX experiment uses a catcher system directly opposite to the target generator to reduce the target flow into the scattering chamber (cf. chapter 6.4). For the same reason, also $\overline{\text{P}}$ANDA will use a cluster beam dump system opposite to the target generator but in a distance of roughly 5 m to the nozzle.

These requirements can be fulfiled by different target types, but the best suitable target depends on the experimental setup and program. In storage ring experiments often used and well established are gas-jet, cluster-jet and pellet targets.

Target Types

The most suited target type for an experiment depends on the requirements and the physical program. For the three experiments, $\overline{\text{P}}$ANDA, MAGIX, and CryoFlash, which are objects of this thesis, the requirements are quite similar. The use of solid targets like thin fibres, wires, or foils are unsuitable, because the interactions with the particle beam or laser pulse destroy these targets, so that they have to be exchanged after every or several interactions. Therefore, targets which provide a continuous flow of target material, like gas-jet, cluster-jet, or pellet targets are well suited. In the case of the $\overline{\text{P}}$ANDA experiment, the thickness of solid targets in the range of 10^{17} atoms/cm^2 to 10^{19} atoms/cm^2 [Eks95] would be much too high to obviate extensive beam heating and the possibility for unwanted secondary interactions. Different to most experiments in the field of laser-plasma physics, the CryoFlash experiment will not investigate the interaction between a laser beam and a typically used solid target. The reason for this is that the cluster-laser interaction leads to different acceleration processes which will be studied in detail (cf. chapter 8.1).

A pellet target provides a continuous stream of frozen droplets, e.g., hydrogen or deuterium. The last running and since 2017 ended experiment with a pellet target was the WASA-at-COSY experiment (Wide Angle Shower Apparatus) in Jülich (Germany) [A$^+$04, Ber09, Ber17, Dem13, Hus12, Hü14, Hü17a, Wil17a]. To generate pellets, liquid hydrogen with a temperature of 14 K and a pressure of 0.07 bar near the triple point [L$^+$09a] is pressed through a glass nozzle with a diameter of 12 µm - 14 µm into the triple point chamber [Hus12], which is filled with helium gas close to hydrogen triple point conditions (20 mbar) [W$^+$07]. The glass nozzle is excited via a piezoelectric transducer and therefore, the liquid hydrogen stream breaks up into periodic monosized droplets. The size of the droplet depends on the nozzle diameter and the frequency of the piezoelectric element. The droplets leave the triple point chamber through a capillary into a vacuum chamber of roughly 10^{-3} mbar and experience thereby an acceleration [W$^+$07]. There, the droplets freeze out to pellets and gain a divergence. The following skimmer only extracts the pellets with a small divergence (< 1 mrad) for the experiment. The production process is shown in Figure 2.2 (right). Such pellet targets reach thicknesses of, e.g., 4×10^{15} atoms/cm^2 in a distance of more than 2 m behind the nozzle. To adjust the thickness, only the

number of pellets in the interaction region can be varied. The pellets themselves have a diameter between $20\,\mu m$ and $30\,\mu m$ and a mean distance of roughly $5\,mm$ [Hus12]. The pellet beam has a diameter of $2\,mm$ to $4\,mm$ [W$^+$07]. Due to the thickness of a pellet target in combination with a pellet tracking system for a precise vertex information of individually pellets, a pellet target will be the second operating target at the $\overline{\text{P}}$ANDA experiment [PAN12d].
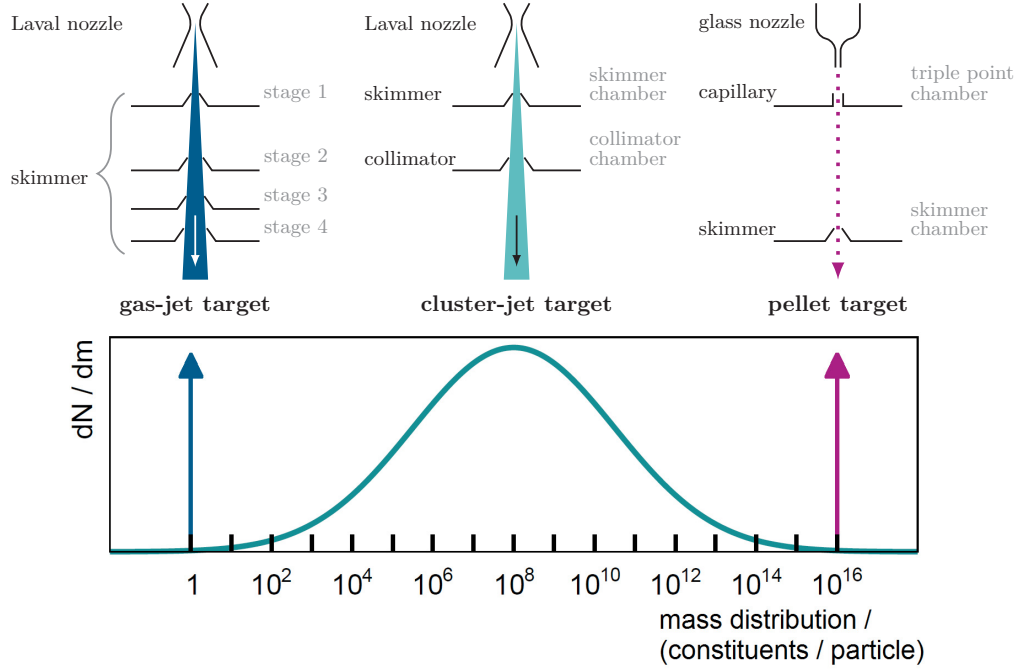
Figure 2.2: Schematic view of the production and preparation of gas-jet, cluster-jet and pellet beams. Gas-jet and cluster-jet targets use a Laval nozzle to produce the beam and a set of skimmers (or collimators) to prepare the beam. The pellet target works with, e.g., a glass nozzle and produces small frozen droplets, called pellets. Below the mass distribution for these three type of targets is shown qualitatively. Gas-jet beams consist of the single gas atoms/molecules and pellets are monosized large particles. Clusters are in-between these two. Cluster beams comprise of clusters with individual size, their mass distribution can be described via a log normal distribution. Generated by E. Köhler (top) and A. Khoukaz (bottom), edited.

Similar to a pellet target, a droplet target generates a continuous stream of droplets. Therefore, liquid hydrogen expands through a glass nozzle with an inner diameter of roughly $5\,\mu m$ into a vacuum chamber and spontaneously breaks up into periodic droplets. The use of a piezoelectric transducer leads to a controlled break up of the droplets. Further investigations and optimizations on this kind of target are in progress at the University of Münster (cf. [Har18]).

The characteristic time structures of these two targets are a disadvantage for some experiments, e.g., the CryoFlash experiment (cf. chapter 8.2) due to the necessary synchronisation of the laser pulse to the droplets.

A gas-jet target produces a continuous stream of target material by passing gas with high pressure of, e.g., 20 bar through a Laval nozzle with its specific convergent-divergent geometry (more details see chapter 3) into vacuum. Thereby, different types of gases are used like hydrogen, helium, or xenon [R$^+$]. The resulting gas-jet beam consists of single atoms or molecules (cf. Fig. 2.2). A possible set of skimmers in combination with a differential pumping system reduces the gas load to the interaction chamber. Gas-jet targets reach high thicknesses in the range of, e.g., 10^{19} atoms/cm^2 directly behind the nozzle, but the thickness decreases rapidly with the distance from the nozzle. Additionally, the gas beam strongly expands in lateral direction. Depending on the vacuum conditions inside the chamber, the formation of a typical node structure can be obtained. Detailed studies on these gas beam characteristics are discussed in chapter 7.2. Due to the rapidly decreasing thickness, a gas-jet target is not suitable for the $\overline{\text{P}}$ANDA experiment, where the interaction with the antiproton beam takes place in a distance of 2.25 m behind the nozzle. At such a distance, a gas-jet target cannot provide a defined target beam. The high gas load in the interaction chamber in combination with the wide spread in lateral direction makes it unsuitable for the MAGIX experiment because this high precision experiment requires sufficient vacuum conditions to reduce the background reactions. Due to the fact that gas beams consist of single atoms or molecules, CryoFlash uses a cluster-jet target generating clusters which are nano-sized accumulations of gas atoms or molecules. Thus the cluster-laser interaction differs from gas-laser interactions resulting in different observable phenomena (cf. chapter 8.1).

Cluster-jet targets also use a Laval nozzle to produce a cluster-jet beam. Thereby, the gas in front of the nozzle with pressures up to 20 bar is, compared to a gas-jet target, cooled down using a cold head. Supplementary, to the supersonic flow at the narrowest point of the nozzle, the injection into vacuum leads to an adiabatic cooling of the target material which allows in combination with collisions between the gas atoms or molecules for a following formation of clusters consisting of more than 10^6 constituents (cf. Figure 2.4) [Kö15].

The number of constituents divide them into different classifications [Pau00b, Ber06]:

- micro clusters ($N \leq 10$)

- small clusters ($10 < N < 100$)

- large clusters ($100 < N < 1000$)

- micro crystals ($N > 1000$)

- nano particles ($N > 10^{16}$).

Hydrogen clusters are bound by the van der Waals force with energies up to a few tenths of electron volts. The Hagena paramter Γ^* gives a semi-experimental access to the prediction of the number of constituents for a cluster [Pau00a, Hag87, HO72, Hag92]

$$\Gamma^* = \frac{\hat{k}p_0 \left(\frac{0.74 d_n}{\tan \alpha_{1/2}}\right)^{0.85}}{T_0^{2.29}}. \tag{2.8}$$

Therein, $\hat{k}_{H_2} = 184$ is a specific gas constant [S$^+$98], p_0 and T_0 the stagnation pressure (mbar) and the temperature (K) of the gas in front of the nozzle, d_n the nozzle inner diameter (μm) and $\alpha_{1/2}$ the half of the expansion angle (degree). The value of the Hagena parameter Γ^* predicts the formation of clusters [Hag87]:

- flow without cluster condensation ($\Gamma^* < 200$)

- transition state of cluster formation ($200 < \Gamma^* < 1000$)

- immense formation of clusters with more than 100 constituents ($\Gamma^* > 1000$).

Moreover, the average cluster size N can be determined using the Hagena parameter in the Hagena's scaling law [Hag92]

$$N = A_N \left(\frac{\Gamma^*}{1000} \right)^{\gamma_N} \tag{2.9}$$

with empirical values $A_N = 33$ and $\gamma_N = 2.35$ in dependency of Γ^* [Hag92].

In the doctoral thesis of E. Köhler [Kö15], the mass distribution of hydrogen clusters produced at the $\overline{\text{P}}$ANDA cluster-jet target prototype was investigated. Within this thesis, the mass distribuation was confirmed as a log-normal distribution

$$f(x, \mu, \sigma) = \frac{1}{x \sigma \sqrt{2\pi}} \exp \left(-\frac{(ln(x) - \mu)^2}{2\sigma^2} \right) \tag{2.10}$$

with μ and σ being location and scaling parameter. Moreover, an agreement with the Hagena's scaling law prediction of the cluster size was obtained by an underestimation with a factor of 2.6.

In addition, cluster-jet targets offer the possibility to use different gases as target material. To achieve a well defined cluster beam after the production, two orifices (skimmer and collimator) can be used to separate the cluster beam from the residual gas and to shape the final size and form of the beam. Therefore, a cluster-jet target offers the possibility to provide a well defined target beam with high thickness of more than 10^{15} atoms/cm^2 even at large distances (2.25 m) [Kö15]. At the COoler SYnchrotron (COSY) in Jülich (Germany) two cluster-jet target experiments were successfully realised. The COSY-11 and the ANKE (Apparatus for Studies of Nucleon and Kaon Ejectiles) experiment used cluster-jet targets, which were designed, constructed and operated by the University of Münster [Kho96, Wil17a, B$^+$96b, D$^+$97, Gos09, Gos13, Fri14, Sch12b, Fri18]. The ANKE cluster-jet target will be adapted for the planned KOALA experiment (chapter 5.1). The $\overline{\text{P}}$ANDA experiment will use a cluster-jet target as the first operating target. Therefore, at the University of Münster, in a first step the prototype and later the final $\overline{\text{P}}$ANDA cluster-jet target were designed, built up, and routinely operated (see chapter 4.3). These two targets fulfil all the requirements for the target for the $\overline{\text{P}}$ANDA experiment. MAGIX as well as CryoFlash also perform their experiments with Münster cluster-jet targets. The interaction of a laser pulse with a cluster leads to different observations than an interaction with an atomic gas beam. MAGIX takes advantage of the well defined target beam in conjunction with a catcher system directly opposite of the nozzle to minimize the

vacuum in the interaction chamber by directly pumping the clusters after the interaction with the electron beam (cf. chapter 6.4).

2.2 Cluster-Jet Targets

High performance cluster-jet targets are highly suited for experiments with hadron, lepton and laser beams. The advantage of this kind of targets in comparison to the other ones (gas-jet or pellet) is the high range (more than 2.25 m) of the high areal target thickness (2×10^{15} atoms/cm^2) in combination with a well defined cluster beam. This section explains the cluster production process and the design and working principle of the cluster sources designed and operated by the University of Münster.

2.2.1 Cluster Production Process

The centrepiece of every Münster cluster-jet target is the Laval nozzle. The specific geometry of the nozzle is essential for the cluster production process and determines the properties of the cluster beam, like velocity, density, and size (Figure 2.3). The short convergent inlet zone of the nozzle decreases continuously to its circular cross-sectional area and merges in the narrowest point of the nozzle. Typically in Münster used Laval nozzle possesses narrowest inner diameters of 20 μm - 500 μm. After the narrowest point the long divergent outlet zone follows which is essential for the cluster beam production process (cf. chapter 5.1).
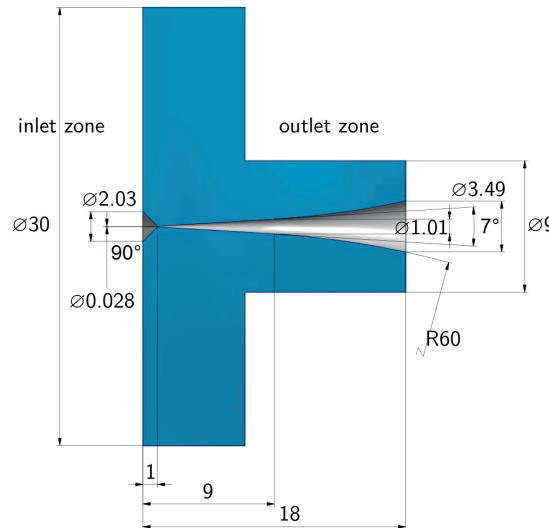
Figure 2.3: Schematic view of a Laval nozzle. The 90° inlet cone ends in the narrowest inner diameter (30 μm) of the nozzle and merges to the long outlet zone with an additionally opening angle. The complete length of the nozzle is 18 mm, whereof the first millimetre corresponds to the inlet zone. The opening angle of the outlet pass over in an additionally radius after 8 mm from the narrowest diameter. Generated by D. Bonaventura, edited.

The used gas in front of the nozzle, i.e. hydrogen, is cooled down to temperatures of $22\,\mathrm{K}$ to $40\,\mathrm{K}$ with high pressures between $2\,\mathrm{bar}$ - $20\,\mathrm{bar}$. At this point the gas constituents still follow a Maxwell-Boltzmann distribution of their relative velocities. The gas passing the Laval nozzle experiences an acceleration, so that at the narrowest inner diameter of the nozzle, the gas reaches a supersonic flow if the inlet pressure is much higher than the outlet pressure. Due to the increase of the volume after the narrowest point of the nozzle, an adiabatic expansion of the gas takes place, supported by the Joule-Thomson effect. As a result of the temperature reduction by these effects, the gas atoms or molecules adjust their relative velocities to each other, so that they travel with nearly the same velocity through the nozzle as depicted in Figure 2.4. Moreover, the low discrepancy in the relative velocity leads to accumulations of the molecules via collisions and the formation of condensation nuclei takes place. This type of collision is called three-body collision, because the binding energy of the two colliding molecules is transferred to a third molecule. The accumulation of more molecules (up to 10^6) to the generated condensation nuclei leads to cluster formation. The advantage of the so formed clusters is the large cluster size and, therefore, their possibility of a high range of more than $5\,\mathrm{m}$ in vacuum (chapter 4.3).
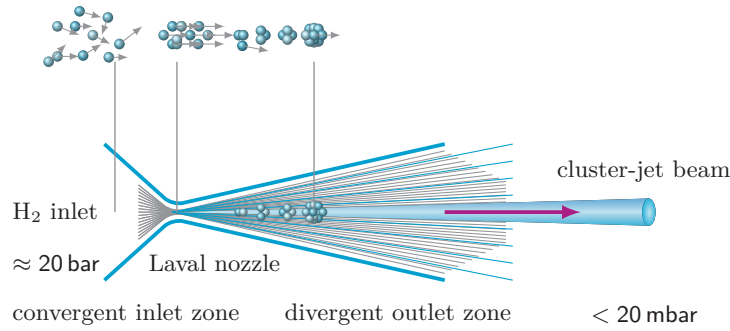
Figure 2.4: Schematic view of the cluster production process within a fine Laval nozzle. The cooled hydrogen ($22\,\mathrm{K}$ - $40\,\mathrm{K}$) in front of the nozzle is pressed with high pressure of up to $20\,\mathrm{bar}$ through the nozzle. Due to the increase of the volume after the narrowest inner diameter, an adiabatic expansion takes place and the hydrogen condensates to clusters. The velocity distributions of the hydrogen in dependence of the nozzle position is shown at the top. In front of the nozzle the hydrogen owns a Maxwell-Boltzmann velocity distribution. At the narrowest point of the nozzle, it reaches a supersonic flow and the relative velocities vanishes and the clusters travels with nearly the same velocity. Generated by E. Köhler, edited.

2.2.2 Münster Cluster Sources

The Laval nozzle, as described in the previous chapter, is essential for the cluster production process and the properties of the cluster beam. Therefore, the Münster cluster-jet target sources have a Laval nozzle as their centrepiece.
In this thesis three Münster cluster-jet targets are described and used: The $\overline{\mathrm{P}}$ANDA cluster-jet target prototype, the jet target for the MAGIX experiment MCT-M, and the cluster-jet target MCT1S for the CryoFlash experiment. These cluster sources are designed with the same basic structure described in this section. The different used

devices for the individually targets are listed in Table 2.1.

For the cluster production cooled and purified hydrogen gas is used in general. The hydrogen is delivered with a purity of 5.0. Additionally, the hydrogen is purified with a hydrogen purifier which consists of a silver-palladium membrane heated up to $400\,°C$ to avoid a clogging of the Laval nozzle. The hydrogen molecules impinging on the hot membrane, ionize and separate themselve and thus can pass through it. Every other impurities, like water, nitrogen, and oxygen, are held back due to their higher atomic radii. After passing the membrane by diffusion, the hydrogen atoms recombine to hydrogen molecules and the gas reaches a purity of 9.0 directly behind the purifier [Joh98]. The purifier have a second output, the bleed out, which allows for flushing the retained impurities in front of the membrane to ensure its functionality. The MAGIX target renounced of a hydrogen purifier due to the relatively large inner diameter (0.5 mm) of the used Laval nozzle. Moreover, two sinter filters (pore size: $20\,\mu m$ and $0.5\,\mu m$) are installed in the gas system to avoid impurities and the consequently clocking of the nozzle. The gas supply is equipped with a pressure control (Brooks) to adjust the pressure of the gas in front of the nozzle and a flow meter (Brooks) to measure the gas flow through the nozzle and to calculate the narrowest inner diameter of the nozzle. This can be used to identify a polluted or frozen nozzle. Moreover, the pressure directly in front of the nozzle is additionally monitored via a capacitative manometer (MKS) placed in the gas return line from the nozzle. Furthermore, this return line is used to flush the complete gas system to remove appearing impurities and overpressure.

Table 2.1: The different used devices to operate, monitor, and control the various Münster targets which are topic of this thesis.

device	target	company and specification
hydrogen purifier	$\overline{\text{P}}$ANDA	Johnson Matthey HE 20 (300 °C)
	MCT1S	Johnson Matthey HP-50 (400 °C)
cold head	$\overline{\text{P}}$ANDA	Leybold 10MD
	MCT1S	Leybold RGD 1245
	MAGIX	Leybold 10MD
compressor	$\overline{\text{P}}$ANDA	COOLPAK 6000 MD
	MCT1S	COOLPAK 6000 H
	MAGIX	COOLPAK 6000 MD
temperature monitoring	$\overline{\text{P}}$ANDA	Lakeshore 331
	MCT1S	Lakeshore 208
	MAGIX	Lakeshore 336
temperature diodes	$\overline{\text{P}}$ANDA	Lakeshore DT 670 (2nd Stage)
	MCT1S	Lakeshore DT 670 (2nd Stage)
	MAGIX	2× Lakeshore DT 670 (1st Stage)
		2× Lakeshore DT 670 (2nd Stage)
heating capacity	$\overline{\text{P}}$ANDA	$2 \times 50\,\text{W}$ (2nd Stage)
	MCT1S	$50\,\text{W}$ (2nd Stage)
	MAGIX	$2 \times 100\,\text{W}$ (1st Stage)
		$2 \times 50\,\text{W}$ (2nd Stage)

The regulated and purified hydrogen gets to a two stage cold head to be cooled down to low temperatures below $40\,\text{K}$ in combination with a helium compressor (Fig. 2.5). The first stage of the cold head is called the warm stage and the second stage the cold stage. Both devices work with the Gifford-McMahon process in a closed helium cycle [Umr97]. Thereby, the displacer separates two volumes in the cold head and allows for a compression and expansion of the helium gas and a heat exchange via the compressor which is connected with two helium pipes (low pressure $< 20\,\text{bar}$ and high pressure $\approx 20\,\text{bar}$). To cool the hydrogen, gas pipes are winded directly around the two stages of the cold head to ensure an optimal heat exchange. Additionally, the gas pipes consists of copper due to their higher thermal conductivity ($\lambda_{\text{copper},20\,°\text{C}} = 384\,\text{W/Km}$) than for stainless steal ($\lambda_{\text{stainless steal},20\,°\text{C}} = 14\,\text{W/Km}$) [F$^+$05]. Only the gas transfer pipes between the two stages and the supply line to the cold head are made of stainless steal because the heat exchange to the surrounding should be as small as possible to reduce the loss of cooling power.
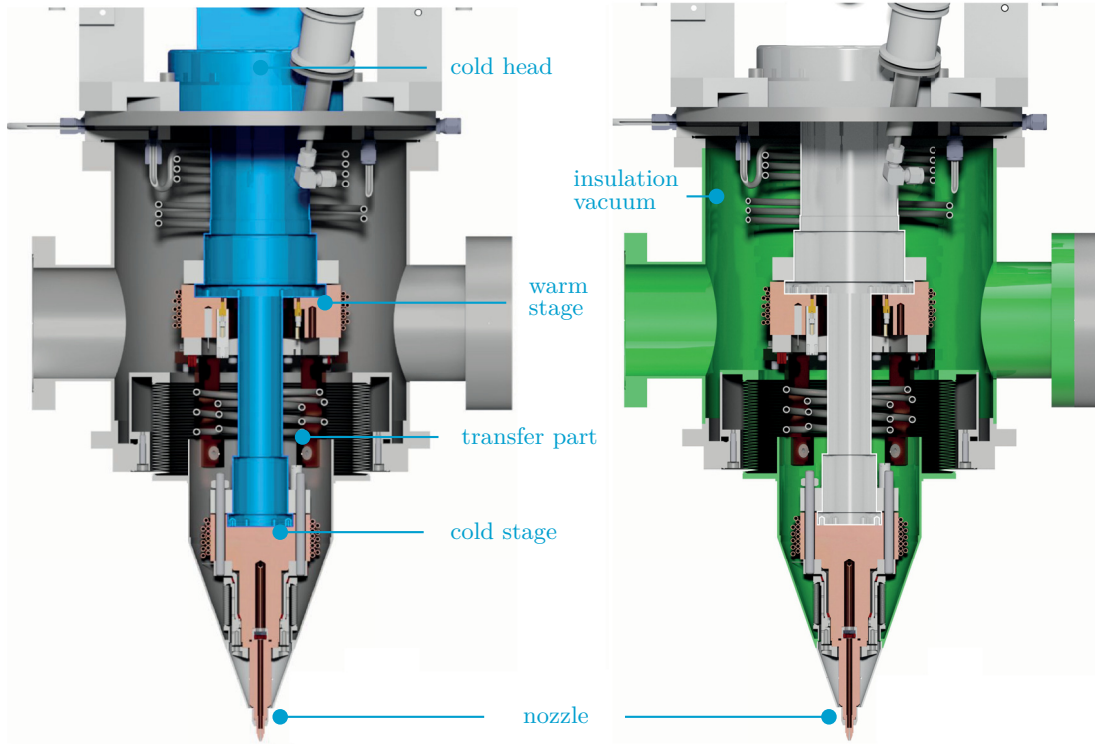
Figure 2.5: Schematic sketches of the MAGIX target as a typical example of a Münster cluster-jet target source. *Left*: Highlighted in blue is the used cold head to cool the gas in front of the nozzle. The Laval nozzle is mounted on the cold stage of the cold head. The gas pipes around the cooling parts of the cold head consist of copper for an optimal heat exchange. The pipes in-between the cooling parts are made of stainless steel to reduce heat transfer between these stages. *Right*: Highlighted in green is the insulation vacuum to reduce the heat transfer to the environment for an optimal cooling of the gas. Generated by D. Bonaventura, edited.

On the cold heads cold stage the Laval nozzle is mounted and sealed with an indium ring. However, in the framework of this thesis a new improved sealing was developed which ensures a clean extraction of the nozzle and is reusable in comparison to the previous used indium sealing (see chapter 3). An additional nozzle holder presses the nozzle with fittings on the cold head. To measure the gas temperature in front of the nozzle silicon diodes are installed at the cold and warm stage of the cold head. Furthermore, to adjust this temperature heating cartridges are mounted on both stages. The readout of the diodes and the control of the heating cartridges is done via a Lakeshore device. The cold head including the gas pipes are placed in the insulation vacuum chamber with pressures less than 10^{-4} mbar to reduce the heat transfer (Fig. 2.5). Based on these Münster cluster source principles, every cluster-jet target is designed, with specific adaptations and specialisations to the individual requirements for the different experiments.

3 Laval Nozzles for Cluster-Jet Targets

The Laval nozzle is one of the main components of a cluster-jet target. The specific convergent-divergent shape of the Laval nozzle generates a supersonic flow of the target material at the narrowest point of the nozzle. Supported by the adiabatic expansion the target gas atoms or molecules condensate to clusters. Essential for the production of clusters are the properties of the Laval nozzle. The short inlet zone converges to the narrowest point of the nozzle and merges into the divergent, long outlet zone. The production of a small inner diameter in combination with the long trumpet part with a well defined opening angle represents a major technical challenge.

In the past these fine Laval nozzles were produced at CERN (Conseil européen pour la recherche nucléaire) but the manufacture was discontinued. Currently, CERN re-established its production process line [Kho18]. Nevertheless, to ensure the production of these fine Laval nozzles for future internal targets and to provide a variety of different nozzle geometries with respect to different experiments an improved production process based on the initial CERN production was recently developed at the University of Münster. This chapter describes the various production processes optimised to the requirements on the Laval nozzle geometries for the different cluster-jet targets and experiments which are topic of this thesis. The detailed investigations on the performance of the nozzles are described in chapter 5.3 and 7.2.
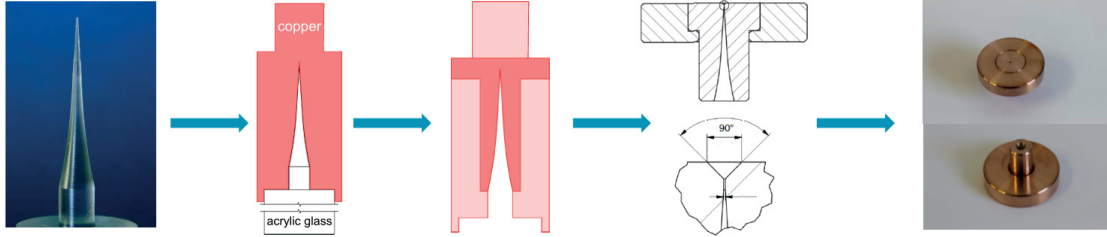
3.1 Production Process of the $\overline{\text{P}}$ANDA Cluster-Target Nozzles

The Laval nozzles produced at CERN provide a stable and well defined cluster beam with high thicknesses. Therefore, the production process developed at the University of Münster is based upon the former CERN production process. The objective is to manufacture Laval nozzles with the same inner geometry (see Fig. 2.3) of the CERN nozzles with an inner narrowest diameter of roughly $30\,\mu\text{m}$.

The CERN production process used a counterpart of the outlet zone made out of steel, whose surface was filed [CER83]. By the galvanic deposition of copper, the nozzle body was formed around the steel pin and the nozzle shape was turned out. Then the pin was mechanically extracted and the inlet zone and connection to the outlet zone was performed via spark erosion.

Monolithic Copper Nozzles

The first established production process is shown in Figure 3.1 and was patented [DBT13]. In the first step, the counterpart of the long outlet zone of 17 mm is turned out of acrylic glass with a tip of roughly 30 μm. The first 8 mm of the outlet zone after the narrowest inner diameter follow a constant opening angle of 7° and pass over in an additionally radius of $R = 60$ mm over the last 9 mm.

**Figure 3.1:** Production process for the $\overline{\text{P}}$ANDA Cluster-Jet Nozzles. In a first step, the counterpart of the nozzle is turned out of acrylic glass. Then, by the galvanic deposition of copper, the nozzle body is formed. After the extraction of the acrylic glass the 90° cone bore as the inlet zone is provided. The connection between inlet and outlet zone is either performed with a laser technique or drilled with a micro drill. At a last step, the nozzle is shrunk with the nozzle holder to fix the nozzle on the cold heads cold stage. Images taken by W. Hassenmeier and D. Bonaventura.

By the galvanic deposition of copper, the nozzle body is formed around the counterpart and the final size and shape is turned out. Chloroform is used to ensure an accurate and clean extraction of the acrylic glass out of the inner nozzle geometry. Afterwards, the inlet zone, a 1 mm long 90° cone bore is drilled from the opposite side into the nozzle body. The now absent connection between inlet and outlet zone is realised via two different processes. The first one is performed by the Micreon GmbH using ultra short laser pulses to drill the connection [Mic]. Thereby, the achieved narrowest inner diameter varies from 15 μm to 100 μm due to the complex geometry of the workpiece. The second one uses a drill with a diameter of 30 μm from SPHINX Werkzeuge AG to drill the passage in combination with the laser technique. There, most of the nozzles, have a narrowest inner diameter of roughly 30 μm. The nozzle is shrunk with a ring to fix the nozzle at the cold stage of the cold head.

In the framework of this thesis a new special polyimide sealing was developed and established. The new sealing allows for a clean extraction of the nozzles from the cold stage compared to the previous used indium sealing. Thereby, the blocking of the nozzle due to remainings of the indium sealing is avoided and the sealing is reusable. As well as the indium sealing, the new sealing, works even at cryogenic temperatures and is radiation resistant which makes it ideally suitable for application in cluster-jet targets used at accelerators.

One of the first produced Laval nozzles with the connection between inlet and outlet zone provided by the use of the laser technique with a narrowest inner diameter of roughly 100 μm was cut via wire erosion to look inside the nozzle (see Fig. 3.2). The inner

geometry is clearly visible, but obviously the narrowest diameters of the inlet and outlet zone are displaced to each other resulting in an incline connection between the two zones. This might originate from the counterpart out of acrylic glass which bends a little at the fine top during the galvanic process. Therefore, investigations on the necessary length of the Laval nozzle were performed (chapter 5.3) to simplify this part of the production process to ensure a reliable and reproducible production of the Laval nozzles.
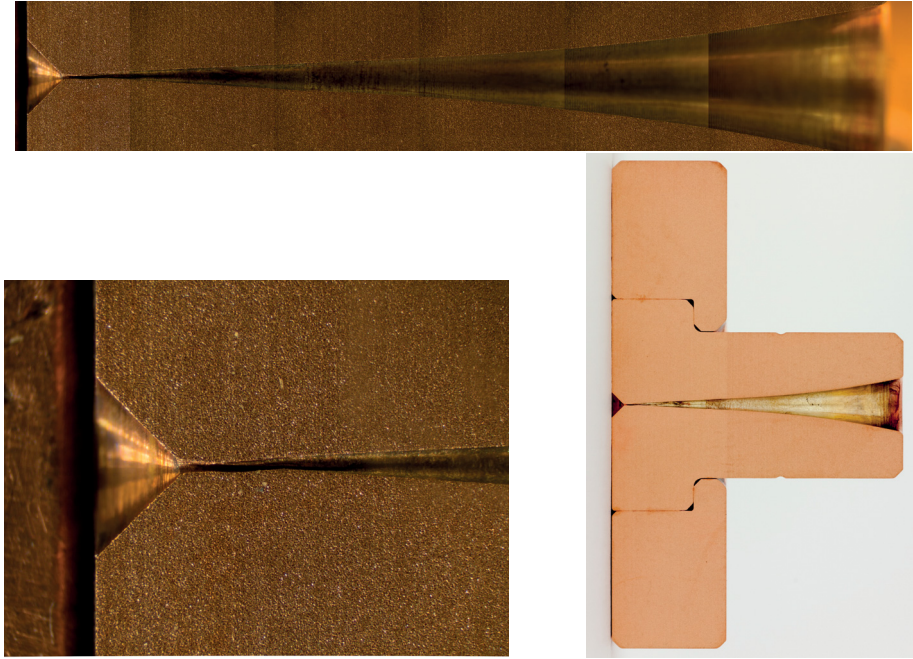

Figure 3.2: Cut through a Laval nozzle by wire erosion. *Top*: Cut through over the full length of the nozzle. *Bottom, left*: The inlet zone, the narrowest inner diameter and the first few millimetre of the outlet zone. The inlet and outlet zones are displaced to each other resulting in an incline connection between them. *Bottom, right*: View of the complete nozzle which was halved. Pictures taken by D. Bonaventura.

Glass Nozzle

A second production process, which was carried out simultaneously to the previous explained process, results in glass nozzles. The company LightFab produced by the selective laser-induced etching of glass the Laval nozzle [Lig]. Due to the available used optics in the year 2015, when the presented nozzle was produced, the size of the nozzle was limited to 3 mm (Fig. 3.3). Currently, larger sizes up to 10 mm are realisable [Lig]. To adapt the nozzle to the geometry of the nozzle seat on the cold stage of the cold head, an adaptation system was developed (Fig. 3.4). The small glass nozzle is sealed with a conical cylindrical polyimide sealing in the nozzle holder and fixed therein with an aluminium ring with thread.

Figure 3.3: Picture of the glass nozzle manufactured by the selective laser-induced etching of glass. The size of the nozzle is limited by the used optics. Picture taken by D. Bonaventura.
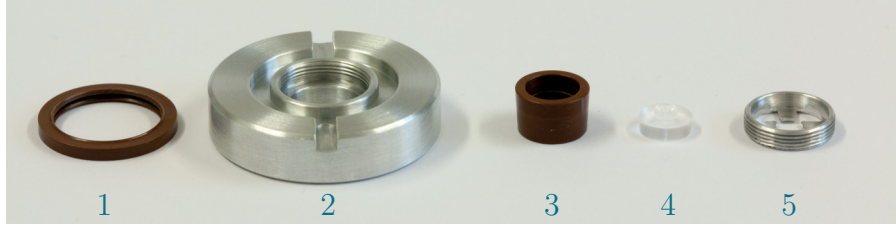
Figure 3.4: Picture of the glass nozzle adaptation system. The small glass nozzle (4) is sealed with a conical cylindrical polyimide sealing (3) in the nozzle holder manufactured of aluminium (2). The nozzle is fixed in the sealing with an aluminium ring with thread (5). The nozzle holder is sealed with the polyimide sealing (1) and fixed with a retaining ring on the cold stage of the cold head. Picture taken by D. Bonaventura.

3.2 Production Process of the GSI Nozzles

An internal target experiment at the ESR storage ring for heavy ions at the GSI facility (Helmholtzzentrum für Schwerionenforschung) in Darmstadt (Germany) uses Laval nozzles to provide cluster beams with different gases as target material from hydrogen to xenon resulting in target thicknesses between 10^{10} atoms/cm^2 to 10^{14} atoms/cm^2 [P$^+$15].

The geometry for the GSI nozzle has to be the same as for the $\overline{\text{P}}$ANDA nozzles except the narrowest inner diameter, which has to be below $15\,\mu$m [Pet15, P$^+$15]. This small narrowest inner diameter results in a low gas flow in the interaction chamber leading to the required vacuum conditions in the ESR. To ensure such a fine narrowest inner diameter, a modified production process was used. The counterpart of the outlet zone and additionally, a counterpart of the inlet zone was manufactured out of aluminium. Using an apparatus with micrometer screws, both parts are adjusted on top of each other. This system was placed in a galvanic bath and the nozzle was monolithically formed around the two parts. After the extraction of the two aluminium parts, the connection between the inlet and outlet zone was provided using the laser technique.

3.3 Production Process of the MAGIX Nozzles

The production process for the Laval nozzles used for the jet target MCT-M for the MAGIX experiment is based on the process for the $\overline{\text{P}}$ANDA cluster-jet target Laval nozzles. Due to the larger narrowest inner diameter of $0.5\,$mm, the nozzle production process was slightly modified. As first step, the counterpart of the nozzles inner geometry was manufactured

as one single aluminium component including the inlet zone, the narrowest inner diameter and the outlet zone (see Fig. 3.5, top). Then, by the galvanic deposition of copper, the nozzle body is formed around the counterpart (see Fig. 3.5, bottom). Afterwards, the counterpart is mechanically extracted, the final outer size and shape of the nozzle body is formed, and the nozzle is shrunk on a nozzle holder (Fig. 3.6). This composite nozzle is mounted with an union nut on the nozzle extension and sealed in-between with the polyimide sealing. This complete nozzle adaptation system is installed via a retaining ring fixed with screws at the cold stage of the cold head and also sealed with the polyimide sealing.
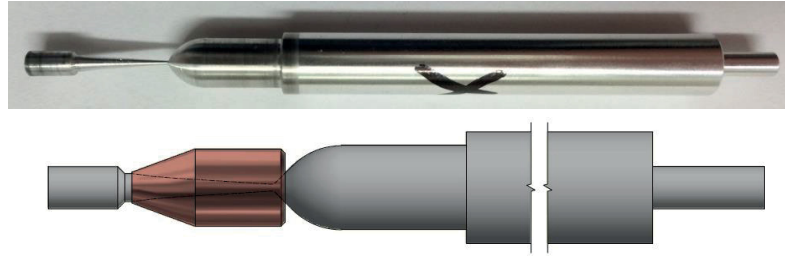

Figure 3.5: Counterpart of the Laval nozzle for the jet target MCT-M for the MAGIX experiment. *Top*: The counterpart, manufactured as one single component, comprise the inlet zone, the narrowest inner diameter and the outlet zone and is made out of aluminium. *Bottom*: Due to the galvanic deposition of copper, the nozzle body is formed around the counterpart. Generated by D. Bonaventura.

Figure 3.6: The final Laval nozzle for the jet target MCT-M for the MAGIX experiment. *Left*: The nozzle holder (right) and the Laval nozzle (left) which is shrunk on the nozzle holder. *Right*: The final nozzle consisting of the Laval nozzle and the nozzle holder. Pictures taken by D. Bonaventura.

Moreover, the composite design of a nozzle extension in combination with a short Laval nozzle with a full length of 10 mm results in a conical tip of 20° of the target to ensure a high detector acceptance at the MAGIX experiment (Fig. 3.7) [Gri]. The use of the nozzle extension and the application of bellows allows for an insulation vacuum chamber up to the nozzle area to minimize the heat exchange between the interaction chamber and the cryogenic parts of the target.
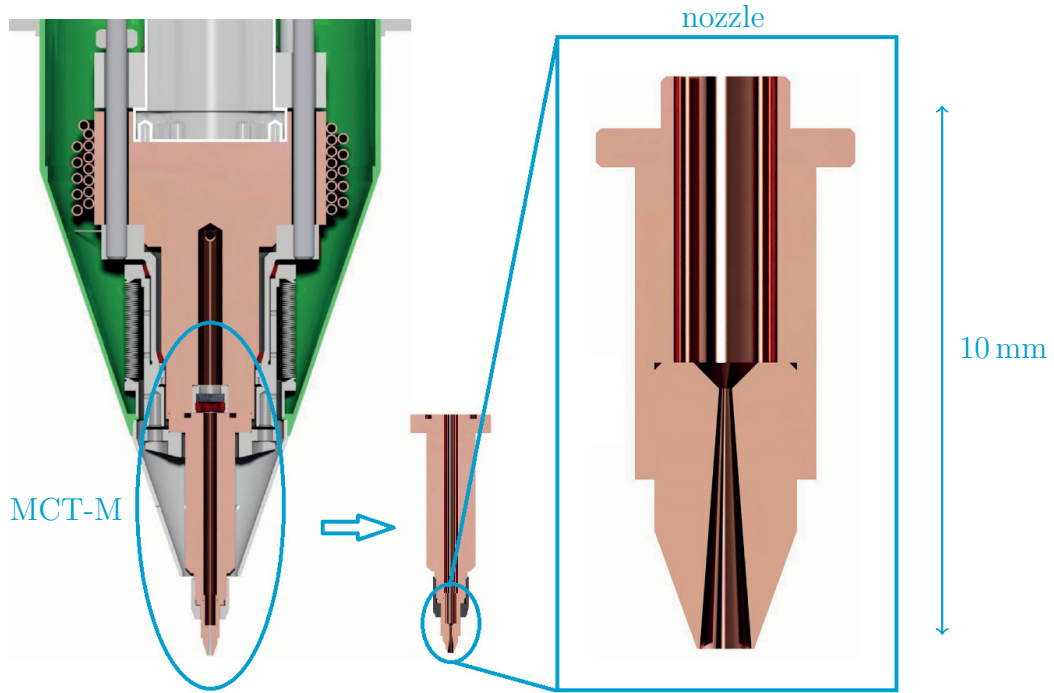
Figure 3.7: The conical tip of 20 ° of the jet target MCT-M for the MAGIX experiment. The Laval nozzle is mounted with a nozzle extension on the cold stage of the cold head. The nozzle is fixed with an union nut on the nozzle extension and comprise the inner geometry. This composite design leads to an insulation vacuum chamber (green) reaching up to the nozzle area to ensure a minimum heat transfer. Generated by D. Bonaventura, edited.

4 $\overline{\text{P}}$ANDA Experiment

The upcoming $\overline{\text{P}}$ANDA experiment (antiProton ANnihilation at DArmstadt) experiment at the future Facility for Antiproton and Ion Research (FAIR) at Darmstadt will use proton-antiproton annihilations to answer the still open questions about the strong interaction, existence of exotic particles, and many other topics. First, the standard model of particle physics, the strong interaction and other topics concerning the theory of hadrons are discussed in this chapter. Then, the FAIR facility including the $\overline{\text{P}}$ANDA experiment is described in detail. At last, the $\overline{\text{P}}$ANDA cluster-jet target prototype is presented, as one of the targets with which measurements have been performed within this thesis.

4.1 Theory of Hadrons

The well established standard model of particle physics describes the known particles of our universe and makes predictions which are nowadays experimentally confirmed, but there are still open questions remaining which cannot be answered within this theory. This includes the deeper understanding of the strong interaction, e.g., the theoretically possible but not yet seen exotic particles, like glueballs and quark molecules. Additionally, the theory of the Quantum ChromoDynamics (QCD) in the low energy regime is not fully understood, including the running coupling constant and the phenomenon called confinement. Due to this effect quarks exist not individually which makes their investigations to a major challenge. The future $\overline{\text{P}}$ANDA (antiProton ANnihilation at DArmstadt) experiment at the future Facility for Antiproton and Ion Research (FAIR) at Darmstadt will face these open questions. The accessible momentum and corresponding mass range for example enables the study of heavy mesons, charmonium states, and possible candidates for glueballs, hybrids, and quark molecules. In order to answer these questions at the $\overline{\text{P}}$ANDA experiment an accelerated antiproton beam interacts with a cluster beam consisting of protons generated by a cluster-jet target described and studied within this thesis.

Standard Model and Strong Interaction

The standard model of particle physics (Fig. 4.1) characterises the elementary particles into quarks, leptons (electron, electron neutrino, muon, muon neutrino, tauon, and tauon neutrino), gauge bosons (gluon, photon, Z boson, and W boson), and the Higgs boson. There exist twelve quarks (up, down, charm, strange, top, and bottom, or u, d, c, s, t, and b, and their anti quarks) which are fermions and therefore have spin 1/2. The uptype quarks up, charm, and top carry the charge $+2/3$ of the elementary charge e and the downtype quarks down, strange, and bottom -1/3 e. Respectively, the anti-quarks carry

the same charge but with opposite sign.

Furthermore, three of the four fundamental forces (electromagnetic, weak, and strong interaction) are described within this theory. The fourth force, gravity, is not yet agreed within this model. The strong interaction mediates between all particles which carry a colour charge, like quarks, and the gluon. Gluons are spin 1 and massless particles and the exchange particles of the strong force mediating between quarks and themselves. The colour charge is a quantum number with six possible values: (anti)red, (anti)blue, and (anti)green. The effect named confinement describes the fact, that quarks cannot exist isolated. The needed energy to separate a quark-antiquark pair exceeds the energy to produce a new pair of them. Using the bag model for this phenomenon, the gluon-gluon interaction also known as colour field between two quarks described by a tube extends its range until it splits and forms two new quark pairs.

Figure 4.1: Elementary particles of the standard model with their masses and the quantum numbers spin and charge. Shown are the six quarks (up, charm, top, down, strange, and bottom), the six leptons (electron, electron neutrino, muon, muon neutrino, tauon, and tauon neutrino), and the four gauge bosons (gluon, photon, Z boson, and W boson). The Higgs Boson, discovered 2012, awarded with the Nobel prize for the theory of his mechanism, explains the origin of mass [A$^+$12, Nobb]. Generated by E. Köhler, edited, [B$^+$on].

A non-abelian gauge theory known as Quantum ChromoDynamics (QCD) describes the strong interaction by assuming the Lagrangian L$_{\mathrm{QCD}}$ [B$^+$on, Pel15]

$$\mathrm{L}_{\mathrm{QCD}} = \sum_q \overline{\Psi}_q \left(\mathrm{i}\gamma^\mu D_\mu - m_q \right) \Psi_q - \frac{1}{4} F_{\mu\nu} F^{\mu\nu} \qquad (4.1)$$

with $q = u, d, c, s, t$ and b, the imaginary unit i, the dirac matrices γ^μ, the covariant derivative D_μ, and the quark mass term m_q. The first term is the gluon-quark interaction, the second term is the quark mass term, and the last term describes the gluon-gluon self interaction. The quark field spinor is denoted with Ψ_q and his dirac adjoint with $\overline{\Psi}_q$. The field tensor $F_{\mu\nu}$ in QCD is defined within

$$F_{\mu\nu} = \partial_\mu \mathcal{A}_\nu^A - \partial_\nu \mathcal{A}_\mu^A - g_s f^{ABC} \mathcal{A}_\mu^B \mathcal{A}_\nu^C \tag{4.2}$$

with the gluon fields $\mathcal{A}_\mu^C$ where C is running from 1 to 8 for the eight gluons, g_s the coupling constant, and f^{ABC} as the structure constant of the SU(3) group. The last term is the gluon-gluon self interaction term and is a striking difference of the QCD in comparison to the QED (Quantum ElectroDynamics). The Lagrangian of QED characterises processes of the electromagnetic force, where the gauge boson, photon, has no self interaction. Additionally, the gluon self interaction term is the origin of the confinement, which does further imply the running coupling constant α_s in first order approximation [Loh05]

$$\alpha_s = \frac{12\pi}{(33 - 2N_f)\ln\mid q^2/\Lambda^2 \mid}, \tag{4.3}$$

which is depending on the energy of the participating particles. Therein, N_f represents the number of quark flavour, q^2 the momentum transfer, and $\Lambda^2 \approx 250\,\text{MeV}/c$ is a scaling parameter [P$^+$08]. This coupling constant defines the quark-antiquark potential (first order approximation)

$$V_s = -\frac{4}{3}\frac{\alpha_s}{r} + kr, \tag{4.4}$$

which neglected the spin-spin interaction, the spin-orbit interaction and other higher order tensor terms. In the case of a large distance r between two quarks, the coupling constant α_s becomes also large and this results in the effect of the confinement and the production of a new quark-antiquark pair at a critical distance. In the opposite case, that the distance r and therefore the coupling constant α_s becomes small, the quark-antiquark potential decreases (see Fig. 4.2).

Hadrons

Particles underlying the strong interaction are named hadrons. Most known representative of hadrons are for example baryons composed of three quarks like the proton or a quark and antiquark pair called meson. Protons consist of two u quarks and a d quark in contrast to the neutron composed of two d quarks and an u quark. A prominent meson is the positive charged pion π^+ containing an u quark and a $\overline{\text{d}}$ quark. The baryons as well as mesons are colourless, because in the case of a baryon the colours red, blue, and green of the three quarks add up to white and by a meson the colour and the anti-colour of the quarks result in a colour-neutral state.
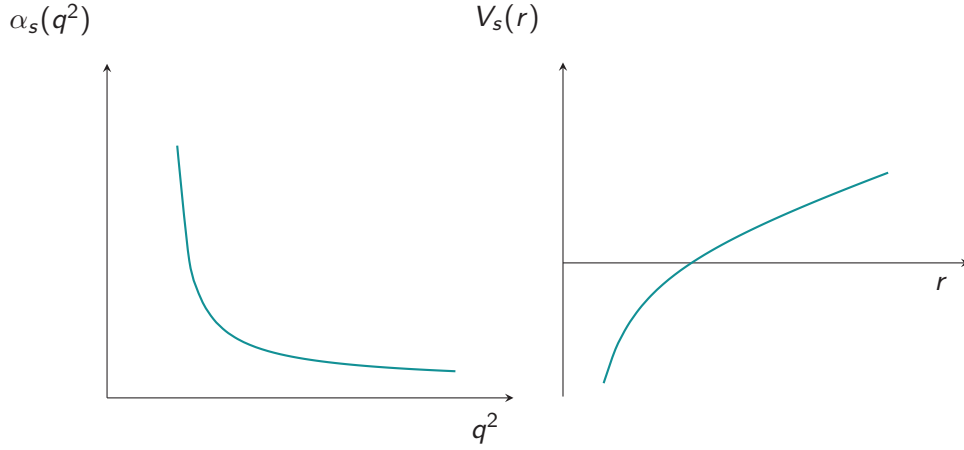
Figure 4.2: Courses of the coupling constant α_s (*left*) and the quark-antiquark potential V_s (*right*). For large distances r between two quarks (small q^2 values), the coupling constant and the potential increases and results in the production of a new quark-antiquark pair (confinement). In case for small distances r (large q^2 values), the coupling constant and the potential decreases. Generated by E. Köhler, edited.

Moreover, hadrons can be characterized by their quantum numbers, the total angular momentum $\vec{J}$, the total parity P, and the charge conjunction C (only for mesons). The angular momentum $\vec{J}$ is defined by

$$\vec{J} = \vec{S} + \vec{L}, \tag{4.5}$$

where $\vec{S}$ is the total spin and $\vec{L}$ the total orbital momentum.
Quarks have the parity $P(q) = 1$ in contrast to anti-quarks with parity $P(\overline{q}) = -1$. Therefore, the parity of the baryons result in

$$P(qqq) = P(q) \cdot P(q) \cdot P(q) \cdot (-1)^l = (-1)^l \tag{4.6}$$

and for mesons

$$P(q\overline{q}) = P(q) \cdot P(\overline{q}) \cdot (-1)^l = (-1)^{l+1}. \tag{4.7}$$

Thereby, l is defined as the orbital angular momentum which can takes zero (ground state) or a positive integer number (radial excited state).
The charge conjunction C

$$C = (-1)^{(l+s)} \tag{4.8}$$

contains the spin of the quark pair that is zero for anti-parallel and 1 for parallel. Baryons described by their quantum number J^P can be further divided into octets $(1/2^+)$ or decuplets $(3/2^+)$. Mesons with their quantum number $J^{P(C)}$ are specified into, e.g., pseudo scalar mesons $(0^{-(+)})$, vector mesons $(1^{-(-)})$, and heavy mesons for example the B meson named by its heaviest constituent the b or $\overline{b}$ quark. Other representative of heavy
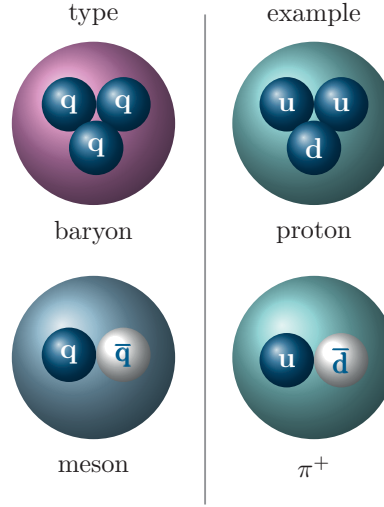
Figure 4.3: Baryon and meson with their quarks and anti-quark. The proton, as a representative of the baryons contains two up and a down quark. The positive pion π^+, a prominent meson, consisting of an up quark and anti-down quark. These particles are colourless. Generated by E. Köhler, edited.

mesons are the quarkonia consisting of a quark and its anti-quark like the charmonium ($c\bar{c}$).
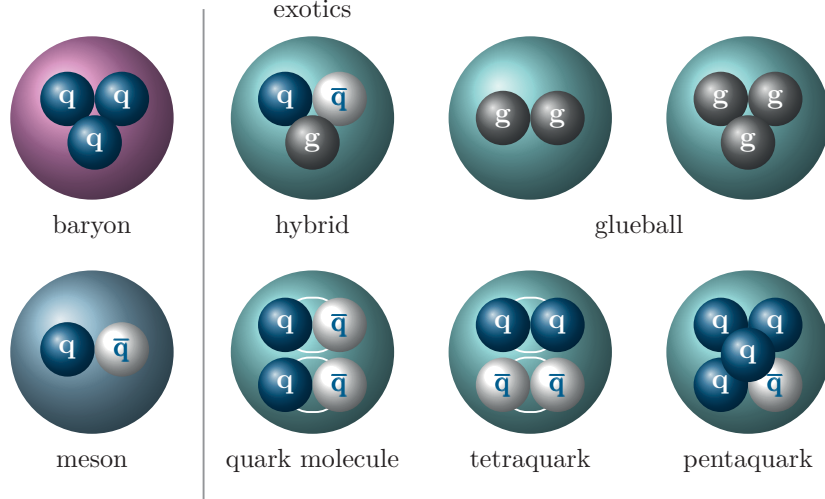
Exotics

Hadrons which do not fit in the standard scheme are named exotics. Their appearance is explained by different QCD models, i.e., lattice QCD, bag model, and QCD sum rules. The most possible exotics are shown in Figure 4.4.

Hybrids consist of a quark and anti-quark pair with an excited colour field between them ($q\bar{q}g$). Due to the excitation of the gluon, hybrids can realise quantum numbers which are forbidden for the standard mesons. Their mass ranges from $1.4\,\mathrm{GeV}/c^2$ to $1.9\,\mathrm{GeV}/c^2$ depending on the model (bag model or lattice QCD) [B$^+$on]. Prominent candidates for hybrids were studied at the Brookhaven National Laboratory (BNL), for example the $\pi_1\,(1400)$ or the $\pi_1\,(1600)$ which was also investigated by the Crystal Barrel experiment [Kle00, A$^+$98]. In addition the BARBAR and Belle collaborations observed the Y(4260) state as a candidate for hybrids [Y$^+$, A$^+$05, Y$^+$07].

Baryons only consisting of gluons are called glueballs (gg or ggg). Glueballs have no quark content and their upper mass limit is $5\,\mathrm{GeV}/c^2$ calculated by lattice QCD [MP99, C$^+$06]. Investigations on glueballs are difficult due to their mass ground state of $1700\,(100)\,\mathrm{MeV}/c^2$ and large decay widths of $250\,\mathrm{MeV}/c^2$, overlapping with scalar mesons [C$^+$06, Ams98]. The $f_0\,(1500)$ was analysed by the Crystal Barrel experiment and the WA102 Collaboration through two different production processes (proton-antiproton annihilation and proton-proton collision) and is the most promising candidate for a glueball [Ams98, B$^+$99].

Beside the already mentioned exotics other exotic states are possible. Exotics composed of two meson pairs ($q\bar{q}$ - $q\bar{q}$) are called quark molecules. The states $a_0\,(980)$ and $f_0\,(980)$ are the most prominent investigated candidates for quark molecules [Y$^+$]. In comparison

to these states a diquark-antidiquark pair (qq$\overline{qq}$) is named tetraquark. Also, a pentaquark consisting of four quarks and an anti-quark (qqqq$\overline{q}$) is feasible. Herein, Θ^+ as a candidate for a pentaquark seen by the Large Hadron Collider beauty (LHCb) collaboration is still under discussion [P$^+$16, A$^+$15].

Figure 4.4: Baryon and meson with their quark content. In comparison some feasible exotics are shown. Hybrids consisting of a quark and anti-quark, and a gluon. Glueballs only comprising of gluons. Mixtures of quarks and antiquarks without gluons called quark molecules, tetraquark, and pentaquarks. Generated by E. Köhler, edited.

## 4.2 $\overline{P}$ANDA Experiment

The future Facility for Antiproton and Ion Research (FAIR) will be an additional research facility besides the already existing Helmholtzzentrum für Schwerionenforschung (GSI) at Darmstadt. The experiments located at FAIR will face different open questions in the science of QCD nature. The $\overline{P}$ANDA (antiProton ANnihilation at DArmstadt) experiment which uses the annihilation of protons and antiprotons will focus on the search for exotics and the fundamentals of the strong interaction.

Facility for Antiproton and Ion Research FAIR

The forthcoming FAIR facility (Facility for Antiproton and Ion Research) at Darmstadt will address a wide variety of questions in different topics of natural sciences. The enhancement of the already operating GSI (Helmholtzzentrum für Schwerionenforschung) will face in detail these four international research projects [GF06b]:

- Atomic, Plasma Physics and Applications (APPA)
  - BIOlogy and MATerial science (BIOMAT)
  - Facility for Low-energy Antiproton and heavy Ion Research (FLAIR)

- High Energy Density matter generated by Heavy iOn Beams (HEDgeHOB)

- Stored Particles Atomic Research Collaboration (SPARC)

- Warm Dense Matter (WDM)

• Compressed Baryonic Matter (CBM)

• NUclear STructure, Astrophysics and Reactions (NUSTAR)

  - DEcay SPECtroscopy/HIgh-resolution SPECtroscopy (DESPEC/HISPEC)

  - ELectron-Ion Scattering in a storage ring (ELISe)

  - Isomeric beams, LIfetimes ans MAsses (ILIMA)

  - Laser Spectroscopy (LaSpec)

  - precision Measurements of very short-lived nuclei with Advanced Trapping System (MATS)

  - Reactions with Relativistic Radioactive Beam (R3B)

  - Super FRagment Separator (SuperFRS)

• antiProton ANnihilation at DArmstadt ($\overline{P}$ANDA)
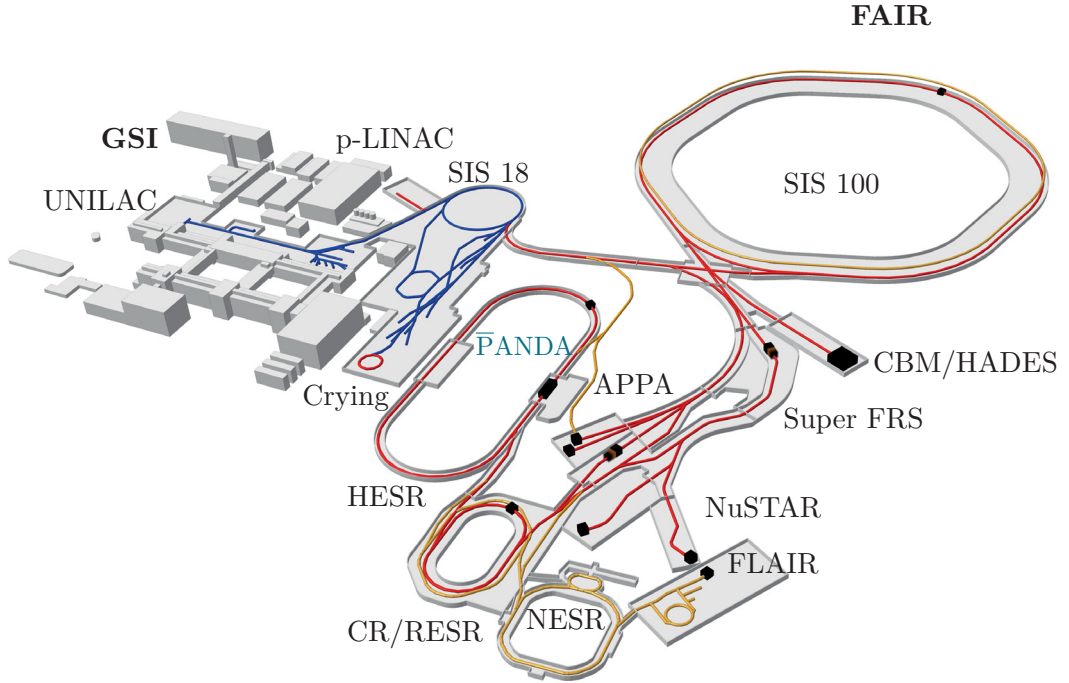
Figure 4.5: FAIR facility with already existing UNILAC linear accelerator, SIS 18 synchrotron, and heavy ion storage ring ESR illustrated in blue. The future components which will be built up modularly are shown in red. Plotted in yellow are possible further upgrades of the facility (Picture copyright by FAIR/GSI).

The final FAIR facility which is shown in Figure 4.5 will be constructed modularly. The first module 0 corresponds to the ion synchrotron SIS 100 which construction was

started in 2017. CBM and HADES are module 1 and module 2 cantaining NUSTAR and SuperFRS. The module 3 includes $\overline{P}$ANDA and the first experiments will start in the end of 2022 by APPA and SPARC [Aug, Het17].

For the $\overline{P}$ANDA experiment FAIR provides all necessary components for the antiproton beam, including the production, collection and acceleration. The proton beam for the annihilation process will be allocated by a cluster-jet target designed, built up and operated by the University of Münster (chapter 4.3).

The foreseen p-LINAC (proton LINear ACcelerator) accelerates protons up to an energy of 50 MeV. Then the proton beam will be injected in the already available SIS 18 synchrotron and leaves it bunched with an energy of 2 GeV. The following SIS 100 accelerates the bunches of protons (2.5×10^{13}) to an energy of 29 GeV. These protons directed on a target produce antiprotons through the reaction [K$^+$12, GF06b]

$$p + p \rightarrow p + p + p + \overline{p}. \tag{4.9}$$

The total energy $E_{\text{total}}^{\text{cm}}$ of a two body system in the center of mass system can be calculated by the relativistic energy mass relation [Hin08]

$$E_{\text{total}}^{\text{cm}} = \sqrt{2E_1 m_2 c^2 + m_1^2 c^4 + m_2^2 c^4}, \tag{4.10}$$

where E_1 and m_1 represents the energy and mass of the projectile and m_2 the mass of the stationary target. In the production process of the antiprotons (see Equation (4.9)) the masses m_1 and m_2 are the proton mass $m_{\text{p}} = 938.27 \, \text{MeV}/c^2$. Therefore, the total energy changes

$$E_{\text{total}}^{\text{cm}} = \sqrt{2E_1 m_{\text{p}} c^2 + 2m_{\text{p}}^2 c^4} \geqslant 4m_{\text{p}}c^2. \tag{4.11}$$

Consequently, the threshold energy of this reaction results in $E_{\text{threshold}} = 6m_{\text{p}}c^2 = 5.63 \, \text{GeV}/c^2$ [Hin08]. The produced antiprotons will be collected (10^8 antiprotons) and pre-cooled in the Collector Ring (CR) and enter the High Energy Storage Ring (HESR) with a momentum of 3.8 GeV/c [GF06a].

High Energy Storage Ring HESR

The $\overline{P}$ANDA experiment will be located at the High Energy Storage Ring (HESR) which will provide antiprotons in the momentum range of 1.5 GeV/c - 15 GeV/c. This corresponds to an energy between 0.83 GeV and 14.1 GeV [PAN12d, PAN09].

The HESR will be equipped with Radio Frequency (RF) cavities [PAN12d, T$^+$, S$^+$]. These resonators are used to modify the beam, especially acceleration, deceleration and bunch manipulation. Due to the interaction of the antiproton beam with targets, the beam is heated up. To counteract these beam heating effect two beam cooling systems will be installed at the HESR. The stochastic cooling comprising of a pick-up and kicker will use a barrier bucket cavity which generates a bunch filling 80 % to 90 % of the storage ring [PAN09, S$^+$, T$^+$]. The pick-up electrode transfers the information about the particle's position to the kicker electrode which adjust the beam angle. The electron cooling system

merges a cold electron beam with the heated ion beam. Therefore, a momentum transfer appears which improves the spread of the antiproton momentum. The electron cooler (2 MeV) from the COoler SYnchrotron (COSY) in Jülich was dicussed as first electron cooler for the start up phase of HESR. Later it should be exchanged by an electron cooler for energies up to 8.9 MeV [D$^+$11b, K$^+$14a].

The HESR can operate in two modes, the High Resolution (HR) and the High Luminosity (HL) mode. The characteristics of these two modes are shown in Table 4.1.

Table 4.1: Characteristics of the two operation modes of the HESR: High Resolution (HR) and High Luminosity (HL) [PAN09, PAN12d].

	High Resolution (HR)	High Luminosity (HL)
momenta	1.5 GeV/c - 8.9 GeV/c	1.5 GeV/c - 15 GeV/c
peak luminosity	2×10^{31} cm^{-2}s^{-1}	2×10^{32} cm^{-2}s^{-1}
number of antiprotons	10^{10} antiprotons	10^{11} antiprotons
momentum spread Δp/p	$\leqslant 4 \times 10^{-5}$	$\sim 4 \times 10^{-4}$

Physics Programm of $\overline{P}$ANDA

The $\overline{P}$ANDA experiment will focus the open questions of the strong interaction and of hadronic matter. Therefore, an antiproton beam with a momentum range between 1.5 GeV/c and 15 GeV/c annihilates with a proton target [PAN12d]. In comparison to an electron-positron annihilation, where all the incoming particles annihilate by exchanging a virtual photon, the proton-antiproton interaction is not quantum number restricted. In this process of annihilation the involved six quarks (proton as well as anti-proton consists of three quarks: uud and $\overline{u}\overline{d}\overline{d}$) have not necessarily to annihilate completely, but rather rearrange. The $\overline{P}$ANDA experiment opens the way for investigations in a mass range of up to 5.5 GeV/c^2 and therefore, the experiment not only can observe standard hadron states in detail, but also search for exotic states like hybrids, glueballs, and quark molecules [PAN12d, PAN09]. Moreover, studies on charmonium, open charm spectroscopy, and hypernuclear physics are possible. Figure 4.6 shows the accessible mass range and momenta of the $\overline{P}$ANDA experiment and also possible particle states which can be studied.

In the past several possible particle states were studied, like 1974 at the Stanford Linear Accelerator Centre (SLAC) and simultaneously at the Brookhaven National Laboratory (BNL). They discovered through electron-positron annihilations the J/ψ state, an excited charmonium state. Two years later the Nobel Price was awarded for this observation [Noba]. A charmonium consists of a charm and an anti-charm quark. This kind of mesons comprising of a quark and its own anti-quark are called quarkonia. The $\overline{P}$ANDA experiment will concentrate on charmonium spectroscopy without quantum number restrictions in the range of the D$\overline{\text{D}}$ threshold at 3.73 GeV/c^2. Thereby, the accuracy of the mass measurements will be in the order of 100 keV/c^2 and the decay width resolution will reach 10 % [PAN09]. Another topic will be the open charm spectroscopy, there the mesons consists of a charm quark and a light quark (up, down, or strange) and
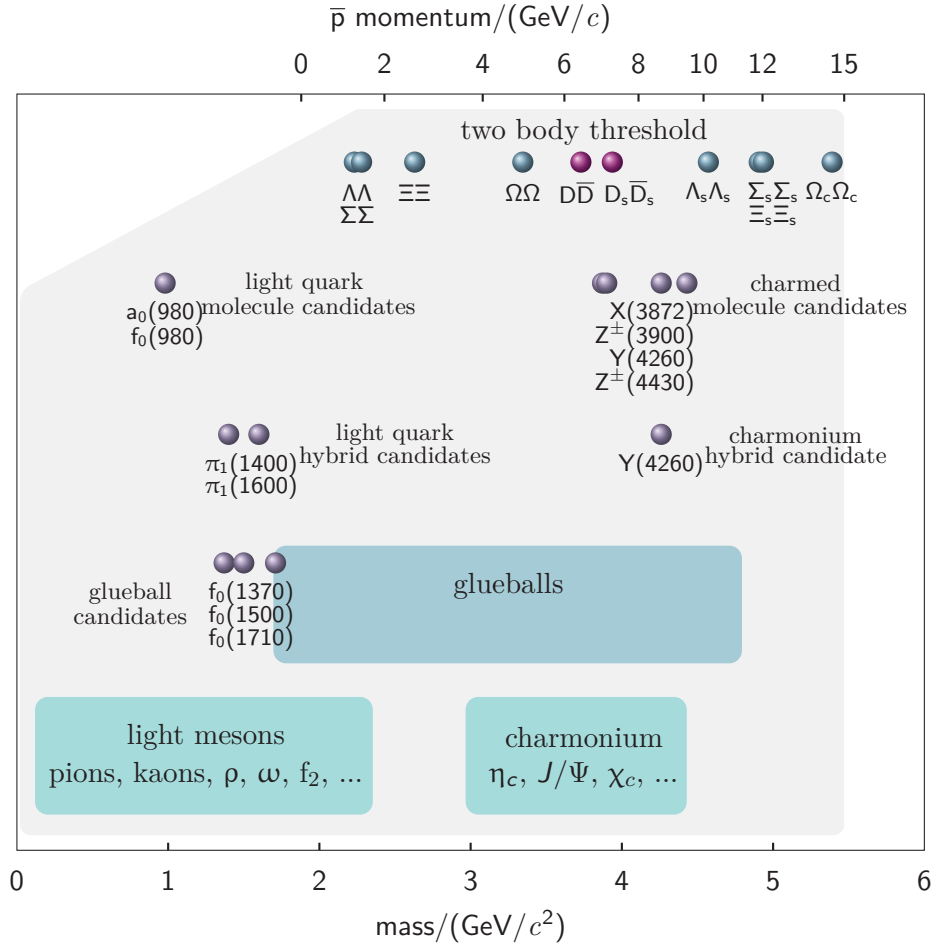
Figure 4.6: Accessible momentum range between $1.5\,\mathrm{GeV}/c$ and $15\,\mathrm{GeV}/c$ shown on the top abscissa and the corresponding accessible mass range up to $5.5\,\mathrm{GeV}/c^2$ on the low abscissa for the $\overline{\mathrm{P}}$ANDA experiment. Plotted are possible explorable hadrons and exotic states with their momentum and mass. In addition the mass ranges of glueballs, light mesons, and charmonium are drawn with filled boxes which will be investigated with the $\overline{\mathrm{P}}$ANDA experiment. Generated by E. Köhler, edited, [PAN12d].

have a charm quantum number unequal zero.

The origin and composition of hadron mass is still an open questions. Due to the confinement quarks cannot be observed individually but calculations allow the determination of their mass. Until now, there is still an inexplicable discrepancy between the mass of a single quark and the mass of hadrons composed of them. One explanation leads to the broken chirality of QCD for hadrons, a distinction in right- and left-handed quarks, which can be repealed if the hadrons are bound in nuclei.

In addition $\overline{\mathrm{P}}$ANDA will investigate the interactions of double hypernuclei and hyperon-hyperon. Hypernuclei are nuclei consisting of nucleons and at least a hyperon. Hyperons

are baryons with at least one charm quark like Λ, Σ, Ξ, and Ω. The interactions will be produced through the two step production process [PAN09]

$$\overline{p}p(n) \rightarrow \Xi^- \overline{\Xi}^+ \left(\overline{\Xi}^0 \right) \tag{4.12}$$

$$\Xi^- + p \rightarrow \Lambda\Lambda. \tag{4.13}$$

All these topics will gain a deeper insight into the strong interaction, e.g., its potential and coupling strength, the hadronic matter, and the nuclear structure which leads to a better understanding of nature.

$\overline{P}$ANDA Experiment

The $\overline{P}$ANDA detector is a fixed internal target experiment. In comparison to collider experiments, where both particle beams where accelerated in opposite directions, in a fixed target experiment, only one beam is accelerated and directed on a target. Due to this composition the products of the interaction have a Lorentz boosted momentum component in forward direction. Therefore, the $\overline{P}$ANDA detector consists of a Target Spectrometer and a Forward Spectrometer. For this purpose two internal targets are planned, a cluster-jet target (chapter 4.3) and a pellet target, whereby, the cluster-jet target will be the first operating target at the $\overline{P}$ANDA experiment. Figure 4.7 shows the interaction point of the anti-proton beam with the cluster-jet target as well as the Target Spectrometer and the Forward Spectrometer [PAN12a, PAN12d].

The **Target Spectrometer (TS)** surrounds the interaction region, provides an angular acceptance of almost 4π, and consists of the following components:

- Micro Vertex Detector (MVD): This detector is directly surrounding the interaction point and is used for precise reconstructions of the vertex point and to observe short-lived particles [PAN12b].

- Straw Tubes Tracker (STT): The particle tracker consists of drift tubes made of aluminium-mylar with a diameter of $1\,\text{cm}$ and an axial length of $150\,\text{cm}$ filled with a mix of $90\,\%$ argon and $10\,\%$ carbon dioxide [PAN12c].

- Gas Electron Multiplier (GEM): The GEMs, up to four layers are planned, track particles in polar angles between $5\,°$ and $22\,°$.

- Detector for Internally Reflected Cherenkov light (DIRC): Planned in disc and barrel shape at the two end caps for particle identification.

- Solenoid: For a successful particle separation and identification the solenoid provides a magnetic field up to $2\,\text{T}$.

The **Forward Spectrometer (FS)** with an angular acceptance of $\pm\,5\,°$ in the vertical and $\pm\,10\,°$ in the horizontal axis comprises of:

- Ring Imaging CHerenkov (RICH): RICH is used for particle identification through aerogel cherenkov counters.

- dipole magnet and drift chambers: This component separates charged particles according to their magnetic momentum of $\pm 10°$ in horizontal and $\pm 5°$ in vertical beam direction.

- LUMInosity detector (LUMI): Scattered antiprotons with polar angles in the range of $3 \, \text{mrad}$ to $8 \, \text{mrad}$ contributes to the determination of the time integrated luminosity.

In addition to these components some are used in both spectrometers (**TS** and **FS**), namely:

- ElectroMagnetic Calorimeter (EMC): Two EMCs consisting of more than 15500 PbWO$_4$ crystals for detectioning photons, electrons, and hadrons are planned. One surrounding the barrel DIRC in the Target Spectrometer and the other one in the Forward Spectrometer [PAN08a].

- MUOn detector (MUO): MUO is used for muon detection [PAN08b].

- Time Of Flight system (TOF): The TOF system provides the velocities of the observed particles.
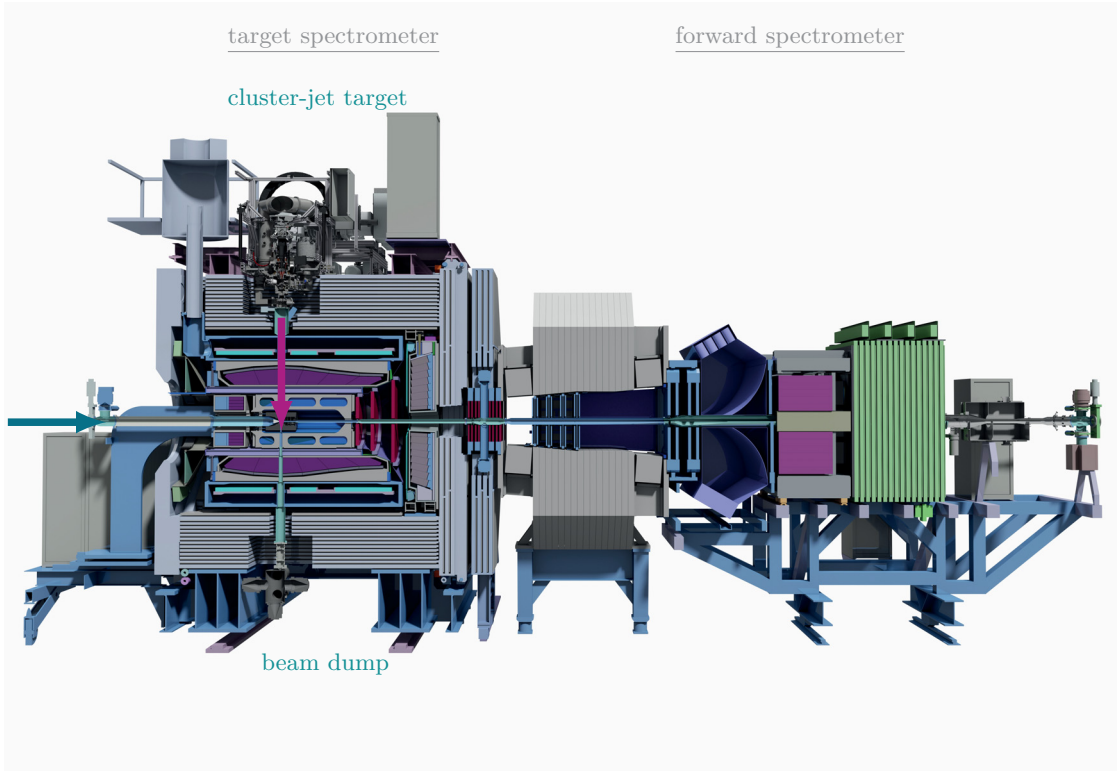
Figure 4.7: The $\overline{P}$ANDA detector comprising of the Target Spectrometer (TS) and the Forward Spektrometer (FS). The complete detector has a length of roughly $15 \, \text{m}$ and a height of roughly $6 \, \text{m}$. Also shown is the cluster-jet target placed on top of the target spectrometer with the cluster beam direction from top to bottom (violet arrow) and the antiproton beam from left to right (green arrow). Generated by D. Bonaventura, edited.
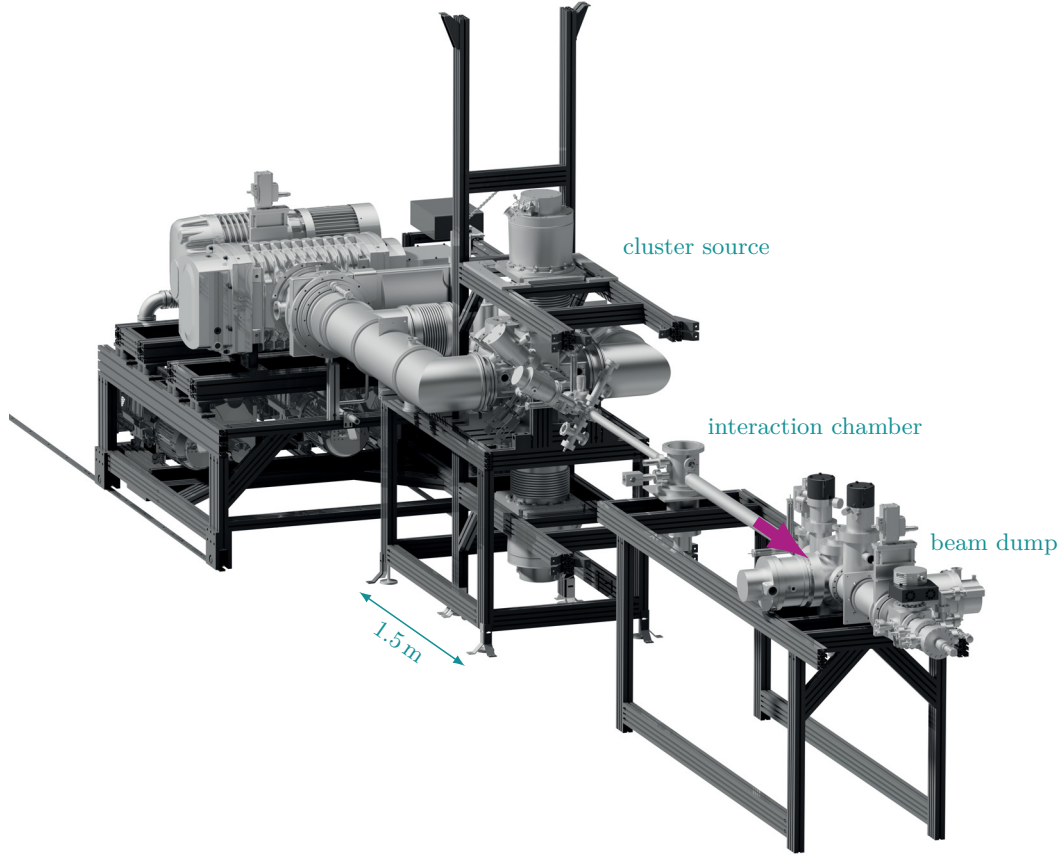
4.3 $\overline{P}$ANDA Cluster-Jet Target Prototype

The $\overline{P}$ANDA experiment is a fixed target experiment. Therefore, only the antiproton beam is accelerated and directed on an internal proton target. A cluster-jet target designed, constructed and set successfully into operation at the University of Münster will be the first operating target at the $\overline{P}$ANDA experiment. Before the design and construction of the final $\overline{P}$ANDA cluster-jet target was started, a cluster-jet target prototype has been built up in nearly $\overline{P}$ANDA geometry. This prototype is reliable and stable running since years. Based on the results and experiences of the prototype the final $\overline{P}$ANDA cluster-jet target was built up and is already operating routinely. Furthermore, with the $\overline{P}$ANDA cluster-jet target prototype it was possible for the first time to achieve a target thickness of more than 2×10^{15} atoms/cm^2 in a distance of 2.1 m from the nozzle. Moreover, the prototype is equipped with a wide variety of different diagnostic tools to study the characteristics of the cluster beam which is essential to ensure the high required performance of the target for $\overline{P}$ANDA and to get a deeper insight into the cluster production process. Figure 4.8 shows the complete setup of the $\overline{P}$ANDA cluster-jet target prototype, with cluster source, interaction chamber, and beam dump system.

Cluster Source

The basic structure of the cluster source of the $\overline{P}$ANDA cluster-jet target prototype is the established and proved design developed by the University of Münster (see chapter 2.2). To achieve the required high target thickness in the distance of 2.1 m from the nozzle in combination with suitable vacuum conditions, a set of two orifices is used to prepare the cluster beam. Figure 4.9 depicts the cluster production process as explained in section 2.2.1 and additionally the principle of the orifices called skimmer and collimator. The task of the skimmer is the separation of the cluster beam from residual gas. Therefore, a skimmer, from Beam Dynamics [BD], out of nickel with a material thickness of 10 μm and with a sharp 0.5 mm round opening is installed. The specific form, small exterior and large interior angle ensures that only a small number of clusters are reflected on the surface of the skimmer. The following collimator, made of stainless steal, shapes and defines the size of the cluster-jet beam. In this thesis a collimator with an opening diameter of 0.7 mm was used. However, the application of specially formed collimators, like slit collimators, was successfully investigated [Kö15, Her13]. Skimmer and collimator are installed on cross tables equipped with stepper motors. Thus, the two orifices are adjustable over a x-y-range of ± 2 mm. Thereby, it is possible to align the cluster beam in the beam tubes and to do fine adjustments of the target thickness.

Both orifices are located in individual chambers, named skimmer and collimator chamber, respectively (see Fig. 4.11). For these chambers a differential pumping system is used. Because of the high gas flow (up to 6 l/min) at highest thicknesses in the skimmer chamber, there is installed a pumping station which achieve a vacuum pressure in the order of 10^{-1} mbar. It consists of two roots pumps in combination with two fore pumps in parallel.

Figure 4.8: Sketch of the complete $\overline{\mathrm{P}}$ANDA cluster-jet target prototype. The target consists of a cluster source with a powerful pumping station of roughly $9800\,\mathrm{m}^3/\mathrm{h}$ where the cluster beam is produced, extracted and shaped, an interaction chamber which corresponds to the later interaction point of the $\overline{\mathrm{P}}$ANDA experiment, and of a beam dump which can be equipped with various analyse tools to investigate the properties of the cluster beam. The target has a total length of roughly $9\,\mathrm{m}$ and the cluster beam direction is from left to right (violet arrow). Generated by D. Bonaventura, [Kö15], edited.

This pumping station is the same as used at the final $\overline{\mathrm{P}}$ANDA cluster-jet target, so all results gained at the prototype can directly be transferred to the final target. The second chamber, the collimator chamber, is due to the lower gas flow pumped by two identically turbomolecular pumps which uses the pumping station as a pre-vacuum system, resulting in a vacuum pressure of $10^{-4}\,\mathrm{mbar}$. This differential pumping systems allows for a successive improvement of the vacuum in cluster-jet beam direction, so that at the interaction point a suitable vacuum pressure $< 10^{-5}\,\mathrm{mbar}$ is achievable. The following vacuum chambers, like the beam dump chambers, of the target are also pumped with turbomolecular pumps or cryopumps in combination with fore pumps. A full sketch of the vacuum design of the $\overline{\mathrm{P}}$ANDA cluster-jet target prototype is shown in Figure 4.10 and the used pumps with their nominal pumping speed is listed in Table 4.2.
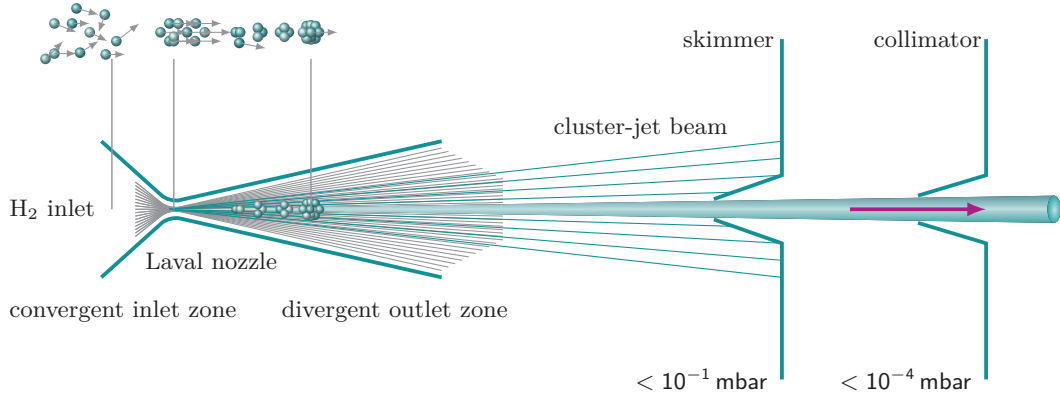
Figure 4.9: Concept of the cluster production process and the preparation and shaping of the cluster beam. Shown is a Laval nozzle with its specific short inlet zone which converges to the narrowest point of the nozzle of about $30\,\mu\text{m}$ and merges into the divergent, long outlet zone. By the expansion of hydrogen at low temperatures of roughly $20\,\text{K}$ and at high pressure of roughly $17\,\text{bar}$ through the nozzle in the skimmer chamber with a pressure in the order of $10^{-1}\,\text{mbar}$ the velocity distribution of the single hydrogen molecules changes (indicated with the cluster molecules and the grey arrows for the velocity above the nozzle). The specific geometry of the Laval nozzle generates a supersonic flow of the target material at the narrowest diameter of the nozzle. Supported by the adiabatic cooling after the narrowest inner diameter, the hydrogen molecules condensate to clusters. To achieve a well defined cluster beam with highest thickness in a distance of $2.1\,\text{m}$ the cluster beam needs to be sized and shaped. Therefore, an orifice, the skimmer, is used to separate the clusters from the residual gas and to extract it in the collimator chamber with a pressure of $10^{-4}\,\text{mbar}$. A second following orifice, the collimator, determines the size and shape of the cluster beam. Generated by E. Köhler, edited.

The skimmer chamber contains two features. The nozzle shutter and an optical monitor system of the cluster beam. The nozzle shutter is a copper sheet that can be placed in the cluster beam. Thereby, the clusters scatter at the surface of the nozzle shutter and remain in the skimmer chamber and therefore, the shutter corresponds to an on/off switch for the cluster beam. The optical monitor system consist of a laser diode in combination with a CCD camera (PCO pixelfly qe). The laser diode ($1\,\text{mW}$, $650\,\text{nm}$, round spot) with a beam expander (beam diameter of roughly $20\,\text{mm}$) illuminates the Laval nozzle and the expanding cluster beam or the cluster beam with the tip of the skimmer, depending on the adjustment of the laser diode. On the CCD camera a macro-planar lense from Zeiss (T* $2.0/100\,\text{mm}$ ZF) is mounted so that the camera can observe the cluster beam. Laser diode and CCD camera are installed through spherical joints in an angle of $35\,^{\circ}$ to each other vertical to the beam direction to adjust them to the wanted display detail. This cluster beam diagnostic system is examined in detail in this thesis (chapter 5.1.2) and is now well established at the Münster cluster-jet targets, because it offers the possibility to gain information of the cluster beam without destroying it. The monitor system installed at the skimmer chamber provides the opportunity to observe structures within the cluster beam, namely highly intense core beams with a higher thickness than the other parts of the beam, and to verify the cluster beam adjustment towards highest thicknesses.
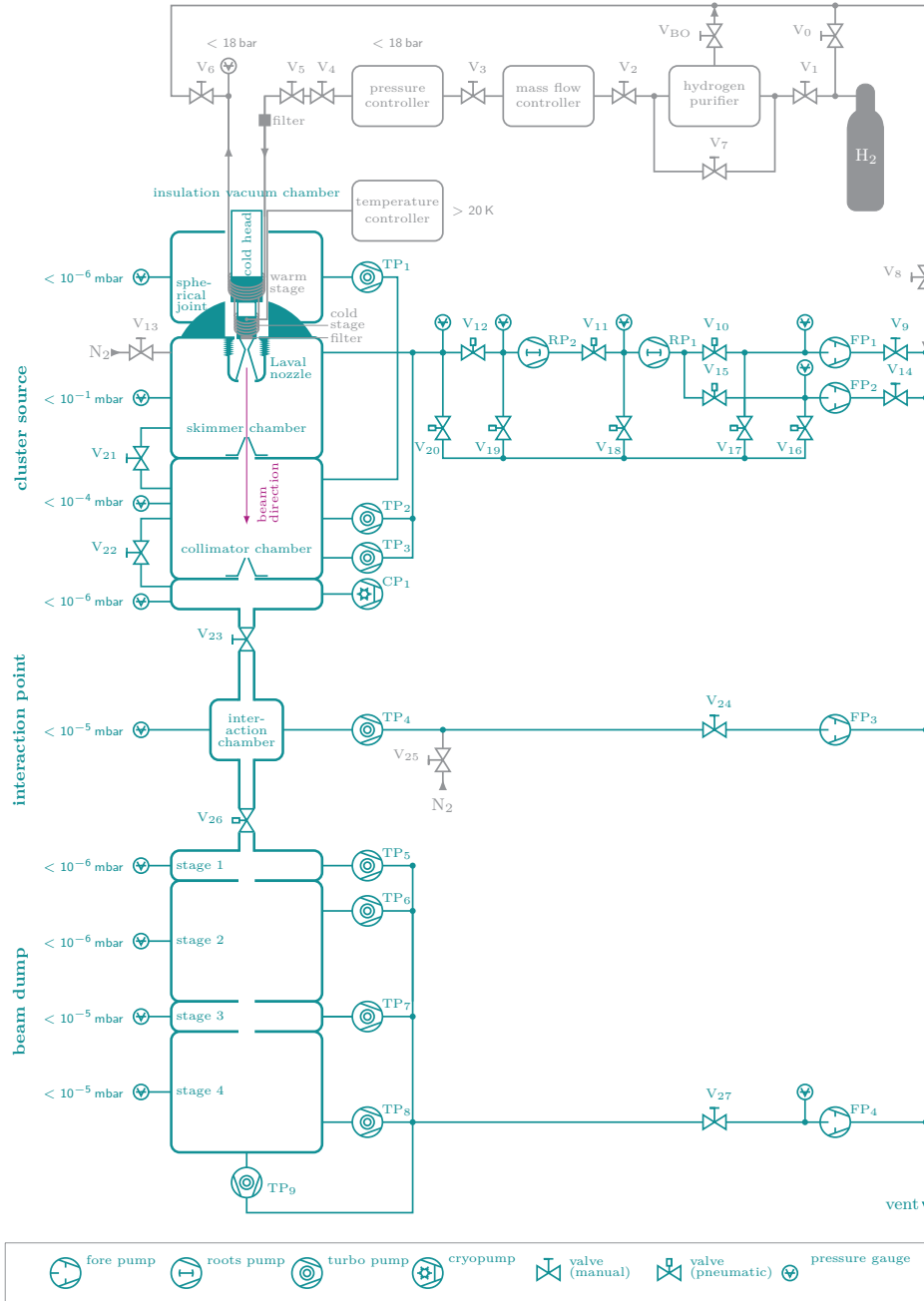
Figure 4.10: The gas and vacuum system of the $\overline{P}$ANDA cluster-jet target prototype. Hydrogen gas H_2 is used as target material and nitrogen gas N_2 to vent the target. All valves are indicated with V_{no}, except for the bleed out valve of the hydrogen purifier (V_{BO}). The different pumps are labelled with FP_{no} (no indicates the individual number) for fore pumps, RP_{no} for roots pumps, TP_{no} for turbomolecular pumps, and the only cryopump is captioned with CP_1. The specifications of the pumps are listed in Table 4.2. Generated by E. Köhler, updated and edited.
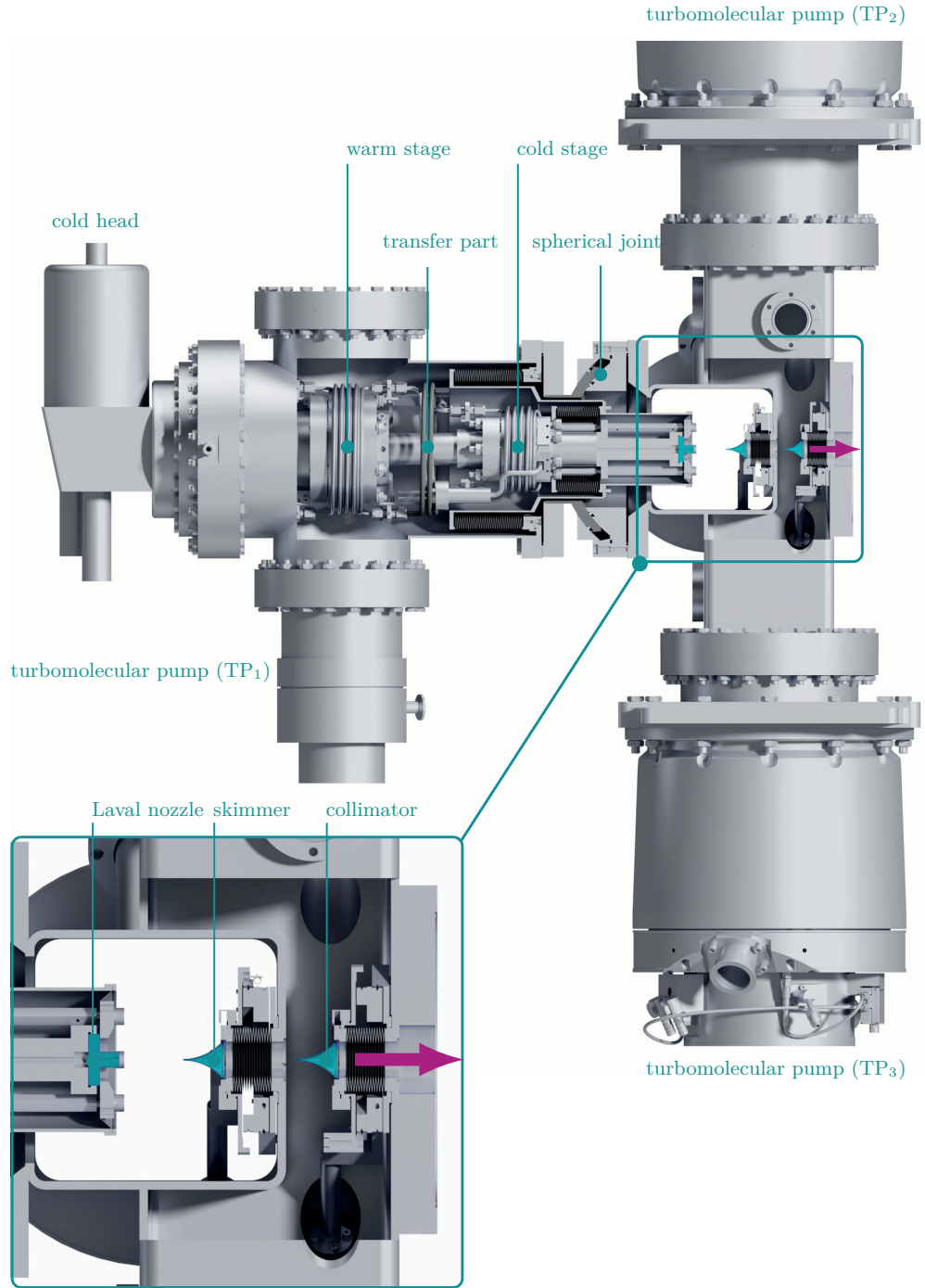
Figure 4.11: Sketch of the complete cluster source of the $\overline{P}$ANDA cluster-jet target prototype. Shown is the cold head with the gas pipes to cool down the hydrogen gas located in the insulation vacuum chamber ($< 10^{-7}$ mbar), the spherical joint to tilt the nozzle (explained later in this section), the nozzle, skimmer and collimator and their vacuum chambers, respectively. The cluster beam is represented with a violet arrow. Generated by D. Bonaventura, [Kö15], edited.

Table 4.2: Specifications and locations of the different pumps used at the $\overline{\mathrm{P}}$ANDA cluster-jet target prototype. FP_{no} represents fore pumps, RP_{no} roots pumps, and TP_{no} turbomolecular pumps. The only used cryopump is labelled with CP_1. The pumping station is donated with ps, the collimator chamber with cc, the scattering chamber with cs, the insulation vacuum with iv, and the beam dump with bd. The two fore pumps used for the cluster source (FP_1 and FP_2) are ATEX certificated (ATmosphères EXplosibles).

| $pump_n$	manufactures and designation Leybold except FP_4	hydrogen pumping speed	location
FP_1	SOGEVAC SV300B	$300\,\mathrm{m}^3/\mathrm{h}$	ps
FP_2	SOGEVAC SV300B	$300\,\mathrm{m}^3/\mathrm{h}$	ps
FP_3	Trivac D 25 B	$25.7\,\mathrm{m}^3/\mathrm{h}$	sc
FP_4	Alcatel T2100A	$120\,\mathrm{m}^3/\mathrm{h}$	bd
RP_1	RUVAC WS2001	$2000\,\mathrm{m}^3/\mathrm{h}$	ps
RP_2	RUVAC WH7000	$9800\,\mathrm{m}^3/\mathrm{h}$	ps
TP_1	Turbovac 450i	$420\,\mathrm{l/s}$	iv
TP_2	Turbovac Mag W 2200 iP(L)	$2200\,\mathrm{l/s}$	cc
TP_3	Turbovac Mag W 2200 iP(L)	$2200\,\mathrm{l/s}$	cc
CP_1	RGD 510		between cc and sc
TP_4	Turbovac 360CSV	$360\,\mathrm{l/s}$	sc
TP_5	Turbovac 450i	$420\,\mathrm{l/s}$	bd
TP_6	Turbovac 1000	$1000\,\mathrm{l/s}$	bd
TP_7	Turbovac MAG W 1300 iP	$1300\,\mathrm{l/s}$	bd
TP_8	Turbovac 1000	$1000\,\mathrm{l/s}$	bd
TP_9	Turbovac MAG W 1300 iP	$1300\,\mathrm{l/s}$	bd
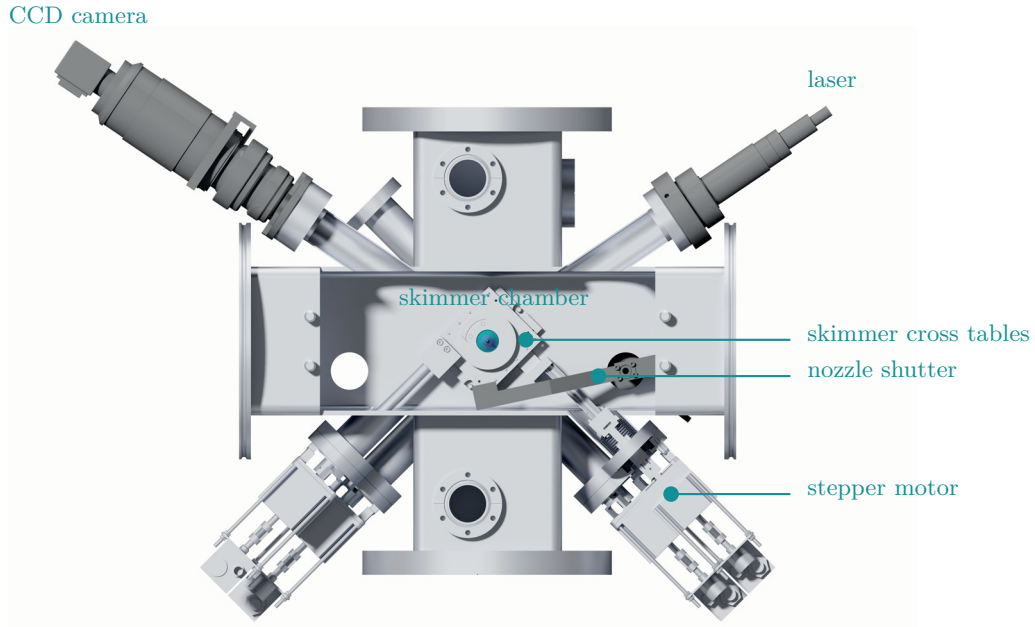
Figure 4.12: The skimmer chamber with its two features, the nozzle shutter as an on/off switch for the cluster beam and the optical monitor system to visualise the cluster beam consisting of a laser and a CCD camera. Additionally, the skimmer mounted on a cross table equipped with stepper motors for adjustments of the cluster beam is shown. The beam direction points into the plane. Generated by D. Bonaventura, [Kö15], edited.

The discovery of these highly intense core beams resulted in an installation of a nozzle tilting system. The system offers the opportunity to tilt the nozzle with angles up to $\pm 3.5°$ in horizontal and vertical direction with the narrowest diameter of the nozzle as point of rotation. Thereby, the extraction of the intense structures of the cluster beam with the skimmer is possible and high thicknesses at the interaction point can be achieved. The system is realised by the use of a spherical joint and a nozzle extension. The nozzle extension made out of copper and connected through an indium sealing makes sure, that the distance between nozzle and skimmer remains the same as before (56 mm). The spherical joint consists of two CF-200 flanges sealed with viton O-rings surrounding the inner part of it. A sliding surface and a retaining ring with a rotation surface in between form the inner part. This spherical joint is installed between the insulation vacuum chamber and the skimmer chamber. Furthermore to avoid heat exchange an additionally thermal shielding out of stainless steal is surrounding the nozzle extension in the skimmer chamber and is connected to the insulation vacuum chamber. The connection between the thermal shielding and the skimmer chamber is vacuum tight sealed by a mylar foil. In the scope of this thesis investigations on the reachable target thickness and cluster velocity distributions in dependence of the tilting angle of the nozzle are investigated (chapter 5.3).
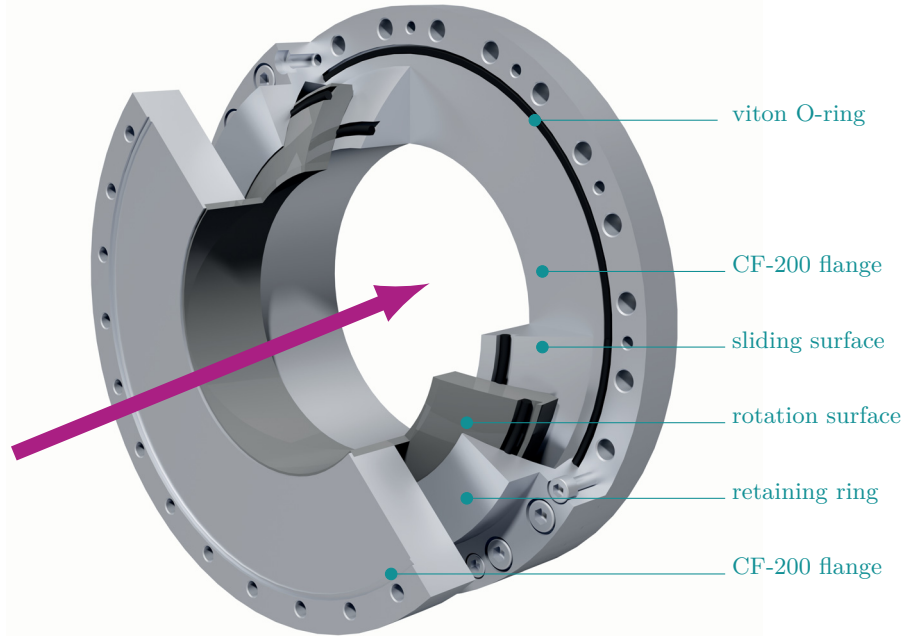
Figure 4.13: Sketch of the spherical joint to tilt the nozzle to extract high intense core beams within the cluster beam. The spherical joint is located between the insulation vacuum chamber and the skimmer chamber and consists of a sliding surface and a retaining ring with a rotation surface in between. The cluster beam is represented with the violet arrow. Generated by D. Bonaventura, [Kö15], edited.
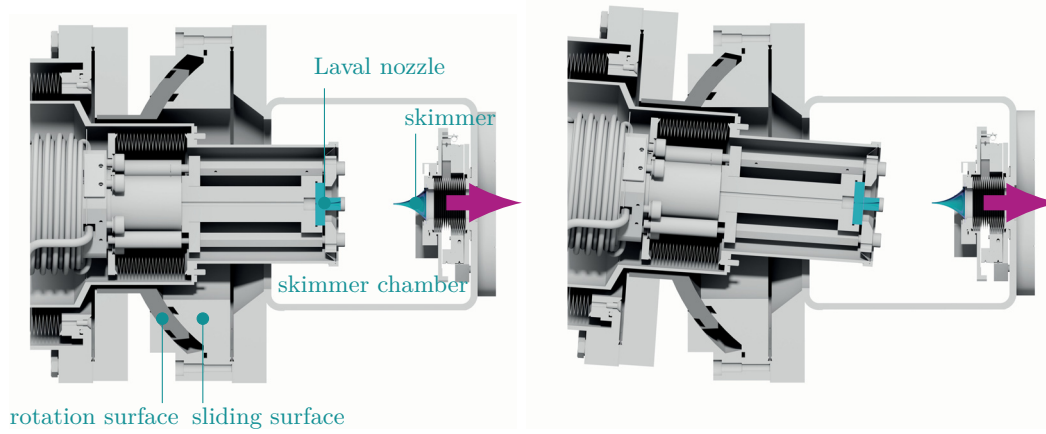
Figure 4.14: Nozzle tilting system including the spherical joint and the nozzle extension. The *left* picture shows the initial position where the nozzle is in zero degree to the skimmer in beam direction (illustrated with a violet arrow). The *right* picture depicts the maximal deflection ($3.5°$) of the spherical joint in vertical direction. Generated by D. Bonaventura, [Kö15], edited.

Behind the cluster source the cluster beam passes a cryopump. This special cryopump was designed and built up at the University of Münster. It consists of several cold sheets at less than 16 K with an opening diameter of 40 mm (significantly larger than the cluster beam) which are coated with activated carbon pellets. When the cluster beam passes the cryopump the surrounding residual gas remains at the cold sheets. Due to their high nominal pumping speed of up to 2200 l/s they were often used at the $\overline{\text{P}}$ANDA cluster-jet target prototype in the past. But the disadvantage of these pumps is the necessary and repetitive regeneration. Therefore, all cryopumps at the beam dump are exchanged by turbomolecular pumps and the final $\overline{\text{P}}$ANDA cluster-jet target comprises only turbomolecular pumps.
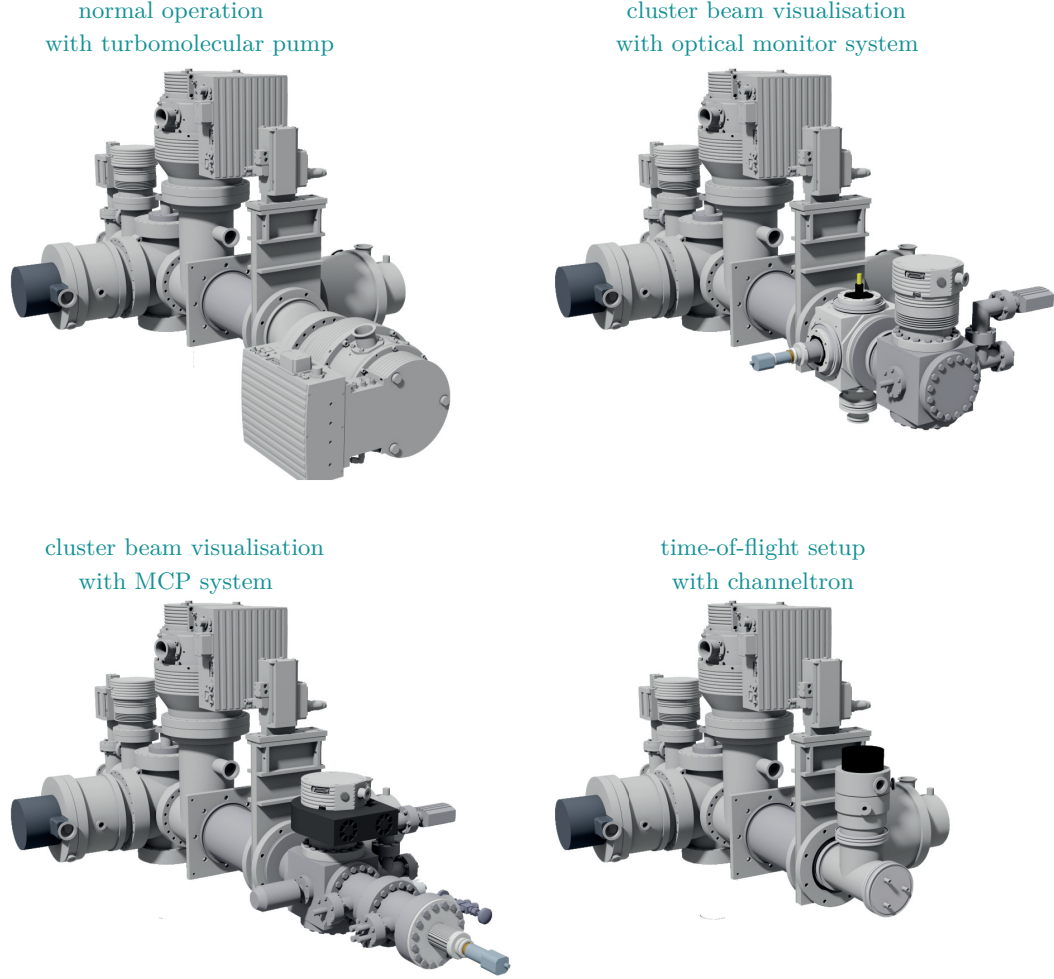
Interaction Chamber

The interaction chamber is assembled in a distance of 2.1 m from the nozzle. The future interaction point of $\overline{\text{P}}$ANDA where the cluster beam annihilates with the antiproton beam will be 2.25 m behind the nozzle so that the $\overline{\text{P}}$ANDA cluster-jet target prototype is built up next to $\overline{\text{P}}$ANDA geometry. The interaction chamber is pumped via a 360 l/s turbomolecular pump in combination with a fore pump. Furthermore, the chamber features a beam diagnostic system, the so called scanning rod system (see Figure 4.15). Two moveable rods with a diameter of 1 mm installed with two stepper motors in vertical and horizontal direction scan the cluster beam. The clusters impinge on the rods, break up which leads to a pressure increase in the chamber. Recording the pressure increase in dependence of the rod position results in a beam profile which contains the position, size, shape, and thickness information of the cluster beam.
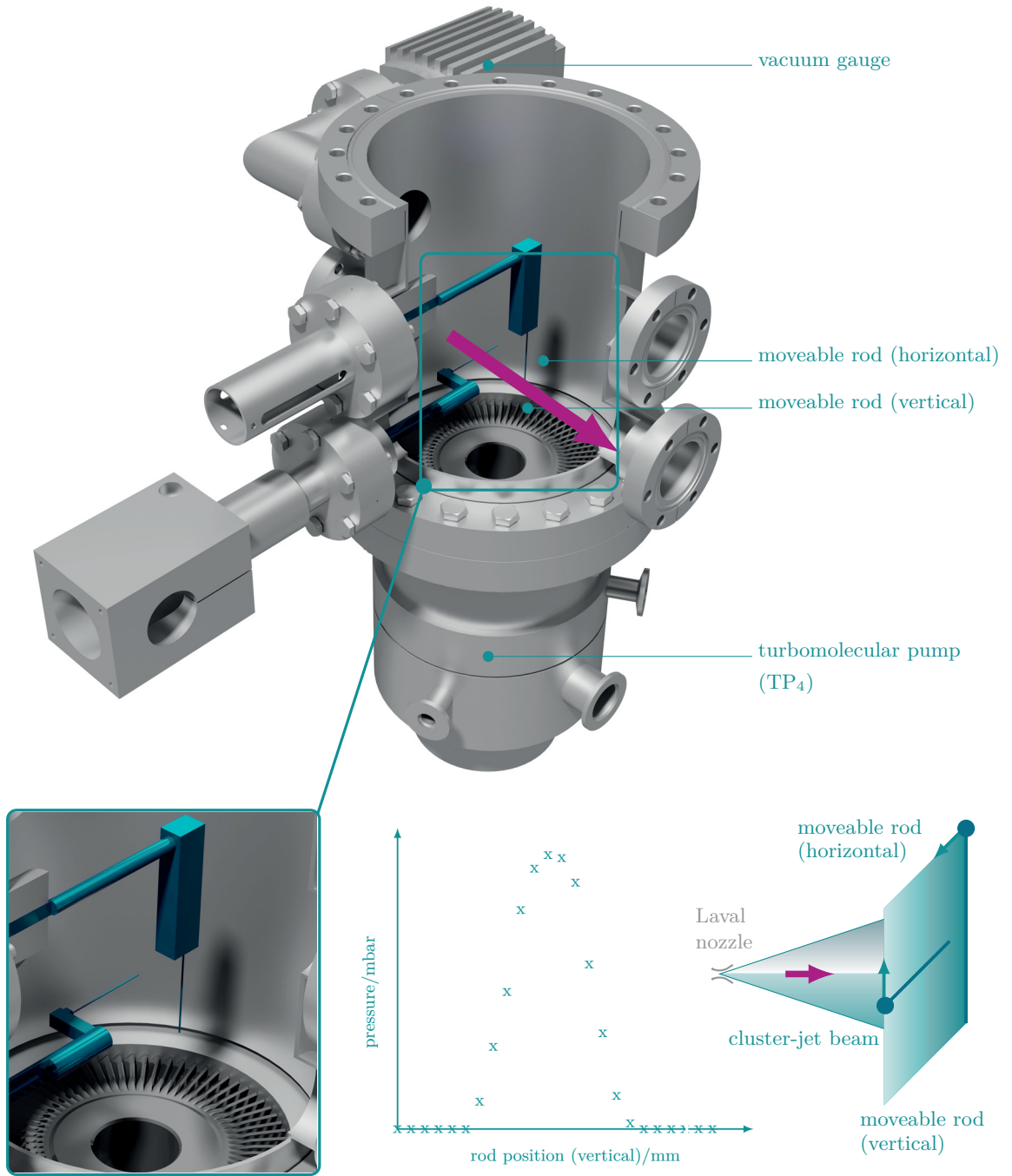
Figure 4.15: Insight into the interaction chamber equipped with the scanning rod system (zoom on the rods on the *bottom*, *left*). Shown are the two moveable rods via stepper motors in vertical and horizontal direction. Scanning the cluster beam with these rods leads to a pressure increase which can be monitored with the vacuum gauge and results in a cluster beam profile with information about the position, size, shape, and thickness of the cluster beam (schematic view on the *bottom*, *center* and *right*). Generated by D. Bonaventura, [Kö15], edited.

Beam Dump System

normal operation
with turbomolecular pump

cluster beam visualisation
with optical monitor system

cluster beam visualisation
with MCP system

time-of-flight setup
with channeltron

Figure 4.16: Different setups of the $\overline{P}$ANDA cluster-jet target prototype beam dump system. *Top, left*: Beam dump without diagnostic tools with a turbomolecular pump at the end to pump away the clusters. *Top, right*: Installation of the optical monitor system at the end of the beam dump to visualise and analyse the cluster beam. *Bottom, left*: MCP system at the end of the beam dump to observe the cluster beam after a flight path of more than 5 m. *Bottom, right*: A channeltron at the end of the beam dump in combination with a pulsed electron gun allows for cluster velocities measurement. Generated by D. Bonaventura, edited.

The cluster beam passes the interaction chamber and after a further flight path of roughly 2 m it get into the beam dump. The beam dump is divided into four stages which are pumped differentially with turbomolecular pumps in combination with fore pumps (cf. Figure 4.10). The cluster beam impinges at the end of the beam dump on the rotors of a turbomolecular pump, breaks up, and is pumped into the exhaust gas line. The differential pumping system upstream reduces the back streaming of clusters in the interaction chamber and therefore minimise the gas background in this chamber.

The beam dump can be equipped with a variety of analytical tools for investigations on the cluster beam (see Fig. 4.16). In the framework of this thesis an optical monitor

system comparable to the system in the skimmer chamber was established at the beam dump (chapter 5.1.2) to validate the system for further applications. Furthermore, a MicroChannel Plate (MCP) detection system was used to visualise the cluster beam and the properties of it at the end of the beam dump (chapter 5.1.2). Moreover, a channeltron at the beam dump head in combination with an electron gun near the cluster source was used to determine the velocity distribution of the clusters depending on the stagnation conditions of the hydrogen in front of the nozzle, the nozzle geometry, and the nozzle tilting angle (cf. chapter 5.2). These three applications of diagnostic tools at the beam dump are used in this thesis to investigate the cluster beam properties.

4.4 $\overline{P}$ANDA Cluster-Jet Target

Based on the results and experiences gained at the $\overline{P}$ANDA cluster-jet target prototype the final $\overline{P}$ANDA cluster-jet target in next to $\overline{P}$ANDA geometry was designed, built up and set successfully into operation at the University of Münster [Het17, Her18, Het18]. The complete setup of the cluster source (cf. Figure 4.17) contains an insulation vacuum chamber with the cold head and gas pipes, the skimmer chamber with nozzle, moveable skimmer, and optical monitor system, the collimator chamber with moveable collimator, and a transition vacuum chamber with a second optical monitor system.

Furthermore, the nozzle tilting system consisting of a gimbal joint mounted on two cross tables equipped with a stepper motor each which enables the tilting of the nozzle with a high accuracy and reproducibility remote-controlled [Het17]. Moreover, the cluster source is assembled with a snapping connector system which allows for a later straightforward, secure, and vacuum tight connection to the beam line at the $\overline{P}$ANDA experiment at FAIR. At a distance of 1.25 m from the nozzle a chamber equipped with a scanning rod system is used to determine the target thickness reachable with the final $\overline{P}$ANDA cluster-jet target. Additionally, in a distance of 2.25 m a vacuum pipe cross is installed to investigate the properties of the cluster beam at the later interaction point of the $\overline{P}$ANDA experiment. At the end of the final $\overline{P}$ANDA target a beam dump system built up by the INFN Genova is assembled which allows the operation of the target and offers the possibility for realistic vacuum studies and especially the gas back flow in the interaction chamber important for the operation at HESR. The complete cluster-jet target with its features and diagnostic tools makes it a powerful state-of-the-art target fulfiling all the requirements of the $\overline{P}$ANDA experiment.

To study the interaction between the cluster beam and an accelerator beam, the final $\overline{P}$ANDA cluster-jet target was installed in summer 2018 at the COSY accelerator in Jülich [Kho16].
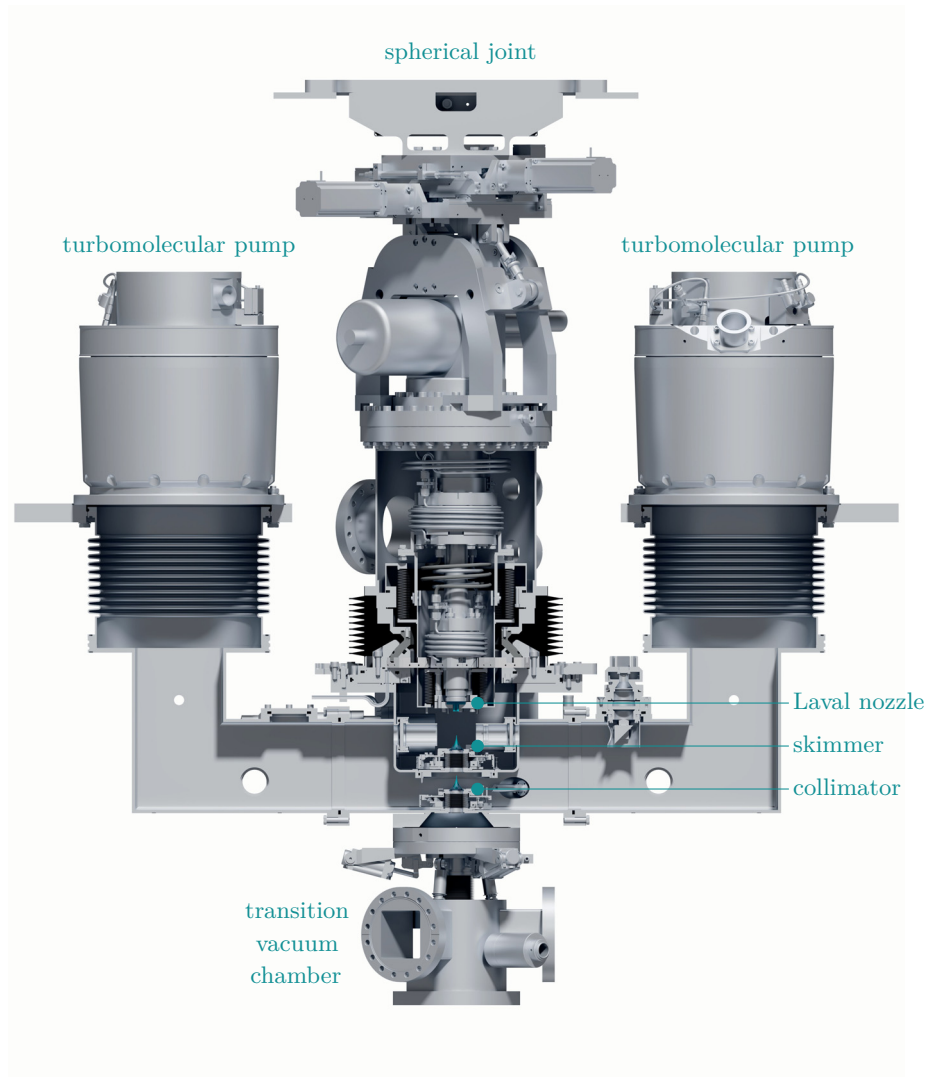
Figure 4.17: Final cluster-jet target source for the $\overline{P}$ANDA experiment. Shown is the cluster source with insulation vacuum chamber with the cold head and gas pipes, the skimmer chamber with nozzle, moveable skimmer, and optical monitor system, the colliamtor chamber with moveable collimator, and the nozzle tilting system controllable via two stepper motors. Additionally, the transition vacuum chamber equipped with a second optical monitor system and the snapping connector system to the later $\overline{P}$ANDA beam line is depicted. Generated by D. Bonaventura, edited.

5 Laval Nozzle Studies at the $\overline{\mathrm{P}}$ANDA Cluster-Jet Target Prototype

A Laval nozzle is the main component of every Münster cluster source. Therefore, the nozzle is essential for the performance of the cluster-jet target. Furthermore, the Laval nozzle geometry defines the characteristic of the cluster beam with respect to its thickness, velocity and beam structures.

In this chapter, the various diagnostic tools are discussed which were used to investigate different Laval nozzles within this thesis. Moreover, the nozzles originating from the production processes of the University of Münster were installed at the $\overline{\mathrm{P}}$ANDA cluster-jet target prototype, studied in their performance and important information were used to improve the nozzles and their production process.

5.1 Methods of Thickness Determination

The performance of experiments with accelerator beams or lasers like $\overline{\mathrm{P}}$ANDA, MAGIX, or CryoFlash mainly depends on their luminosity. For the luminosity the particle density of the applied cluster-jet target is an essential factor. Therefore, the knowledge of the performance of the cluster-jet targets are from highest importance. Thus, a variety of different systems to analyse the cluster-jet beam and his properties are developed and currently in use.

With respect to storage ring or electron accelerator experiments, the areal thickness $\rho_{\mathrm{areal}} = \left[\mathrm{atoms/cm^2}\right]$ has to be considered. The MAGIX experiment requires a luminosity of $L = 10^{35}\,\mathrm{cm^{-2}s^{-1}}$, leading to an areal thickness of $\rho_{\mathrm{areal}} \approx 1.6 \times 10^{18}\,\mathrm{atoms/cm^2}$ directly behind the nozzle where the interaction between the cluster beam and the electron beam takes place and the highest thickness can be achieved. In comparison, $\overline{\mathrm{P}}$ANDA is aiming for a luminosity of $L_{\mathrm{max}} = 2 \times 10^{32}\,\mathrm{cm^{-2}s^{-1}}$ which corresponds to an areal thickness of $\rho_{\mathrm{areal}} = 4.5 \times 10^{15}\,\mathrm{atoms/cm^2}$ at the interaction point in a distance of $2.25\,\mathrm{m}$ from the nozzle to realise an almost 4π acceptance of the $\overline{\mathrm{P}}$ANDA detector (cf. Section 2.1).

In the case of CryoFlash, the volume density $\rho = \left[\mathrm{atoms/cm^3}\right]$, located in the focus volume of the applied laser, is from interest. Through also in this experiment the interaction takes directly place behind the nozzle. Both values are inter-linked, therefore, the areal thickness describes the volume density integrated along the target beam diameter r

$$\rho_{\mathrm{areal}} = 2 \int_0^\infty \rho_{\mathrm{volume}}\left(r\right)\,\mathrm{d}r. \tag{5.1}$$

The target thickness provided by a cluster-jet target directly behind the nozzle is determined by both, the stagnation conditions of the gas in front of the Laval nozzle and the nozzles geometry. Under the assumption of a homogeneous distribution within the jet beam, the volume density is defined by [W$^+$88]

$$\rho_{\text{volume}} = \frac{\dot{m}}{v \cdot A_{\text{beam}}} \cdot \frac{N_A}{M}, \tag{5.2}$$

with $\dot{m}$ being the mass flow through the nozzle, v the cluster velocity, A_{beam} the cluster beam cross section, N_A the Avogadro constant, and M the molar mass of the gas. The mass flow $\dot{m}$ is proportional to the volume flow q_v, the normal pressure and normal temperature $p_N = 1.01325$ bar and $T_N = 273.15$ K, and the universal gas constant R

$$\dot{m} = \frac{q_v \cdot M \cdot p_N}{R \cdot T_N}. \tag{5.3}$$

The volume flow q_v itself can be described by

$$q_V = A^* \frac{p_0}{\sqrt{MT_0}} \frac{T_N}{p_N} \left(\frac{2}{\kappa + 1} \right)^{\frac{\kappa+1}{2(\kappa-1)}} \sqrt{\kappa R}, \tag{5.4}$$

wherein, the stagnation conditions of the gas in front of the nozzle are given by p_0 and T_0, the cross-section area of the nozzle at the narrowest point is A^*, and with the heat capacity ratio $\kappa = C_p/C_V$. As a result, the volume flow q_v through a specific Laval nozzle and the resulting areal target thickness directly behind the nozzle can be calculated in dependence of the stagnation conditions of the gas in front of the nozzle.

The realisation of the interaction directly behind the nozzle is not possible in reality due to the experimental setup and the individual used devices or detectors, thus, normally between interaction point and nozzle is a small distance of less than 3 cm. The areal thickness as well as the volume density decrease with the distance from the nozzle. The propagation of the cluster beam underlies the intercept theorems, consequently a cylindrical volume element of the beam especially its radius increase with increasing distance (cf. Figure 5.1). As a result the volume density decreases proportional to s^{-2} and the areal thickness to s^{-1} by enlarging the distance from the nozzle. This relation between thickness or density and distance from the nozzle has to be considered by the analysis of the different interactions with respect to the cluster beam properties. This shows the challenge to achieve an areal thickness of $\rho_{\text{areal}} = 4.5 \times 10^{15}$ atoms/cm^2 at a distance of 2.25 m from the nozzle for the $\overline{P}$ANDA cluster-jet target.

The cluster-jet target areal thickness and the particle flow $\dot{N}_p$ determine the luminosity of the performed experiments (cf. Eq. (2.2)). In the case of internal storage ring experiments, like the upcoming $\overline{P}$ANDA experiment, the accelerated particle beam is guided during a cycle of 30 minutes through the beam line of the storage ring experiment. After the cycle, the accelerated beam is dumped and a new particle beam is injected after a preparation time of five minutes. During a cycle, the accelerated particle beam experiences beam current losses. The major contribution to these losses results from the interaction with

the internal cluster-jet target divided in hadron interaction, Coulomb scattering, and deceleration of the beam particles. In addition, beam intern scattering can occur. More details on these beam loss effects can be found in [Hor15].

Despite these losses, the luminosity of the experiment should be constant and the experiment should make an optimum use of the accelerated particle beam. A luminosity too high leads to high dead times of the detector, a luminosity too low means a low utilization of the experiment. Therefore, a constant adjusted areal target thickness leads to a decrease of the intensity of the beam and of the event rate. In case of the $\overline{\text{P}}$ANDA experiment, assuming an initial beam momentum of $9\,\text{GeV}/c$ and an event rate of $12 \times 10^6\,\text{s}^{-1}$ results due to beam losses in an event rate of $4 \times 10^6\,\text{s}^{-1}$ after 100 min. In order to prevent a decreasing luminosity, the areal target thickness has to be adjusted to the decreasing particle flow.

The areal target thickness is adjustable during the running experiment by changing the temperature and/or the pressure of the target gas in front of the nozzle (cf. Equations (5.1) - (5.4)). In the bachelor thesis of F. Hordt [Hor15] the adjustment of the target thickness to the cycle of the particle beam was successfully demonstrated with the cluster-jet target MCT1S. A slow control routine was used to automatically adjust the temperature of the hydrogen to the duration of the measurement. Thereby, no operator activity was necessary during the measurement. One of the measurements were performed with a constant pressure of 9 bar and a decreasing temperature between 22.5 K and 30 K of the hydrogen gas in front of the nozzle. Due to the decrease of the temperature, the target thickness increases. Under the assumption of a life time of 1800 s (30 min) of the accelerated beam and a preparation time for the next injection of 300 s (5 min), the cooling time of the hydrogen target gas was determined to 1800 s and the heating period takes 900 s. The heating time was extended due to the low heating power of the used cluster-jet target MCT1S, the later used final $\overline{\text{P}}$ANDA cluster-jet target have sufficient heating power. The stability of the thickness during the ramp was measured over 9 h corresponding to 11 ramps in a row. The results are shown in Figures 5.2 and 5.3.
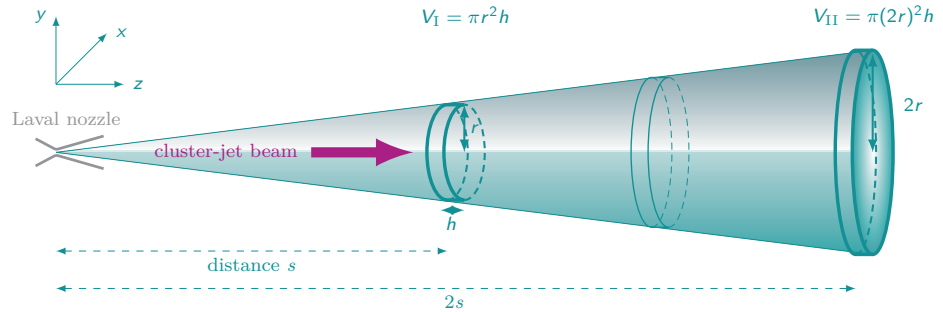
Figure 5.1: Propagating cluster beam from left to right. The voulume density ρ_{volume} decreases with distance s from the nozzle: $\rho_{\text{volume}} \propto s^{-2}$. Generated by E. Köhler, edited.
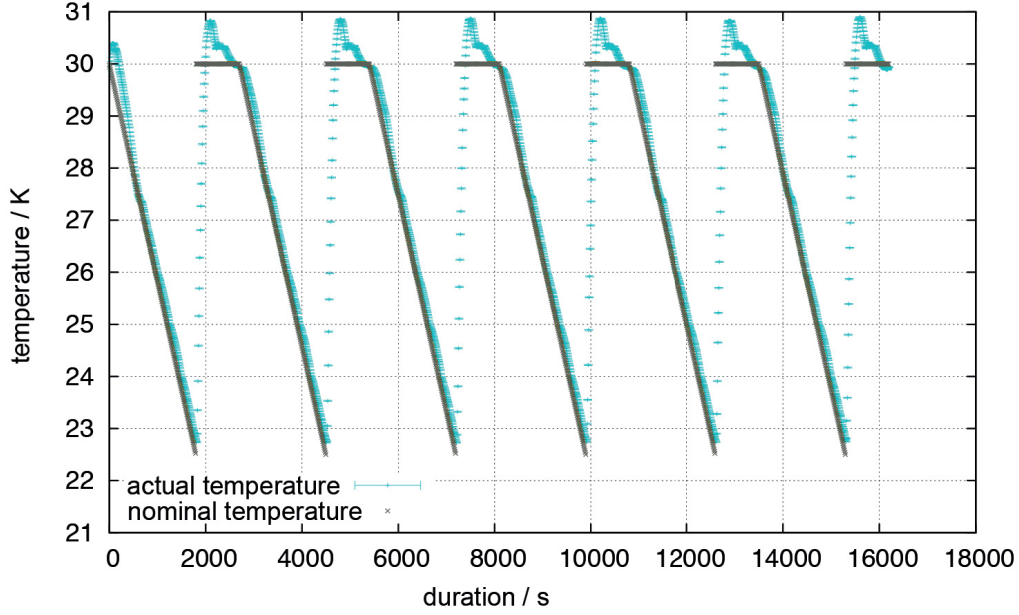
Figure 5.2: Several thickness ramps out of a measurement performed with a constant pressure of 9 bar and a decreasing temperature between 22.5 K and 30 K of the hydrogen gas in front of the nozzle. The cooling time is 1800 s and the heating duration 900 s. The actual temperature (green) follows the nominal temperature (gray) with offset. In the heating phase, the temperature perform an overshoot which automatically regulated itself during the heating phase. This overshoot would not be obstructive, because meanwhile the accelerated particle beam is prepared and no interaction takes place [Hor15].
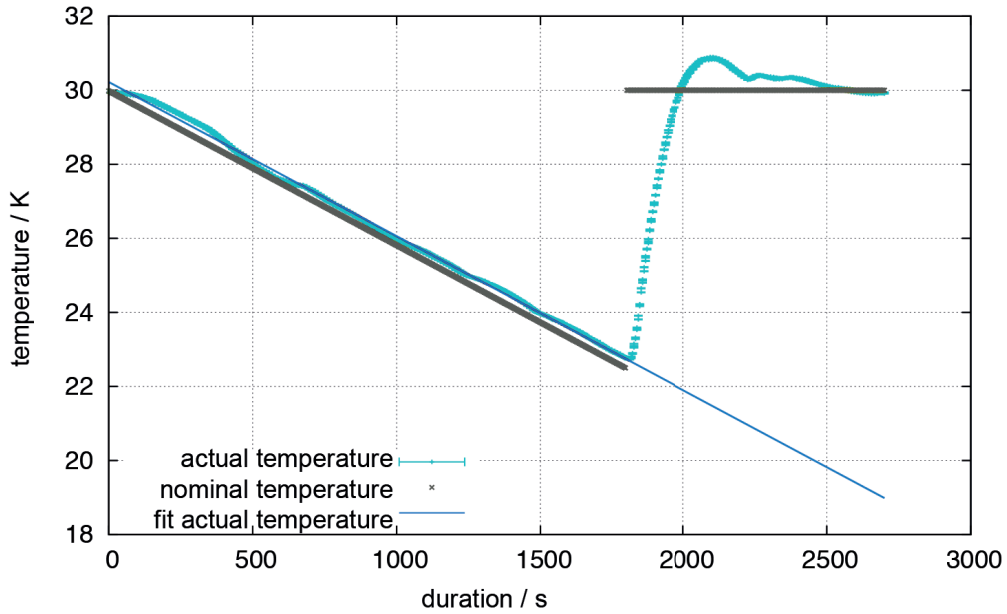
Figure 5.3: Summation over the 11 ramps in a row. The actual temperture shows a stable course. In combination with the stable pressure, the target thickness consequently stable. The discrepancy between nominal (gray) and actual temeprature (green) and the overshoot is typically for the applied PI controller and the inertia of the system [Hor15].

This first successfully measurements shows the possibility to automatically adjust the target thickness to the life time of the accelerated beam to guarantee a constant luminosity and therefore a constant event rate of the experiment.

The decrease of the areal target thickness with distance to the nozzle and the use of orifices to size and shape the beam do not allow to determine the areal target thickness with Equations (5.2) - (5.4) in larger distances to the nozzle. Therefore, various systems to measure the areal target thickness of a cluster beam are developed. The different systems and their analysis to investigate the areal thickness of cluster-jet targets and moreover its properties like size, shape, and position are described in this chapter. They can be divided into two categories. The first ones are named as destructive methods, because during the measurement of the thickness the cluster beam is affected and is not available for the experiment. In comparison to that, the non-destructive methods does not influence the cluster beam and therefore, during these measurements the real experiment can take place.

5.1.1 Destructive Methods

The destructive thickness determination methods works by measuring instruments which were placed inside of the beam, which move through the beam or which pile up parts or the whole beam. Due to the interaction of these instruments with the cluster beam, the cluster beam is complete or particular destroyed and therefore, the beam is not available for experiments at the same time. For this reason, more and more non-destructive methods were applied, to perform cluster beam studies during the running experiment. But nevertheless, the destructive methods are very important to guarantee a fast and uncomplicated absolute target thickness determination and thus are well suited in laboratory systems.

Scanning Rod System

The determination of the absolute target thickness at the $\overline{\text{P}}$ANDA cluster-jet target prototype uses a scanning rod system (cf. Fig 4.15). This system is installed in the interaction chamber at a distance of $2.1\,\text{m}$ from the nozzle. The system consists of two moveable rods with diameters of $1\,\text{mm}$ which are equipped with stepper motors to scan the cluster beam in vertical and horizontal direction. A rod entering the cluster beam leads to a break up of the clusters which impinge on the rod and results in a pressure increase in the chamber measured with a vacuum gauge. The pressure in the chamber as a function of the position of the rod shows two beam profiles (vertical and horizontal) with information about the position, size, shape, and absolute thickness of the cluster beam (cf. chapter 4.3).

The volume density ρ_{volume} of the cluster beam mainly depends on the maximal pressure increase in the chamber p_0 and the velocity of the clusters v

$$\rho_{\text{volume}} \propto \frac{p_0}{v}. \tag{5.5}$$

The pressure increase is monitored via a vacuum gauge and depends on the pressure and temperature of the hydrogen gas in front of the Laval nozzle. To identify the maximal pressure increase p_0 an adaptation of the beam profiles with a suitable distribution is realised. Moreover, this distribution depends on the beam shape. In the framework of this thesis a round collimator to size and shape the cluster beam was used, therefore, only the description of the adaptation of beam profiles with circular shaped cluster beams are discussed. Details on the application and description of a rectangular collimator and the resulting cluster beam profiles which is foreseen at the final $\overline{\text{P}}$ANDA cluster-jet target can be found in [Kö15].

The cluster velocity v is an important figure for the determination of the target thickness and depends also on the stagnation conditions of the hydrogen in front of the Laval nozzle. Moreover, the velocity distribution indicates a mass distribution within the cluster beam and allows for a deeper insight into the cluster production process within the Laval nozzle. The production process and its influence on the cluster beam characteristics and additionally the impact of the nozzle geometry can be studied. The cluster velocity distribution can be measured at the $\overline{\text{P}}$ANDA cluster-jet target prototype with a time-of-flight setup (see chapter 5.2) [Kö10, Kö15]. Additionally, the mean cluster velocity is predictable via a simulation using a quasi-one-dimensional flow [Tä12] or a three-dimensional calculation [Bra18] (cf. chapter 5.2.2).

The pressure p in the interaction chamber depends on the accumulation of the cluster beam but also on the volume flow q_{pV} in the chamber and the pumping speed S of the mounted vacuum pump system

$$p = \frac{q_{pV}}{S}. \tag{5.6}$$

The effective pumping speed S of the interaction chamber was determined by E. Köhler to (215.4 ± 6.0) l/s [Kö10].

The following derivation of the description of the hydrogen volume density and the adaptation function on the beam profiles is derived from [Kö15, Tä12]. The ideal gas law can be written as

$$pV = nRT, \tag{5.7}$$

with p, V, T, R being the pressure, volume, temperature, and the universal gas constant. The number of moles of the used gas is described by n and can also be defined by the mass of the gas m and the molar mass M in the way $n = m/M$ which leads to

$$pV = \frac{mRT}{M}. \tag{5.8}$$

The variation over time

$$p\frac{dV}{dt} = \frac{dm}{dt}\frac{RT}{M} \tag{5.9}$$

$$q_{pV} = q_m \frac{RT}{M} \tag{5.10}$$

contains the volume flow q_{pV} and the mass flow q_m.

The volume density of an accumulated cluster beam propagating in z-direction by a rod with a diameter d and larger than the cluster beam in y-direction at the position x

describes the mass $m(x)$. The mass flow $q_m(x)$ itself is given by the time derivation of the mass $\dot{m}(x)$

$$q_m(x) = \int\limits_{x-d/2}^{x+d/2} \mathrm{d}x' \int\limits_{-\infty}^{+\infty} \mathrm{d}y' \int \frac{d}{dt} \mathrm{d}z' \rho(x', y', z'). \tag{5.11}$$

Assuming that the volume density does not change in z-direction and that the cluster velocity is defined as the time derivation of the distance ($dz/dt = v$), the mass flow $q_m(x)$ can be rewritten as:

$$q_m(x) = \int\limits_{x-d/2}^{x+d/2} \mathrm{d}x' \int\limits_{-\infty}^{+\infty} \mathrm{d}y' \int \frac{d}{dt} \left(v\, \mathrm{d}t\right) \rho(x', y') \tag{5.12}$$

$$q_m(x) = v \int\limits_{x-d/2}^{x+d/2} \mathrm{d}x' \int\limits_{-\infty}^{+\infty} \mathrm{d}y' \rho(x', y'). \tag{5.13}$$

Moreover, the volume density distribution $\rho(x', y')$ is a multiplication of an absolute height ρ_0 and a shape $\tilde{\rho}(x', y')$. The maximal volume density corresponds to ρ_0, because the function $\tilde{\rho}(x', y')$ is normalized to one. Furthermore, $\tilde{\rho}(x', y')$ can be adapted to the shape of the cluster beam, e.g., a circular or rectangular shaped cluster beam. In this thesis a circular shapes collimator is used, therefore, the derivation for a circular shaped cluster beam $\tilde{\rho}_{\mathrm{circ}}(x)$ is described in detail.

To gain a reliable statement with low uncertainty of the volume density, an accurate adaptation of the measured beam profile has to be performed. A precise description of the beam profile can be done with a convolution of a step function [Kö15, Tä12]

$$f(x)_{\mathrm{step}} = \begin{cases} 1, & \text{if } |x| \leqslant R_c \\ 0, & \text{if } |x| > R_c \end{cases} \tag{5.14}$$

with R_c being the cluster beam radius determined by the used collimator and a normalised Gaussian distribution

$$g(x) = a \exp\left(\frac{-bx^2}{2}\right) \tag{5.15}$$

with $a = \sqrt{b/2\pi}$. The Gaussian function describes the cluster beam shape and the edge effects induced by the used collimator, e.g., smearing. In the case of a circular beam shape an one-dimensional treatment like above is correct but considering a rectangular cluster beam a two dimensional treatment has to be done. The convolution of a step function and a normalised Gaussian distribution precisely describes the recorded circular shaped beam profile [Kö15, Tä12]

$$\tilde{\rho}_{\mathrm{circ}}(x) = f(x) * g(x) = \int\limits_{-\infty}^{+\infty} f(\tau) g(x - \tau)\, \mathrm{d}\tau. \tag{5.16}$$

Solving this equation is shown in detail in Appendix A.1. Applying the modified ideal gas law (Eq. (5.10)) to this solution leads to the pressure profile of a circular shaped beam

$$p(x) = \rho_0 \frac{vRT}{SM} \int_{x-d/2}^{x+d/2} \mathrm{d}x' \int_{-\infty}^{+\infty} \mathrm{d}y' \tilde{\rho}(x', y') + p_{\mathrm{back}} \tag{5.17}$$

with p_{back} being the residual gas background in the interaction chamber and

$$\tilde{\rho}_{\mathrm{circ}}(x) = \frac{1}{2} \left(\mathrm{erf} \left(\frac{x + R_c}{\tilde{s}} \right) - \mathrm{erf} \left(\frac{x - R_c}{\tilde{s}} \right) \right) \tag{5.18}$$

with the smearing parameter $\tilde{s}$ and the error function erf. Figure 5.4 shows a recorded beam profile with this adaptation.
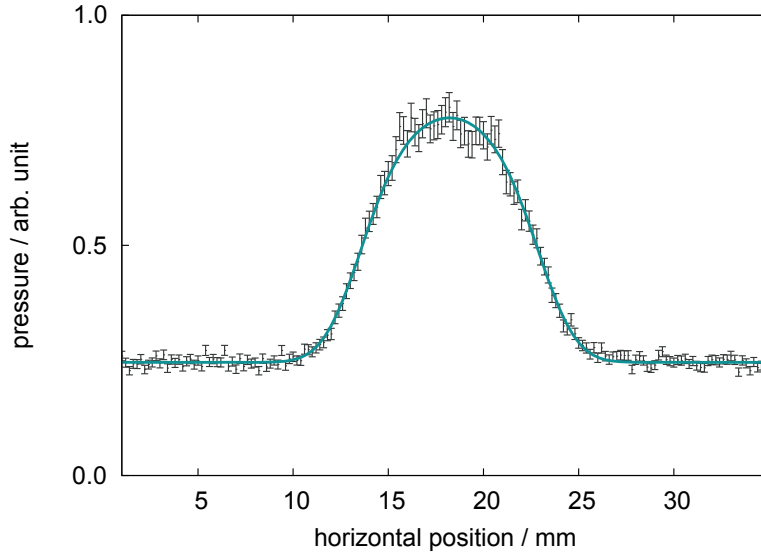
Figure 5.4: Recorded beam profile with the scanning rod system in the interaction chamber of the $\overline{\mathrm{P}}$ANDA cluster-jet target prototype in a distance of 2.1 m from the nozzle. The A21 nozzle was used with a hydrogen pressure of 18 bar and a temperature of 22 K. Additional, the adaptation with equation 5.17 is shown to determine the target thickness.

A description of the measured beam profile with this equation leads to the volume density $\rho_0 = \left[\mathrm{kg/cm^3} \right]$

$$\rho_0 = p_{0/A} \frac{SM}{vRT}, \tag{5.19}$$

wherein $p_{0/A}$ represents the maximal height.

Consequently, the particle volume density $\rho_N = [\text{atoms/cm}^3]$ is given by

$$\rho_N = p_{0/A} \frac{SM}{vRT} \frac{1}{m} = p_{0/A} \frac{SM}{vRT} \frac{N_A}{M_a} \tag{5.20}$$

with the mass $m = \frac{M_a}{N_A}$ being the quotient of the molar mass M_a and the Avogadro constant N_A.

In the case of hydrogen, the volume density ρ_H reveals to

$$\rho_N = p_{0/A} \frac{2SN_A}{vRT}. \tag{5.21}$$

The key figure of a cluster-jet target is the areal target thickness ρ_{areal} which can be calculated with Equation (5.1) using this volume density. Furthermore, to determine the volume density, the velocity of the clusters is a crucial parameter. The velocity depends on the stagnation conditions of the hydrogen in front of the nozzle. Therefore, intense velocity measurements were performed (cf. section 5.2) and simulated (cf. 5.2.2).

Pitot Tube

Another destructive method to measure the target thickness is the use of a pitot tube [V+05]. The pitot tube will pass through the cluster beam and measures the total pressure of the accumulated gas in dependency of its position. Thereof, similar to the scanning rod system, a cluster beam profile will be recorded and the pressure is proportional to the target thickness which then can be determined.

### 5.1.2 Non-Destructive Methods

The disadvantage of destructive methods to influence the cluster beam during the measurements make them not suitable for running experiments. Therefore, a wide range of non-destructive methods to analyse the cluster beam are developed and routinely in use. Furthermore, some of them will be installed at the final $\overline{\text{P}}$ANDA cluster-jet target to analyse the cluster beam during the running experiment. Several of the non-destructive methods to analyse the cluster beam properties works with the scattering of light or particles on the clusters.

Optical Monitor System

The optical monitor system was first developed, tested and elaborated in a recent master thesis [Gri14]. It allows for a determination of the position, size, shape, and relative thickness of the cluster beam. In the framework of this thesis this system was used in combination with a conical collimator, therefore, only this results are presented. Nevertheless, the system is also applicable in combination with a slit collimator, which is established at the final $\overline{\text{P}}$ANDA cluster-jet target [Het17].

The system was installed in the interaction chamber of the MCT1S cluster-jet target (cf. chapter 8.3) in a distance of $33\,\text{cm}$ from the nozzle. It consists of a CCD camera

(pco.pixelfly usb) and a diode laser (Laser Components, 650 nm, 1 mW) which are mounted in 90° to each other (see Fig. 5.5). Furthermore, opposite of the laser, a laser beam dump is installed, to reduce the reflections in the interaction chamber. Additionally, the vacuum window of the laser is blacked out and coated with black cardboard except for a small hole for the laser beam to further reduce the reflections of the laser in the chamber. To analyse the cluster beam, two pictures have to be taken. The first one was recorded with an open nozzle shutter and shows the cluster beam as a bright spot illuminated by the laser diode in the middle and some reflections at the bottom of the picture (see Fig. 5.6 left). The second picture was taken with a closed nozzle shutter and only displays the reflections in the interaction chamber (see Fig. 5.6 right). A subtraction of the second from the first picture to reduce the background signal shows a cluster beam clearly visible in the middle with nearly no remaining reflections (see Fig. 5.7). The vertical line with the width of the cluster beam in Figure 5.6 (left) is an effect of a CCD camera called smear and is induced by a bright spot (cluster beam) leading to unwanted charge carries during the read out of the image sensor [PCO].
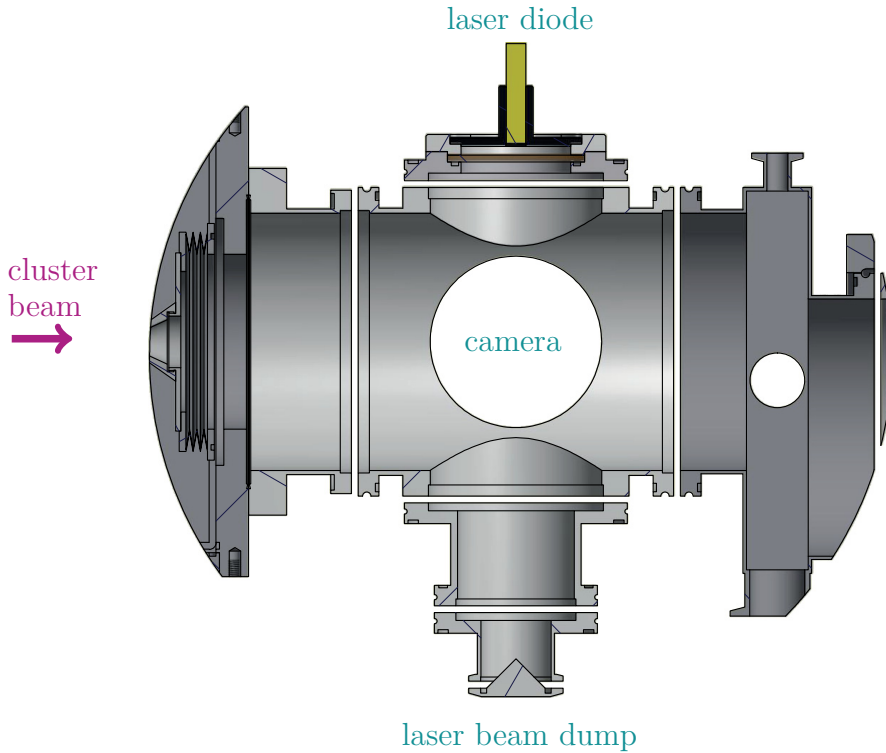

Figure 5.5: Sketch of the optical monitor system at the cluster-jet target MCT1S. The cluster beam direction is from left to right. The laser diode is mounted on the top of the interaction chamber and illuminates the cluster beam. Opposite to the laser diode a laser beam dump is installed to reduce the reflections of the laser in the chamber. The camera is mounted perpendicular to the laser and cluster beam axis. Generated by D. Bonaventura, edited.
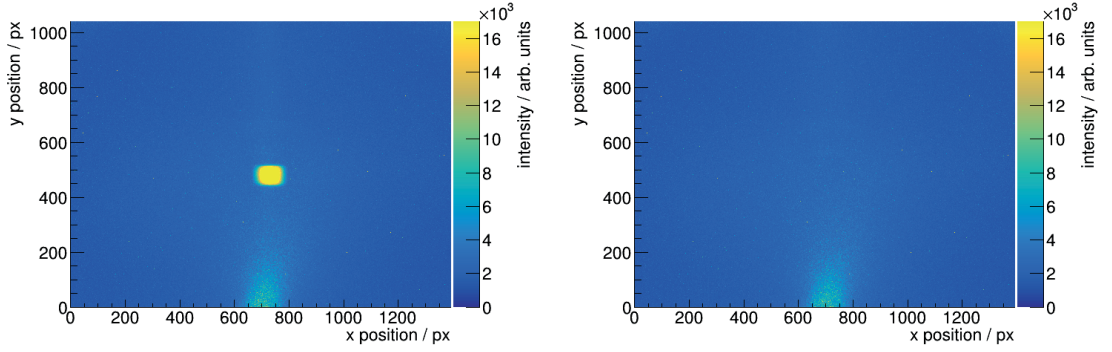
Figure 5.6: Pictures taken in the interaction chamber of the cluster-jet target MCT1S in a distance of 33 cm from the nozzle. The pictures were recorded with a pressure of 16 bar, a temperature of 22 K of the hydrogen in front the nozzle with an exposure time of 15 s. The cluster beam direction is from left to right and the laser beam is coming from top to bottom. The *left* picture shows the cluster beam recorded with an open nozzle shutter and it is clearly visible in the middle of the picture. The *right* one shows a picture taken with a closed nozzle shutter and only the reflections in the interaction chamber are recorded.
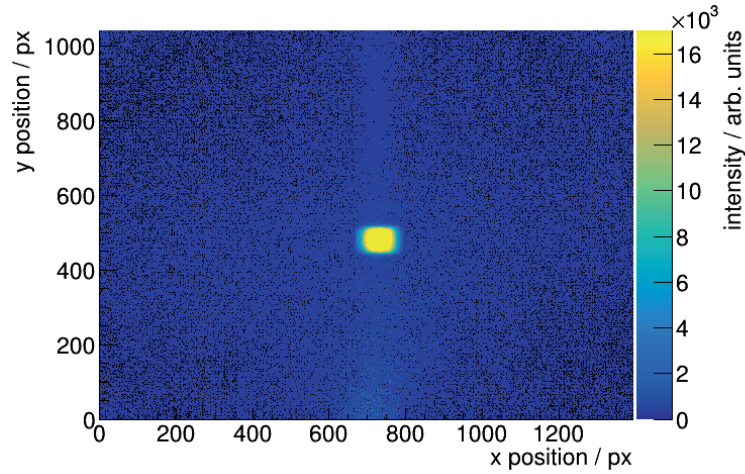
Figure 5.7: Difference of the two pictures displayed in Fig. 5.6. Visible is the cluster beam in the middle of the picture with nearly no remaining reflections in the chamber.

The projection of the recorded cluster beam on the ordinate reflects its characteristics. Because the laser beam has no complete parallel beam path, but is conical widen, the boundary effects of the laser with the cluster beam are included in the projection. To prevent this, only a small vertical area of the cluster beam which is homogeneous illuminated with the laser beam is used for the projection for the cluster beam analysis (cf. Fig. 5.8 indicated with the two white lines).

The projection shows a cluster beam profile like the one recorded with the scanning rod system, the main difference is, that the optical monitor system recorded an intensity in dependence of a position within the cluster beam cross section and the scanning rod
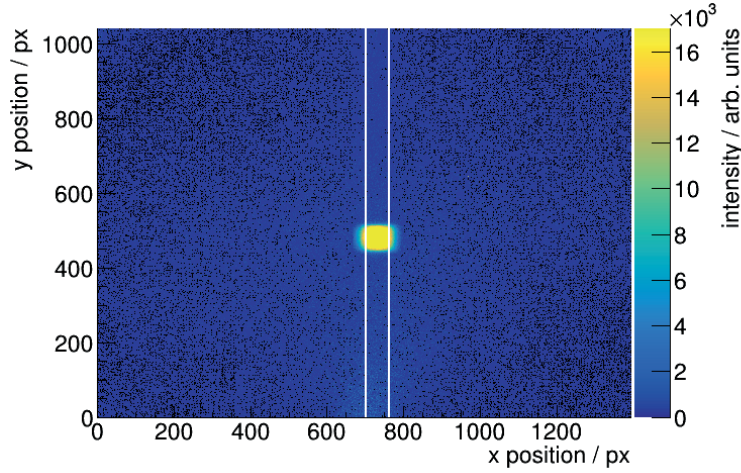
Figure 5.8: Difference of the two pictures displayed in Fig. 5.6. Visible is the cluster beam in the middle of the picture with nearly no remaining reflections in the chamber.

system a pressure in dependence of the rod which is equivalent to a position within the cluster beam cross section. For this reason nearly the same function to describe the beam profile is chosen (cf. Eq. (5.17))

$$I(y) = I_0 \int\limits_{-\infty}^{+\infty} \mathrm{d}x' \int\limits_{y-d/2}^{y+d/2} \mathrm{d}y' \tilde{\rho}(x', y') + I_{back} \tag{5.22}$$

with I_0 being a scale factor, I_{back} the background, and $\tilde{\rho}(x', y') = \tilde{\rho}(r)$ the density distribution. The distance of the distribution to the centre is described by $r = \sqrt{x'^2 + y'^2}$. The width of the resolution is given by d which is equal to 1 pixel, because the picture is recorded by single pixels.

The same assumption as before, that the density distribution $\tilde{\rho}(r)$ is a convolution of a step function with a Gaussian distribution in combination with $x > 0$ and $R_c/\tilde{s} \gg 1$, leads to

$$\tilde{\rho}(r) = \frac{1}{2} \left(1 - \mathrm{erf}\left(\frac{r + R_c}{\tilde{s}} \right) \right). \tag{5.23}$$

where erf is the error function (cf. Eq. (A.7)), R_c the cluster beam radius, and $\tilde{s}$ the smearing parameter.

Thereof, for the description of the beam profile follows

$$I(y) = I_0 \tilde{I}(y - y_0) + I_{back} \tag{5.24}$$

with

$$\tilde{I}(y) = \int\limits_{-\infty}^{+\infty} \mathrm{d}x' \int\limits_{y-d/2}^{y+d/2} \mathrm{d}y' \frac{1}{2} \left(1 - \mathrm{erf}\left(\frac{r + R_c}{\tilde{s}} \right) \right). \tag{5.25}$$

Thereby, I_0 is the height of the peak in the beam profile and y_0 corresponds to the position of the peak.

Figure 5.9 shows a resulting beam profile recorded with the optical monitor system and the associated adaptation with Eq. (5.24). From this beam profiles, the position of the cluster beam y_0, the cluster beam radius R_c, the smearing parameter $\tilde{s}$, and the relative thickness expressed by the intensity I_0 can be extracted.

Furthermore, this system was used to align the MCT1S cluster-jet target to the U1 laser system in Düsseldorf (see chapter 9.1). The preceding analysis of the relative thickness at the cluster-jet target MCT1S with this optical monitor system was used to define the optimal stagnation conditions of the hydrogen in front of the nozzle for the studies of the cluster-laser interaction. The results are presented in Figure 5.10. They show a pressure of 14 bar and a temperature of 27 K to reach the highest with this target realisable thickness. Clearly visible is that lower temperatures and higher pressures leads to higher thicknesses. The underlying reason for the discrepancies from this structure is the existence of highly intense core beams [Kö15, Gri14].

The previous ANKE cluster-jet target was maintained and is now planned to be used for the KOALA experiment at COSY [H$^+$18]. This experiment will measure small angle elastic proton-proton scattering. The now called KOALA cluster-jet target is related to the cluster-jet target MCT1S. The main difference is the nozzle mount on the cold head whereby the cluster beam direction is perpendicular to the cold head. To optimise the collimator dimensions and thereby the cluster beam size and shape, and to adjust the cluster beam in the middle of the interaction chamber the optical monitor system was installed at the interaction chamber. The adjustment towards the centre is important for the planned Mie scattering measurements to determine the cluster size. An initial measurement shows here again the successful application of this system. The recorded image (Fig. 5.11) displays the cluster beam (background subtracted) illuminated with a
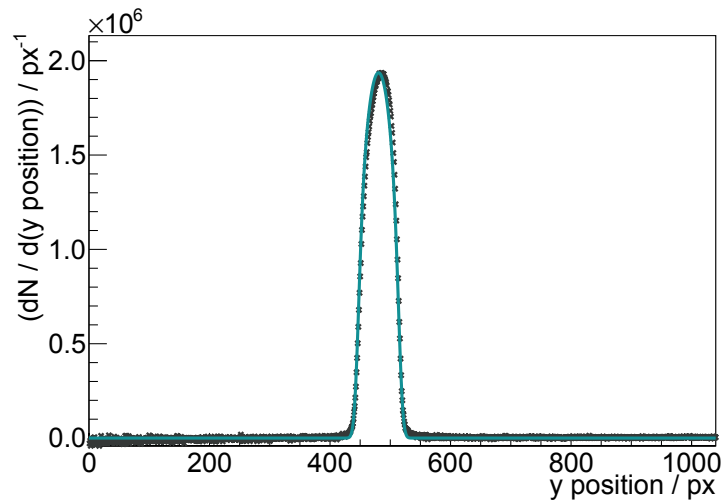
Figure 5.9: Projection of the area between the two white lines of Figure 5.8 on the ordinate. Additionally, the adaptation of the beam profile with Eq. (5.25) is displayed.
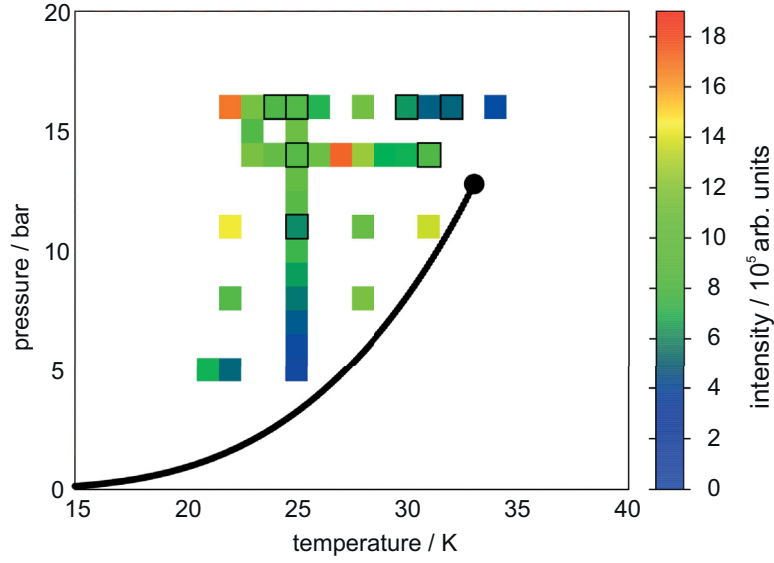
Figure 5.10: Relative thicknesses measured with the optical monitor system in the interaction chamber of the cluster-jet target MCT1S in a distance of 33 cm from the nozzle in dependence of the pressure and temperature of the hydrogen in front of the nozzle. Additionally, the pressure vapour curve is drawn for hydrogen. For every data point, 20 pictures with opened and 20 pictures with closed nozzle shutter with an exposure time of 15 s were recorded. Some settings were measured several times, therefore, the mean value is shown. The black bordered settings shows more than 10 % discrepancy of the individual measurements to each other. These discrepancies occur with respect to the present core beams [Gri14].

laser diode in a distance of roughly 40 cm from the nozzle. The laser beam diameter is in the same range as the cluster beam diameter of roughly 5 mm and therefore, not the whole cluster beam is illuminated. Additionally, the visible area is very large compared to the cluster beam. Therefore, the setup, especially the laser and the objective of the camera, has to be exchanged. Then an analysis of the cluster beam can be performed. The first test measurement with subsequent analysis with Eq. (5.25) leads to a cluster beam centre at pixel 2160 on the abscissa. The resolution of the camera is (4272×2848) pixel, therefore, the middle of the camera and due to the adjustment of the camera, the middle of the interaction chamber is at pixel 2136. The shift of the cluster beam to the left corresponds to approximately 0.55 mm. Furthermore, the diameter of the cluster beam was determined to 4.59 mm. These results should be handled with care due to the not yet optimal setup for the analysis.

Mach-Zehnder Interferometer

A Mach-Zehnder interferometer installed around a jet target allows for the investigation of the properties of the jet target with respect to the target thickness and the size and shape of the beam. Moreover, an image of the jet beam can be reconstructed. In this thesis a Mach-Zehnder interferometer was used to study the jet generated by the jet target for the MAGIX experiment. Therefore, the working principle, design, and analyses of this method are described in chapter 7.2.
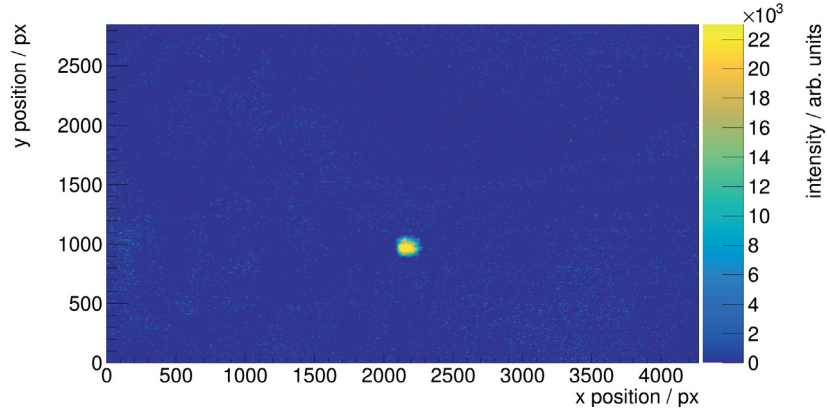
Figure 5.11: Difference of a picture with opened and one with closed nozzle shutter recorded at the interaction chamber of the KOALA cluster-jet target with an exposure time of $30\,\mathrm{s}$ with the optical monitor system. The cluster beam with nearly no background is clearly visible.

Scanning with an Electron Beam

The presence of an accelerated electron beam allows for cluster beam profile and thickness determination. The jet target for the MAGIX experiment was installed at the MAMI accelerator in Mainz (cf. chapter 6.5). There, first measurements on the cluster-electron interaction were investigated. Furthermore, the electron accelerator offers the possibility to scan the cluster beam. A determination of the luminosity for every vertex point allows to calculate the cluster beam profile and therefore the target thickness. More details on the measurements and the results are describes in chapter 7.3.

Schlieren Photography

The schlieren photography is a photographic technology whereby the research object is illuminated with parallel light. Opposite to the light source and behind the object is an objective which display the object on a screen. Thereby, local variations of the refraction index induced by a cluster beam can be imaged and thereof the thickness can be determined (cf. chapter 7.2).

MicroChannel Plates (MCP)

MicroChannel Plates (MCP) are used to visualise charged particles, like ions, protons or electrons. They can be used in a wide range of applications as a detector. This thesis shows the implementation of MCPs as a detector for protons and electrons accelerated by the interaction of a high intense laser beam with a cluster beam (cf. chapter 9.2), for visualisation of the cluster beam to determine its properties, and to display an accelerated proton beam (COSY) with the use of a cluster beam. Moreover the MCP system was used to determine the cluster mass distribution within the thesis of E. Köhler [Kö15].
A MCP consists of millions of microscopic electron multiplier channels (pore diameter of $(12.0 \pm 0.5)\,\mu\mathrm{m}$) made out of conductive glass and bundled together [Ham06]. The top and bottom sides of the plate are equipped with electrodes to apply voltages in the range

of a few kV generating a homogeneous electric field in the channels. Charged particles impinge on the channels and produce secondary electrons which are accelerated to the backside of the MCP due to the electric field. The channels are arranged in an angle of roughly $5\,^{\circ}$ - $15\,^{\circ}$ [Ham06] with respect to the perpendicular axis of the MCP front side to allow a multiple interaction of the electron with the channel walls resulting in an electron avalanche of 10^4 electrons per channel [Zan12]. Figure 5.12 shows the setup and the working principle of a MCP. Additionally, a second MCP is installed directly behind the first MCP with contrary tilted channels, called chevron assembly, to increase the amplification of up to 10^7 electrons per channel. Moreover, the effect of the ion feedback, generated by the residual gas on the back site of the MCP ionised by the electrons leading to additionally multiplied electrons, is reduced with the use of two MCPs.

An important characteristic of a MCP is their gain g [Ham06]:

$$g = \exp\left(G \cdot \alpha\right), \qquad (5.26)$$

with a gain factor G describing the characteristics of the secondary electron emissions and the ratio $\alpha = L/d$ of channel length to diameter.

The efficiency of the detector depends on the type of particles (UV rays, X-rays, α, charged particles, neutrons, electrons), their energy, the attack angle to the channels, and the surface of the channels. Details on these efficiencies are listed in Table 5.1. Mostly, MCPs are used in combination with a phosphor screen to visualise the particles and to get a two-dimensional intensity distribution of the particles.

The application of the MCP as a detector for accelerated electrons and protons are described and analysed in chapter 9.2.4 and 9.2.5.

The MCP system to visualise the cluster beam was first implemented in [Zan12] and is since then routinely in use for cluster beam analyses at the end of the beam dump stage of the $\overline{P}ANDA$ cluster-jet target prototype (see Fig. 4.16) [Kö15].

Table 5.1: Typically efficiencies of a MCP for different radiations with various energy distributions [Ham06].

| type of particles	energy / wavelength	efficiency
electrons	0.2 keV - 2 keV	50 % - 85 %
	2 keV - 50 keV	10 % - 60 %
ions (e.g. H^+, He^+, Ar^+)	0.5 keV - 2 keV	5 % - 58 %
	2 keV - 50 keV	60 % - 85 %
	50 keV - 200 keV	4 % - 60 %
UV rays	30 nm - 110 nm	5 % - 15 %
	110 nm - 150 nm	1 % - 5 %
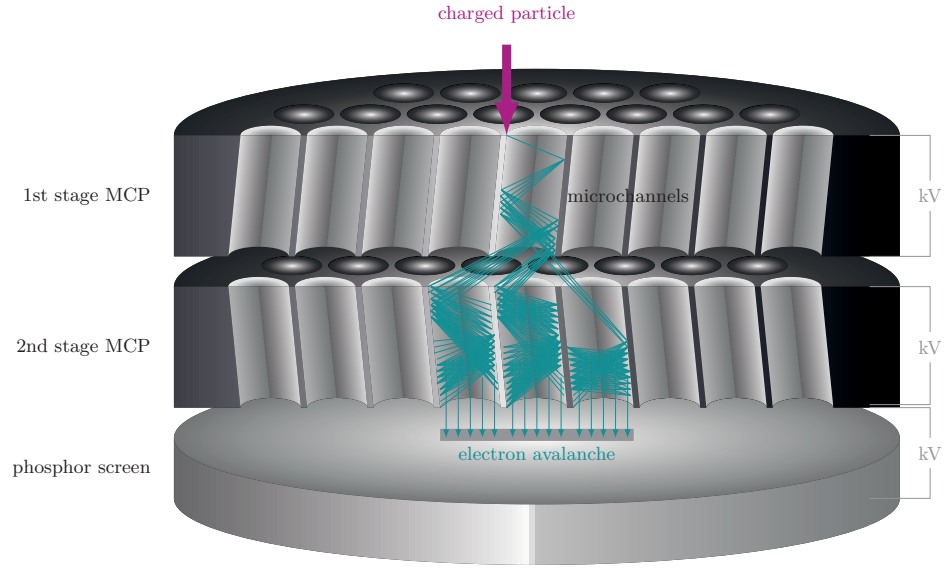
Figure 5.12: Sketch of a MCP (chevron assembly) in combination with a phosphor screen. Charged particles impinging on a capillary leads to an electron multiplication, because each capillary works as an electron multiplier. The electrons generate a two-dimensional image on the phosphor screen. Generated by E. Köhler, edited.
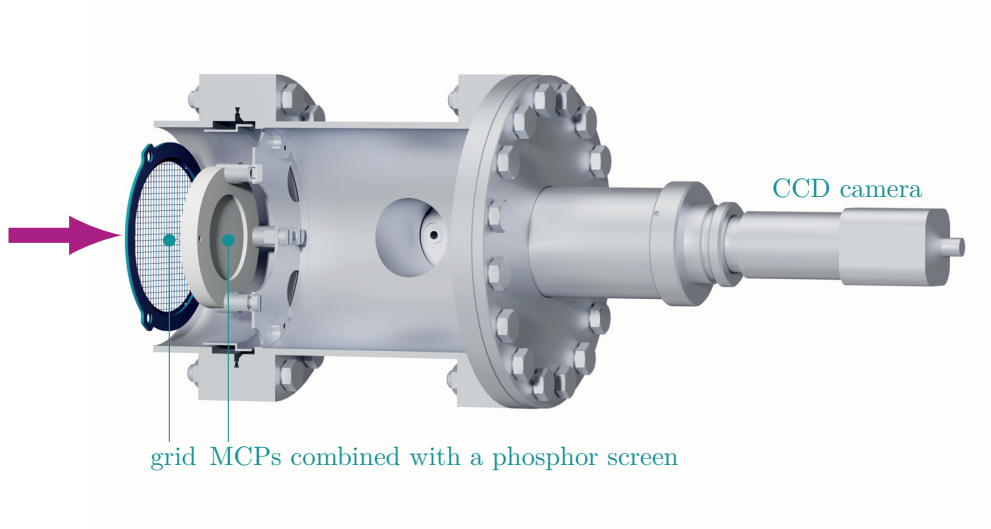
Figure 5.13: The MCP in combination with a phosphor screen installed at the end of the beam dump of the $\overline{\text{P}}$ANDA cluster-jet target prototype. In front of the MCP, a grid is installed to minimise the background on the MCP and to have a size comparison. A CCD camera shows and saves the recorded pictures of the phosphor screen. Generated by D. Bonaventura, [Kö15], edited.

To observe the clusters with the MCP, the clusters have to be ionised before impinging on the MCP. Therefore, a continuously operating electron gun in a distance of 76 cm from the narrowest point of the Laval nozzle ionises the clusters (cf. Fig. 5.14). Details on the setup and working principle of the electron gun is presented in chapter 5.2. After a flightpath of

roughly 4.2 m they enters a grounded grid with 2.7 mm center-to-center of the linies and then the MCP system. A CCD camera (pco.pixelfly usb) takes pictures of the phosphor screen in order to analyse the cluster beam properties or show a real time image of the phosphor screen. Details on the applied MCP and it's specifications can be found in [Kö15].
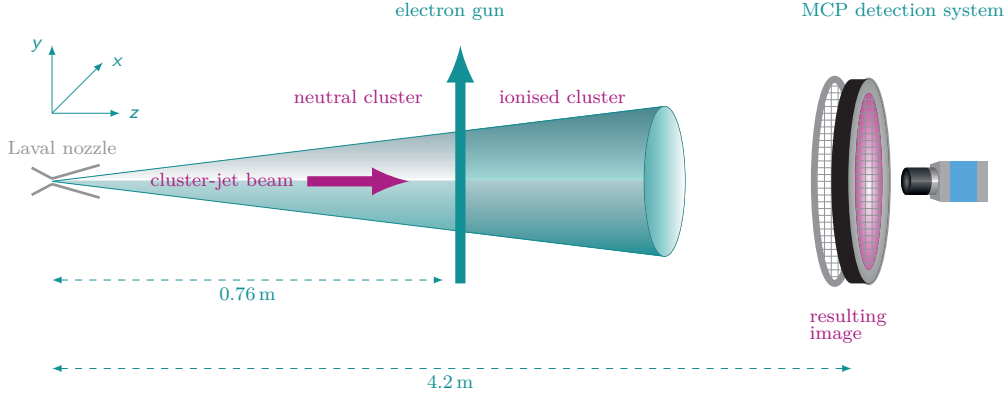
Figure 5.14: Sketch of the setup of the MCP system at the $\overline{P}$ANDA cluster-jet target prototype to visualise the cluster beam. The cluster beam is ionised by an electron gun and inpinges on the MCP resulting in an image of the cluster beam which can be recorded via a camera. Based on [Kö15].

This MCP detection system allows for beam analysis with respect to the size, shape, position, and intensity distribution which corresponds to a relative target information determination. Moreover, the adjustment of the cluster beam can be checked and possible disturbances due to the setup can be observed. Figure 5.15 shows a picture of a cluster beam produced with a glass nozzle recorded with the MCP system. The hydrogen gas in front of the glass nozzle (details on the nozzle and the production precess are described in chapter 3.1) was cooled down to 22 K and the pressure was increased of up to 17 bar. This measurement demonstrates that the glass nozzle is able to produce a cluster beam out of the liquid phase of hydrogen, which travels over a distance of more than 5 m with clusters consiting of more than 10^6 atoms/cluster. Moreover, an intensity distribution can be recorded and analysed (cf. Fig. 5.15). The picture shows a round and unaffected cluster beam with a diameter of roughly (27.5 ± 2.5) mm (determined by the grid size) which is in good agreement with the expected diameter of (26.0 ± 1.0) mm in this distance from the nozzle. Therefore, the cluster beam produced with a glass nozzle has the same lateral divergence like the cluster beams generated with the copper nozzles (chapter 3.1). Moreover, the cluster beam is fully visible which corresponds to a good adjustment, only a small shift to the top-right and a lower intensity in the upper left part of the beam can be observed. Additional, the grid of the MCP system is visible. This visualisation system also allows for the determination of the shape of the cluster beam. To reduce the gas flow of the cluster beam in the interaction chamber of the later $\overline{P}$ANDA experiment, the application of specially formed collimators are planned [Her13] and currently used at COSY. A slit collimator is from highest interest, because there the cluster beam
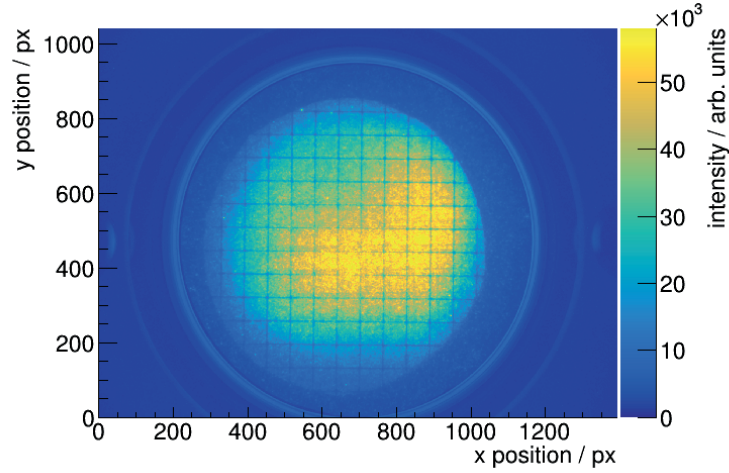
Figure 5.15: Recorded picture with the MCP system installed at the $\overline{\text{P}}$ANDA cluster-jet target prototype shown in false colour representing the intensity distribution. The hydrogen in front of the glass nozzle was at a pressure of 17 bar and a temperature of 22 K. The highest intensity is located in the middle and decreases at the margin of the beam. Additional, the grid of the MCP system is visible. A well defined cluster beam reaches the end of the beam dump in a distance of more than 5 m from the nozzle. This shows the possibility to generate a defined cluster beam even over large distances with the use of a glass nozzle.

has the same shape like the accelerator beam with minimal excessive clusters around the accelerator-cluster beam interaction zone. With the MCP system the possibility to shape the cluster, e.g., as a rectangular beam with a rectangular shaped collimator, was successfully demonstrated [Zan12].

Figure 5.16 shows MCP images with a cluster beam effected by a vertical and horizontal rod. The two rods belong to the manual scanning rod system of the target in a distance of roughly 3 m from the nozzle. This absolute thickness determination system works like the scanning rod system assembled in the scattering chamber, the only difference is that the other system is driven via stepper motors and therefore, it allows for an automatic recording of cluster beam profiles. The rods offers the possibility to distinguish between the cluster beam and background signal on the MCP, because only the cluster beam propagating through the rod generates a shadow of the rod on the MCP images. Moreover, mechanical disturbances of the cluster beam can be visualised and corrected.

This MCP system was first planned to adjust the cluster beam of the cluster-jet target MCT1S in Düsseldorf to the laser focus. The verification of this possibility was proofed in cooperation with C. Hargens [Har16]. First the electron gun was assembled in a distance of roughly 30 cm from the MCP, because the system has to be very compact due to the setup in Düsseldorf. But due to this small distance between electron gun and MCP system, a bright spot in the size of the expected cluster beam was observed on the pictures, but the rod was not visible. Therefore, the spot corresponds to residual gas ionised by the electron gun. Solutions, like the application of a Faraday cage to get rid of the excessive electrons of the electron gun which enters directly the MCP system or the apply of a positive voltage on the grid to create a barrier for the ionised residual gas
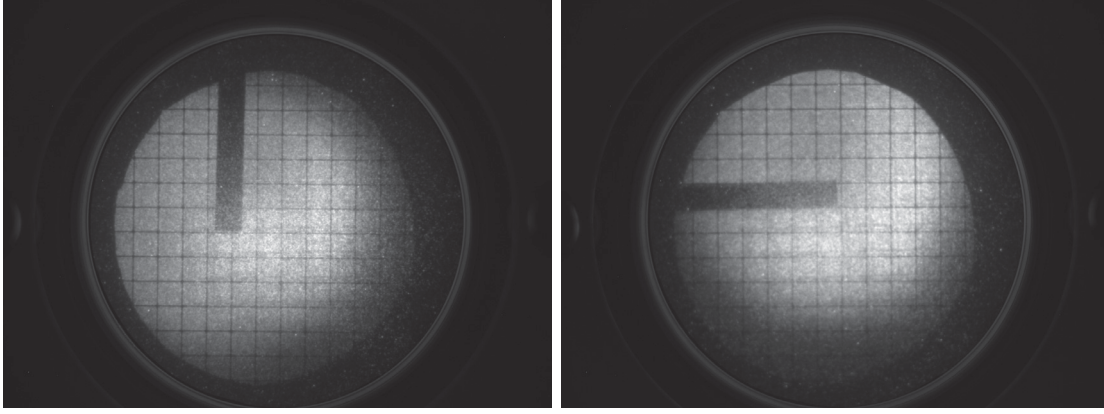
Figure 5.16: MCP image of a cluster beam effected by a vertical and horizontal rod in the cluster beam line. The rods offers the possibility to distinguish between the cluster beam and background signal. Only a cluster beam from liquid hydrogen shows the clear shadows of the rods. A background signal will not travel over the large distance between the rods and the MCP system (roughly 2 m). Furthermore, mechanical disturbances within the cluster beam can be imaged and then corrected.

were unsuccessfully. Therefore, this system works not as a adjustment system for the MCT1S target in Düsseldorf, but nevertheless a second system was checked successfully and finally installed at the target system in Düsseldorf to adjust the cluster beam to the laser focus (cf. chapter 9.1).

The MCP system in the current status works not in a compact design, but this system allows for a visualisation of the vertex zone of an accelerator in storage ring experiments, e.g., COSY, P̄ANDA at HESR. There the accelerator beam interacting with the cluster beam ionises the clusters, due to the smaller diameter of the accelerator beam (1 mm - 2 mm) compared to the cluster beam (10 mm), only the vertex zone will be ionised and contributes to the intensity distribution on the picture which is correlated to the luminosity distribution. This application of the MCP system was studied at the ANKE cluster-jet target at the COSY accelerator in Jülich, Germany (Fig. 5.17) [K$^+$14b]. The MCP system was assembled at the end of the beam dump of the target and the interaction of the cluster beam with the accelerator beam takes in a distance of 70 mm from the nozzle place. There target thicknesses of roughly 10^{14} atoms/cm^2 out of the liquid phase of hydrogen were realised. This measurements neither affects the cluster beam nor the accelerator beam, therefore, this measurement can be performed during the running experiment.

Figure 5.18 shows pictures recorded with the MCP system installed at the ANKE cluster-jet target at COSY [K$^+$14b]. The top picture shows the injection of the protons with a beam momentum of 300 MeV/c. The abscissa and ordinate present the dimensions of the cluster beam, with the ordinate corresponding to the direction of the accelerator beam. The accelerator beam is only visible till pixel 700 on the ordinate, due to the cool sheets of cryopumps installed at the cluster-jet target. After the acceleration of the protons of up to 2100 MeV/c and the additionally use of the adiabatic cooling of the beam, the
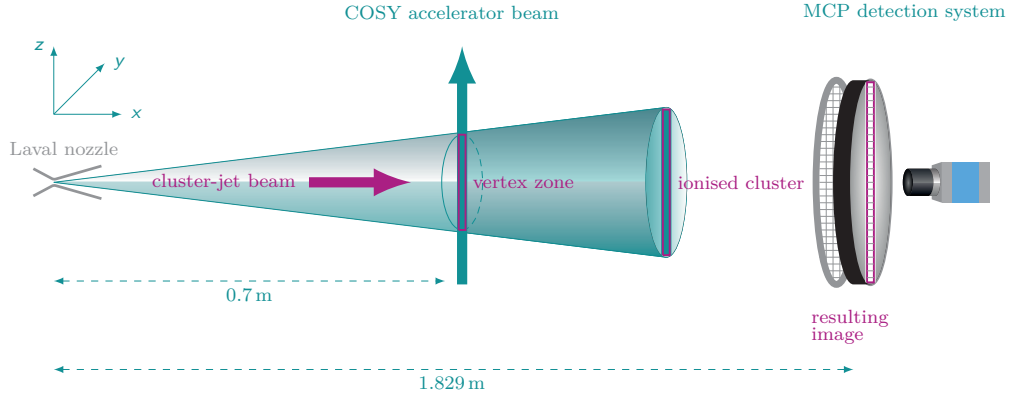
Figure 5.17: Sketch of the setup of the MCP system at the ANKE cluster-jet target at COSY to visualise the accelerated particle beam. The COSY acccelerator beam is used to ionise the clusters within the interaction zone. Thereof, only the ionised clusters cause a signal on the MCP and the COSY beam is visible. A camera allows for recoding the images. Based on [Kö15].

picture in the middle was recorded. There, the broad intensity distribution beforehand changed to a small diameter of the accelerator beam. There, the proton beam diameter of the COSY accelerator at the vertex zone was determined to roughly 1.2 mm (RMS) with a resolution of 150 μm [K+14b]. The bottom picture shows the proton beam shifted by the application of a steerer magnet to adjust the beam to the experimental setup. This shift is also visible with the MCP system. On the basis of these measurements, for the $\overline{\text{P}}$ANDA experiment a MCP system at the end of the beam dump exchangeable with a turbmolecular pump is planned to visualise the cluster beam and moreover the vertex zone of the HESR accelerator beam during the running experiment [Kho18].

5.2 Velocity Distributions within Cluster Beams

### 5.2.1 Measurement of Velocities using a Time-of-Flight Setup

The cluster velocity is an important characteristic figure of the cluster beam. The velocity is used to determine the target thickness using the scanning rod system (cf. chapter 5.1.1). Moreover, it allows for a deeper insight into the cluster production process within the nozzle and cluster beam structures within the beam. In the Diploma thesis of E. Köhler [Kö10], a large data set of velocity distributions using the $\overline{\text{P}}$ANDA nozzle were measured. Based on this measurements, A. Täschner [Tä12] developed a model calculation to predict the cluster mean velocity (cf. chapter 5.2.2). The time-of-flight setup used for the determination of the cluster velocity was developed and tested in [Ott07]. Thereby, a pulsed electron gun, located between collimator and interaction chamber, ionises the cluster beam and generates a start signal for the measurement (Fig. 5.22). The pulse duration, the electron current and the energy of the electrons are determined in such a way, that only one cluster is ionised per pulse. After a flight path of (4.56 ± 0.02) m
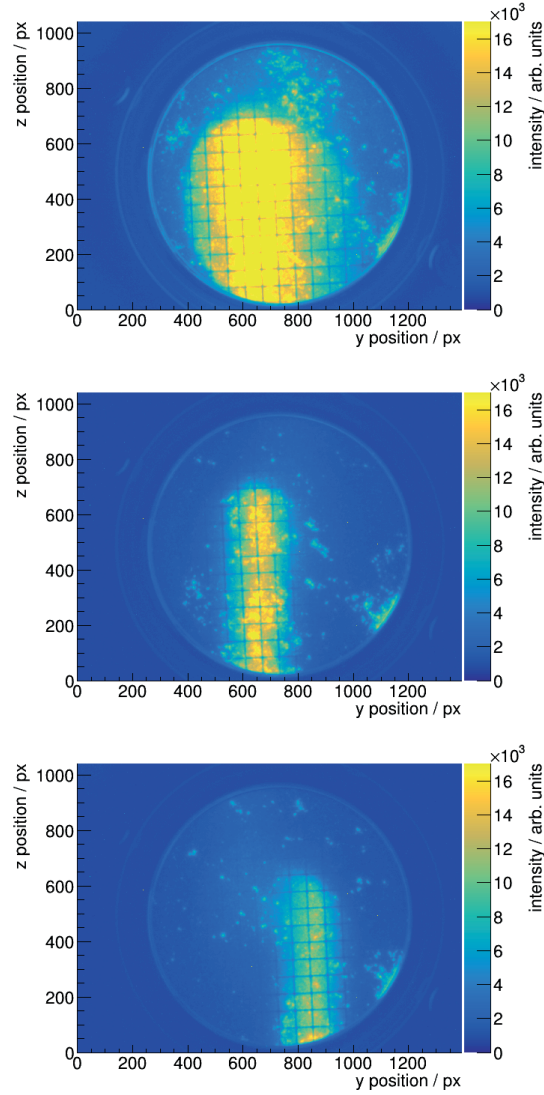
Figure 5.18: Visualisation of the vertex zone of the ANKE cluster-jet target with the COSY accelerator beam. *Top*: Injection of the protons with a beam momentum of 300 MeV/*c*. *Center*: After the acceleration of the protons of up to 2100 MeV/*c*. *Bottom*: Proton beam shifted by the application of a steerer magnet.

the clusters impinges on a channeltron which gives the stop signal for the time-of-flight measurement. The flight length was determined using a tape measure. The time difference between the start and stop signals is calculated via a microcontroller and transferred to a computer.

The electron beam is produced via an electron gun which uses thermionic emission to generate electrons from a filament and an applied electric field accelerates the electrons in the direction of the cluster beam. The pulsed electron gun (Fig. 5.19) has an axial filament to minimize the width of the generated electron beam. The filament consist of a glowing spiral of a halogen lamp without glass bulb. It is enclosed with an extraction aperture consisting of a reflector electrode and an orifice. The filament and the reflector
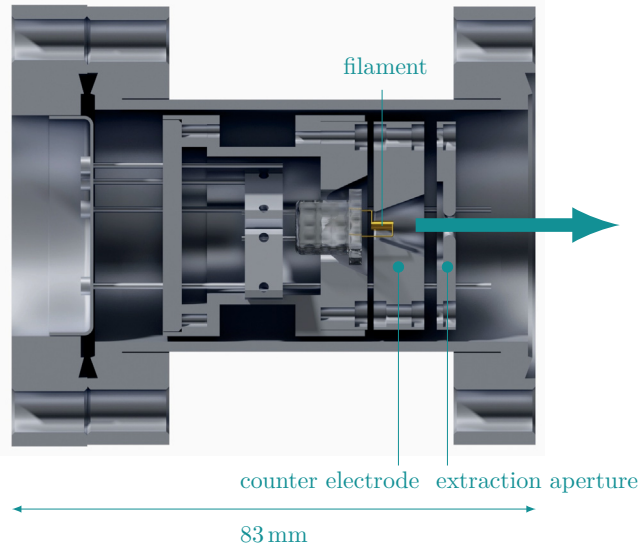
Figure 5.19: Sketch of the electron gun to ionise the clusters. The filament generating the electrons is a glowing spiral of a halogen lamp without glass bulb. The extraction aperture consisting of a reflector electrode and an orifice and allows for a pulsed extraction of the electrons. The electron beam direction is from left to right, indicated with the green arrow. The pulsed electron gun ionize the clusters and generates thereby a start signal for the time-of-flight measurement. Generated by D. Bonaventura, [Kö15], edited.

electrode are equipped with a negative potential with respect to the cluster-jet target to extract and accelerate the electrons out of the electron gun. At the end of the electron gun, a round orifice with a diameter of 3 mm is installed which allows for a fast switching between two states. In the first case, the orifice owns a negative voltage higher than the filament, thereby no electrons will be extracted. In the other case, a grounded orifice leads to an extraction of the electrons. The detailed electrical circuit of the electron gun can be found in [Tä12].

The channeltron to detect the clusters after the flight path and stop the measurement is shown in Fig. 5.20. The orifices in front of the channeltron are used for a mass measurement [Tä12] and grounded for the time-of-flight measurement. The channeltron is installed in a hollow cylinder with a hole of 6 mm in the cap so that the clusters can enter the channeltron. The efficiency of the channeltron to detect single clusters depends on the applied voltage at the entrance and was investigated in the Diploma thesis of E. Köhler [Kö10]. An increase in the applied voltage leads to an increase of the count rate. At a voltage of 2000 V the count rate is at its maximum and a higher voltage results in a saturation. In addition, the channeltron lifetime is affected by the applied voltage. Therefore, the channeltron runs on 2000 V during the measurements performed within this thesis (cf. Table 5.2). The deteiled electrical circuitry of the channeltron and the signal path can be found in [Tä12].
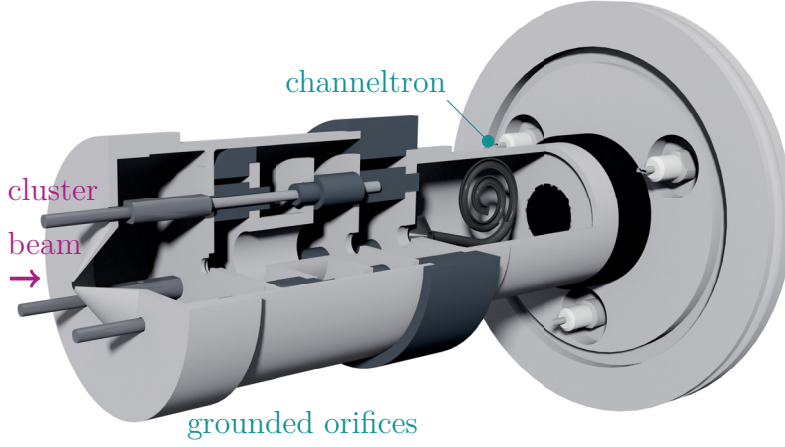
Figure 5.20: Detection system for the ionised clusters at the end of the beam dump of the $\overline{P}$ANDA cluster-jet target prototype. It consists of a channeltron and orifices in front which are grounded during the time-of-flight measurement and only used for mass measurements. The ionized clusters impinges on the channeltron generate a stop signal for the time-of-flight measurement. Generated by D. Bonaventura, edited

A calibration source was used to calculate the time offset of the clusters, caused by the time-of-flight setup and the signal processing of the electrical components. A measurement with the calibration source is shown in Figure 5.21 and its inner working can be found in [Tä12]. The measurement shows four signals at $4\,\mu s$, $37\,\mu s$, $53\,\mu s$, and $64\,\mu s$ corresponding with increasing flight time to photons, and positive charged ions: H^+, H_2^+, H_3^+. To determine the time offset, the flight times in dependency of the kinetic energy of the ions were measured. The velocity v of the ions is proportional to the square root of the acceleration voltage U (ion energy) [Tä12]

$$v = \sqrt{\frac{2qU}{m}}, \tag{5.27}$$

with the charge q and the mass m of the ions. The flight time of the ions t is given by the flight path s and the velocity v under the consideration of the time offset t_0
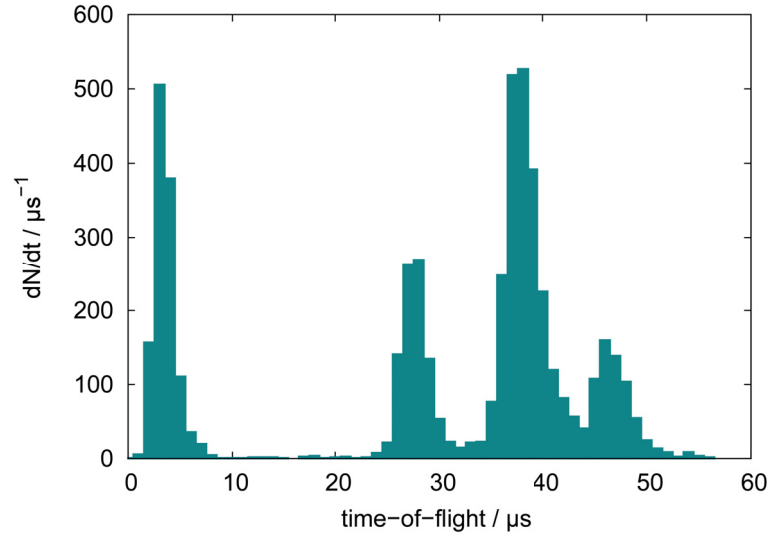
$$t = \frac{s}{v} + t_0. \tag{5.28}$$

These two equations lead to a description of the flight time with respect to the ion energy

$$t\,(s, t_0, U) = s\sqrt{\frac{m}{2qU}} + t_0. \tag{5.29}$$

The performed measurement (cf. Fig. 5.21) within [Kö10] and the analysis result in an average time offset of $\langle t_0 \rangle = 14\,\mu s$ with an accuracy of $\Delta t_0 = 2\,\mu s$ (details can be found in [Kö10, Tä12]).

Figure 5.21: Calibration source for the time-of-flight setup. Clearly visible are four signals ($4\,\mu s$, $37\,\mu s$, $53\,\mu s$, and $64\,\mu s$) corresponding to photons, and positive charged ions: H^+, H_2^+, H_3^+ [Kö15].

Table 5.2: Parameter settings of the time-of-flight measurement.

electron gun	filament	7 V - 10 V
	reflector electrode	90 V
	extraction orifice	110 V
	repetition rate	20 Hz
	duty cylce	$20\,\mu s$
channeltron	channeltron voltage	2000 V
	acceleration voltage	2000 V

5.2.2 Mean Velocity Simulations

The cluster velocity distributions shows a strong variation of value, width, and shape in dependency of the stagnation conditions of the hydrogen gas in front of the nozzle generating the clusters. The velocity is an essential parameter for determining the areal target thickness. Therefore, a precise knowledge is highly relevant with respect to the luminosity of the later experiments. The experimental determination of the velocity by the time-of-flight setup for every possible operating stagnation conditions is not suitable. Hence, a model calculation based on previous velocity measurements at the $\overline{P}ANDA$ cluster-jet prototype [Kö10] were developed in the doctoral thesis of A. Täschner [Tä12]. This model enables for a prediction of the cluster mean velocity by an accuracy of $5\,\%$. Furthermore, this model calculations, including different cluster production processes inside the nozzle, allows in combination with the velocity measurements for a deeper insight into the cluster production process.

To describe the gas flow through a Laval nozzle, a quasi-one-dimensional flow is used.
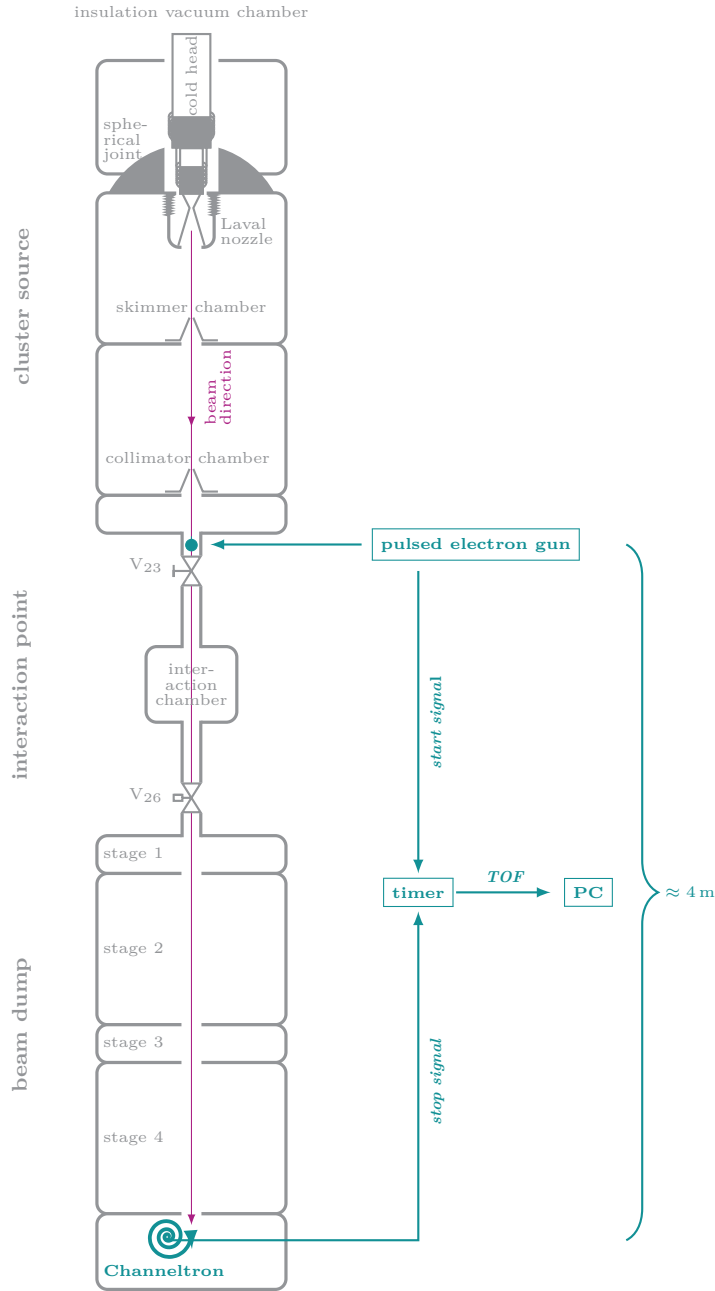
Figure 5.22: Sketch of the time-of-flight setup at the $\overline{P}$ANDA cluster-jet target prototype. The pulsed electron gun ionises the clusters and generated a start signal. The channeltron at the end of the beam dump detects the clusters and gives a stop signal. A timer is used to determine the time between start and stop signal as the cluster flight time. Generated by E. Köhler, edited.

There, the cross-sectional area $A(z)$ of the object changes in the direction of the flow z in contrast to an one-dimensional flow, where the area stays constant (cf. Fig. 5.23).
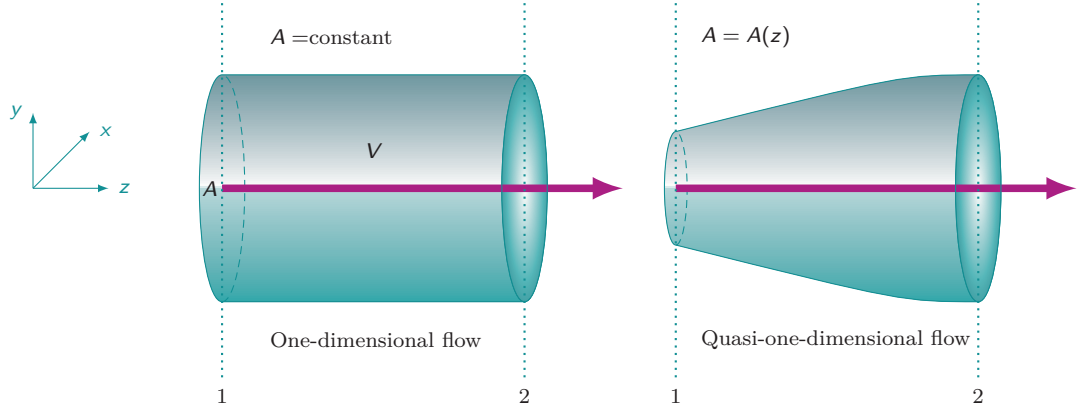
Figure 5.23: *Left*: One-dimensional flow with a constant cross-sectional area A of the object in the direction of the flow z. *Right*: Quasi-one dimensional flow, which is used for the model calculations due to the varied cross-sectional area $A(z)$ of the object in the direction of the flow z. This is comparable with a flow through a Laval nozzle. Generated by E. Köhler, edited.

The basis equations for the model calculations of the quasi-one dimensional flow are the continuity conversation

$$\rho_1 v_1 A_1 = \rho_2 v_2 A_2, \tag{5.30}$$

the momentum conversation

$$p_1 A_1 + \rho_1 v_1^2 A_1 + \int_{A_1}^{A_2} p \, \mathrm{d}A = p_2 A_2 + \rho_2 v_2^2 A_2, \tag{5.31}$$

and the energy conversation

$$h_1 + \frac{v_1^2}{2} = h_2 + \frac{v_2^2}{2}. \tag{5.32}$$

Therein, $\rho = \rho(z)$ represents the target density, $v = v(z)$ the cluster velocity, $A = A(z)$ the cross-sectional area, $p = p(z)$ the pressure, and $h = h(z)$ the enthalpy. The derivations lead to

$$d(\rho v A) = 0, \tag{5.33}$$

$$dp = -\rho v \, dv, \tag{5.34}$$

$$dh + v \, dv = 0. \tag{5.35}$$

Introducing the Mach number $Ma = v/c$ with c being the speed of sound a area-velocity relation can be established assuming an isentropic flow (entropy $\hat{s} = $ constant) without friction, diffusion, conduction of heat, or viscosity

$$\frac{dA}{A} = \left(Ma^2 - 1\right) \frac{dv}{v}. \tag{5.36}$$

Depending on the Mach number three different scenarios are possible:

- $Ma < 1$: Subsonic flow, $v \uparrow \Longleftrightarrow A \downarrow$

- $Ma = 1$: Sonic flow, $v = c$, A is minimal

- $Ma > 1$: Supersonic flow, $v \uparrow \Longleftrightarrow A \uparrow$

In case of a Laval nozzle (cf. Figure 5.24) the inlet zone is convergent, leading to a decrease of the area A and consequently to an increase in velocity v resulting in a subsonic flow ($Ma < 1$) for $z < 0$ (cf. Fig. 5.24). At the narrowest point of the nozzle (parameters marked with *), the area A^* is at its minimum and $v^* = c$, which corresponds to a sonic flow ($Ma = 1$) for $z = 0$. The long divergent outlet zone results in an increase of the area A and an increase in the velocity v, $Ma > 1$: Supersonic flow, for $z > 0$.

Equation (5.32) and the assumption of a stationary gas in front of the nozzle $v_i = 0$ results in

$$v(z) = \sqrt{2(h_i - h_z)}, \tag{5.37}$$

with enthalpy (initial and local) $h_{i/z} = h\left(T_{i/z}, \rho_{i/z}\right)$ and the temperature $T_{i/z}$. At the narrowest point of the nozzle, the enthalpy h^* and the constant entropy $\hat{s}(T,p) = \hat{s}(T_i, p_i) = \hat{s}(T^*, p^*)$ allows for the determination of $T^*(h^*, \hat{s})$, $p^*(h^*, \hat{s})$, and $\rho^*(h^*, \hat{s})$. The continuity equation (Eg. (5.30)) gives the local parameters in dependence of the parameters at the narrowest point of the nozzle [Tä12]

$$\rho^* v^* A^* = \rho(h_z \hat{s}) v(h_z \hat{s}) A(z). \tag{5.38}$$

First, the velocity was calculated assuming a perfect gas, which is an ideal gas with constant heat capacity. The results do not describe the data in the liquid phase of
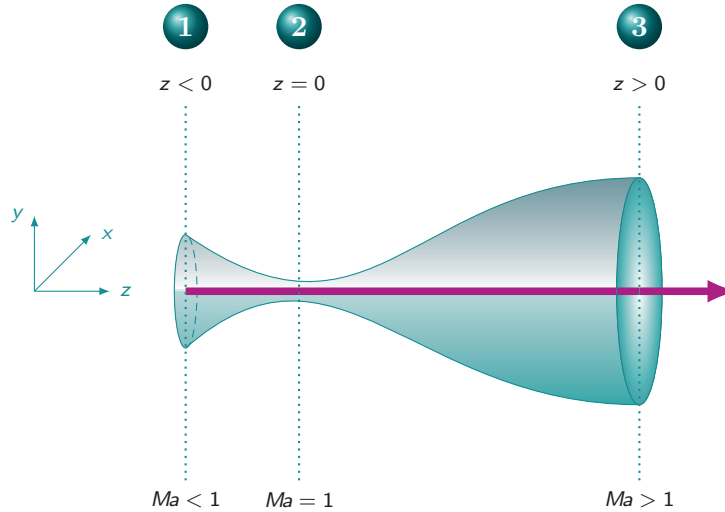

Figure 5.24: Quasi-one-dimensional flow through a convergent-divergent Laval nozzle. Generated by E. Köhler, edited.

hydrogen, see Figure 5.25 represented by the solid line. Introducing the van der Waals equation

$$\left(p + a\frac{n^2}{V^2}\right)(V - nb) = nRT \tag{5.39}$$

leads to predictions of the velocity with an accuracy of $5\,\%$ (cf. Fig. 5.25 dashed lines). Therein, the amount of substance $n = N/N_A$ is defined by the number of particles N and the Avogadro's constant N_A and R represents the universal gas constant. The parameters a and b are material constants describing the size and the interaction of the molecules.
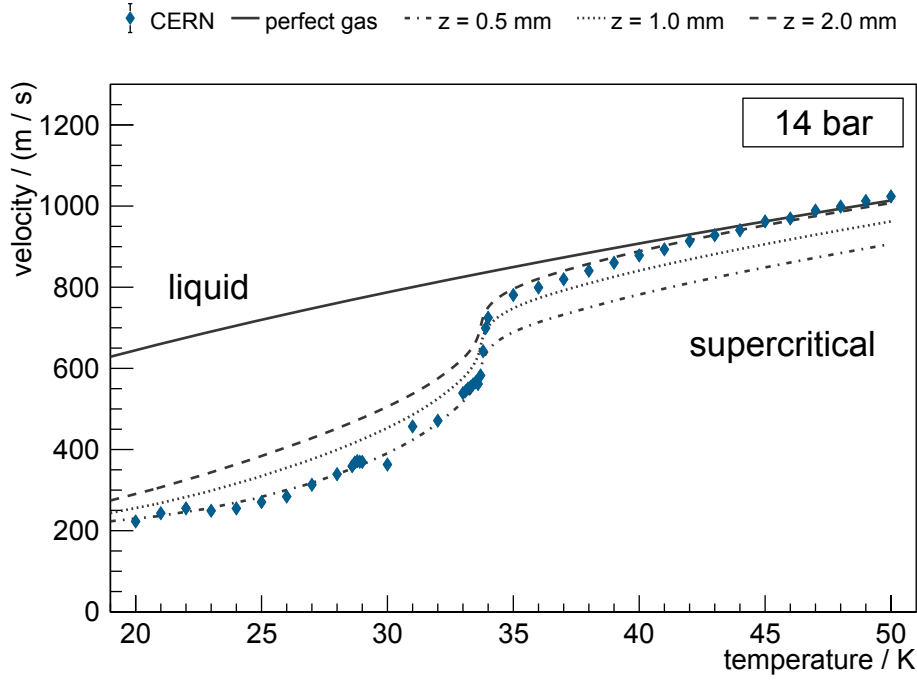
Figure 5.25: Measured velocities in dependence of the temperature with a pressure of $p = 14\,\text{bar}$ of the hydrogen in front of the nozzle at the $\overline{\text{P}}$ANDA cluster-jet target prototype (MCT2) by E. Köhler (blue). In comparison calculations performed by A. Täschner assuming a perfect gas (solid line) and a van der Waals gas (dashed lines) are shown. The perfect gas does not describe the measurement. The three different lines for the van der Waals gas describe different z parameters, where the clusters decouple from the gas within the nozzle. The value of the z parameter depends on the phase of the hydrogen in front of the nozzle. Data extracted from [Tä12].

Furthermore, the data show, that the clusters do not decouple from the surrounding gas at the narrowest point of the nozzle. Thus, the parameter z is implemented in the calculations, representing the distance from the narrowest point, where the decoupling within the nozzle occurs. Depending on the stagnation conditions of the hydrogen in front of the nozzle, vapour or liquid, two different production processes takes place. In the case of vapour hydrogen cluster condensation and in case of liquid hydrogen cluster fragmentation occurs. Therefore, two different z parameters were determined, $z_{\text{vapour}} = (1.67 \pm 0.20)$ mm and $z_{\text{liquid}} = (0.445 \pm 0.014)$ mm. Further details on the calculations can be found in [Tä12]. On the basis of these calculations, new calculations were performed within this thesis, to

compare the new gained results with the theoretical description.

Currently simulations of the velocity and thickness distribution within the nozzle and the resulting beam are performed with OpenFOAM by P. Brand [Bra18] and S. Vestrick [Ves18]. There, also the three Equations (5.30) - (5.32) in combination with different equations of state for gases are used. The main difference is the possibility to perform a three-dimensional calculation assuming a wedge with axisymmetric boundary conditions.

5.3 Investigations on different Laval Nozzles

A Laval nozzle is the main component of each Münster cluster source (cf. chapter 2.2). The geometry of the nozzle is essential for the cluster production process and determines the properties of the clusters. To ensure the availability and a diversity of different Laval nozzles, several production processes were developed at the University of Münster (cf. chapter 3). Wide-ranging measurements on the cluster characteristics allow for a deeper insight into the cluster production process and lead to an optimised nozzle geometry towards highest performance.

The manufactured and already presented different nozzles (cf. chapter 3) were installed at the $\overline{\text{P}}$ANDA cluster-jet target prototype (cf. chapter 4.3). There, various diagnostics are available to investigate the cluster beam with respect to its thickness, size, shape, velocity, and the structure within the cluster beam. The diagnostic tools were already presented in the beginning of this chapter. The results on the cluster beam depending on the different nozzles are discussed in this chapter.

5.3.1 $\overline{\text{P}}$ANDA Nozzle

As a first step, the already extensive studied $\overline{\text{P}}$ANDA nozzle was reinstalled at the $\overline{\text{P}}$ANDA cluster-jet target [Kö15]. The $\overline{\text{P}}$ANDA nozzle originates from the CERN nozzle production process (cf. chapter 3). The nozzle has a narrowest inner diameter of $\varnothing_{\overline{\text{P}}\text{ANDA}} = 28\,\mu\text{m}$. The previous measurements were performed in the framework of the doctoral thesis of E. Köhler [Kö15]. Nevertheless, some important measurements were additionally taken to understand the effects of the geometry and the manufacturing process of the nozzle on the cluster beam.

Moreover, the results gained with this high performance nozzle forms the basis for the comparisons with the new nozzles. A target thickness mapping with a pressure of $17\,\text{bar}$ of the hydrogen in front of the nozzle in dependency of the temperature of the gas is shown in Figure 5.26. This characterisation was done by E. Köhler, additionally she shows the (up to this thesis) record achievable target thickness of $2 \times 10^{15}\,\text{atoms/cm}^2$ in a distance of $2.1\,\text{m}$ from the nozzle [Kö15].
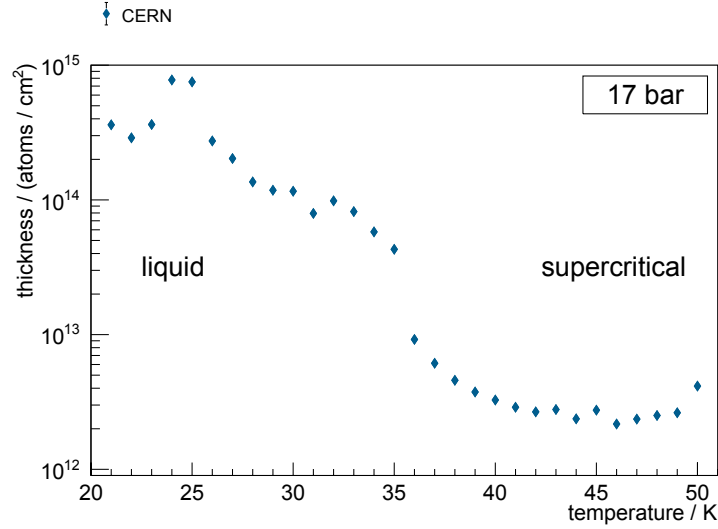
Figure 5.26: Target thickness mapping for a pressure of 17 bar of hydrogen in front of the nozzle in dependency of the temperature of the gas performed with the $\overline{\mathrm{P}}$ANDA nozzle. The target thickness is adjustable over several orders of magnitude by changing the stagnation conditions of the hydrogen gas. The increase of the thickness at a temperature of 24 K and 25 K is caused by the existence of highly intense core beam. Data extracted from [Kö15].

The target thickness increases with decreasing temperature. Moreover, a step in the thickness course is visible between the temperatures 34 K and 35 K. There, the physical state of hydrogen in front of the nozzle changes from gaseous to supercritical (cf. Fig. 5.30). As already mentioned in the previous chapter 5.2.2, the cluster production process varies with the hydrogen phase. Vapour hydrogen leads to cluster condensation and liquid hydrogen results in fragmentation, and supercritical hydrogen to both. Therefore, the characteristics of the cluster beam with respect to thickness, velocity, mass, and cluster beam structures change rapidly by passing the hydrogen vapour pressure curve. By changing the stagnation conditions of the hydrogen in front of the nozzle, the target thickness is adjustable over several orders of magnitude during an experiment and this will be used to ensure a constant luminosity at the upcoming $\overline{\mathrm{P}}$ANDA experiment (cf. chapter 5.1).

In additions, an enhancement of the thickness at the temperatures of 24 K and 25 K is clearly visible. This effect is induced by the existence of highly intense core beams represtend in an inhomogenous thickness distribution within the cluster beam [Kö15]. Images of the cluster beam recorded with the visualisation system in the skimmer chamber show structures within the cluster beam (cf. Fig. 5.27). The presence of the nozzle tilting system in combination with the moveable skimmer and collimator allow for an extraction of the bright part of the cluster beam and that shows a high thickness in this cluster beam part. Thus, the use of the highly intense core beam leads to the (up to this thesis) record thickness of 2×10^{15} atoms/cm^2 in a distance of 2.1 m from the nozzle. The formation of these highly intense core beam depends on the stagnation conditions of the hydrogen in front of the nozzle, intensive studies were performed in [Kö15]. Moreover, the generation and structure of the core beam is based on the nozzle geometry and therefore,
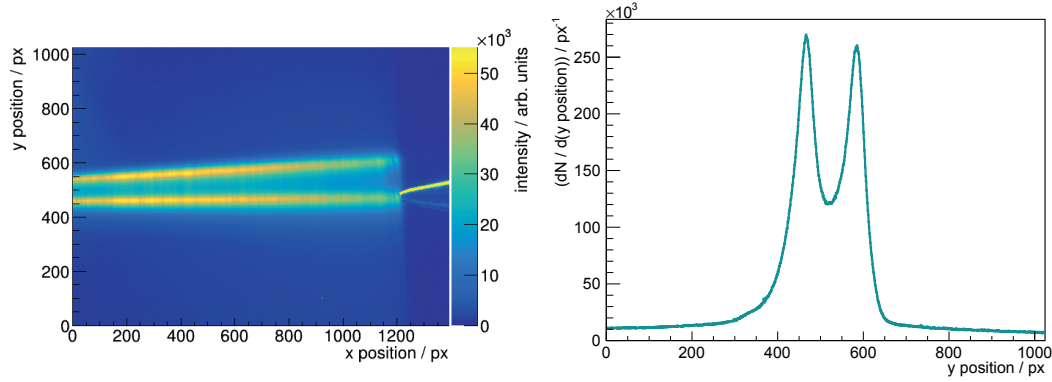
Figure 5.27: *Left*: False colour image of the cluster-jet beam recorded with the visualisation system in the skimmer chamber at 17 bar and 23 K. The exposure time was 5 s. The beam direction is from left to right. On the left side, the skimmer tip is visible, which only extracts a small part of the cluster beam. Brighter parts within the cluster beam are clearly visible and corresponding to a higher thickness in comparison to the darker parts. *Right*: Projection of the cluster beam on the ordinate for the abscissa range between 800 and 805. Also here, the two highly intense core beams are visible showed by a higher intensity.

the manufacturing process of these. Nevertheless, the core beam structures are stable and reproducible for a fixed nozzle in combination with specified stagnation conditions.

Table 5.3: Stagnation conditions of hydrogen in front of the nozzle for the velocity measurements in Figures 5.29, 5.32, and 5.33.

data point	pressure / bar	temperature / K	physical state of hydrogen
🟢	17	25	liquid
🔴	10	22	liquid
🔴	14	30	supercritical/liquid
⚪	15	35	supercritical
🔵	7	30	gaseous

The measurement in Figure 5.27 were performed within this thesis. Additionally, a determination of the velocity with the time-of-flight setup (cf. chapter 5.2) was realised due to the importance for calculating the target thickness. The measured velocity distribution for 18 bar and 22 K is depicted in Figure 5.28. An extremely narrow distribution occurs with a mean velocity of (249 ± 1) m/s and a standard deviation of 11 m/s. In comparison to the previous data, the velocity distribution for liquid hydrogen is typically a wide distribution (see Fig. 5.29, top and bottom left (green and red)). Moreover, the velocity was determined and predicted with the calculations from A. Täschner to (265 ± 13) m/s assuming a $z_{\text{liquid}} = (0.445 \pm 0.014)$ mm [Tä12]. So a discrepancy between the new measured velocity and the previous measurement and model calculation occurs. A. Täschner showed in his thesis, that the z parameter is depending on the used cluster-jet target to determine the velocity. It seems reasonable to assume that the velocity and therefore, the z parameter, depends on the orientation of the nozzle and the nozzles

geometry. This will be further investigated later in this section.
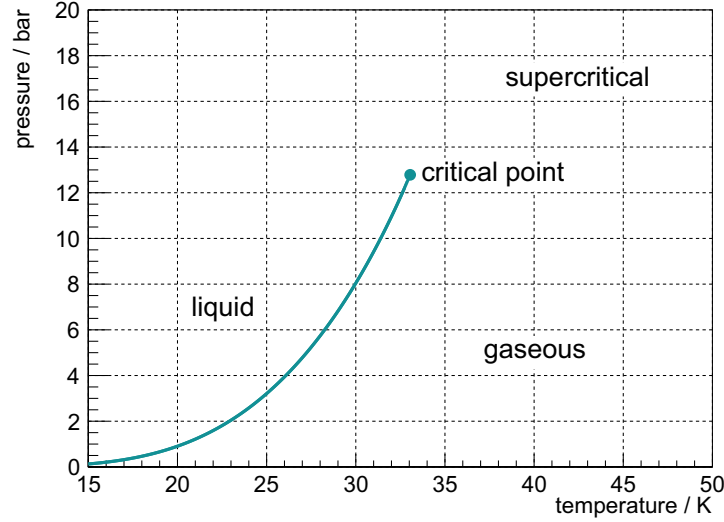
Figure 5.30: Hydrogen vapour pressure curve. The physical states of hydrogen in dependency of the pressure and temperature. Additionally, the critical point at 12.964 bar and 33.145 K [L+09a] is displayed.

The previous velocity measurements were performed before the spherical joint was installed at the $\overline{\text{P}}$ANDA cluster-jet target. Therefore, the possibility to extract a certain part of the cluster beam was missing and an arbitrarily chosen part of the cluster beam was investigated. Now, extracting only the high intense core beam leads to a sharp velocity distribution with slower clusters. A new performed calculation based on the calculation of A. Täschner results in a z value of $z_{\text{liquid}} = (0.22 \pm 0.01)$ mm.
The measured velocity of (249 ± 1) m/s results in the new calculated z parameter and in combination with new performed target thickness measurements via the scanning rod system a new record target thickness of $(4.85 \pm 0.24) \times 10^{15}$ atoms/cm^2 at a distance of 2.1 m from the nozzle at 18 bar and 22 K was achieved. This was the first time the designed $\overline{\text{P}}$ANDA target thickness of 4.5×10^{15} atoms/cm^2 was achieved and even exceeded by the use of a cluster-jet target in such a nozzle distance.

The measured velocity distribution with the possibility to chose certain parts of the cluster beam realised with the spherical joint shows the importance of the velocity determination for different parts of the cluster beam. This measurement was a first hint, that the mean velocity and furthermore, the velocity distribution vary with the angle of the spherical joint resulting in an extraction of different parts of the cluster beam. This aspect will be further investigated in the next section 5.3.2.

5.3.2 Monolithic Copper Nozzles: A21 and A19

The new manufactured monolithic nozzles A21 and A19 were extensively studied with respect to their impacts on the cluster beam within this thesis. Their production process
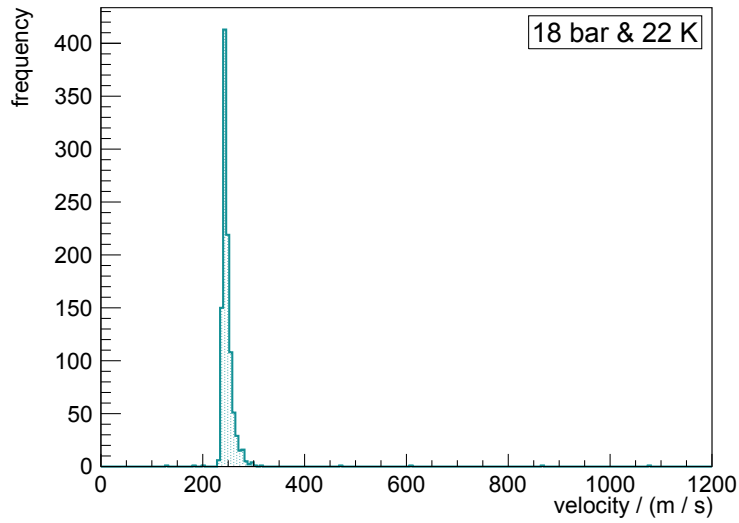
Figure 5.28: Velocity distribution at 18 bar and 22 K measured within this thesis. A narrow distribution with a standard deviation of 11 m/s is visible.
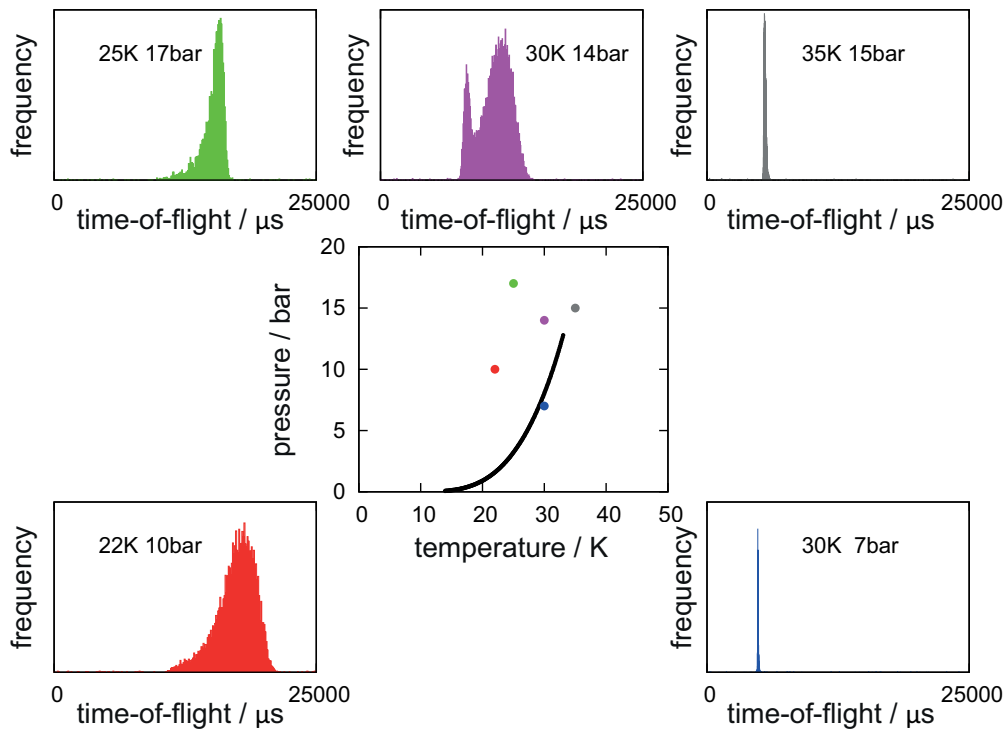
Figure 5.29: Typical time-of-flight distributions for different stagnation conditions. The individual stgnation conditions can be found in Table 5.3. In the case of liquid hydrogen (green, red) a wide velocty distribution is measured. Gaseous hydrogen (blue) leads to a sharp velocity distribution. Supercritical hydrogen (magenta, gray) is in-between and shows a double peak structure or also a sharp distribution depending on the certain stgnations conditions. The reason for the different distributions lies in the different cluster production processes: cluster condensation and fragmentation [Kö10].

is explained in detail in chapter 3. Due to their similar production processes both are treated together in this section. Figure 5.31 shows the microscopic views of the narrowest inner diameters of the two nozzles. The diameters were calculated to $\varnothing_{A21} = 25\,\mu m$ and $\varnothing_{A19} = 33\,\mu m$ by measuring the hydrogen volume flow through the nozzle (cf. Eq. (5.4)).
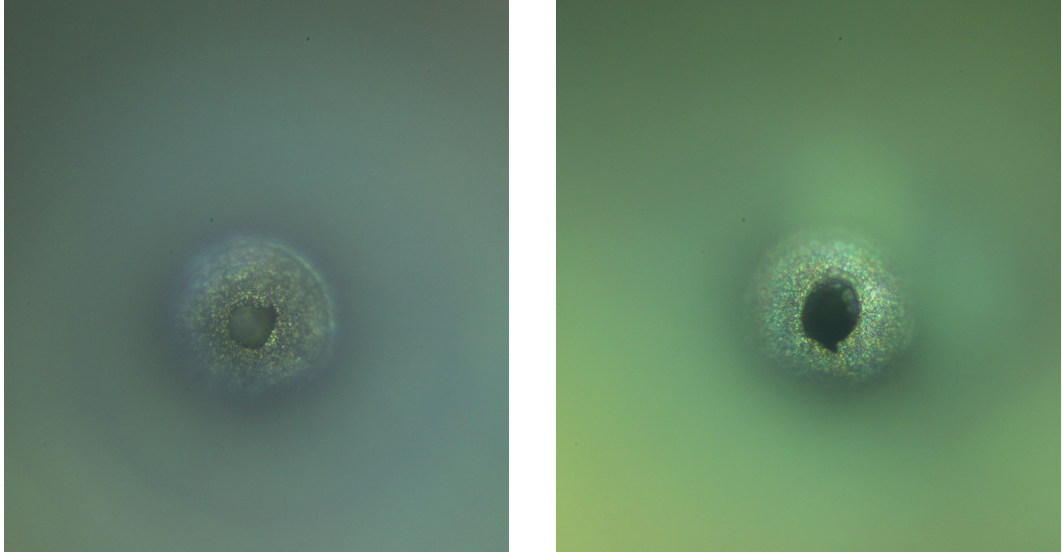

Figure 5.31: Microscopic views of the narrowest inner diameters of the monolithic copper nozzles: A21 (*left*) and A19 (*right*).
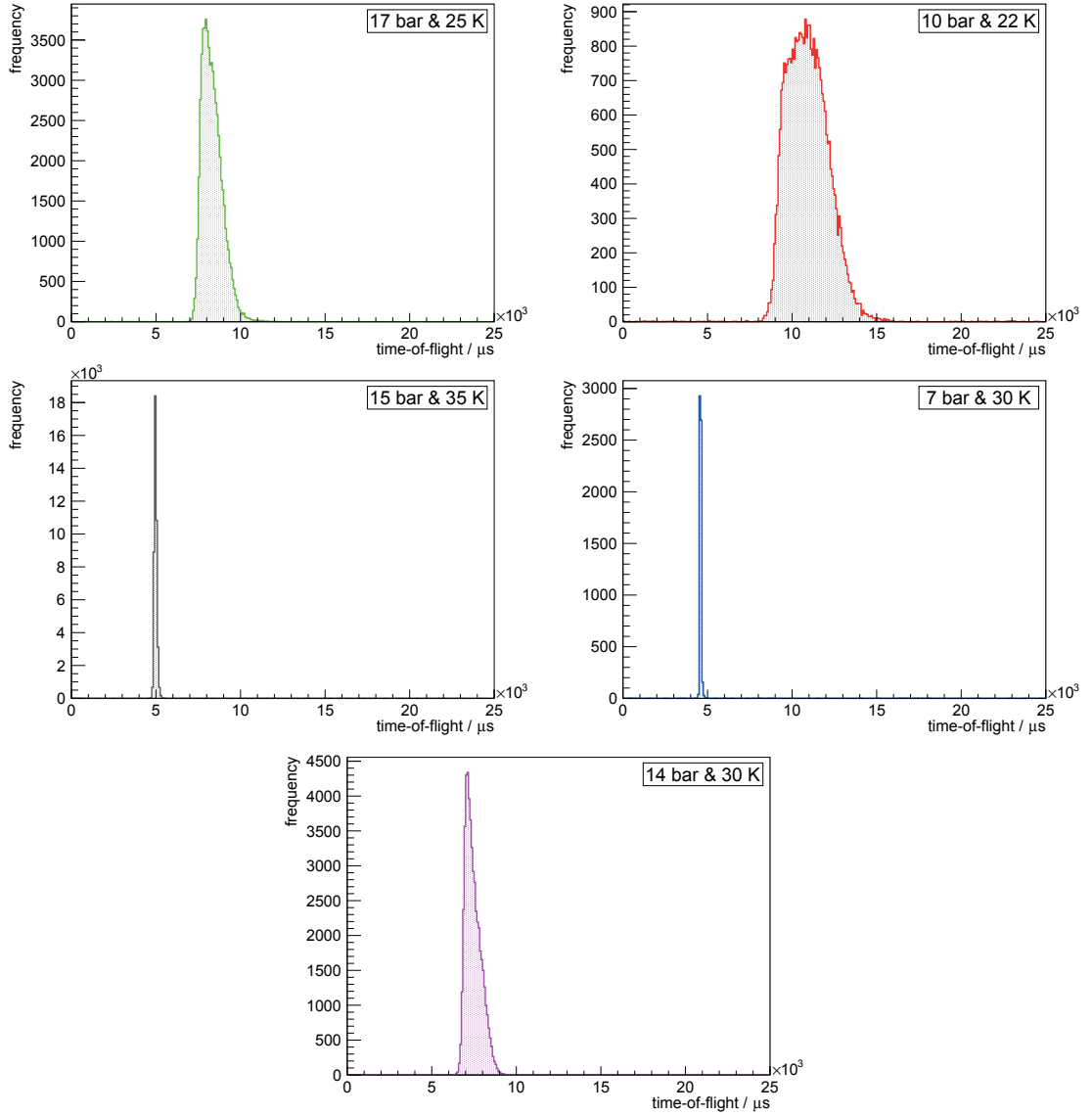
Velocity Distributions

Based on the results from the velocity measurement with the $\overline{P}ANDA$ nozzle, showing a different velocity than measured before, the velocities for both nozzles were determined. Figure 5.32 for A21 and Fig. 5.33 for A19 show the results of the time-of-flight distributions for different stagnation conditions. To compare these data with the $\overline{P}ANDA$ nozzle data, the same stagnation conditions were chosen and the measurements are coloured in the same way. For every measurement setting, 50000 individual time-of-flight data were recorded. Gaseous hydrogen results in a sharp distribution with standard deviations of $5\,m/s$ to $10\,m/s$ and the supercritical measurement show a sharp distribution with a slightly distinctive double peak with standard deviations of $14\,m/s$ to $52\,m/s$. Liquid hydrogen leads to wide distribution with standard deviations of $39\,m/s$ to $57\,m/s$.
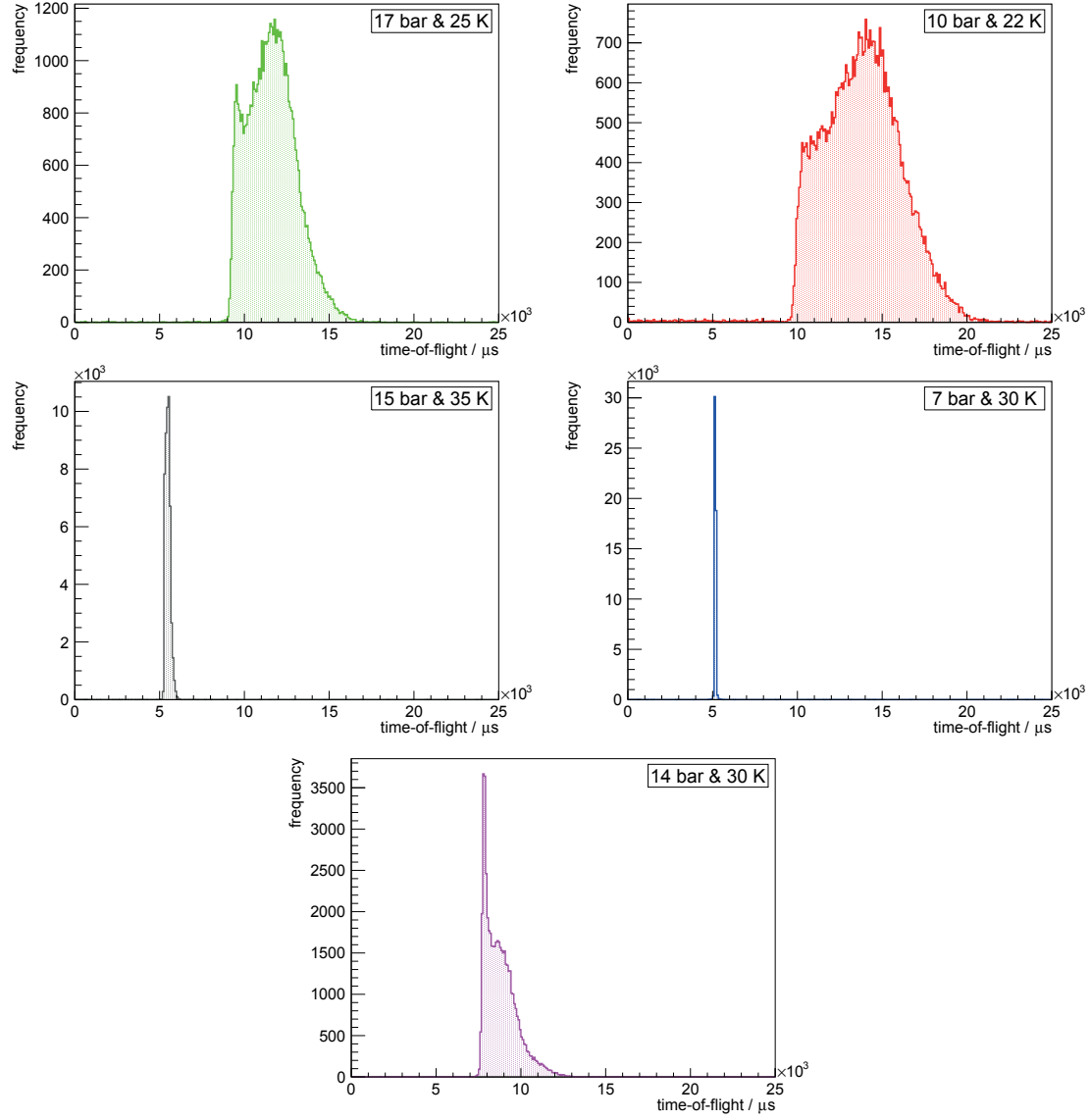
Figure 5.32: Measured time-of-flight distributions for the A21 nozzle for different stagnation conditions (cf. Table 5.3). Liquid hydrogen in front of the nozzle (*top*) leads to a wide velocity distribution with foothills to large time-of-flight times in contrast to the results gained with the $\overline{P}$ANDA nozzle. Gaseous hydrogen (*center*) results in a sharp distribution and the supercritical measurement (*bottom*) shows a sharp distribution with a slightly distinctive double peak. For every setting, 50000 individual time-of-flight data were recorded.

A19

Figure 5.33: Measured time-of-flight distributions for the A19 nozzle for different stagnation conditions (cf. Table 5.3). The velocity distributions all show a sharp velocity distribution in comparison to the $\overline{P}$ANDA and A21 nozzle. The two measurements performed with liquid hydrogen (*top*) results in a little wider distribution. Additionally, no clear double peak structure occurs within supercritical hydrogen (*center*) in front of the nozzle. For every setting, 50000 individual time-of-flight data were recorded.

The mean velocities calculated from the time-of-flight measurements (Fig. 5.32 and 5.33) are listed in Table 5.4. The cluster velocities measured with the A19 nozzle are slower than the clusters generated with the A21 nozzle. Additionally, the velocity distributions of the A19 nozzle are in most cases narrower than the distributions measured with the A21 nozzle. However, both show the similar behaviour.

Table 5.4: Measured mean velocities corresponding to the measurements presented in Fig. 5.32 and 5.33. A smaller velocity, assuming the other variables to be constant, leads to a higher target thickness.

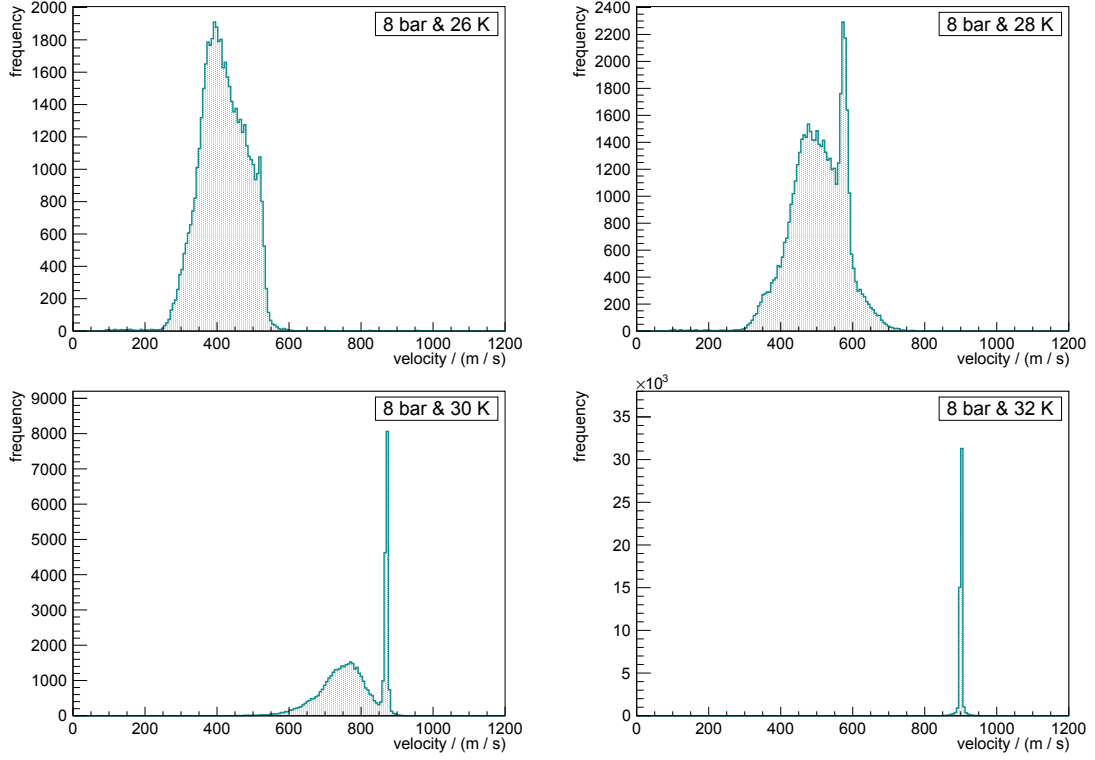| nozzle	pressure	temperature	velocity	standard deviation
	bar	K	(m/s)	(m/s)
A21	17	25	393 ± 2	50
	10	22	331 ± 1	58
	14	30	519 ± 2	52
	15	35	833 ± 4	22
	7	30	885 ± 4	5
A19	17	25	548 ± 2	39
	10	22	417 ± 2	46
	14	30	612 ± 3	37
	15	35	917 ± 4	15
	7	30	987 ± 5	10

Liquid hydrogen leads to slow clusters, gaseous hydrogen to fast clusters and the supercritical hydrogen lies in-between.

A measurement series performed with the A21 nozzle with a pressure of 8 bar with temperatures between 26 K and 32 K in steps of 2 K shows the dependency of the velocity distribution from the stagnation conditions (Fig. 5.34). This series starts in the liquid phase of hydrogen and ends in the gaseous phase. Thereby, to the wide velocity distribution with a standard deviation of 66 m/s at 26 K, a second sharp and small peak occurs at 28 K. The sharp peak increases and at the same time, the wide peak decreases. At 32 K, only the sharp peak is visible with a standard deviation of 7 m/s. The corresponding mean velocities are shown in Table 5.5. During this measurement, for every setting, 50000 individual time-of-flight data were recorded. The corresponding measurement for the A19 nozzle is presented in Appendix A.2.

In order to calculate the thicknesses reached with the two monolithic copper nozzle, the z parameter has to be determined to simulate the velocities. On the basis of the result within the thesis of A. Täschner, that the z parameter depends on the cluster-jet target, it is obvious that the z value also depends on the nozzle mounting and the nozzle itself.

Table 5.5: Mean velocities for the measurement series performed with a pressure of 8 bar with temperatures between 26 K and 32 K in steps of 2 K (Fig. 5.34). The mean velocities developed as expected, a decrease of the temperature leads to faster clusters.

nozzle	pressure	temperature	velocity	standard deviation
	bar	K	(m/s)	(m/s)
A21	8	26	409 ± 2	66
	8	28	495 ± 2	76
	8	30	723 ± 3	79
	8	32	902 ± 4	7

Figure 5.34: Measurements series with the A21 nozzle with a pressure of 8 bar with temperatures between 26 K and 32 K in steps of 2 K. In case of liquid hydrogen, a wide velocity distribution is visible *(top, left)*. An increase of the temperature leads to a second sharp peak *(top, right)*. Another increase in temperature leads to a rise of the sharp peak and a drop of the wide peak *(bottom, left)*. Gaseous hydrogen results in a single sharp peak *(bottom, right)*. The corresponding mean velocities are shown in Table 5.5. For every setting, 50000 individual time-of-flight data were recorded.

Therefore, velocity measurements series were performed for an isobar of 14 bar and an isotherm of 30 K for both nozzles (Fig. 5.35 and 5.36). The first measurement series shows the transition from liquid to supercritical hydrogen in front of the nozzle and the second one the transition from vapour to liquid. Some data points show different results in comparison to the previous presented data. The reason for that is the readjustment of the spherical joint, leading to another velocity (more details later in this chapter). Additionally, some curves for different z values are shown. The determined z value for the liquid and the gaseous phase of hydrogen for both nozzles were determined and listed in Table 5.6. These values were calculated by minimizing the distance between the simulated curves and the measured data points.

The performed measurements show that the value of the z parameter not only depends on the cluster-jet target but furthermore on the used nozzle and its specific geometry. Due to the same production process of the two monolithic copper nozzles, the discrepancy of the z parameter can only occur from the narrowest inner diameter of the nozzles. All the other parts of the nozzle are exactly the same.
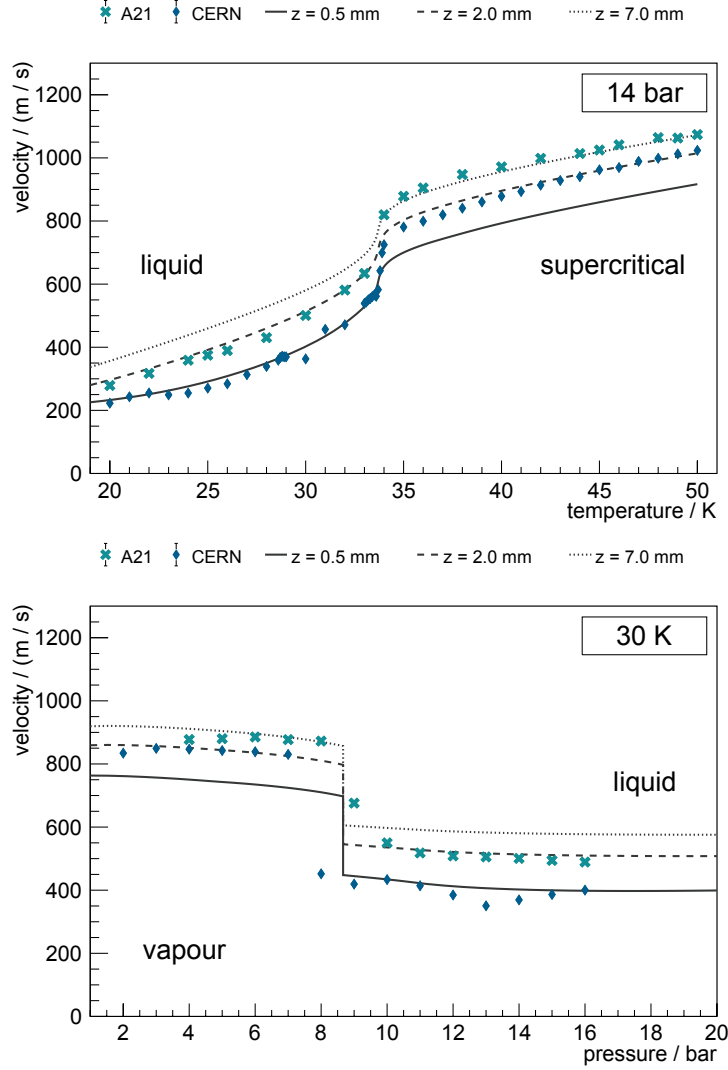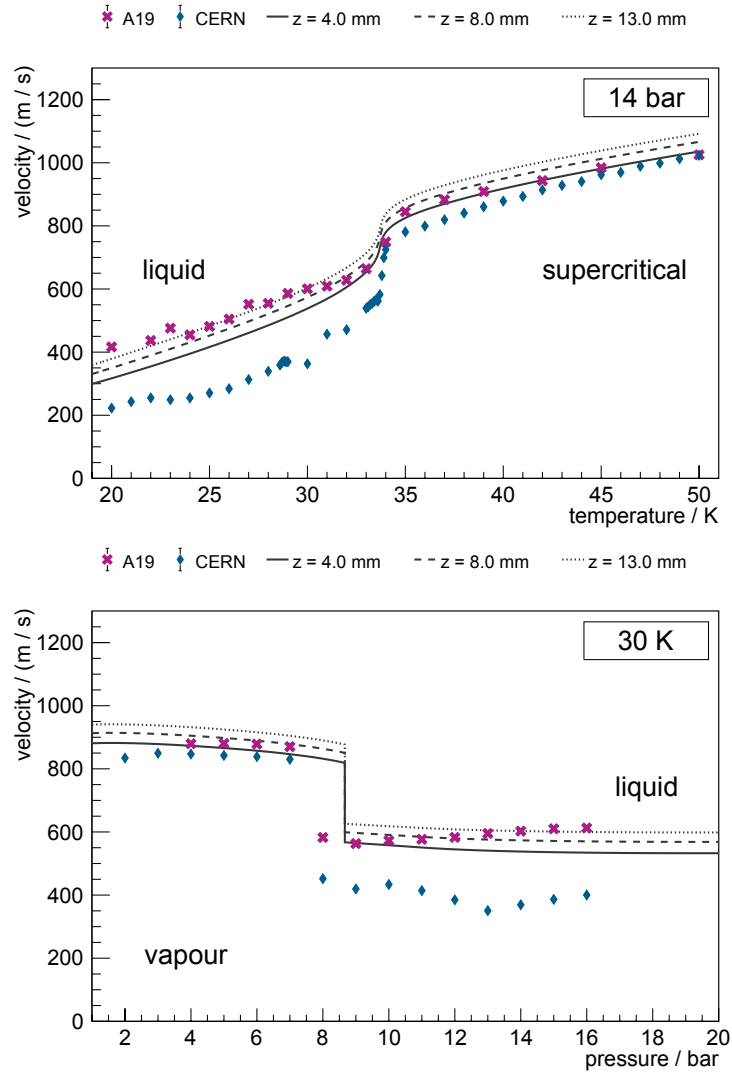
Figure 5.35: Mean measured velocities with the nozzle A21. *Top*: Isobar for a pressure of 14 bar in dependency of the temperature. *Bottom*: Isotherm for a temperature of 30 K in dependency of the pressure. Additionally, data from E. Köhler measured with the $\overline{P}$ANDA nozzle are shown (blue). Values of the z parameter for the liquid and the gaseous phase using the A21 nozzle geometry were calculated by simulations within this thesis to $z_{\mathrm{liquid}} = (2.0 \pm 0.5)$ mm and $z_{\mathrm{vapour}} = (7.0 \pm 1.0)$ mm.

Table 5.6: Calculated z values for liquid and gaseous hydrogen for the nozzles A21 and A19 based on the measurements presented in Fig. 5.35 and 5.36.

nozzle	z value / mm
A21	$z_{\mathrm{liquid}} = 2.0 \pm 0.5$
	$z_{\mathrm{vapour}} = 7.0 \pm 1.0$
A19	$z_{\mathrm{liquid}} = 13.0 \pm 1.0$
	$z_{\mathrm{vapour}} = 4.0 \pm 1.0$

Moreover, the resulting z parameters are stable within a given cluster-jet target configuration which is apparent by measurements over hours. Additional, reproducibility measurements were done by reaching the same highest thickness stagnation conditions of the target from standby conditions resulting in the same z values each time.

Figure 5.36: Determined mean velocities for the A19 nozzle. Data obtained together with S. Vestrick [Ves18]. *Top*: Isobar for a pressure of 14 bar in dependency of the temperature. *Bottom*: Isotherm for a temperature of 30 K in dependency of the pressure. Additionally, data from E. Köhler measured with the $\overline{\mathrm{P}}$ANDA nozzle are shown (blue). Values of the z parameter for the liquid and the gaseous phase using the A19 nozzle geometry were calculated by simulations within this thesis to $z_{\mathrm{liquid}} = (13.0 \pm 1.0)$ mm and $z_{\mathrm{vapour}} = (4.0 \pm 1.0)$ mm.

Thicknesses Determination

Based on these measurements and simulations the target thickness can be determined. With the A21 nozzle a highest target thickness of $(4.79 \pm 0.34) \times 10^{14}$ atoms/cm^2 at 18 bar and 19 K and with the A19 nozzle a highest target thickness of $(5.36 \pm 0.37) \times 10^{14}$ atoms/cm^2 at 18 bar and 25 K was achieved. The target thickness is an important quantity for cluster-jet targets, and therefore, for the used Laval nozzles. Most experiments are aiming for a high thickness which leads to a high luminosity of the experiment. The thicknesses for the two nozzles are different, due to structures within the cluster beam caused by the little differences in the nozzle geometry. The record thickness of the $\overline{\text{P}}$ANDA nozzle is not yet achieved, but the measured thicknesses are in the upper range of thicknesses gained with cluster-jet targets in a distance of 2.1 m from the nozzle. With respect to the nozzle production process, this is a remarkable progress and the production process is well-understood.

Moreover, thickness mappings, comparable with previous data taken with the $\overline{\text{P}}$ANDA nozzle, were performed (Fig. 5.37 and 5.38). The first measurement series shows the transition from liquid to supercritical hydrogen in front of the nozzle, the second one the transition from liquid to vapour, and the third one is completely in the liquid phase of hydrogen. Clearly visible are the steps in the target thickness by exceeding the hydrogen vapour pressure curve (cf. Fig. 5.30). Additionally, the thickness changes over several orders of magnitude by changing the stagnation conditions which is useful during the running experiment to adjust the target thickness to the number of accelerated particles to ensure a constant luminosity. Thus, a detailed thickness mapping in dependency of the nozzle and the stagnation conditions is necessary, to adjust the target thickness to the desired one.

In case of the isobars the thickness of the A21 nozzle is in most of the settings the highest. For the 8 bar measurement, the thickness of the A19 nozzle is only slightly below the thickness of the A21 nozzle. There, the $\overline{\text{P}}$ANDA nozzle reaches the worst thicknesses.
The measurement by 17 bar shows the same behaviour for supercritical hydrogen. Liquid hydrogen leads to a change of the thicknesses of the A19 and $\overline{\text{P}}$ANDA nozzle. The two high data points recorded with the $\overline{\text{P}}$ANDA nozzle at the temperatures of 24 K and 25 K are induced by the appearance of the highly intense core beams. The nozzles A21 and A19 also shows structures within the cluster beam but not as significant as the $\overline{\text{P}}$ANDA nozzle (cf. Fig. 5.27, 5.39, 5.40 and 5.41).
The isotherm at 25 K shows at low pressures an agreement of the thicknesses for all three nozzles. With increasing pressure, the thickness of the $\overline{\text{P}}$ANDA nozzle increases the most, followed by the A21 nozzle and then by the A19 nozzle. The $\overline{\text{P}}$ANDA nozzle represents in this measurement the highest thicknesses, because the formation of the highly intense core beam is strong for 25 K. The two high thicknesses at pressures of 13 bar and 18 bar achieved with the A19 nozzle also corresponds to the extraction of highly intense core beams.
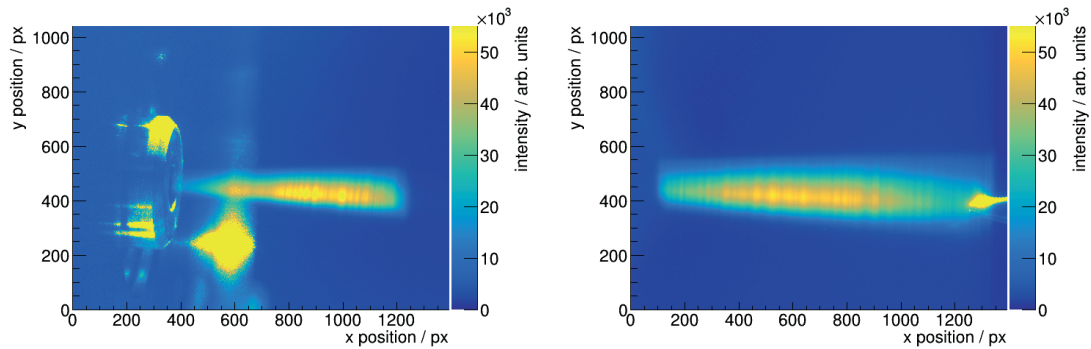At the skimmer chamber a system is installed to visualise the cluster beam. Thereby,
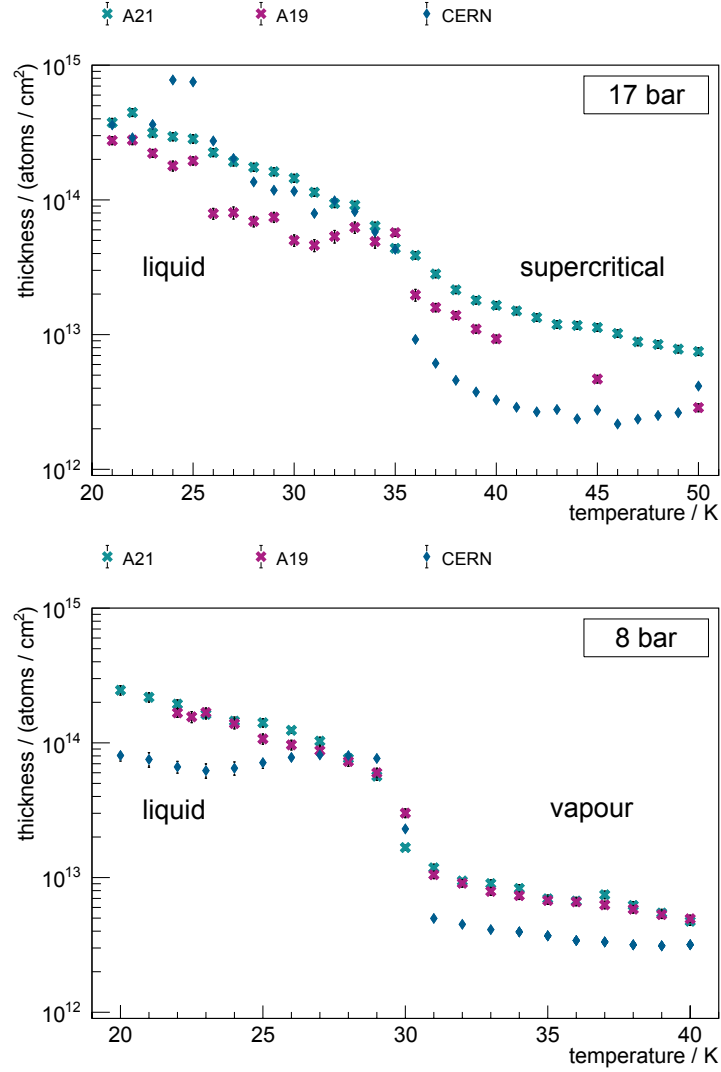
Figure 5.37: Target thickness mappings for the isobars 17 bar and 8 bar. The 17 bar measurement shows the transition from liquid to supercritical hydrogen in front of the nozzle. The transition from liquid to vapour hydrogen occurs within the 8 bar measurement. Data taken with the $\overline{P}$ANDA nozzle from E. Köhler (blue). Data for 17 bar with the A19 nozzle obtained together with S. Vestrick [Ves18].

a laser diode illuminates the cluster beam and at an angle of 90° relative to the laser diode and a CCD camera is mounted to record the cluster beam. The resulting pictures are presented in Fig. 5.39, 5.40 and 5.41. The system offers the possibility to image the Laval nozzle with the expanding beam (Fig. 5.39, left) or to display the cluster beam with the skimmer tip, to see the part of the cluster beam which will be extracted (Fig. 5.39, right). Moreover, this system allows for investigation of the highly intense core beam resulting in a brighter part with respect to their appearance in dependency of the stagnation conditions, size, shape, and relatively intensity.

Images recorded with this system with the A21 nozzle are presented in Fig. 5.39 and 5.40 in false colour. The cluster beam direction is from left to right. A well defined cluster
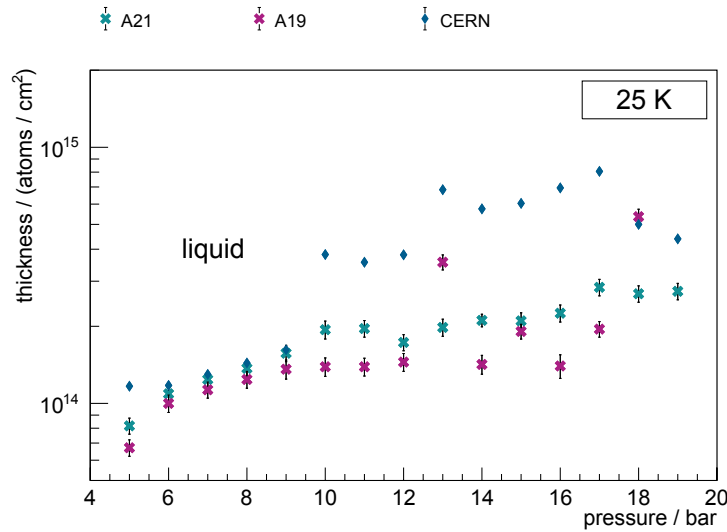
Figure 5.38: Target thickness for an isotherm of 25 K in dependency of the pressure. This complete measurement was taken in the liquid phase of hydrogen. Data taken with the $\overline{\text{P}}$ANDA nozzle from E. Köhler (blue) [Kö15]. Data for the A19 nozzle obtained together with S. Vestrick [Ves18].

Figure 5.39: Images in false colour recorded with the visualisation system installed at the skimmer chamber at 17 bar and 25 K. The exposure time was 2 s. The beam direction is from left to right. *Left*: The A21 nozzle and a well defined cluster beam is visible. *Right*: The cluster beam and the skimmer tip is shown, which only extracts a small part of the beam. The images were recorded directly behind after each other, with a readjustment of laser and camera in-between.

beam leaves the nozzle (left) and a small part is extracted with the skimmer (right). These two pictures were recorded directly behind each other with a fast readjustment of the laser and the camera in-between. A second measurement recorded at 15 bar and 35 K shows a structure within the cluster beam. The projection on the ordinate represents the structure within the beam and shows a not homogeneous distribution but a wide increase with a double peak structure and an additional smaller peak at the left side corresponding to the lower part of the cluster beam.

The cluster beam image generated with the A19 nozzle at 16 bar and 30 K (cf. Fig. 5.41) shows two intense core beams within the cluster beam. This is additionally clarified in
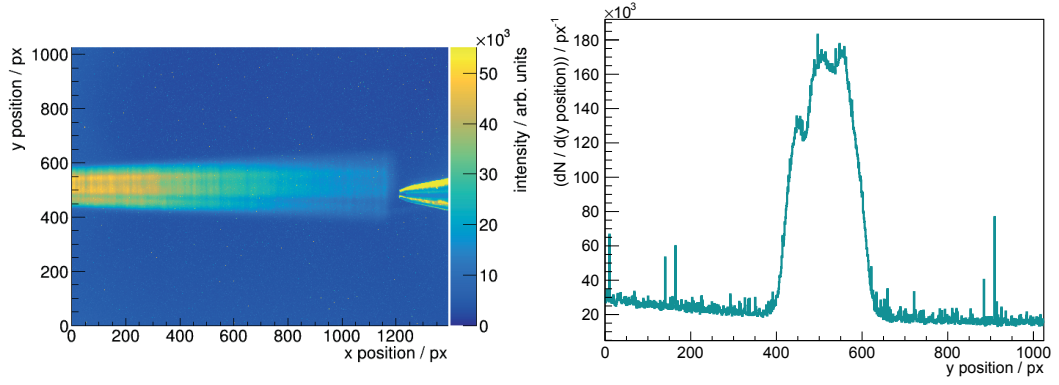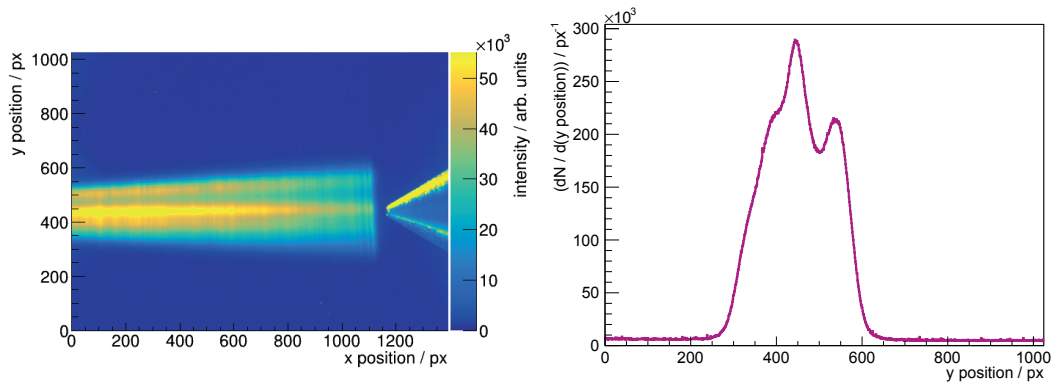
Figure 5.40: *Left*: False colour image of the cluster-jet beam at 15 bar and 35 K produced with the A21 nozzle. The exposure time was 5 s. The beam direction is from left to right. On the left side, the skimmer tip is visible, which only extracts a small part of the cluster beam. Some brighter parts within the cluster beam are visible corresponding to a higher thickness in comparison to the darker parts. *Right*: Projection on the ordinate for the abscissa range between 800 and 805. The maximum wide peak shows a double peak structure and at the left flank an additional peak is visible which corresponds to a lower part within the cluster beam.

the projection, where two clear peaks of the intensity are visible. The extraction of these core beams leads to the high thicknesses achievable with this nozzle.

Reproducibility and Stability of Thickness

The reproducibility and stability of the target thickness is from highest importance. Assuming a stable accelerator beam in combination with a stable target thickness leads to a constant and uniform luminosity. This is very important to realise constant event rates for the data acquisition system, to minimize dead times of the detectors, and to

Figure 5.41: *Left*: False colour image of the cluster-jet beam generated with the A19 nozzle at 16 bar and 30 K. The exposure time was 10 s. The beam direction is from left to right. On the left side, the skimmer tip is visible, which only extracts a small part of the cluster beam. In this case, the highly intense core beam is extracted leading to a high target thickness. Two brighter parts within the cluster beam are clearly visible. *Right*: Projection on the ordinate for the abscissa range between 800 and 805. A double peak structure in the intensity distribution is visible corresponding to the two core beams.
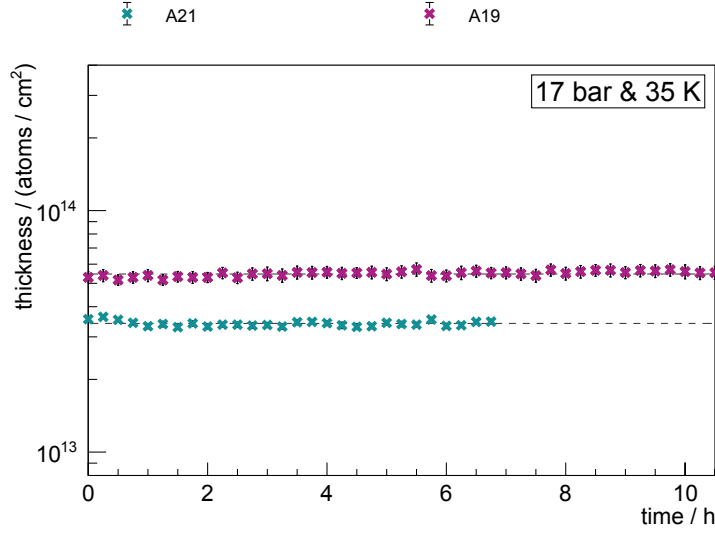
Figure 5.42: Long-term stability for the A21 and A19 (data obtained together with S. Vestrick [Ves18]) nozzle at 17 bar and 35 K over more than 7 h with logarithmic scale. Systematic uncertainties (velocity, pressure gauge, and pumping speed), which account below 10 %, are not shown.

achieve a maximum utilization of the experiment.

The adjustment of the target thickness to the cycle of the accelerator beam was successfully shown (cf. chapter 5.1). Therefore, a precise thickness mapping is necessary to determine the suitable stagnation conditions (cf. Fig. 5.37 and 5.38) for every desired thickness. Additionally, the target thicknesses should be stable and reproducible. Once determined the target thickness, every time adjusting the same stagnation conditions of the hydrogen in front of the nozzle, the same target thickness is reached.
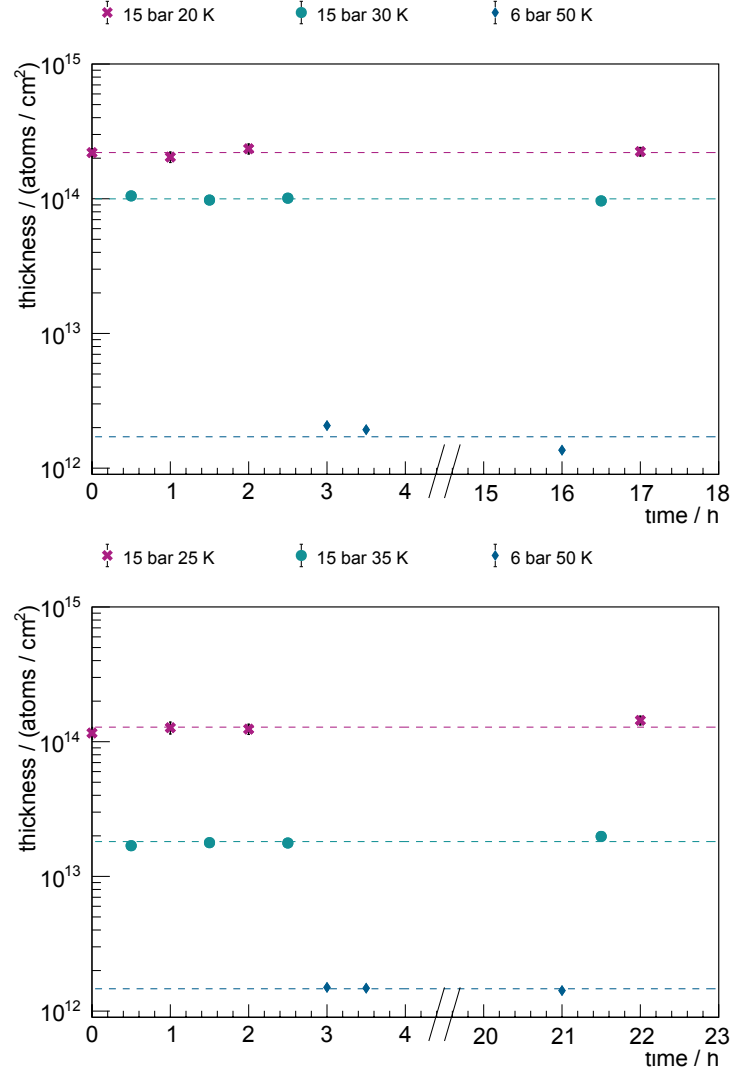
Therefore, stability measurements of the target thickness were performed with both nozzles at 17 bar and 35 K over more than 7 h (Fig. 5.42). Thereby, every 15 minutes a beam profile was recorded and analysed. The average target thickness for the A21 nozzle was determined to 3.41×10^{13} atoms/cm^2, and for the A19 nozzle to 5.46×10^{13} atoms/cm^2 with a stability in both cases better than 10 %.

The reproducibility was investigated by switching between low, high thickness, and to the standby conditions (6 bar and 50 K). The standby stagnations are chosen to be in the gaseous phase of hydrogen, where the gas flow through the Laval nozzle is lower than in the liquid phase which minimizes the gas consumption of the target during stand-by time. Nevertheless, the stagnation conditions for highest thicknesses can be re-established in a minimal amount of time from the chosen standby stagnation conditions.

In case of the A21 nozzle (cf. Fig. 5.43, top), the thickness changes between $> 2 \times 10^{14}$ atoms/cm^2, roughly 1×10^{14} atoms/cm^2 and $< 1 \times 10^{13}$ atoms/cm^2. For the A19 nozzle (cf. Fig. 5.43, bottom), the thickness changes between $> 1 \times 10^{14}$ atoms/cm^2, $< 1 \times 10^{14}$ atoms/cm^2 and $< 1 \times 10^{13}$ atoms/cm^2.

The measurements show high reproducibilities with no further needed adjustments which

is essential for the automatically adjustment of the target thickness to the accelerated particle beam at, e.g., $\overline{\mathrm{P}}$ANDA.

Figure 5.43: Variation and reproducibility measurement of the target thickness with logarithmic scale for the nozzles A21 (*top*) and A19 (*bottom*) for different stagnation conditions.

Spherical Joint Dependence on Thickness and Velocity

The observed structures within the cluster beam and the different velocity determination with the $\overline{\mathrm{P}}$ANDA nozzle in comparison to previous data lead to the assumption, that the mean velocity and the velocity distribution depend on the location within the cluster beam. Moreover, a previous mass measurements showed a dependency of the cluster mass from the nozzle tilting angle (cf. Fig. 5.44) [Kö15].
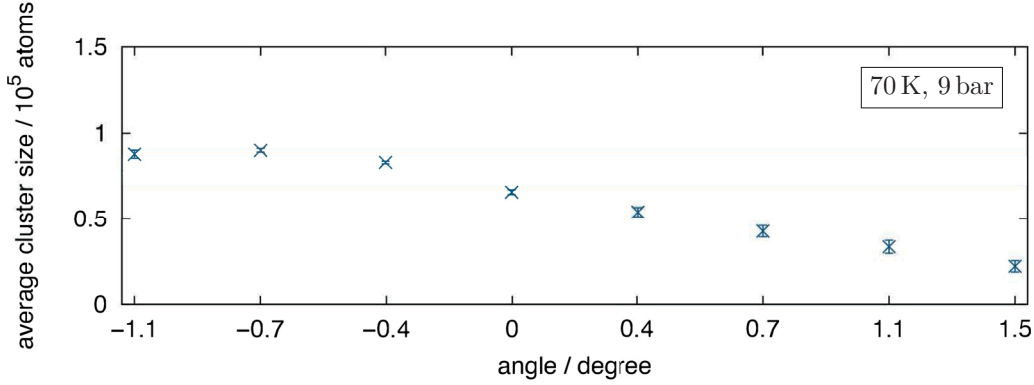
Figure 5.44: Average cluster size in dependency of the nozzle orientation angle at 9 bar and 70 K. A decreasing cluster size with increasing tilting angle is clearly visible [Kö15].

The installed nozzle tilting system allows for a measurements of different parts of the cluster beam with respect to its thickness and velocity distribution. Therefore, for both nozzles, three measurements of the thickness and velocity in dependency of the nozzle tilting angle were performed. The first measurements series used gaseous hydrogen in front of the nozzle at stagnation conditions of 8 bar and 32 K. The results are depicted in Figure 5.45. The velocity distributions show sharp peaks for both nozzles (cf. Fig. 5.34 and A.1). The thickness for the A21 nozzle is homogeneously distributed and the velocity distribution follows the thickness distribution as expected. At the edges the thickness and the velocity decrease. A possible reason for this is a friction of the jet with the inner nozzle boundary. The same measurement performed with the A19 nozzle shows the same behaviour with a decrease in the center of the beam.

The unsymmetrical courses are caused by the nozzle tilting system. The design of the nozzle tilting system does not allow for a precise determination of the $0\,°$ position which means an orientation of the tilting system parallel to the ground floor and extracting the center part of the cluster beam. Moreover, the used nozzle fixation means and nozzle sealing do not allow for a perfect nozzle alignment. Furthermore, the reproducibility of the nozzle tilting angles is limited by the nozzle tilting screw pitch and play. Thus, the here given angles are the nominal angles extracted from the construction drawing of the nozzle tilting system. The measurements start at the lowest angle of $-2.31\,°$ and ends at a maximum angle of $2.16\,°$.

Additionally, simulations within this thesis on the cluster velocity for different z parameters for these two nozzles were performed and mapped in Figure 5.45. Due to the different mean velocities within the cluster beam, also the z parameter changes in dependency of the tilting angle and therefore, of the different cluster beam parts. The velocities of both measurements could be explained with z parameters between 2.0 mm and 7.0 mm. A higher z parameter corresponds to a higher velocity.
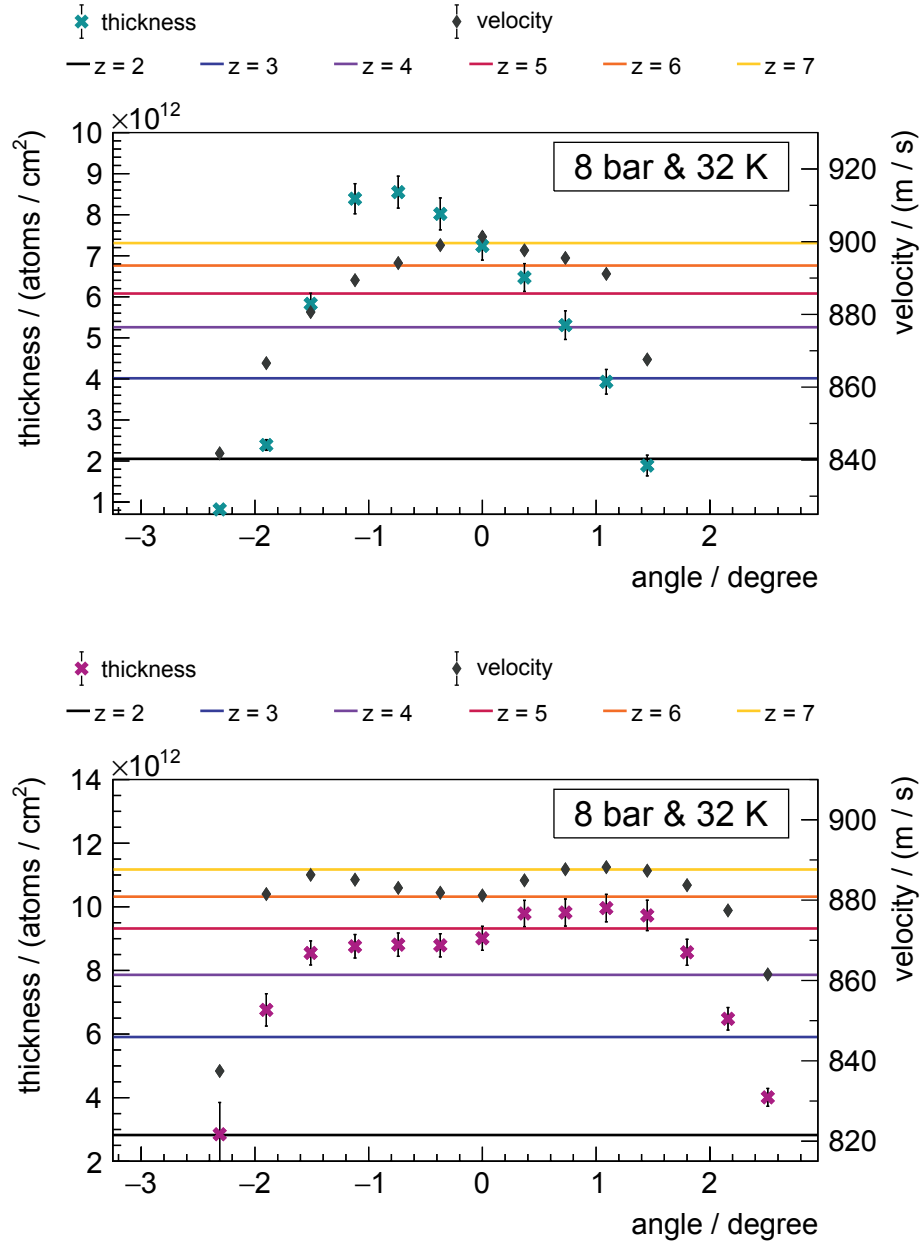
Figure 5.45: Spherical joint measurements of the thickness and velocity in dependency of the nozzle tilting angle at gaseous hydrogen (8 bar and 32 K) for the A21 (*top*) and A19 (*bottom*) nozzle. Both show the homogeneous distribution as expected. For both measurements the z parameter varies between 2.0 mm and 7.0 mm (coloured curves). Data for the A19 nozzle obtained together with S. Vestrick [Ves18].

The measurements series performed with supercritical hydrogen in front of the nozzle allow for an additionally visualisation of the cluster beam structures. Figure 5.46 shows images taken from the cluster beam produced with the A21 nozzle in the scattering chamber. On the left side the skimmer tip and the beam parts, which are extracted for the further analysis, are visible. The pictures starts at an angle of $-2.31°$ and ends at

an angle of 2.16 °. To improve clarity only every second nozzle tilting position is shown. For the 0 ° position, the projection on the ordinate showing the cluster beam structure is additionally presented. There, a high rising intensity from left to right (bottom to top within the cluster beam) with some small fluctuations are visible. Figure 5.47 shows the corresponding velocity distribution for the different nozzle tilting angles. The lower part of the cluster beam represents a sharp peak with a shoulder to the low velocities. This shoulder decreases by extracting higher parts of the cluster beam. At the 0 ° position, the shoulder is at its minimum. Extracting the higher parts of the cluster beam leads to a rise of a shoulder at low velocities. This shoulder increases till a wide velocity distribution occurs at the bottom of the cluster beam.

The resulting spherical joint measurements and additionally, the measurement for the A19 nozzle is depicted in Figure 5.48. Both show an inhomogeneous thickness and velocity distribution. The measurement for the A21 nozzle presents a rising thickness from the bottom to the top of the cluster beam like expect from Figure 5.46. The mean velocity shows the contrary development. A high thickness leads to a low velocity and vice versa. The performed simulations are consistent with z parameters from 0.5 mm to 16.0 mm.

The same measurement taken for the A19 nozzle (Figure 5.48, bottom) shows three peaks in the thickness and a decreasing velocity with increasing thickness. The corresponding image of the cluster beam and the thereof resulting projection on the ordinate is presented in Fig. 5.49. There, only two peaks are visible. The first peak in the spherical joint measurement (low thickness) is not visible in the projection due to inhomogeneous illumination by the laser diode and because of the too low intensity. The performed simulations leads to z parameters from 2.0 mm to more than 17.0 mm. The z parameter is the distance from the narrowest point of the nozzle within the nozzle, where the clusters decouple from the surrounding gas. The used Laval nozzle has a full length of 18 mm, but only an outlet zone of 17 mm. Therefore, simulations for a higher z value than 17.0 mm make no sense with respect to the definition of the z parameter. Probably, there the decoupling occurs after leaving the nozzle. It has to be noted that such large velocities do not violate energy conservation, since here only a sub-sample of the gas is detected.
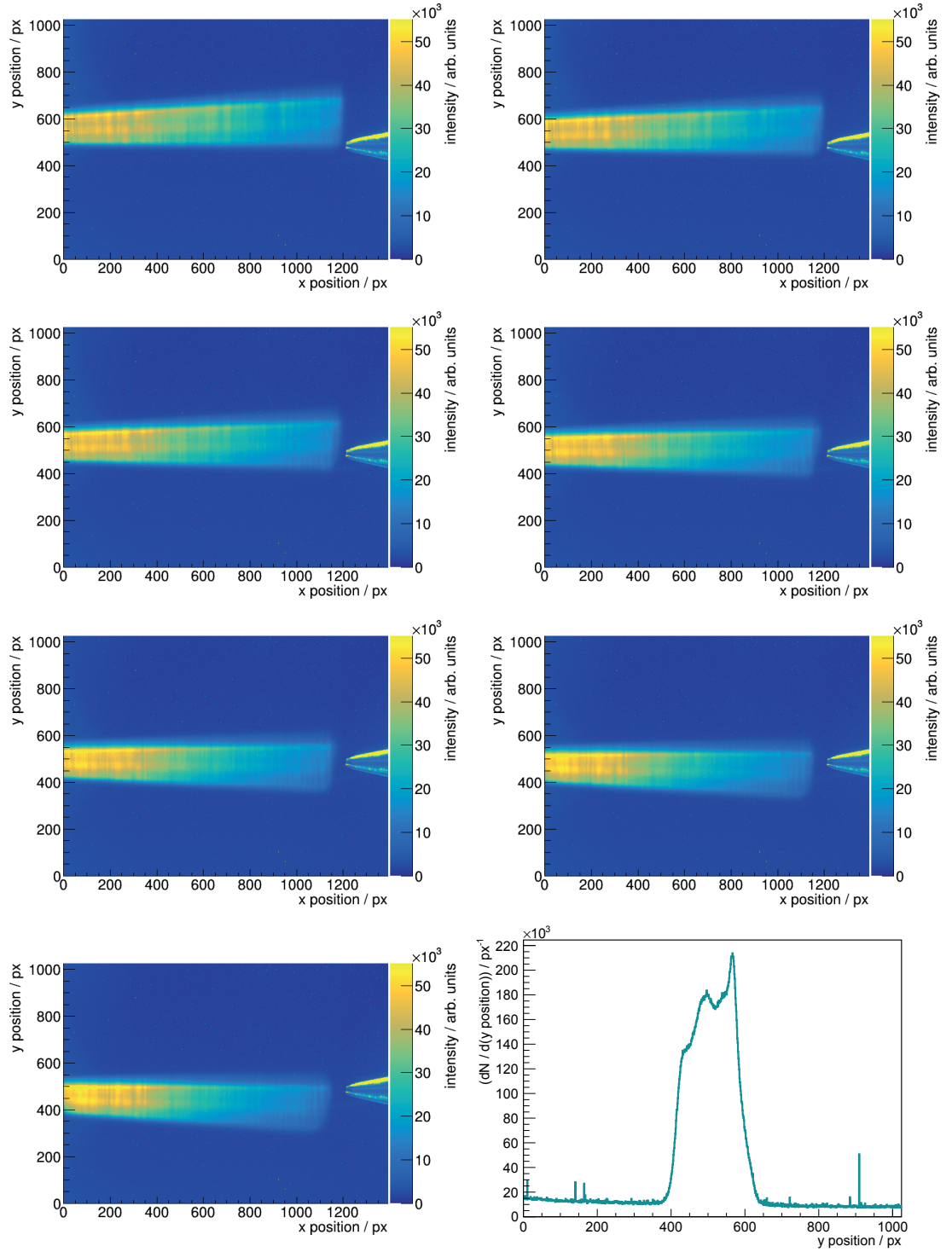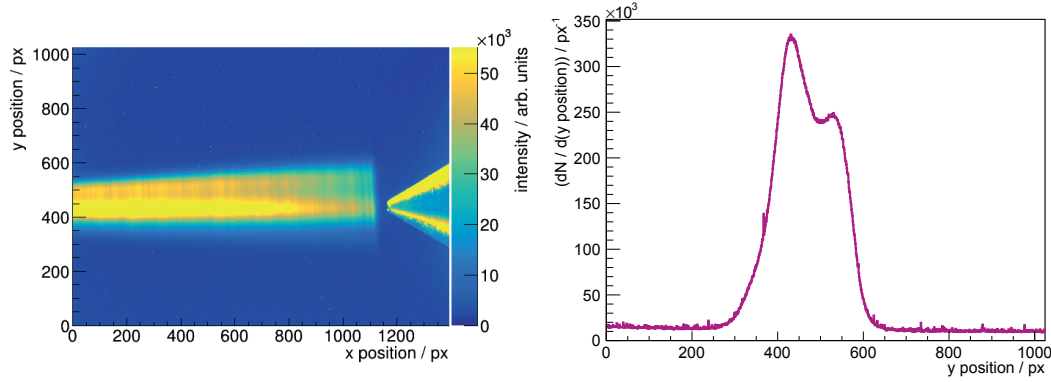
Figure 5.46: Images of the cluster beam with the A21 nozzle recorded at the skimmer chamber (17 bar and 35 K). The cluster beam direction is from left to right. The exposure time was 25 s. The different cluster beam parts are clearly visible which are extracted by the skimmer and further analysed. The pictures starts at an angle of $-2.31\,°$ and ends at an angle of $2.16\,°$, every second nozzle tilting position is shown. For the $0\,°$ position, the projection on the ordinate showing the cluster beam structure is additionally presented.
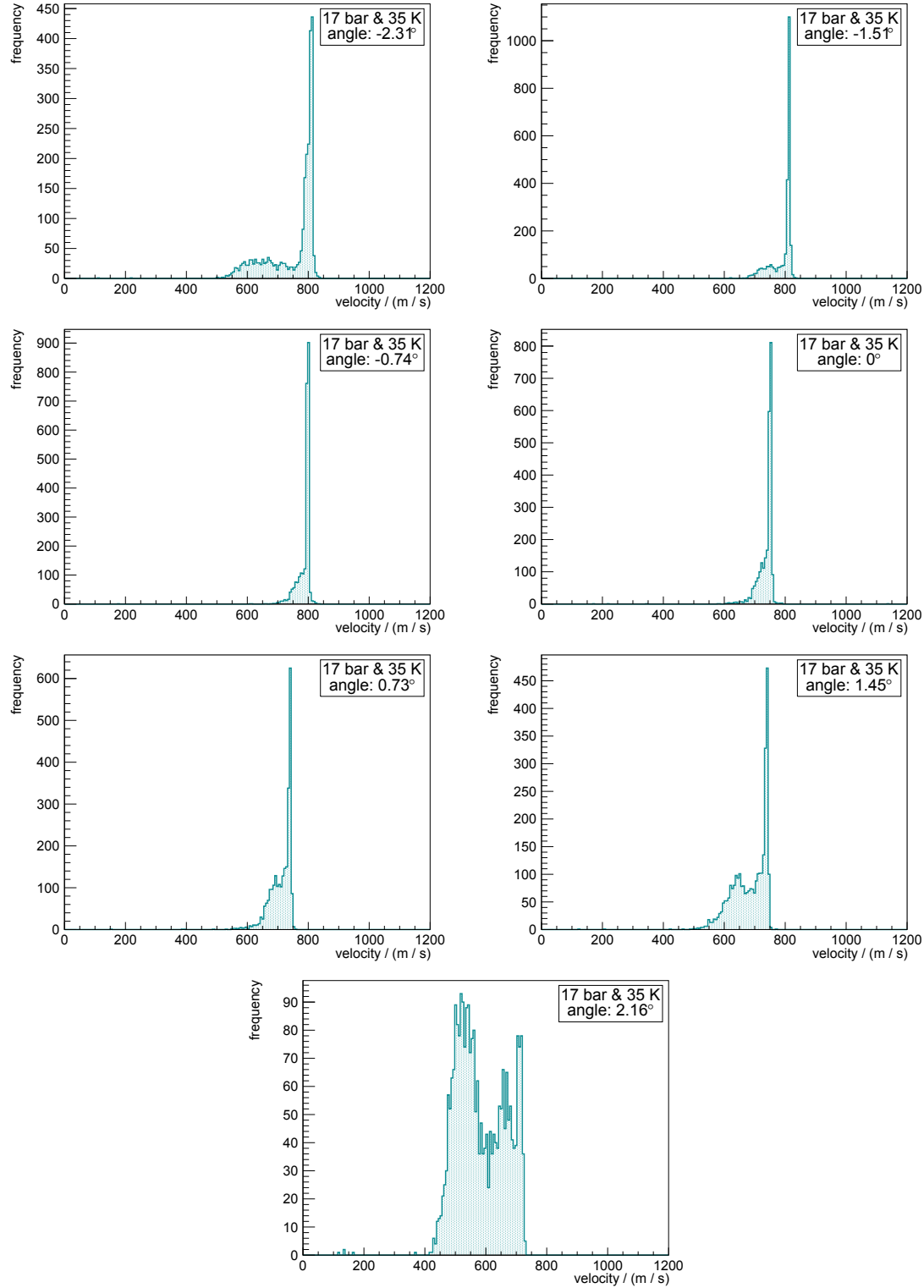
Figure 5.47: Measured velocity distribution of the cluster beam with the A21 nozzle (17 bar and 35 K). The pictures starts at an angle of $-2.31\,^{\circ}$ and ends at an angle of $2.16\,^{\circ}$, every second nozzle tilting position is shown. Extracting the lower part of the cluster beam results in a sharp peak with a shoulder to the low velocities. This shoulder decreases by tilting the nozzle. At the $0\,^{\circ}$ position, the shoulder is at its minimum. The higher parts of the cluster beam result in a rise of a shoulder at low velocities. This shoulder increase till a wide velocity distribution occurs at the bottom of the cluster beam.
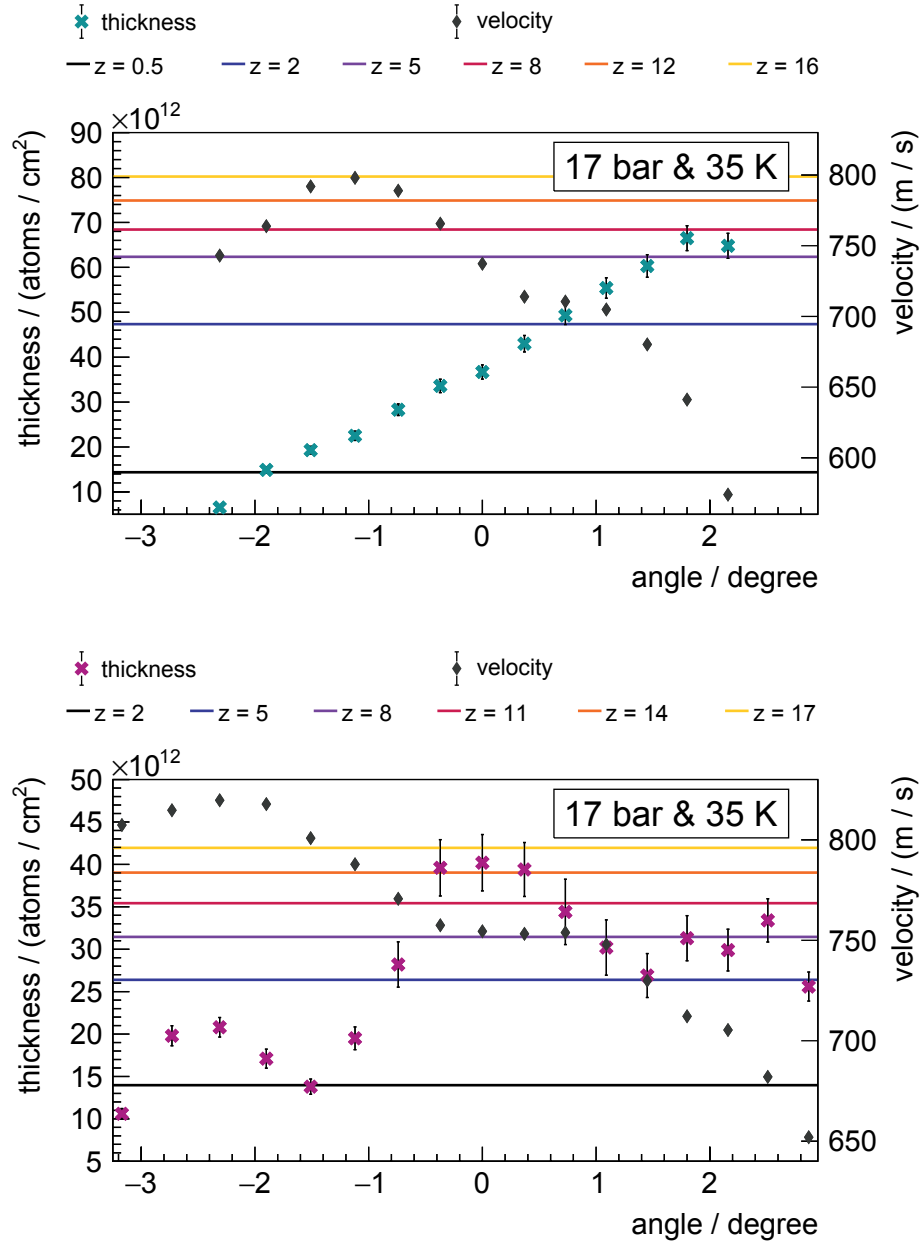
Figure 5.48: Spherical joint measurement of the thickness and velocity in dependency of the nozzle tilting angle at supercritical hydrogen (17 bar and 35 K) for the A21 (*top*) and A19 (*bottom*) nozzle. Both show an inhomogeneous distribution for the thickness and velocity. The z parameter varies between 0.5 mm and over more than 17.0 mm (coloured curves).
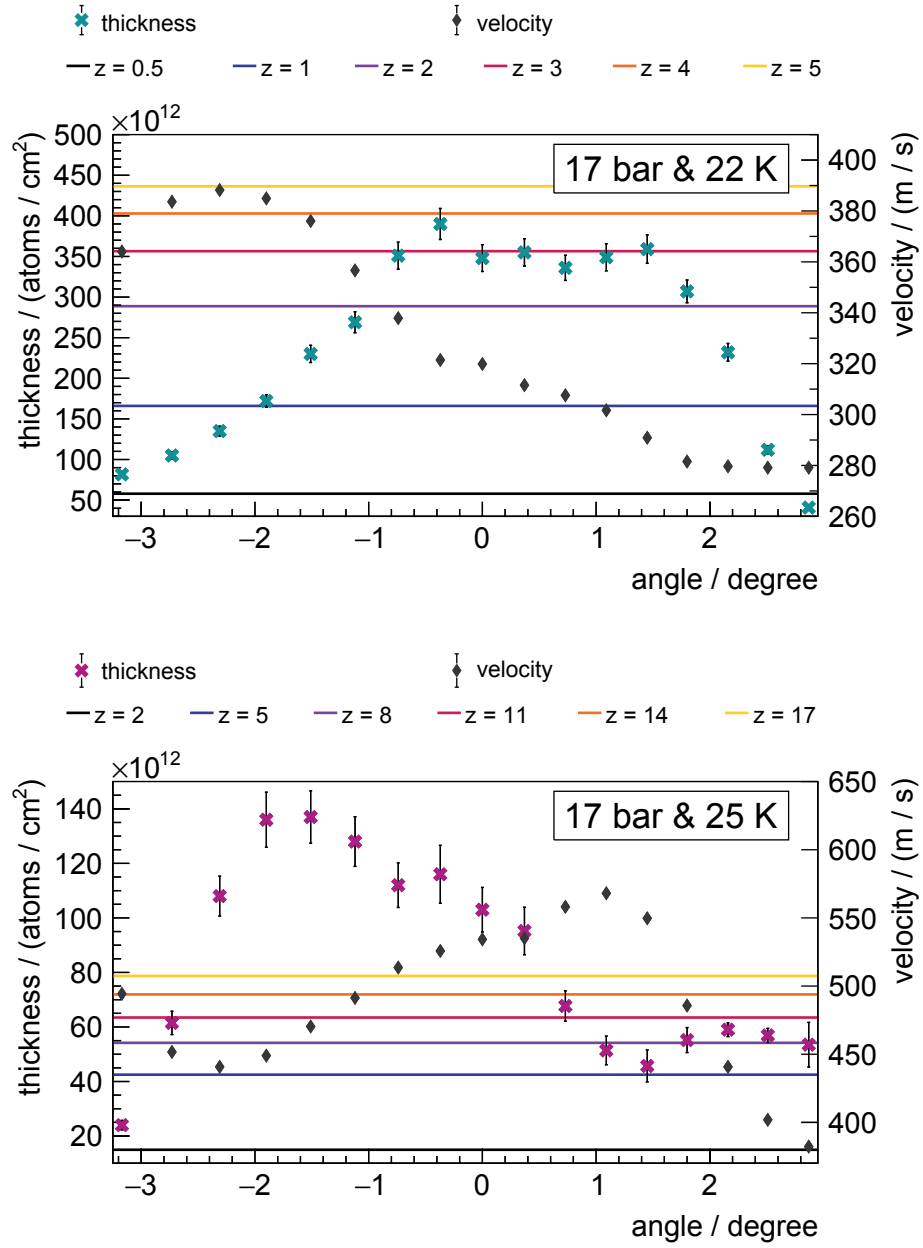
Figure 5.49: *Left*: False colour image of the cluster-jet beam generated with the A19 nozzle at 17 bar and 35 K. The exposure time was 30 s. Two brighter parts within the cluster beam are visible. *Right*: Projection of the cluster beam on the ordinate for the abscissa range between 800 and 805 showing two peaks. The peak corresponding to the lower part of the beam is higher than the peak to the upper part.

Measurement series of the thickness and velocity in dependency of the nozzle tilting angle for liquid hydrogen is shown in Fig. 5.50 for the A21 nozzle at 17 bar and 22 K (top) and for the A19 nozzle at 17 bar and 25 K (bottom). The corresponding images recorded with the visualisation system installed at the skimmer chamber are presented in Fig. 5.51 and 5.52.

The A21 nozzle shows a relatively homogeneous thickness distribution as expect from the projection of the cluster beam image. The measurements can be explained with z values between 0.5 mm to 5.0 mm. The A19 nozzle has a high peak at the lower part of the cluster beam and a little shoulder in the upper part. This is represented by the thickness distribution measured in dependency of the nozzle tilting angle. Also here, the z parameters starts at 2.0 mm and exceeds the 17.0 mm.

A reproducibility measurement for the spherical measurements series were performed to ensure a correct determination of the thickness and the velocity. Therefore, with the A21 nozzle, the same measurements for supercritical hydrogen at 17 bar and 35 K were done in a temporal distance of 12 days with changing the stagnation conditions in-between. The result is shown in Fig. 5.53. The filled points represents the measurement from Fig. 5.48 and the unfilled points shows the second performed measurement. With respect to the already mentioned uncertainty of the reproducibility of the nozzle tilting angle, both data are in good agreement.

To ensure an independence of the direction of the measurement, from low to high angles or the other way around, a measurement with the A19 nozzle was done (Fig. 5.54). Therein, the filled points show the already discussed measurement with supercritical hydrogen at 17 bar and 35 K (cf. Fig. 5.48). The unfilled data points represents the same measurement performed one day later with the measurement direction from high angles $2.16\,°$ to low angles $-2.31\,°$. All other measurements were done the other way around. Also here, both data show a good agreement. Therefore, it was shown, that the measurements of the spherical joint are reproducible and independent from the measurement direction.

Figure 5.50: Resulting spherical joint measurement of the thickness and velocity in dependency of the nozzle tilting angle at liquid hydrogen (17 bar and 22 K/25 K) for the A21 (*top*) and A19 (*bottom*) nozzle. Both show an inhomogeneous distribution for the thickness and velocity. The z parameter varies between 0.5 mm and over more than 17.0 mm (coloured curves).
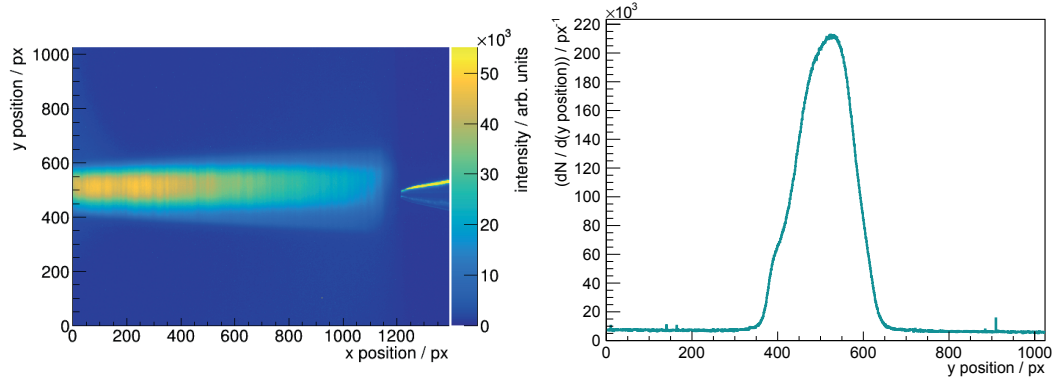
Figure 5.51: *Left*: False colour image of the cluster-jet beam generated with the A21 nozzle at 17 bar and 22 K. The exposure time was 5 s. *Right*: Projection of the cluster beam on the ordinate for the abscissa range between 800 and 805. A relatively homogeneous cluster beam with the highest thickness in the center is visible.
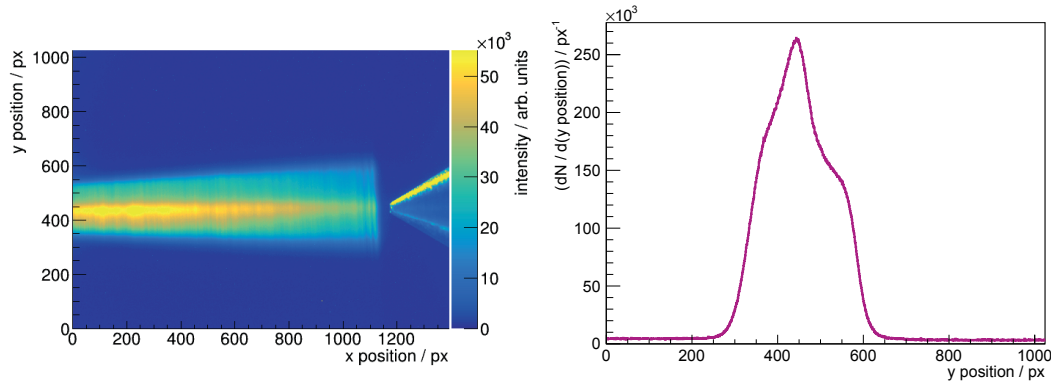

Figure 5.52: *Left*: False colour image of the cluster-jet beam generated with the A19 nozzle at 17 bar and 25 K. The exposure time was 5 s. *Right*: Projection of the cluster beam on the ordinate for the abscissa range between 800 and 805. A high intensity is visible at the lower part of the cluster beam and a second step, but not as high as the first, at the upper part of the cluster beam.

Table 5.7: Calculated z values for the spherical joint measurements for the nozzles A21 and A19.

nozzle	pressure bar	temperature K	physical state of hydrogen	z value mm
A21	8	32	gaseous	$2.0 - 7.0$
	17	35	supercritical	$0.5 - 16.0$
	17	22	liquid	$0.5 - 5.0$
A19	8	32	gaseous	$2.0 - 7.0$
	17	35	supercritical	$2.0 - > 17.0$
	17	25	liquid	$2.0 - > 17.0$
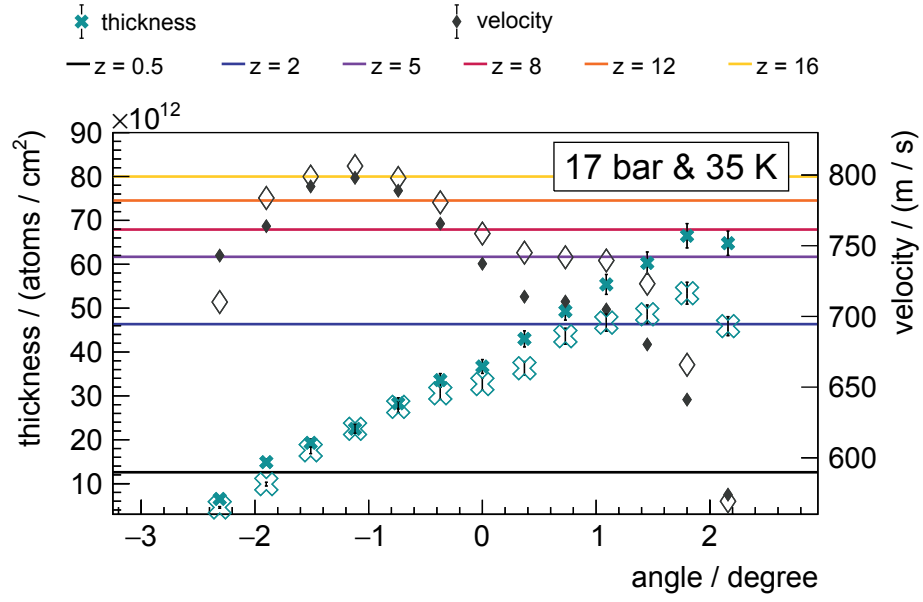
Figure 5.53: Reproducibility measurement for the spherical measurement with the A21 nozzle at 17 bar and 35 K. The same measurement was performed once again 12 days later. Both data are in a good agreement with respect to the uncertainty of the reproducibility of the nozzle tilting angle.
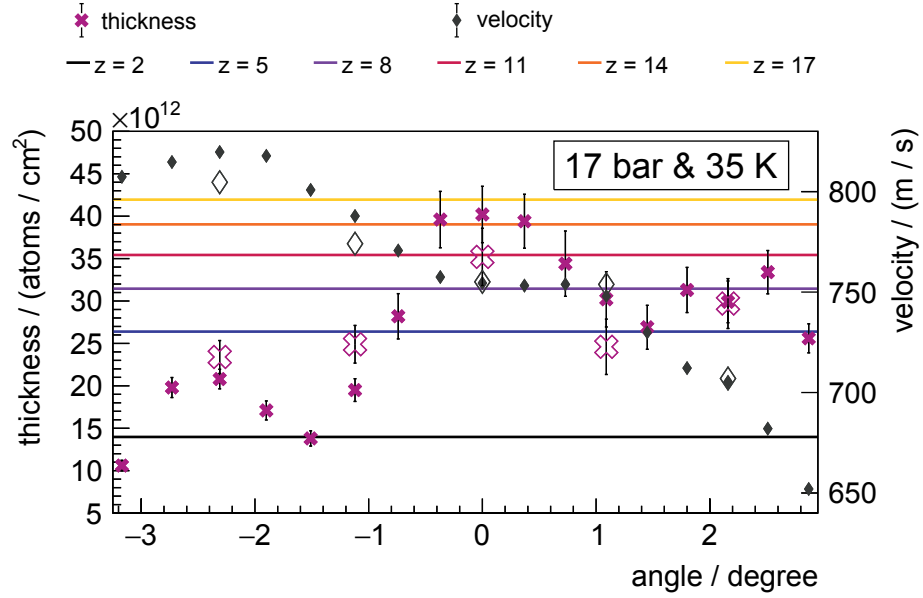
Figure 5.54: Measurement to show the independence of the direction of the spherical joint measurement performed with the A19 nozzle at 17 bar and 35 K. The filled data were obtained by enlarging the tilting angle, the unfilled data were measured by decreasing the nozzle tilting angle. Both data are in a good agreement with respect to the uncertainty of the reproducibility of the nozzle tilting angle.

The presented and discussed measurements proof, that the beam structures within a cluster beam not only result in different thicknesses but furthermore in different velocities. Higher cluster masses with lower velocities lead to higher target thicknesses (cf. Eg. (5.2)). Measurements on the cluster mass in the liquid and supercritical phase of hydrogen are planned. These measurements will additionally clarify the mass composition within the cluster beam and will give a deeper insight into the cluster production process.

The different velocities within the cluster beam result from an uneven distribution of the energy within the nozzle during the cluster production process. There, the energy conservation (Eq. (5.32)) has to be hold true. Therefore, only an inhomogeneous energy distribution at the narrowest point of the nozzle, where the clusters are produced, might be the reason. Different energies within the cluster beam then results in the different velocities. These energy differences can only be generated by the nozzles geometry at the narrowest inner diameter. An ideally formed nozzle, with a perfect circled inner diameter, will result in random turbulences of the energy. Every time, the energy distribution at the narrowest point will look different. Due to the fact, that the velocity and thickness structures within the beam are reproducible supports an origin in individually formed narrowest inner diameter of the nozzles. The deviations from the perfect circled geometry lead to the occurrence of highly intense core beams and different compositions within the cluster beam with respect to thickness, velocity, and mass. The pictures of the narrowest inner diameters of the two monolithic copper nozzles both show a comma-shaped gap in the circled diameter. This might be the reason for the occurring structures.

With respect to manufacture a high performance nozzle, an ideally circled narrowest inner diameter is not the best choice. Deviations from the perfect design leads to the formation of highly intense core beam which are necessary to achieve the high thicknesses of more than $5 \times 10^{14} \, \text{atoms/cm}^2$ achieved with the A-series nozzles. This is owned by the higher cluster mass and the lower velocity of the clusters within the core beams.

Additionally, the resulting z parameters of the nozzles has to be as low as possible leading in low velocities and therefore high target thicknesses. The $\overline{\text{P}}$ANDA nozzle posseses the lowest z values, followed by the A21 nozzle and last the A19 nozzle. The nozzle production process developed at the University of Münster results in nozzles with higher z values than the CERN production process. By the production process of the Münster nozzles, during the galvanic composition of copper around the acrylic glass negative, the extremely spike tip of the negative bends a bit. This results in a broader layer of copper between inlet and outlet zone of the nozzle. For this reason, the connection between these to parts, with the use of a laser or a micro drill, are longer than expect. This results in a canal between the inlet and outlet. It therefore seems obvious that a short canal, or better an infinite short canal, leads to small z values which are desired.

Influence of the Nozzle Geometry

After the investigations on the A19 nozzle performed in the framework of this thesis, S. Vestrick [Ves18] studied the influence of the nozzle geometry on the cluster beam properties in the framework of her bachelor thesis [Ves18]. Thereby, the nozzle tilting system was

adjusted to the 0° position. Thus, possibly no core beam will be extracted due to the fact, that the positions of the core beams depending on the hydrogen stagnation conditions and the nozzle geometry. Hence, not the highest achievable thicknesses will be measured, which was not the intention of this measurement. The attention by this measurment was focussed on an alignment of the cluster beam in the center of the beam line to avoid edge effects or possible disturbances between cluster beam and chamber or beam line walls. In a first step, the narrowest inner diameter was enlarged from 33 µm to 35 µm by an intensive chemical cleaning procedure. Table 5.8 shows the differences in the measured thickness and velocity in dependency of the diameter for different stagnation conditions. Thereby, the nozzle has a total length of 18 mm. In-between two measurements the nozzle has to be dismounted out of the $\overline{\text{P}}$ANDA cluster-jet target prototype, will be modified, and mounted back in the target. Thereby, the orientation and the tilting of the nozzle would not be ideally the same as before. Thereof, some discrepancies may occur within the measurements. More details can be found in [Ves18].

The enlargement of the narrowest inner diameter leads to a higher gas flow in the skimmer chamber through the nozzle, resulting in a higher vacuum pressure. The nozzle placed within the skimmer chamber limits the cooling power of the cold head. Thereof, the two measurements taken in the liquid phase of hydrogen had not exactly the same stagnation conditions. Nevertheless, the development of the velocity and thickness can be obtained. The velocity decreased with increasing diameter. Moreover, the thickness increased with increasing diameter, due to the higher gas flow through the nozzle.

Two measurements were performed with the same length and narrowest inner diameter to see the reproducibility of the measurement principle (Table 5.8). The discrepancy measured with the same diameter of 35 µm with liquid hydrogen in front of the nozzle is induced by the appearance of highly intense core beams. Probably, due the dismounting and following remounting of the nozzle in the target, the orientation and angle were not exactly the same leading to an extraction of the core beam during the second measurement, but not by the first.

The results obtained by shortening the nozzle from initial 18 mm to 15 mm are shown in Table 5.9. The reduction of the nozzle by 3 mm presents no differences in thickness and velocity. The data obtained during the measurements agree mostly within their uncertainties. The other data obtained, is due to statistical fluctuations nevertheless of the same order of magnitude and displays no significant dependence on the nozzle length.

The enlargement of the narrowest inner diameter of the nozzle leads to an increased gas flow through the nozzle and therefore, to an increase in the thickness and decrease in the velocity. In the presence of highly intense core beams, this hold not true. Because, the core beams own a higher thickness than achievable with a nozzle with no beam structures with a larger narrowest inner diameter. Moreover, the shortening of 3 mm of the length of the nozzle has no influence on the resulting cluster beam. This information is important and useful for the nozzle production process, due to the fact, that the long outlet zone is the most challenging part during the manufacturing. An possible shortening of the nozzle

Table 5.8: Thicknesses and velocities for different sizes of the narrowest inner diameter of the nozzle A19.

diameter μm	pressure bar	temp. K	physical state of hydrogen	thickness atoms/cm^2	velocity m/s
33	17	25	liquid	$(1.29 \pm 0.07) \cdot 10^{14}$	490 ± 2
	10	24	liquid	$(1.26 \pm 0.07) \cdot 10^{14}$	466 ± 2
	14	30	liquid	$(2.17 \pm 0.36) \cdot 10^{13}$	606 ± 3
	15	35	supercritical	$(9.91 \pm 0.59) \cdot 10^{12}$	834 ± 4
	15	45	supercritical	$(2.64 \pm 0.15) \cdot 10^{12}$	1007 ± 4
	7	30	gaseous	$(4.63 \pm 0.23) \cdot 10^{12}$	877 ± 4
	10	45	gaseous	$(1.79 \pm 0.10) \cdot 10^{12}$	1033 ± 5
35	16	27	liquid	$(6.50 \pm 1.40) \cdot 10^{13}$	456 ± 2
	10	25	liquid	$(9.30 \pm 1.42) \cdot 10^{13}$	324 ± 1
	14	30	liquid	$(8.70 \pm 0.89) \cdot 10^{13}$	541 ± 2
	15	35	supercritical	$(1.90 \pm 0.22) \cdot 10^{13}$	773 ± 3
	15	45	supercritical	$(3.92 \pm 0.22) \cdot 10^{12}$	954 ± 4
	7	30	gaseous	$(5.82 \pm 0.69) \cdot 10^{12}$	840 ± 4
	10	45	gaseous	$(3.40 \pm 0.18) \cdot 10^{12}$	993 ± 4
35	16	27	liquid	$(2.51 \pm 0.14) \cdot 10^{14}$	480 ± 2
	10	25	liquid	$(2.45 \pm 0.14) \cdot 10^{14}$	425 ± 2
	14	30	liquid	$(7.78 \pm 0.78) \cdot 10^{13}$	560 ± 3
	15	35	supercritical	$(1.73 \pm 0.20) \cdot 10^{13}$	782 ± 3
	15	45	supercritical	$(3.48 \pm 0.23) \cdot 10^{12}$	962 ± 4
	7	30	gaseous	$(9.38 \pm 1.14) \cdot 10^{12}$	846 ± 4
	10	45	gaseous	$(3.13 \pm 0.35) \cdot 10^{12}$	1000 ± 4

length will result in a more simplified production step within the process.

Within the measurements performed with the two monolithic copper nozzles A21 and A19, first important insights into the cluster production precesses were obtained. Additionally, useful information with respect to the nozzle manufacturing towards high performance nozzles were gained.

5.3.3 GSI Nozzles

In the framework of this thesis, additionally two more monolithic copper nozzles were installed at the $\overline{P}$ANDA cluster-jet target prototype to perform investigations on the resulting cluster beam. Due to their later application at GSI, they were named GSI nozzles. More details on the production and their later application can be found in chapter 3. The aim hereby was to find a high performance nozzle with a narrowest inner diameter below 15 μm.

Table 5.9: Thicknesses and velocities for different lengths of the nozzle A19.

| length mm	pressure bar	temp. K	physical state of hydrogen	thickness atoms/cm^2	velocity m/s
17	16	27	liquid	$(1.25 \pm 0.16) \cdot 10^{14}$	485 ± 2
	10	25	liquid	$(1.31 \pm 0.13) \cdot 10^{14}$	445 ± 2
	14	30	liquid	$(1.06 \pm 0.09) \cdot 10^{14}$	545 ± 2
	15	35	supercritical	$(2.42 \pm 0.18) \cdot 10^{13}$	787 ± 3
	15	45	supercritical	$(3.97 \pm 0.20) \cdot 10^{12}$	965 ± 4
	7	30	gaseous	$(8.36 \pm 0.68) \cdot 10^{12}$	842 ± 4
	10	45	gaseous	$(3.59 \pm 0.26) \cdot 10^{12}$	1004 ± 4
16	16	28.3	liquid	$(1.97 \pm 0.10) \cdot 10^{14}$	501 ± 2
	10	26	liquid	$(2.03 \pm 0.11) \cdot 10^{14}$	4478 ± 2
	14	30	liquid	$(1.13 \pm 0.06) \cdot 10^{14}$	555 ± 2
	15	35	supercritical	$(3.08 \pm 0.15) \cdot 10^{13}$	807 ± 4
	15	45	supercritical	$(4.15 \pm 0.25) \cdot 10^{12}$	967 ± 4
	7	30	gaseous	$(1.23 \pm 0.06) \cdot 10^{13}$	849 ± 4
	10	45	gaseous	$(3.81 \pm 0.30) \cdot 10^{12}$	997 ± 4
15	16	27	liquid	$(1.29 \pm 0.08) \cdot 10^{14}$	482 ± 2
	10	26	liquid	$(1.62 \pm 0.09) \cdot 10^{14}$	430 ± 2
	14	30	liquid	$(1.14 \pm 0.06) \cdot 10^{13}$	533 ± 2
	15	35	supercritical	$(2.99 \pm 0.16) \cdot 10^{13}$	794 ± 4
	15	45	supercritical	$(3.73 \pm 0.23) \cdot 10^{12}$	963 ± 4
	7	30	gaseous	$(1.12 \pm 0.06) \cdot 10^{13}$	841 ± 4
	10	45	gaseous	$(3.22 \pm 0.21) \cdot 10^{12}$	1000 ± 4

GSI 12

The diameter of the first installed nozzle, GSI 12, was determined to $\varnothing_{\text{GSI12}} = 39\,\mu\text{m}$. Unfortunately, the diameter is to large for the planed experiment, but nevertheless some measurements were performed. The highest thickness was determined as the key numbers for every nozzle and is listed in Table 5.10. The velocities and thicknesses were calculated with the lowest possible z parameter $z_{\text{liquid}} = (0.445 \pm 0.014)$ mm [Tä12] and the highest possible $z_{\text{liquid}} = (17 \pm 1)$ mm determined in this thesis. The results gained with the lower z value can be seen as upper limit and the other one as a lower limit. The highest achievable thickness of $1.89 \times 10^{14}\,\text{atoms/cm}^2$ was obtained at 11 bar and 29 K. The relatively large inner diameter leads to a high gas flow through the nozzle in the skimmer chamber resulting in a vacuum of $> 5 \times 10^{-2}\,\text{mbar}$. Due to the fact, that the nozzle is located in the skimmer chamber in combination with the high vacuum, the cooling power of the cold head is at its limits, and the low temperature of 20 K are not realisable. Therefore, the thickness is not as high as it could be with a lower temperature of the hydrogen.

With this nozzle an image of the cluster beam with the visualisation system installed at the skimmer chamber was obtained (cf. Fig. 5.55). The measurement at 16 bar and 32 K

Table 5.10: Velocities and thicknesses determined for the first GSI nozzle. The results gained with the lower z value can be seen as upper limit and the other one as a lower limit.

z parameter mm	pressure bar	temperature K	velocity m/s	thickness atoms/cm^2
0.445 ± 0.014	11	29	333 ± 17	$(1.89 \pm 0.20) \cdot 10^{14}$
17 ± 1	11	29	595 ± 29	$(1.06 \pm 0.11) \cdot 10^{14}$
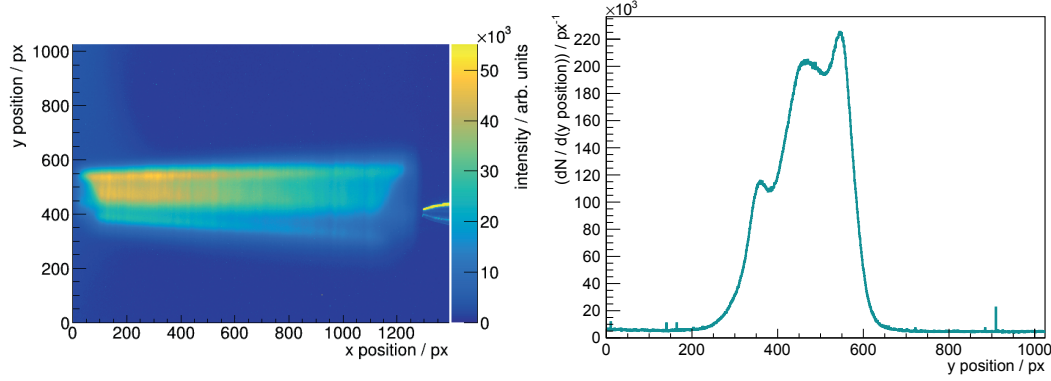
Figure 5.55: Image from the cluster beam in the skimmer chamber for a measurement at 16 bar and 32 K with an exposure time of 10 s. The projection shows three intensity peaks corresponding to structures within the cluster beam.

depicts a structure consisting of three intensity peaks within the cluster beam.

GSI 19

The diameter of the second installed nozzle, GSI 19, was determined to $\varnothing_{\mathrm{GSI19}} = 12\,\mu\mathrm{m}$. Therefore, the diameter fits the desired inner diameter. Thus, a velocity measurement was performed to calculate the target thickness and the value of the z parameter (Fig. 5.56). The velocity distribution at 18 bar and 22 K shows a wide velocity distribution with a standard deviation of 40 m/s. The mean velocity was determined to (396 ± 2) m/s. The corresponding z value was calculated to be $z_{\mathrm{liquid}} = (2.5 \pm 0.1)$ mm. This is the smallest z value achieved for a nozzle investigated at Münster.

Using the determined mean velocity and the consequential z value, the highest achievable thickness occurs at 18 bar and 22 K in a distance of 2.1 m from the nozzle: $(1.09 \pm 0.10) \times 10^{14}$ atoms/cm^2 with a velocity of (396 ± 2) m/s.

Due to the later application at GSI with respect to the future experiment performed with this nozzle aiming for a constant luminosity, a stability measurement was taken (Fig. 5.58). The measurement was performed at 18 bar and 22 K, where the highest thickness was obtained. The stability measurement does not show the high thickness, due to the fact, that the nozzle angle was varied in comparison to the previous measurement due to measurements performed in-between. During this measurement, every 5 min a
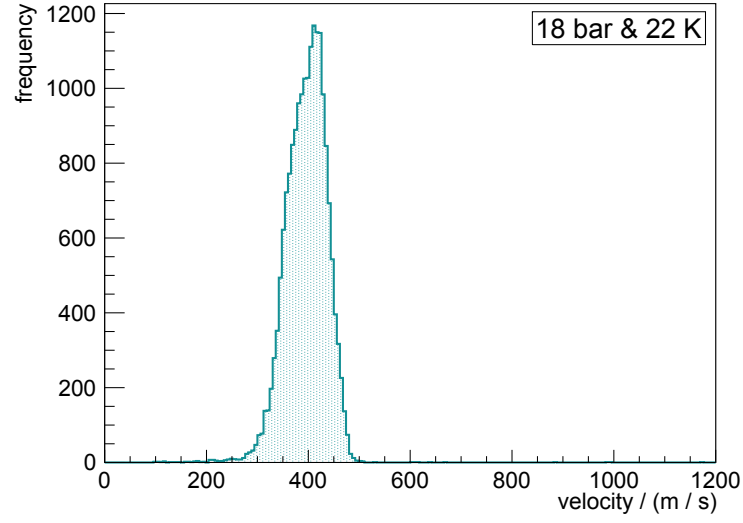
Figure 5.56: Velocity distribution measured with the GSI 19 nozzle at 18 bar and 22 K.
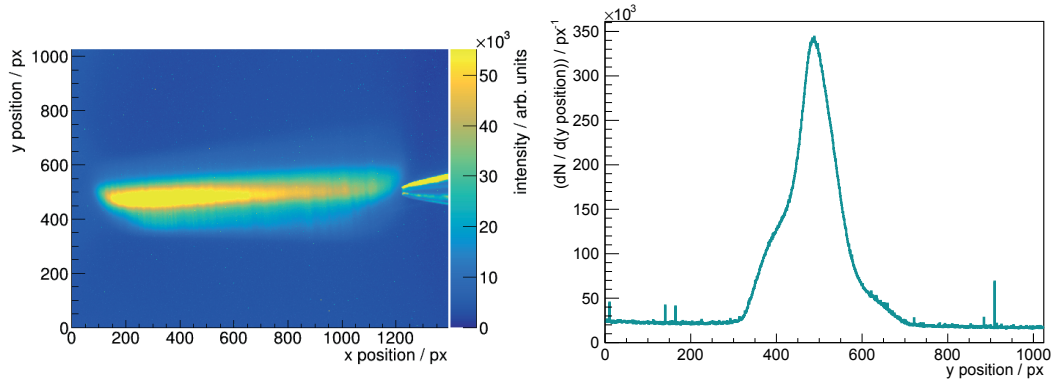

Figure 5.57: Images from the cluster beam in the skimmer chamber. Measurement at 18 bar and 22 K, where the highest thickness was measured. The exposure time was 35 s. The measurement shows a relative homogeneous thickness distribution within the cluster beam.

beam profile was recorded and analysed. The average target thickness was determined to 6.11×10^{13} atoms/cm^2 with a stability of better than 10 %.

5.3.4 Glass Nozzle

A second production process results in nozzles out of glass (cf. chapter 3). The glass nozzle G1N30 has a narrowest diameter of $\varnothing_{\text{glass}} = 30\,\mu\text{m}$ and is perfectly circled due to the production process (cf. Fig. 5.59).

An installation of this nozzle in the $\overline{\text{P}}$ANDA cluster-jet target prototype and a following visualisation of the resulting cluster beam in the skimmer chamber is presented in Figure 5.60. The nozzle exit is not visible due to the short nozzle length of 3 mm. Displayed is the retaining ring of the nozzle with a diameter of 50 mm at the left side, which fix the nozzle in its seat. The beam direction is from left to right. The measurement was performed
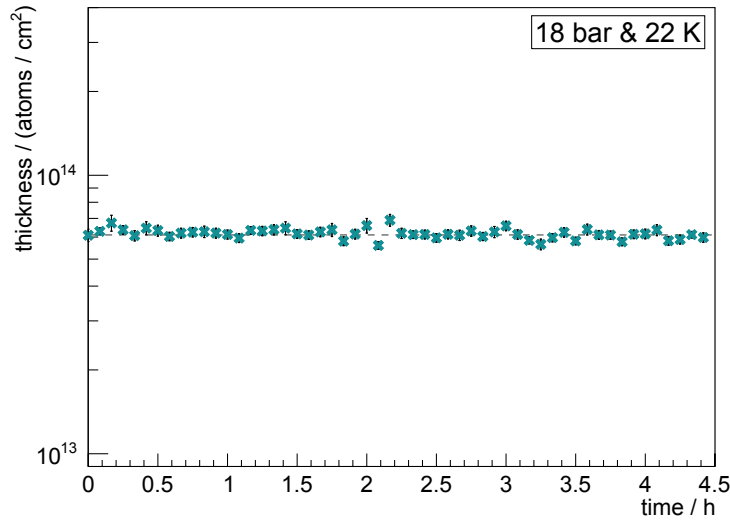
Figure 5.58: Stability measurement at 18 bar and 22 K over 4.5 h with logarithmic scale. Systematic uncertainties (velocity, pressure gauge, and pumping speed), which are account 10 % are excluded.
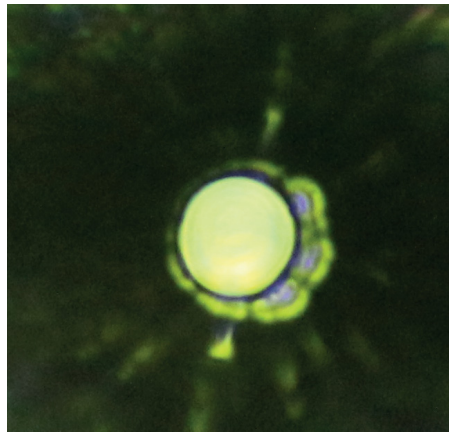

Figure 5.59: Microscopic view of the narrowest inner diameter of the glass nozzle. A perfect round narrowest inner diameter of $\varnothing_{\text{glass}} = 30\,\mu\text{m}$ is visible.

at 8 bar and 25 K. The first picture (top, left) shows a weak visible cluster beam leaving the nozzle. Additionally, several chaotic and some screwed traces are displayed resulting from frozen micro sized particles and supplementary an ice chunk occurs at the top of the retaining ring. The next picture (top, right) shows the grow of the ice chunk and finally it blocks the complete nozzle (bottom, left). Then, the ice chunk drops and a high intense cluster beam explode out of the nozzle with the additionally frozen particles (bottom, right). This procedure repeats itself.

This observation was not unexpected, due to previous studies in the framework of the thesis of E. Köhler. There, the beam origin within the nozzle was determined to be at roughly (6 ± 2) mm from the narrowest point of the nozzle. Due to the full length of the glass nozzle of 3 mm, the beam origin is not located within the nozzle. Thus, there is no
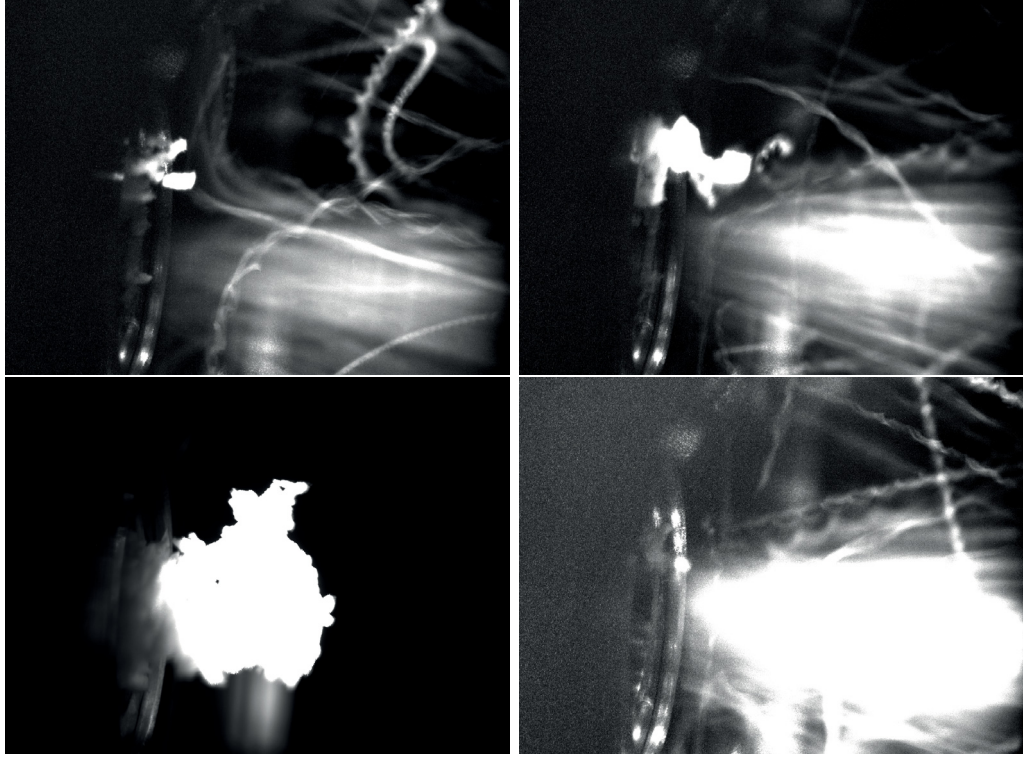
Figure 5.60: Measurement performed with the glass nozzle at 8 bar and 25 K. The pictures are recorded with the visualisation system in the skimmer chamber. The nozzle exit is not visible, but the retaining ring of the nozzle at the left side. A weak cluster beam leaves the nozzle with additionally frozen particles. Moreover, an ice chunk grows at the retaining ring.
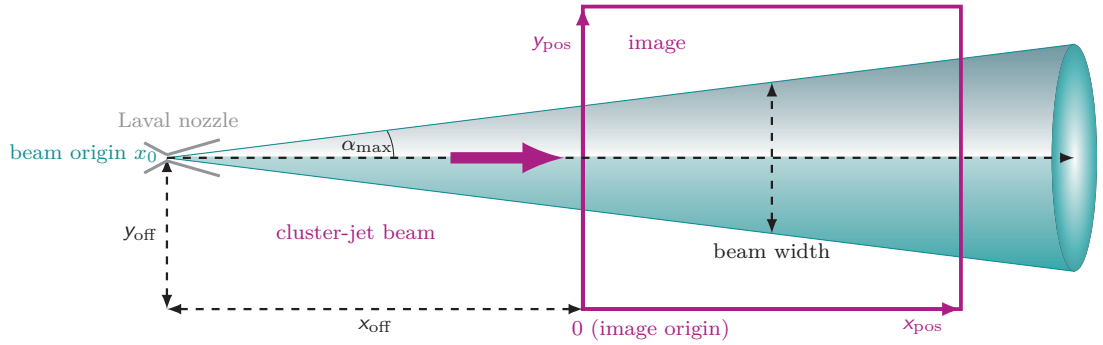
Figure 5.61: Principle to calculate the cluster-jet beam origin in horizontal (x position offset, x_{off}) direction. The violet rectangle represents an image of the cluster beam recorded in the skimmer chamber. Generated by E. Köhler, edited.

possibility to produce a well defined cluster beam and chaotic structures occur (cf. Fig. 5.60). The cluster-jet beam origin offset in horizontal (x_{off}) direction was calculated with measurement series performed with the visualisation system in the skimmer chamber (cf. Fig. 5.61).
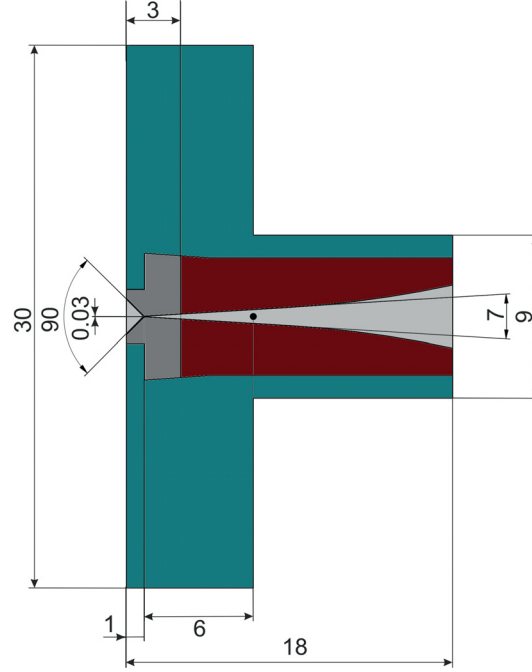
Figure 5.62: Sketch of the glass nozzle (gray) in combination with the extension (red). For comparison, the $\overline{P}$ANDA nozzle is drawn in green and the cluster beam origin is marked with a black point. Generated by D. Bonaventura, edited.

Therefore, for each image for every x pixel position a projection on the ordinate was done. This projections represent the width of the cluster beam at every x pixel position. For each individual image, the width can be fitted with a linear function $f(x_{\text{off}})$ and the x_{off} are calculated to be $f(x_{\text{off}}) = 0\,\text{px}$. The beam origin within the nozzle then can be estimated with [Kö15]

$$x_0 = x_{\text{off}} + x_{\text{skimmer}}. \tag{5.40}$$

Therein, x_{skimmer} corresponds to the distance of the skimmer tip to the image origin. More details can be found in [Kö15].

Glass Nozzle with Extension 1

The previous section shows, that the cluster beam origin is not located within the nozzle. Therefore, a composite design of the glass nozzle in combination with an extension manufactured of aluminium to achieve the same nozzle length as usual was designed. The extension was mounted with an additional sealing directly behind the glass nozzle. Figure 5.62 shows a schematic view of the composite nozzle. Therein, the glass nozzle is drawn in gray, the extension in red, and for comparison the $\overline{P}$ANDA nozzle in green. Additionally, the cluster beam origin is marked with a black point and is now located within the nozzle.
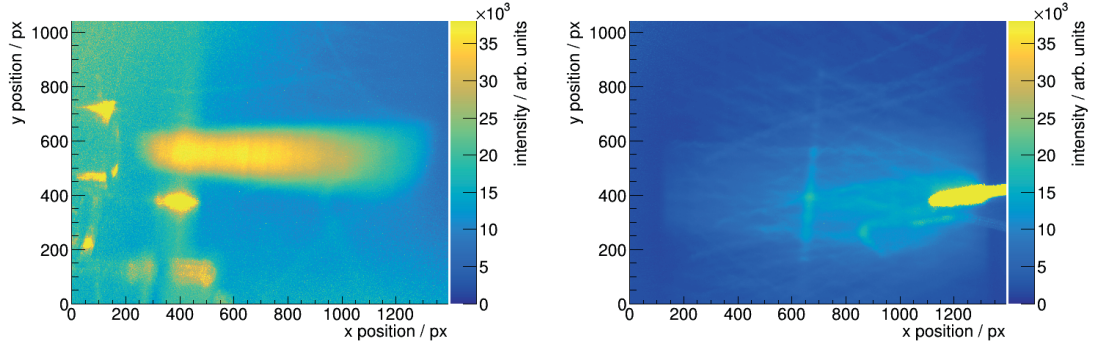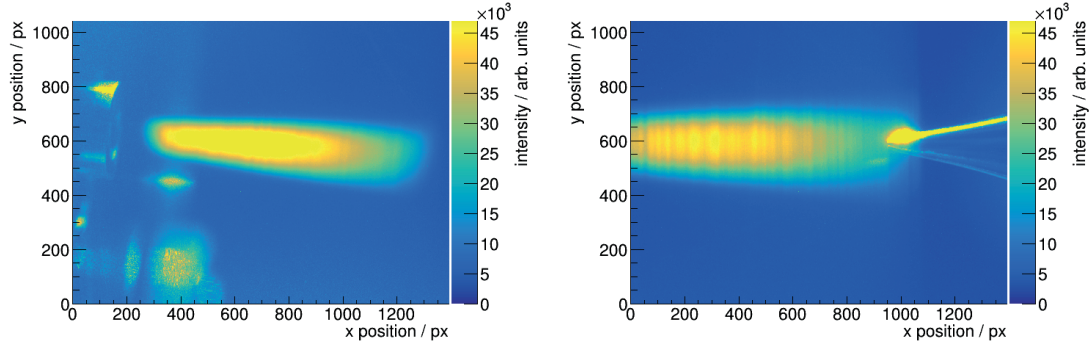
Figure 5.63: Recorded images of the cluster beam. *Left*: The exit of the nozzle extension is visible with a well defined cluster beam (17 bar and 32 K) and only some chaotic frozen particles. *Right*: The skimmer tip is visible, but no defined cluster beam (8 bar and 25 K). During the propagation between nozzle and skimmer the cluster beam gets affected by the chaotic frozen particles.

The first tested extension has a transition diameter (the diameter, where the transition from glass nozzle to extension is placed) of 530 μm. The resulting images recorded from the cluster beam are displayed in Fig. 5.63. Now the exit of the extension is visible on the left side (Fig. 5.63, left). A well defined cluster beam leaves the extension with only some remaining frozen particles (visible as weak traces). Figure 5.63 on the right side shows the skimmer tip, but no defined cluster beam. During the propagation from the nozzle to the skimmer, the cluster beam interacts with the frozen particles and is affected by them.

A first beam profile could be measured in the interaction chamber leading to a target thickness of $(4.62 \pm 0.39) \cdot 10^{12}$ atoms/cm² at 17 bar and 36 K. Thereby, a velocity of (741 ± 38) m/s with a z value of $z_{\text{vapour}} = (1.67 \pm 0.20)$ mm [Tä12] was assumed.

Glass Nozzle with Extension 2

The second tested extension has a transition diameter of 280 μm and is therefore, smaller than the first one. Additionally, this transition diameter is closer to the exit opening diameter of the glass nozzle of roughly 250 μm. A resulting image is displayed in Figure 5.64 at 17 bar and 25 K. A well defined cluster beam leaves the nozzle and reaches the skimmer tip. The highest achievable thickness was measured at 17 bar and 22 K to $(1.22 \pm 0.27) \cdot 10^{14}$ atoms/cm². Thereby, a velocity of (258 ± 13) m/s with a z value of $z_{\text{liquid}} = (0.445 \pm 0.014)$ mm [Tä12] was assumed. Moreover, at the end of the beam dump, after a flight path of roughly 5 m a well defined cluster bean was observed with the MCP detection system (cf. Fig. 5.15). Furthermore, measurements on the cluster beam produced with the glass nozzle were performed with the optical monitor system at the beam dump of the $\overline{\text{P}}$ANDA cluster-jet target prototype. Figure 9.1 shows a resulting picture. These measurements show the possibility to generate a well defined cluster beam even at large distances with the use of a glass nozzle.

Figure 5.64: Recorded images of the cluster beam at 17 bar and 25 K. A well defined cluster beam leaves the nozzle (*left*) and reaches the skimmer (*right*). This measurement was performed using the composite design of the glass nozzle in combination with the second extension to achieve the same length of the nozzle as usual.
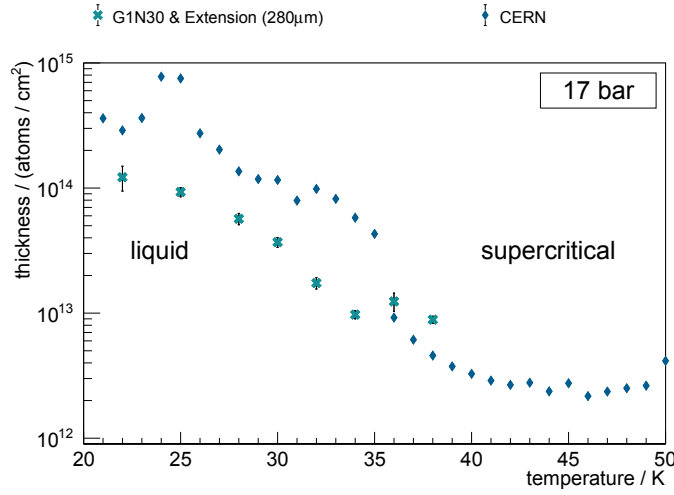
Figure 5.65: Thickness mapping at 17 bar for the glass nozzle with extension 2 depending on the temperature.

Due to the generation of a well defined cluster beam with the glass nozzle with this extension, a thickness mapping was performed with a pressure of 17 bar in front of the nozzle (Fig. 5.65).

In the liquid phase of hydrogen, the thickness is below the thickness measured with the $\overline{P}$ANDA nozzle. In case of a supercritical hydrogen, the thickness is higher than for the $\overline{P}$ANDA nozzle. The considerable smaller thickness of the glass nozzle with extension will be provoked due to the composite design. The extension with the larger transition diameter shows, that turbulences occur at the transition. There, the turbulences are strong enough to affect the cluster beam. In the case of the extension with the smaller transition diameter, also turbulences appear, resulting in a cluster beam with lower thickness. Therefore, the composite design needs to be matched better or a full length glass nozzle has to be produced and tested.

6 MAGIX at MESA Experiment

The future Mainz Energy-Recovering Superconducting Accelerator (MESA) is part of the cluster of excellence PRISMA (Precision Physics, Fundamental Interactions and Structure of Matter) of the Johannes Gutenberg-University of Mainz. MESA will be a multi turn linear superconducting electron accelerator with the possibility of an energy recovery mode for electrons. The infrastructure of MESA is currently under construction and the accelerator will be put into full operation in 2022 [Cai18].

6.1 Experimental Program and Objectives

The upcoming MAGIX (MESA Gas Internal target eXperiment) experiment at MESA will focus on low energy high precision experiments like the determination of the proton radius, the search for dark photons, and the determination of the astrophysical S-factor.

Proton Radius Puzzle

The proton radius values show a discrepancy depending on the measuring method. Muonic hydrogen measurements resulted in a proton radius of $r_{\mathrm{p}} = (0.84184 \pm 0.00067)$ fm [A$^+$11]. The CODATA (Committee on Data for Science and Technology) [COD] value of $r_{\mathrm{p}} = (0.8751 \pm 0.0061)$ fm is determined by the investigations of laser spectroscopy with hydrogen and deuterium and by the study of elastic electron-proton scattering [M$^+$16]. The CODATA value is, compared to the value resulting from the muonic hydrogen, where the electron of the hydrogen is exchanged by a muon, $5\,\sigma$ higher and ten times more imprecise. Moreover, the values combined in the CODATA value show fluctuations, so more high precission measurements are necessary. A measurement at the MAinz MIcrotron (MAMI) using elastic electron-proton scattering results in a charged proton radius of $r_{\mathrm{p}} = (0.879 \pm 0.008)$ fm [B$^+$10]. This measurement enlarged the previous discrepancy up to $7\,\sigma$ to the CODATA value.

The determination of the proton radius by elastic electron-proton scattering data uses the electrical form-factor $G_{\mathrm{E}}\left(Q^2\right)$. It can be extracted from the total cross section by the Rosenbluth-Separation (more details see chapter 7.3) [B$^+$14]:

$$\left(\frac{d\sigma}{d\Omega}\right)_0 = \left(\frac{d\sigma}{d\Omega}\right)_{\mathrm{Mott}} \left(\frac{G_{\mathrm{E}}^2\left(Q^2\right) + \tau G_{\mathrm{M}}^2\left(Q^2\right)}{1+\tau} + 2\tau G_{\mathrm{M}}^2\left(Q^2\right)\tan^2\frac{\theta}{2}\right). \qquad (6.1)$$

The proton radius can then be extracted by

$$r_{\mathrm{p}}^2 = -6\hbar^2 \frac{d}{dQ^2} G_{\mathrm{E}}\left(Q^2\right)|_{Q^2=0} \tag{6.2}$$

at the the limit of the four momentum transfer $Q^2 \to 0$.

To determine the proton radius, an extrapolation of the data to $Q^2 = 0$ is needed. Previous measurements of the proton charge form-factor were performed in Q^2 ranges above $0.004\,\mathrm{GeV}^2/c^2$ [S+80,B+10,M+74]. Therefore, more data below $Q^2 = 0.004\,\mathrm{GeV}^2/c^2$ are necessary.

A new technique to measure the proton charge form-factor is the initial state radiation (ISR) method [M+17,Mih17,M+14b], which is used by MAMI and will be used by MAGIX. Data on elastic electron-proton scattering show a radiative tail, which is dominated by the coherent sum of two Bethe-Heitler diagramms (see Fig. 6.1, left). Thereby, the ISR radiation corresponds to a photon which is emitted by the initial electron before scattering at the proton. Whereas, the FSR radiation, the final state radiation, corresponds to a real photon emitted by the electron after the scattering. These two processes result in two significantly different signals within the detectors and a comparison of these data with simulations allows for an extraction of the ISR information (Fig. 6.1, right) and therefore, for the determination of the form-factors $G_{\mathrm{E}}\left(Q^2\right)$.

First performed measurements lead to a charged proton radius of $r_{\mathrm{p}} = (0.810 \pm 0.082)\,\mathrm{fm}$ [M+17]. This experiment used a cell target filled with liquid hydrogen. This setup results in high uncertainties compared to the previous measurements. Therefore, MAMI will
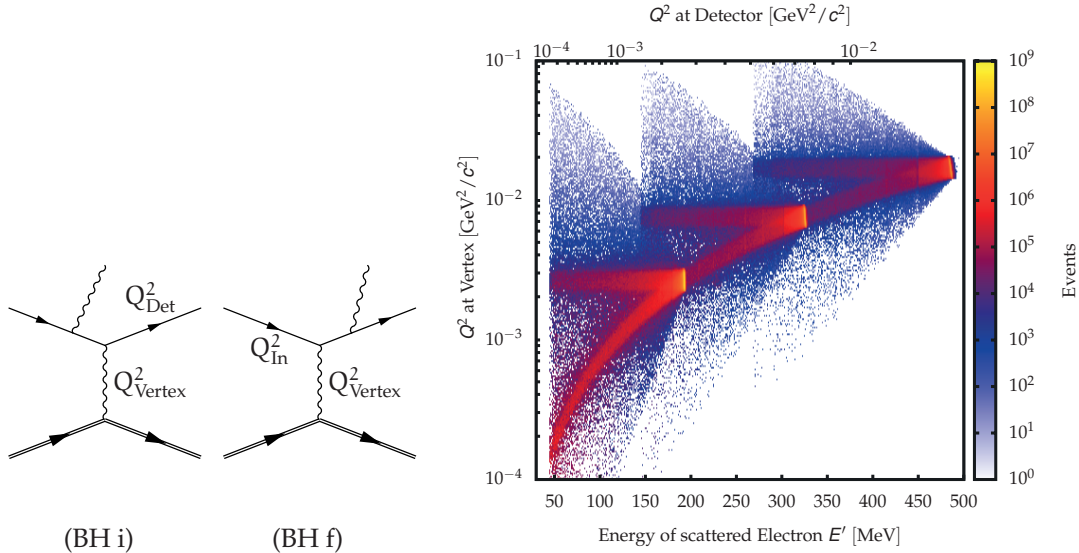
Figure 6.1: Principle of the ISR technique. *Left*: Two Bethe-Heitler-diagramms for the initial state (BH i) and the final state (BH f) radiation. Both are the main components to the radiative tail in elastic electron-proton scattering data. *Right*: The analysis allows for a distinction between ISR and FSR. Additionally performed simulations lead to an extraction of the form-factors, from [M+14b]. Thanks to M. Mihovilovic (UNILJ).
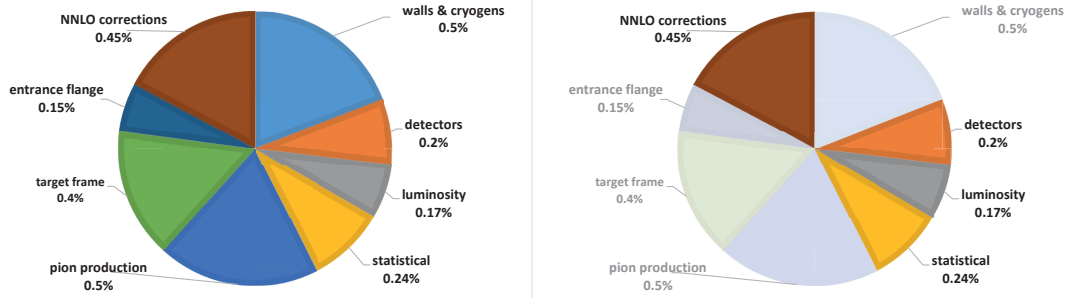
Figure 6.2: Individual contributions to the statistical uncertainties of the cross section by the ISR technique. *Left*: Uncertainties caused by the use of a cell target filled with liquid nitrogen [M$^+$17]. *Right*: Expected uncertainties using a Münster jet target for the ISR measuremnt at MAMI. Moreover, the measurements will be performed below the pion production threshold to minimise the uncertainties caused by the pion production. Thereby, the total systematic uncertainty of the cross section can be reduced by a factor of roughly two, from $\leq 1\,\%$ to $\leq 0.5\,\%$. Based on [Mih17].

rerun the experiment using a jet target from Münster. Furthermore, the measurements will be performed below the pion production threshold to minimise the uncertainties caused by the pion production. The statistical uncertainties can thus be reduced by a factor of roughly two (see Fig. 6.2).

Dark Photons

The well established standard model of particle physics which was already discussed in section 4.1 describes the known particles of our universe. Next to the open questions concerning the strong interaction, e.g., the proof of existence of exotic particles, the existence of dark matter in the universe is an evidence for new physics beyond the standard model. It can be expected, that a structure like the standard model is also existing for the dark sector with minimal interaction between these dark particles and the standard model particles. The search for the dark photon γ' is one promising approach to strengthen this theory [M$^+$14a].
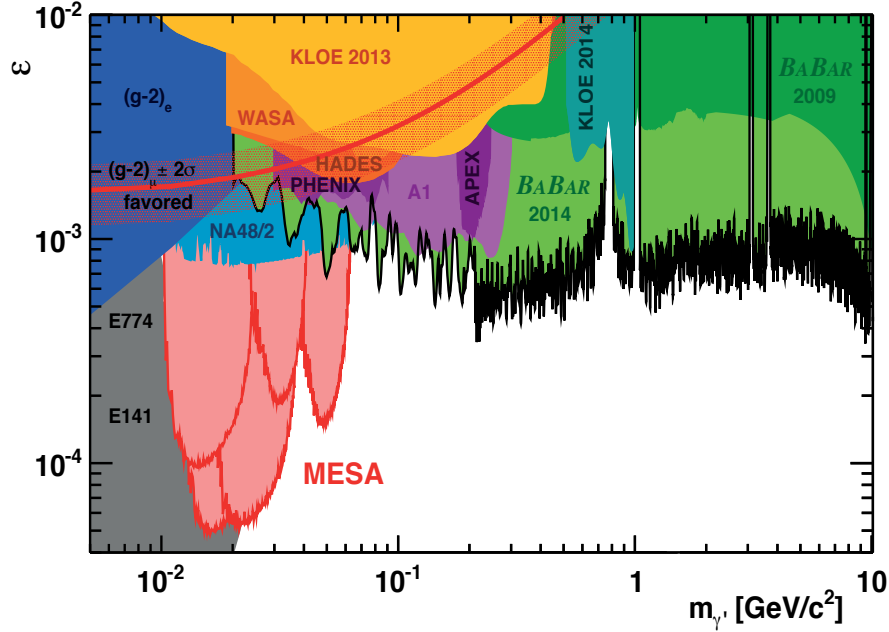
The strength of the interaction ε between a standard photon and a dark photon is given by their electromagnetic coupling constants [M$^+$14a]

$$\varepsilon = \sqrt{\frac{\alpha'}{\alpha}}. \tag{6.3}$$

The predicted value of ε depends on the model and ranges from 10^{-12} to 10^{-2}. The decay of the dark photon is highly suppressed in dark particles. Therefore, it will decay in standard model particles, namely in an electron-positron pair, which are detectable [Den16]. MAGIX will use this decay channel and Figure 6.4 shows the accessible mass range of MESA. By Magix, the accelerated electron scatters with a target and the scattered electron emits analogous to the bremsstrahlung a dark photon. This photon decays into an electron-positron pair and the two high resolution spectrometers will measure the momentum and coincidence of these two particles. The dark photon will give a very narrow signal drop in the missing mass spectra of the electron-positron pair over the QED

background [Den16].

Previous measurements at the Mainz Microtron resulted in exclusion limits in the mass range between $40\,\mathrm{MeV}/c^2$ and $300\,\mathrm{MeV}/c^2$ [M$^+$14a].

Figure 6.3: The accessible dark photon range for the MESA accelerator. The abzissa shows the accesible mass range and the ordinate the strength of the interaction ε (see Eq. (6.3)). MAGIX will use the decay of the dark photon in an electron-positron pair which will be detected via the two high resolution spectrometers. Taken from [Den16]. Thanks to H. Merkel (JGU) and Y. Guo (JGU).
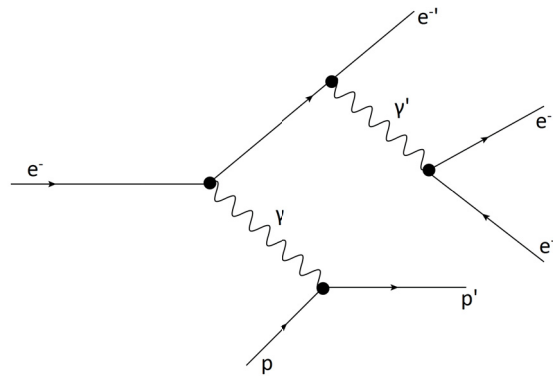
Figure 6.4: Decay channel for the dark photon used by the MAGIX experiment. The scattered electron emits a dark photon which decays in an electron-positron pair. The momentum and coincidence of these two particles are measured with the two high resolution spectrometers of MAGIX. Based on [Aul14].

Astrophysical S-Factor

The stellar burning cross section $\sigma(E)$ is given by [Hos14] as

$$\sigma(E) = \frac{1}{E}S(E)\exp(-2\pi\eta(E)) \qquad (6.4)$$

with $\exp(-2\pi\eta(E))$ describing the probability to tunnel through the Coulomb barrier. Thereby, $\eta = Z_1 Z_2 \alpha c/v$ with Z_1 and Z_2 being the proton number of the nuclei, v being the velocity between the two nuclei, and α being the fine structure constant. The astrophysical S-factor $S(E)$ describes the discrepancy to the Gamow peak model. The Gamow peak describes the transmission probability by tunnel effect, and is given by the convolution of the probability for a Maxwell-Boltzmann distribution and the Coulomb barrier transmission and depends on the reaction and temperature. For extrapolations from known data to the energies from astrophysical interest, the astrophysical S-factor can be used. Therefore, mostly $^{12}C(\alpha,\gamma)^{16}O$ is used, because of the low mass of the nuclei and missing resonances in the stellar energy sector (cf. Fig. 6.5). The Gamow peak for the reaction $^{12}C(\alpha,\gamma)^{16}O$ is at roughly $E_{\text{c.m.}} = 300\,\text{keV}$, thus the cross section has to be extrapolated to this energy. The precise knowledge of the astrophysical S-factor allows for a deeper understanding of supernova explosions, the abundance of elements, and nucleosynthesis.

At MAGIX, the time reversal reaction $^{16}O(\gamma,\alpha)^{12}C$ will be measured with the inelastic scattering of an electron on an oxygen target (cf. Fig. 6.6). The momentum of the scattered electron will be measured with the GEM detectors in combination with the spectrometers and the α particle will be detected in a silicon strip detector [Mer17a,Lun17]. These two detectors allow for a coincidence measurement of the two particles.
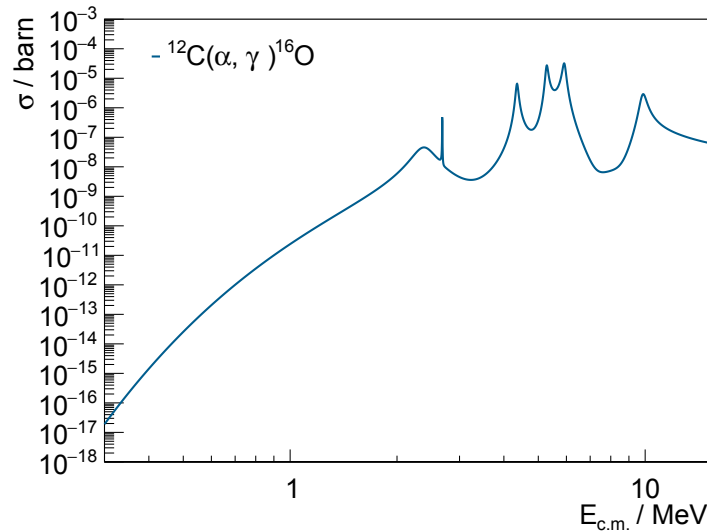
Figure 6.5: Cross section of $^{12}C(\alpha,\gamma)^{16}O$. The region of interest, the sun burning, is at roughly $E_{\text{c.m.}} = 300\,\text{keV}$. The cross section shows resonances for high center of mass energies, therefore, measurements have to be performed to detemine the cross section at low energies. Generated from the simulations performed by S. Lunkenheimer (JGU) which are based on the data from [d$^+$17].
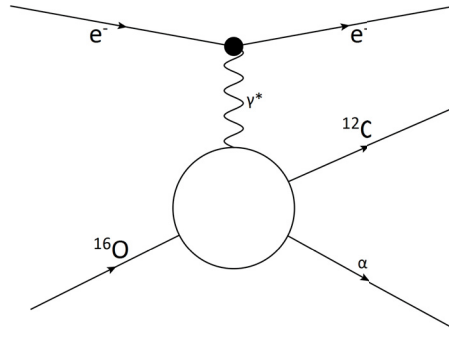
Figure 6.6: Reaction to measure the astrophysical S-factor at MAGIX. The time reversal reaction $^{16}O\,(\gamma,\alpha)\,^{12}C$ will be measured, because the scattered electrons and the α particle can be measured coincidently by the setup of MAGIX. Based on [Lun17].

6.2 Mainz Energy-Recovering Superconducting Accelerator MESA

The electron accelerator MESA (Fig. 6.7) will offer the possibility to operate in two different beam operation modes [H+17b, Hei15, Cai18]. The first mode, is the extracted beam mode (EB) with energies up to 155 MeV and currents of 150 μA. In this mode, it is possible to polarize the electron beam. The second mode, the energy recovery linac mode (ERL) allows for energies up to 105 MeV and currents of 1 mA in the first stage. Later it will be upgraded to currents of up to 10 mA.

The electron source STEAM (Small Thermalized Electron source At Mainz) generates electrons due to the photoelectric effect [FA15]. Thereby, a pulsed laser extracts electrons of the surface of a photo cathode, which will be accelerated and leave the source consequently with energies of up to 100 keV. Afterwards the electrons pass a Wien filter to distinguish
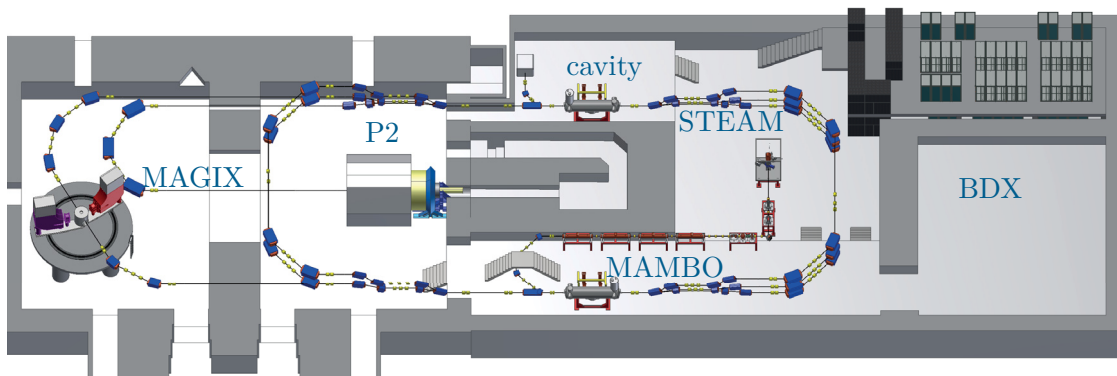
Figure 6.7: Sketch of the future MESA accelerator. The electron source STEAM provides electrons which are further accelerated in the linear pre-accelerator MAMBO and then injected in the main accelerator with two superconducting cavities. The P2 experiment uses the extracted beam mode and behind the beam dump the BDX experiment is located. The energy recovery linac mode is provided for the MAGIX experiment. From [Mer16a]. Thanks to D. Simon (JGU) and K. Aulenbacher (JGU).

between electrons with a velocity of $v = E/B$ and other electrons [Gel74]. The electrons with $v \neq E/B$ experience a Lorentz force, induced by the electric and magnetic field of the Wien filter vertical to the electron beam direction and perpendicular to each other, and leave the electron beam. The resulting electron beam is injected into the linear pre-accelerator MilliAMpere BOoster (MAMBO) consisting of four Radio Frequencies (RF) cavities and accelerates the electrons up to energies of 5 MeV corresponding to a $\beta = v/c = 0.9957$. Inside the cavities, a standing wave with a frequency of 2.449 GHz at room temperature is provided via the reflections of an electromagnetic wave at the walls. The electrons are injected in phase, so that they are accelerated due to the alternating electromagnetic field.

After MAMBO the electrons enter the main accelerator, also a linear accelerator, which is equipped with two cavities. The accelerator beam line is built up in a ring structure, so that the electrons pass the cavities up to three times. These cavities are cooled down to 2 K with the use of helium, leading to a superconducting material. Therefore, higher electromagnetic field strengths with a frequency of 1.3 GHz [S+15] are applied. Every turn through two cavities allows for an energy gain of 50 MeV. To focus and guide the electron beam through the beam line, 100 quadrupoles and 60 dipole magnets are used. In the EB mode, the electrons pass the two cavities three times resulting in an energy of 155 MeV. Afterwards the beam is extracted and directed to the P2 (Precision experiment 2) experiment [B+]. The P2 experiment is a beam dump experiment which uses an external cell target filled with hydrogen at a temperature of 20 K. The detector, a solenoidal spectrometer is used to detect the scattered electrons. Furthermore, the detector suppresses background, like bremsstrahlung and Møller scattering, and measures the momentum transfer Q^2.

The main focus of this experiment is the determination of the electroweak mixing angle θ_W (Weinberg angle) with high precision. Weak interaction violates parity, thus the cross sections σ for the two different polarisations R and L for the elastic electron-proton scattering leads to an asymmetry term A^{PV} [B+]

$$A^{PV} = \frac{\sigma_L - \sigma_R}{\sigma_L + \sigma_R} = \frac{G_F Q^2}{4\sqrt{2}\pi\alpha} \left(Q_W + F\left(Q^2 \right) \right). \tag{6.5}$$

Therein, G_F is the Fermi constant, Q^2 the squared four momentum transfer, α the fine structure constant, $Q_W = 1 - 4\sin^2\theta_W$, and $F(Q^2)$ the proton form-factor. In case of low Q^2, the Q_W term gives the main contribution to the asymmetry term A^{PV}. Therefore, P2 will measure at low momentum transfer Q^2 with different polarized electron beams to calculate the cross sections resulting in the Weinberg angle.

The beam dump experiment BDX will also use the EB mode and is located behind the beam dump of the P2 experiment in electron beam direction and runs parallel to P2 (see Fig. 6.7). The search for dark matter particles is the main objective of BDX. Therefore, the beam dump in front is used to shield the detectors against neutron background [H+17b]. Due to the fact, that MESA provides energies below the pion production threshold, the background of BDX will be neutrino free [Den16].

In case of the ERL mode, the electron beam passes the two cavities two times giving

an electron energy of 105 MeV and afterwards it is directed to the MAGIX (MESA Gas Internal target eXperiment) experiment. After the interaction of the electrons with the protons of the internal jet target MCT-M, the electrons are redirected in the main accelerator with a phase shift of π induced by the accelerator path length. This phase shift leads to a deceleration in the cavities with a decrease in the electron energy of 25 MeV by passing each cavity and the energy is transferred to the electromagnetic wave in the cavity. At a residual energy of 5 MeV the electron beam is dumped. The gained energy by the deceleration of the electrons is used to accelerate the following electrons resulting in an energy-efficient operation mode of MESA.

6.3 MAGIX Experiment (MESA Gas Internal target eXperiment)

The MAGIX experiment will consist of a Münster jet target (see section 6.4) and two high resolution magnetic spectrometers equipped with GEM detectors (Gas Electron Multipliers) [Cai18].
The two spectrometers each consisting of a dipole and a quadrupole magnet are mounted moveable around the interaction point and therefore, they are independent adjustable in angle. They are used to measure the momentum and angle distribution of the scattered electrons. The magnetic field deflects the electrons due to their momentum on different positions on the focal plane, where the GEM detectors are located. With respect to the high precision measurements planned with the MAGIX experiment, the spectrometers have a design resolution for the scattering angle of < 0.9 mrad and a momentum resolution of $\Delta p/p < 10^{-4}$ [Gag18].

The GEM detectors will cover an active area of 1.20 cm $\times$ 0.30 cm, count the electrons and determine their energies. Due to the separation of the amplifying stage and the readout layer, GEM detectors are highly suited for experiments with high readout rates, like MAGIX aiming for a luminosity of 10^{35} cm^{-2}s^{-1}. The amplifying stage consists of a 50 µm thick polymer foil enclosed with two 5 µm thick copper plates with holes with a diameter and a distance to each other of roughly 70 µm. The two copper plates are applied with voltages of 0.1 kV to 1 kV resulting in high electric field strengths within the holes leading to a multiplication of incoming charged particles in the order of 10^3. The construction of several amplifying stages in a row allows for even higher amplification. After the amplifying stage, the electrons reach the readout layer comprising of a two-dimensional arrangement of electrode wires to determine the position of the electrons.
The main research topics of the MAGIX experiment will focus on high precision measurements which were already described in section 6.1.

6.4 Jet Target MCT-M for MAGIX at MESA

The MAGIX experiment will use two different targets: a jet target and a tube-target. The tube-target is a t-shaped tube made out of mylar foil [Aul14]. The target gas is injected from top in the middle of the tube and flows on both sides out of the target in the scattering chamber. Therefore, this target allows for measurements with polarised gases. In the framework of this thesis the jet target MCT-M was designed, built up, set into operation, and measurements were performed using this target. Therefore, the focus here will be on the jet target.

The MAGIX experiment is aiming for a luminosity of $10^{35}\,\mathrm{cm}^{-2}\mathrm{s}^{-1}$, therefore, the thickness of the jet beam provided by the jet target has to be in the order of $\mathcal{O}\left(10^{19}\,\mathrm{atoms/cm}^2\right)$. With respect to the different research topics MAGIX will cover, different gases have to be used as target material like hydrogen, oxygen, and more. The advantage of the jet target compared to the tube-target is the direct integration of the target beam in the scattering chamber. Therefore, the electron beam directly interacts with the target beam without windows or other possible disturbances in-between. This allows for a minimised background, which is essential for high precision experiments.

Moreover, a catcher system equipped with a powerful pumping station with a pumping speed of $7000\,\mathrm{m}^3/\mathrm{h}$ located opposite to the Laval nozzle with the interaction point in-between is installed to directly pump the target beam away to optimise the vacuum conditions. The catcher system will be designed and constructed by S. Aulenbacher [Aul18].
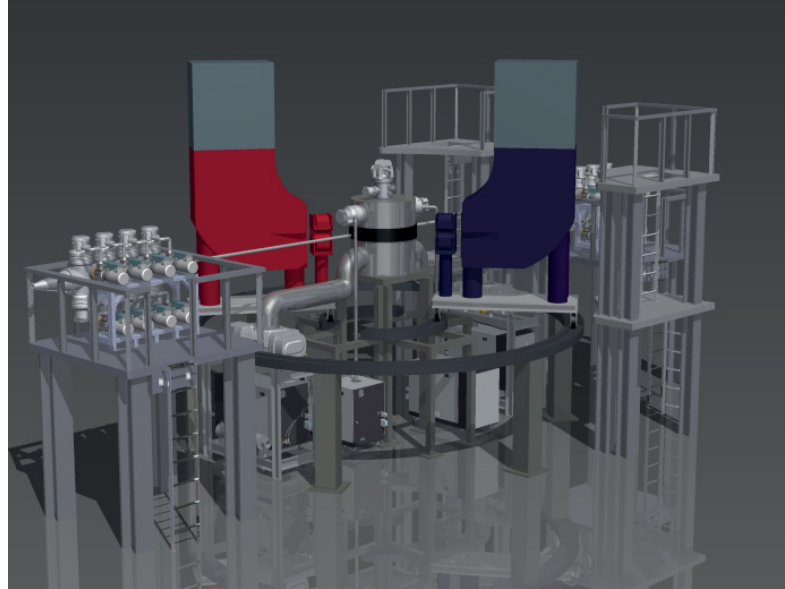

Figure 6.8: Sketch of the future MAGIX experiment. The scattering chamber with the jet target on top is placed in the center with the target beam direction from top to bottom. Around the interaction point, two moveable spectrometers will be installed (red and blue), each equipped with GEM detectors (gray). The electron beam line is differentially pumped to ensure a suitable vacuum in the accelerator. Thanks to S. Aulenbacher (JGU).

The design of the jet target is based on the already described layout of the Münster cluster-jet target sources. Figure 6.9 shows a CAD drawing of the target and Figure 6.10 a sketch of the gas and vacuum system. The inner design was already shown in Fig. 2.5.
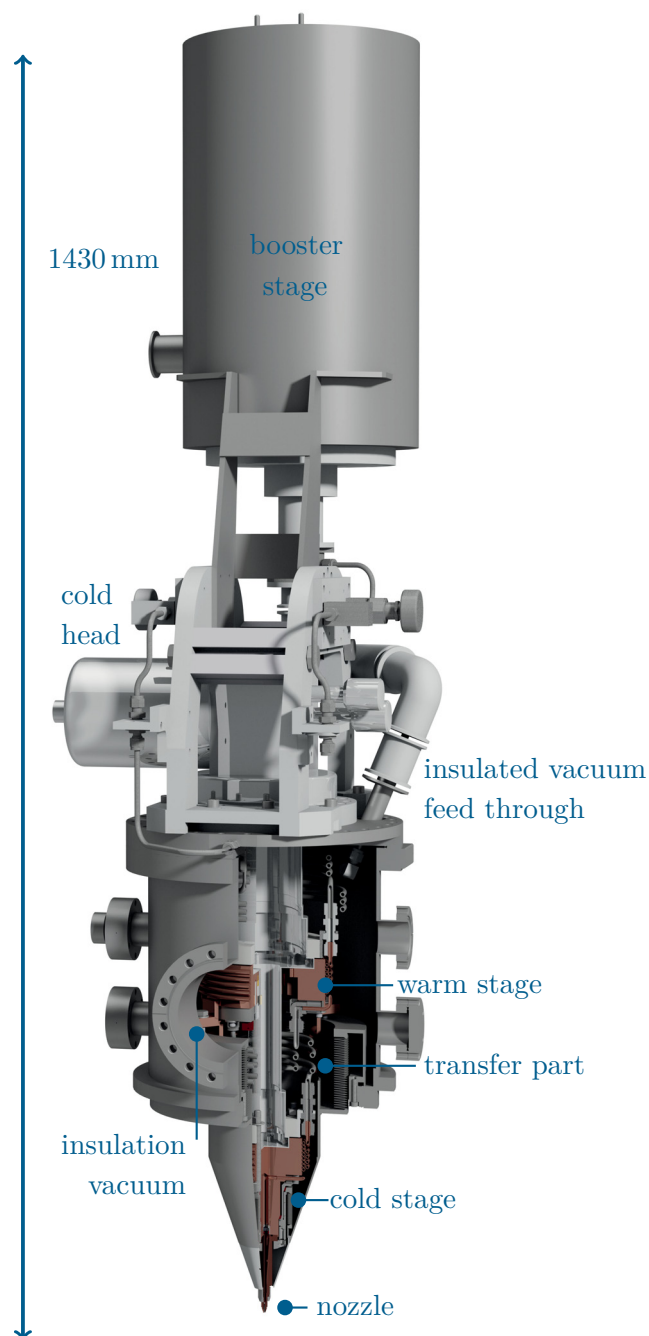

Figure 6.9: Sketch of the jet target MCT-M for the MAGIX experiment. The use of a booster stage in combination with a cold head allows for lowest temperature of roughly 40 K at a gas flow of 40 l/min through the nozzle. A nozzle extension is installed between nozzle and cold stage of the cold head which allows for a conical tip of 20° of the target to ensure a high detector acceptance at MAGIX. Generated by D. Bonaventura, edited.
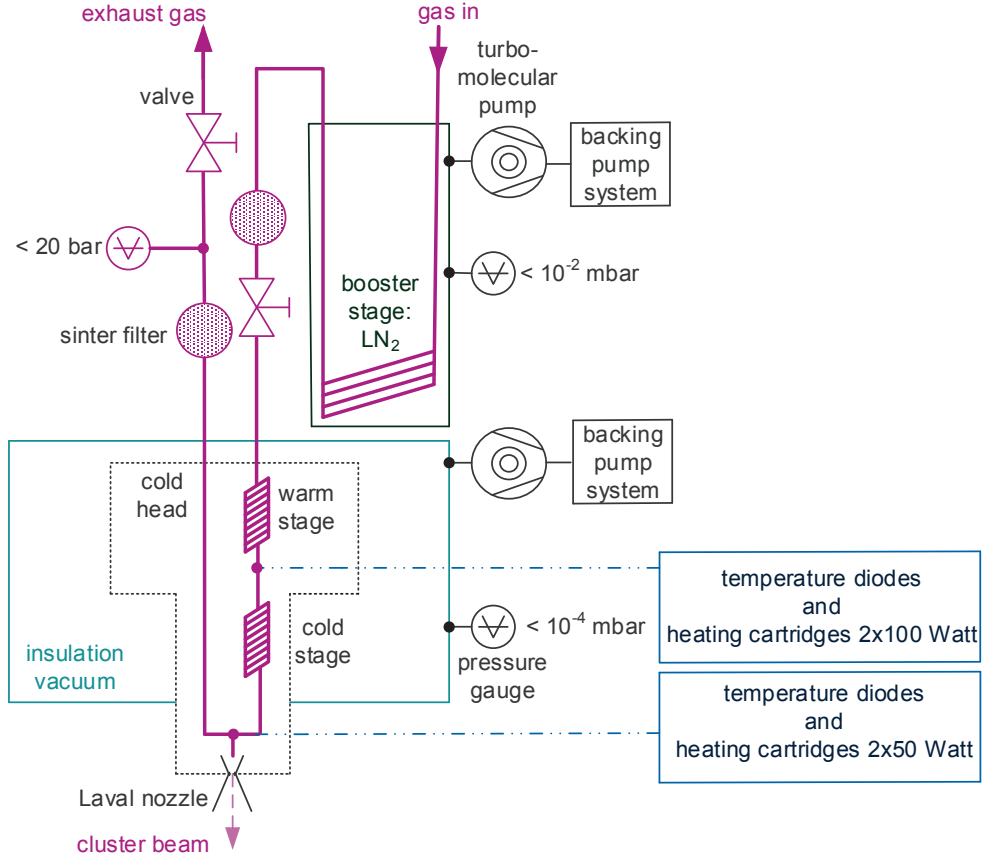
Figure 6.10: Sketch of the gas and vacuum system of the jet target MCT-M.

The main differences compared to other Münster cluster-jet target sources is the tip of the target where the Laval nozzle is located. Due to the later application at the MAGIX experiment in combination with two high resolution magnetic spectrometers, an angle acceptance as high as possible is required. Therefore, a nozzle extension between the Laval nozzle and the cold head was installed to realise a conical tip of $20\,^\circ$ of the target (cf. chapter 3). The use of the nozzle extension together with the use of bellows inside the target leads to an insulation vacuum chamber up to the nozzle area to ensure an optimal insulation between the cryogenic parts of the target and the interaction chamber.

To achieve the design thickness of $10^{19}\,\text{atoms/cm}^2$ a gas flow of $40\,\text{l/min}$ through the nozzle has to be realised (cf. Eq. (5.2) - (5.4)). Details on the design stagnation conditions and the nozzle design are described in chapter 3 and 7.1. To cool the gas flow down to the necessary lowest temperatures of $40\,\text{K}$ or to even lower temperatures, a booster stage is installed. The booster stage consists of a double walled vessel, filled with $14\,\text{l}$ liquid nitrogen to pre-cool the target gas, with insulation vacuum inside to minimize heat exchange and nitrogen consumption (see Fig. 6.11). The hydrogen gas is directed through windings of copper pipes inside the vessel before entering the cold head. The pre-cooled target gas at a temperature of roughly $77\,\text{K}$ is directed through an insulated pipe by a vacuum feedthrough and then enters the cold head.
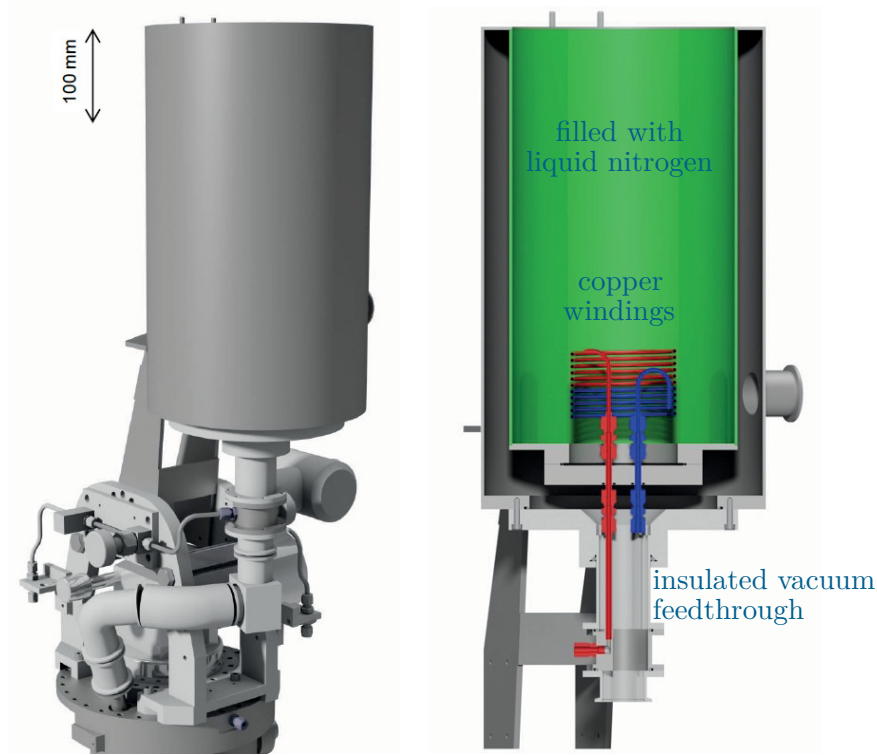
Figure 6.11: Schematic view of the booster stage of the jet target. *Left*: External sight. *Right*: Interior view. The target gas is directed through windings of copper pipes. The double walled vessel is filled with 14 l liquid nitrogen (green). The red pipes indicate the pipes with the target gas at room temperature and the blue pipes the pre-cooled target gas. After the booster stage, the gas enters the cold head through an insulated pipe. Generated by D. Bonaventura, edited.

6.5 A1 Experiment at the MAinz MIcrotron (MAMI)

The infrastructure for the MESA accelerator and the accelerator itself is currently under construction. The jet target MCT-M for the MAGIX experiment, as described in the previous section, is already completed and ready for use. Therefore, the jet target was installed in August 2017 at the conventional electron accelerator MAinz MIcrotron (MAMI) at the University of Mainz to investigate the cluster accelerator beam interaction and to perform first measurements on their interaction.

MAinz MIcrotron (MAMI)

The MAMI accelerator provides a high intensity electron beam with beam energies between 180 MeV and 1.6 GeV and beam currents of 10 pA - 100 μA [K+08a,D+11a,Jan06,HFK+76]. MAMI (Fig. 6.12) possesses two electron sources to provide the electrons. The thermionic source generates currents of 100 μA, whereas, the other source provides polarised electrons using the photoemission from semiconductors induced by a laser [A+97]. The following linear accelerator accelerates the electrons up to energies of 3.97 MeV and injects the electron beam into the first of three race track microtrons (RTMs).
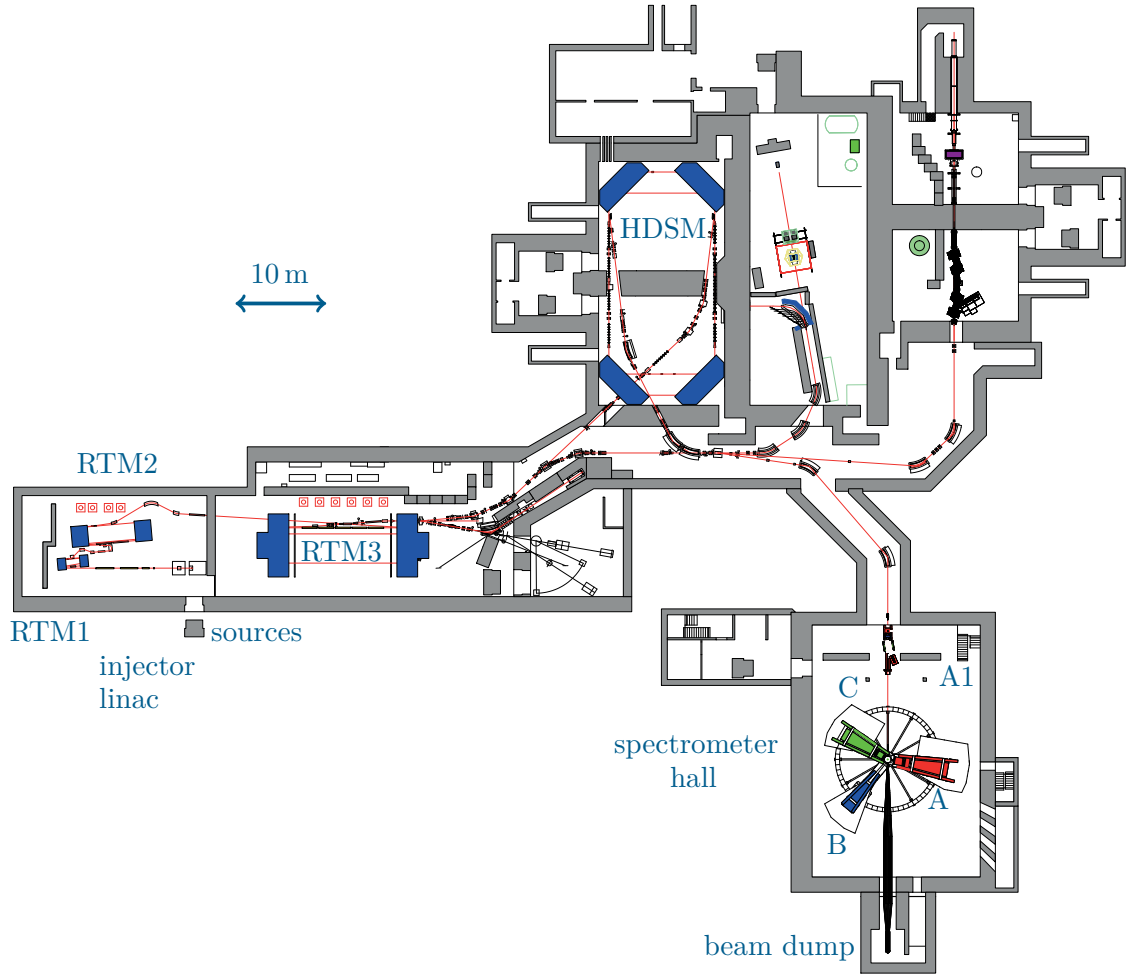
Figure 6.12: Sketch of the electron accelerator MAMI at Mainz. The electron sources provide electrons which are further accelerated by a linear accelerator. Afterwards the eletrons are guided into the first two RTMs (race track microtrons). The electron beam is then either extracted to the experimental halls or directed in the third RTM. The fourth stage, a harmonic double sided microtron (HDSM) allows for energies of up to 1.6 GeV. The measurements performed within this thesis are located at the A1 experimental hall (bottom, right). Thanks to H. Merkel (JGU).

Each RTM consist of an acceleration section and two magnets at the short sides of the RTM to guide the electrons back in the acceleration section. Thus, the electron beam circulates 18 times in the first RTM and leaves it with an energy of 14.86 MeV. After 51 turns in the second RTM, the electron beam carries an energy of 180 MeV. This beam can be extracted and made available at the three possible experiments, skipping the rest of the accelerator. To gain even more energy, the electron beam is guided into the third RTM. There, the electron beam circulates 90 times which results in an energy of 855 MeV. The third RTM offers the possibility to extract the electron beam after every second circulation with the use of a kicker magnet. Hence, the energy is adjustable in steps of 15 MeV.

After passing the three RTMs, the electron beam can be further accelerated with the use of a harmonic double sided microtron (HDSM). The HDSM consists of two acceleration

sections in combination with four magnets to guide the electron beam in the acceleration sections. The electron beam leaves the HDSM after 43 turns with an energy of $1.6\,\text{GeV}$. Within the measurements presented in this thesis, the electron beam circulates 36 times in the third RTM and is then directed in the A1 experimental hall with an energy of $450\,\text{MeV}$.

A1 Experiment

The experimental hall of the A1 collaboration is equipped with three high resolution magnetic spectrometers, named A, B, and C (Fig. 6.13), which make this experiment highly suited for high precision electron scattering experiments. The spectrometers are mounted rotatable around the center to adjust the angle of the spectrometers with respect to the electron beam axis. The spectrometers A and C consist of a quadrupole, a sextupole, and two dipoles magnets. This two spectrometers have an acceptance of roughly $28\,\text{msr}$ and they are ideally suited to measure the momentum and the angle of the scattered particles with high precession. Spectrometer B can be additionally tilted and comprises of a dipole in a clamshell setup with an acceptance of roughly $5.6\,\text{msr}$ with a higher spatial resolution than the other two spectrometers. In the framework of this thesis, spectrometer B was used to measure the scattered electrons under angles between $19\,^\circ$ and $33\,^\circ$. Thereby, the spectrometer has to be adjusted in-between the different measurements. Spectrometer A was used to measure the luminosity under an angle of $42\,^\circ$ and spectrometer C was not used. Table 6.1 lists the main parameters of the two used spectrometers. Moreover, deflecting magnets installed at the electron beam line before the scattering chamber allow for a periodic change of the electron beam positions and therefore, for a scan of the target beam profile. More details are described in chapter 7.3.

Table 6.1: Characteristics of the two used spectrometers A and B of the A1 experiment at MAMI [Ber10].
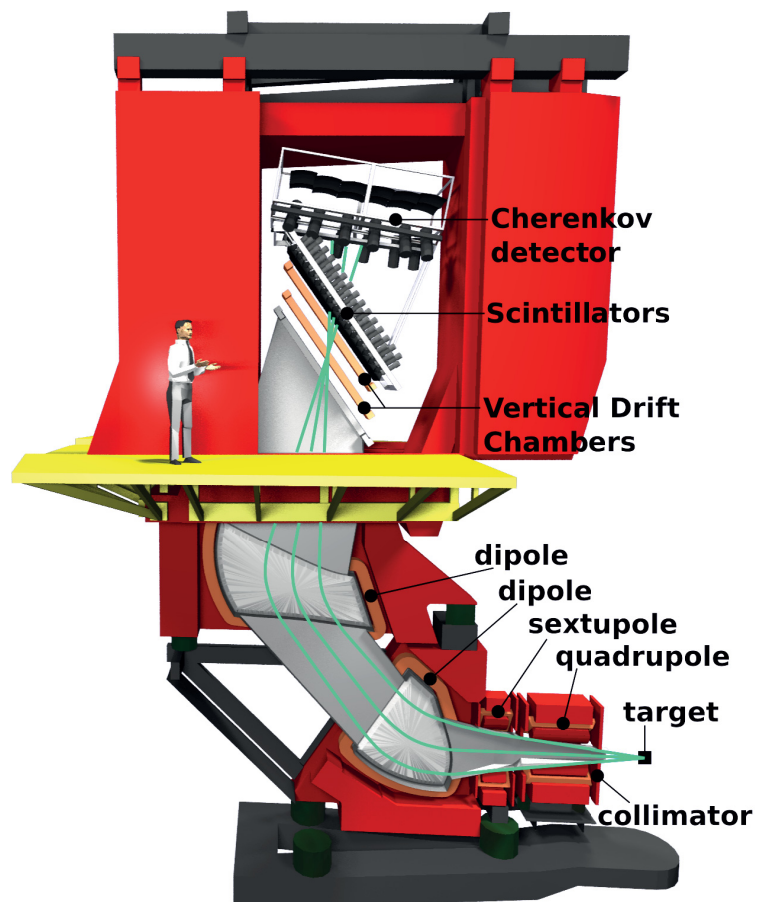
	spectrometer A	spectrometer B
magnet configuration	QSDD	D (clamshell)
maximum momentum	$735\,\text{MeV}/c$	$870\,\text{MeV}/c$
reference momentum	$630\,\text{MeV}/c$	$810\,\text{MeV}/c$
central momentum	$665\,\text{MeV}/c$	$810\,\text{MeV}/c$
maximum solid angle	$28\,\text{msr}$	$5.6\,\text{msr}$
momentum acceptance	$20\,\%$	$15\,\%$
momentum resolution	10^{-4}	10^{-4}
angular resolution at target	$< 3\,\text{mrad}$	$< 3\,\text{mrad}$
position resolution at target	$3\,\text{mm}$ - $5\,\text{mm}$	$1\,\text{mm}$
length of central path	$10.75\,\text{m}$	$12.03\,\text{m}$

Figure 6.13: Photography of the A1 hall with the three spectrometers A (red), B (blue), and C (green). The electron beam direction is from bottom right (red frame) to the gap between spectrometer A and B. The scattering chamber with the jet target will be installed in the center of the three spectrometers. Taken from [Wei03].

The spectrometers A,B, and C are equipped with identically detector systems (cf. Fig. 6.14). The scattered electrons first pass two pairs of vertical drift chambers (VDCs) used for track reconstruction of the particles. Then the particles enter two scintillator planes for particle identification, for a time-of-flight measurement, and for energy loss measurements. Additionally, they are used as a trigger signal. The following Cherenkov detector allows for an distinction between electrons and heavier particles and is therefore used for identification of the electrons.

Figure 6.14: Schematic view of spectroemter A. The scattered electrons enter the spectrometer through the kollimator and the magnets deflect them on the focal plane. Different detectors are used to indetify the particles and to measure their momentum at the interaction point. Thanks to H. Merkel (JGU).

7 Jet Beam Investigations with the MCT-M for MAGIX

The upcoming MAGIX at MESA experiment will consists of a Münster jet target and two high resolution spectrometers to perform high precision low energy physics. MAGIX is aiming for a luminosity of $10^{35}\,\mathrm{cm^{-2}s^{-1}}$ in combination with low intrinsic background. To realise the design luminosity, a target thickness in the order of $\mathcal{O}\left(10^{19}\,\mathrm{atoms/cm^2}\right)$ is required. To ensure this target thickness with a minimal gas load in the scattering chamber, detailed studies on the cluster beam characteristics in dependency of the nozzle geometry and different stagnation conditions were performed which additionally lead to an optimised catcher system opposite to the nozzle to pump the clusters directly away after the interaction with the accelerator beam to ensure good vacuum conditions.

The jet target MCT-M is already operable and was installed at the electron accelerator MAMI in Mainz. There, further investigations on the target thickness were performed using the measured elastic electron-proton cross section.

The presented calculations and the beam studies using the Mach-Zehnder interferometer are published in [G+18].

7.1 Design Stagnation Conditions for the Target

The MAGIX experiment is aiming for a design target thickness of $10^{19}\,\mathrm{atoms/cm^2}$ to reach a luminosity of $10^{35}\,\mathrm{cm^{-2}s^{-1}}$. Calculations were performed using a Laval nozzle with a narrowest inner diameter of $0.5\,\mathrm{mm}$ and an outlet diameter of $1.0\,\mathrm{mm}$ (cf. Fig. 7.1), which allows a target thickness of $5 \times 10^{18}\,\mathrm{atoms/cm^2}$. This target thickness is achievable by different stagnation conditions of hydrogen in front of the nozzle which is shown as a blue line in Figure 7.1. The dotted lines correspond to different gas flows through the nozzle realised by different temperature-pressure pairs of the hydrogen in front of the nozzle. The intersections of the gas flow lines and the thickness line corresponds to the stagnation conditions, which yield a thickness of $5 \times 10^{18}\,\mathrm{atoms/cm^2}$ at given gas flow. To achieve this thickness a high pressure and a high temperature leading to a high gas flow or vice versa, a low pressure and a low temperature resulting in a low gas flow, can be chosen as design stagnation conditions. With respect to the vacuum conditions in the scattering chamber, which has to be as low as possible to reduce background reactions, the gas flow through the nozzle has to be as low as possible. Therefore, the design stagnation conditions are defined at a gas flow of $40\,\mathrm{l_n/min}$ and a temperature of $40\,\mathrm{K}$ to achieve the design target thickness of MAGIX with a minimal gas flow in combination with a reliable and well known cooling system. Another advantage of the lower temperature is the formation of clusters, described by the Hagena formula (cf. Eq.
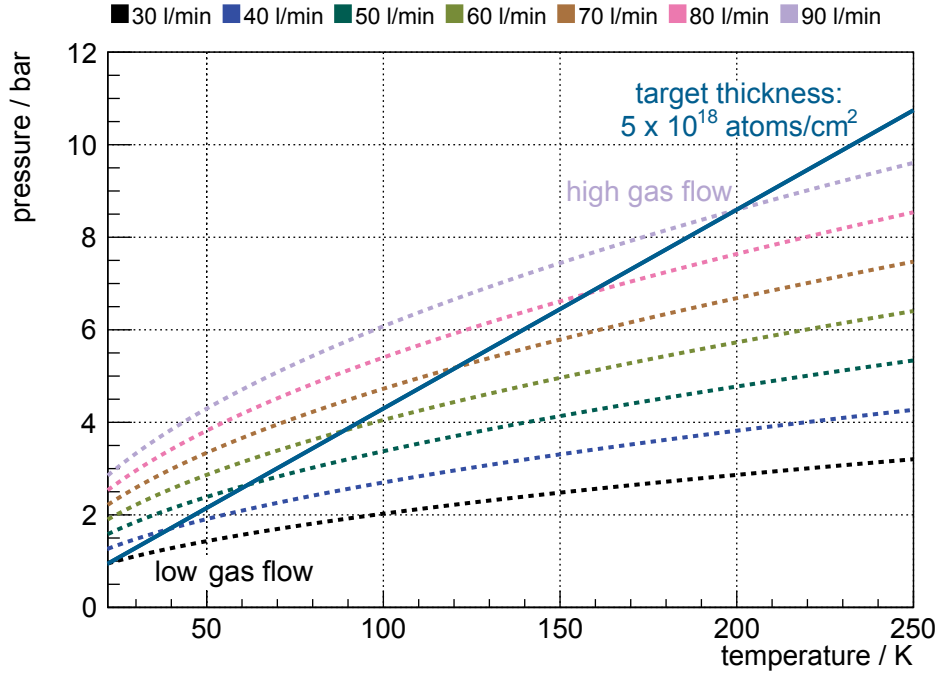
Figure 7.1: The blue line shows a constant target thickness of 5×10^{18} atoms/cm^2 achievable with a nozzle with a narrowest inner diameter of $0.5\,\text{mm}$ and an outlet diameter of $1.0\,\text{mm}$ using different pressure-temperature stagnation conditions of hydrogen in front of the nozzle. The dotted coloured lines present lines with constant gas flows through the nozzle caused by different stagnation conditions of hydrogen. The intersections between the solid and dotted lines show possible design stagnation conditions where the design thickness is achieved. The same thickness can be realised with either a high temperature, pressure, and gas flow, or with a low temperature, pressure, and gas flow. With respect to the vacuum conditions and the formation of clusters, the low temperature, pressure, and flow has been chosen as design stagnation conditions.

(2.8)). The formation of clusters leads to a well defined jet beam with a high range of the target thickness compared to a conventional gas beam. This will be further studied by the use of a Mach-Zehnder interferometer in section 7.2.

The previously presented typical Laval nozzle is not sufficient to achieve the design target thickness. Therefore, a new nozzle geometry is designed. Such a Laval nozzle with the same narrowest inner diameter of $0.5\,\text{mm}$, but with a rectangular outlet of $(0.5 \times 2.0)\,\text{mm}^2$ increases the target thickness for the accelerated electron beam by a factor of two. This nozzle design and other ones are studied later in this section with the use of a Mach-Zehnder interferometer to second the calculations.

To cool down the gas flow of $40\,\text{l/min}$ to the low temperature of $40\,\text{K}$ a two staged cold head is used. This cold head, Leybold 10 MD, was extensively studied in the framework of two previous bachelor theses C. Hargens [Har16] studied the cold head in a test setup and R. Balske [Bal17] investigated the cold head within the final jet target setup. Thereby, an instrinsic heating power for the additionally components, like pipes, are determied to $(11.3 \pm 6.3)\,\text{W}$ at the cold stage with a temperature of $12\,\text{K}$ by comparing his data [Bal17]

with the ones taken by C. Hargens [Har16]. The results of [Bal17] are used for the following calculations of the achievable end temperature of the gas by cooling it with the cold head assuming a gas flow of $40\,l_n/min$. Due to the fact, that the two cooling stages of the cold head do not work independently from each other, the determination has to be done iterative. The available power of the stages are depending on the temperatures of both stages.

The final temperature using the cold head can be calculated as the equilibrium between cooling power of the cold head and the power for cooling down the gas. The power needed for cooling down the gas is given by

$$P = \dot{Q} = \dot{m} \cdot c_p \cdot \Delta T \tag{7.1}$$

with the mass flow $\dot{m}$ itself (Eq. (5.3))

$$\dot{m} = \frac{q_v \cdot M \cdot p_N}{R \cdot T_N} \tag{7.2}$$

and the heat capacity ratio c_p. Here it was assumed that $c_{p_{300\,K}} = 14.31\,kJ/kgK$ is constant in the temperature of interest [L$^+$09a]. This leads to the function

$$T\left(T_{initial}, \dot{Q}, q_v\right) = T_{initial} - \frac{\dot{Q} \cdot R \cdot T_N}{c_p \cdot q_v \cdot M \cdot p_N}. \tag{7.3}$$

Assuming a hydrogen gas flow of $40\,l_n/min$ and a gas temperature of $293\,K$ at the first stage of the cold head a temperature of $(141.6 \pm 2.9)\,K$ with a heating power of $(129.4 \pm 2.8)\,W$ is achieved. The cooled gas is guided to the second stage of the cold head under the assumption that the temperature does not change in between. The gas then leaves the second stage of the cold head with a temperature of $(109.8 \pm 2.1)\,K$ with a heating power of $(27.3 \pm 0.4)\,W$. This calculation shows, that the cold head does not achieve the design temperature of $40\,K$. A corresponding performed measurement leads to temperatures of $(127.0 \pm 0.1)\,K$ at the warm stage and $(95.0 \pm 0.1)\,K$ at the cold stage. The discrepancy between measurement and calculation is due to the assumption of a constant c_p (cf. Eq. (7.3)) and the extrapolation of the measured data in the temperature range between $11\,K$ and $113\,K$ to temperatures up to $293\,K$.

Therefore, calculations were performed using a booster stage filled with liquid nitrogen to cool down the gas to temperatures of $77\,K$ before entering the cold head. Measurements performed in parallel with a preliminary booster stage to second the calculations, showed that the hydrogen gas enters the cold head with a temperature of $(126.0 \pm 0.1)\,K$. Therefore, this temperature was assumed as initial temperature, to compare the calculations with the measurements. The final temperature was calculated to $(53.6 \pm 1.2)\,K$ with a heating power of $(61.9 \pm 1.4)\,W$ at the warm stage and $(31.9 \pm 0.7)\,K$ with a heating power of $(18.6 \pm 0.5)\,W$ at the cold stage. The measurement with additional booster stage results in a temperature of $(51.0 \pm 0.1)\,K$ at the warm stage and $(41.0 \pm 0.1)\,K$ at the cold stage which is in very good agreement with the calculations.

As a result, a final booster stage to pre-cool the gas before entering the cold head was

designed and installed at the jet target MCT-M. The following operation of the target showed, that the design conditions are realisable with this design.

7.2 Jet Beam Studies using a Mach-Zehnder Interferometer

To ensure that the produced Laval nozzles (cf. section 3.3) fulfil the design target thickness conditions and to optimise the catcher system with respect to the size and shape of the jet beam of distance from the nozzle, a Mach-Zehnder interferometer was built up to investigate the jet beam properties.

An interferometer allows for the visualisation of a cluster or gas-jet beam thickness profile by superimposing two coherent light waves. The initial light wave is divided into two identically sub light waves and these waves pass different but known paths, so that the two waves have a fixed phase relationship in time and space. The superimposition of these two waves leads to an interference pattern. Introducing the object to be investigated in or changing the length of the path of one of the two sub light waves leads to a phase change in the resulting interference pattern. Thereby, the curvatures of surfaces, refraction indices, thicknesses, and much more can be determined [Bom14].

There are different types of interferometers, the most known interferometers, are the Michelson interferometer and the Mach-Zehnder interferometer. Depending on the purpose of the interferometer, every interferometer has its advantages and disadvantages.

The Michelson interferometer is a one-trace interferometer. Thereby, the light beam is divided with a beam splitter into two sub beam. Each of them is directed under $90\,°$ on a mirror and reflected back to the beam splitter. There, the two sub beams superimpose and lead to interference fringes on the screen. This interferometer is primary used to investigate modifications of the geometrical wavelength caused by surface curvature or layer thicknesses.

The Mach-Zehnder interferometer is a dual-trace interferometers which allows for a setup of the interferometer around a jet target, where one of the sub beams passes the jet beam to investigate its properties. In contrast to the Michelson interferometer, the sub beam passes only one times the research object. Therefore, the Mach-Zehnder interferometer is ideally suited to investigate the refraction index of objects. Moreover, the Mach-Zehnder interferometer allows in comparison to the Michelson interferometer for a two-dimensional image of the target beam profile.

The design of a Mach-Zehnder interferometer is displayed in Figure 7.2. Thereby, the laser beam is divided via a beam splitter into two equal sub beams, which travel the same distances. One of them, the reference beam is reflected by a mirror onto a second beam splitter. The other one, the measuring beam, is reflected by a mirror through the research object onto the same beam splitter. There, the two sub beams superimpose and this results in interference fringes on the screen.

The laser beam can be described via an electromagnetic wave with alternating electric and magnetic fields. These fields are perpendicular to the direction of propagation of the
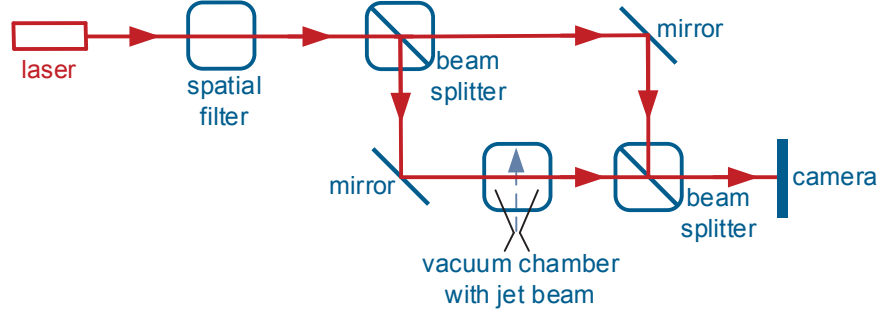
Figure 7.2: Sketch of a Mach-Zehnder interferometer. The optimised and enlarged laser beam is splitted with a beam splitter into two sub beams. One beam, the reference beam is directed by a mirror on a second beam splitter. The second beam is guided by a mirror through the research object and then onto the second beam splitter. There, the two sub beams superimpose and interference fringes can be seen on a screen or recorded with a camera.

laser and to each other. The assumption that the electric $\vec{E}$ and the magnetic $\vec{B}$ fields are in phase leads to a complete description of the light wave by using only the electric field component

$$E\left(\vec{r}\right) = \mid E \mid e^{i\left(\vec{k}\cdot\vec{r}-\omega t+\Phi\right)}. \tag{7.4}$$

Therein, $E\left(\vec{r}\right)$ is the electric field strength at position $\vec{r}$, $\mid E \mid$ the maximal field strength, $\vec{k}$ the wave vector, ω the frequency, and Φ the phase of the wave. This wave is now divided into two sub beams travelling the same path length z with the same propagation time t and then superimposed after at the second beam splitter. A propagation direction of both beams in $\vec{e_z}$ then leads to

$$E_1\left(z,t\right) + E_2\left(z,t\right) = \left(\mid E_1 \mid e^{i\Phi_1} + \mid E_2 \mid e^{i\Phi_2}\right)e^{i(k_z z-\omega t)} = \mid E_{total} \mid e^{i(k_z z-\omega t)}. \tag{7.5}$$

The intensity results in

$$I \propto \mid E_{total}\mid^2 = \left(\mid E_1 \mid e^{i\Phi_1} + \mid E_2 \mid e^{i\Phi_2}\right)\cdot\left(\mid E_1 \mid e^{-i\Phi_1} + \mid E_2 \mid e^{-i\Phi_2}\right) \tag{7.6}$$

$$= \mid E_1 \mid^2 + \mid E_2 \mid^2 + 2\mid E_1 \mid\mid E_2 \mid \cos\Delta\Phi \tag{7.7}$$

$$I = I_1 + I_2 + 2\sqrt{I_1 I_2}\cos\Delta\Phi, \tag{7.8}$$

with $\Delta\Phi = \Phi_1 - \Phi_2$. A maximal constructive interference corresponds to a maximal intensity and occurs for $\cos\Delta\Phi = 1$ or $\Delta\Phi = 0$. In contrast, $\cos\Delta\Phi = -1$ or $\Delta\Phi = \pi$ leads to a destructive interference with minimal intensity.

In the case of the Mach-Zehnder interferometer used in the framework of this thesis, after the laser (helium-neon laser, 633 nm, 2.5 mW) a spatial filter was utilized to adjust and to enlarge the diameter of the laser from 1 mm to approximately 35 mm to ensure a large visible area around and above the jet nozzle. The spatial filter consists of a focussing lens focussing the laser beam. In the focal point a pinhole with a diameter of 15 μm is placed to cut off the the noise of the Gaussian shaped laser beam profile without reducing its intensity. Behind the pinhole a collimating lens defines the laser beam. The
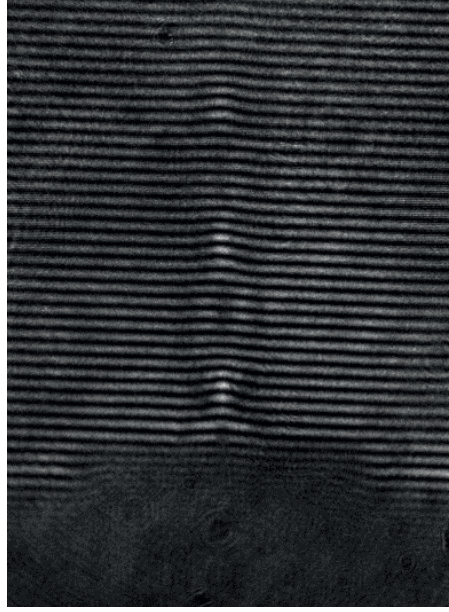
Figure 7.3: A resulting picture showing the interference pattern generated with a Mach-Zehnder interferometer. The dark shadow at the bottom of the picture represents the nozzle. Horizontal parallel interference pattern are visible. Above the the nozzle in the middle of the nozzle exit the effect of the jet beam can be seen as a phase shift in the interference pattern. This picture shows a measurement with nitrogen with a temperature of 292 K and a pressure of 10 bar in front of the nozzle. Picture recorded by [Wes16].

focal length of the collimating lens (10 cm) and its distance to the pinhole determines the enlargement factor of the laser spot. The laser beam is adjusted on the middle of the beam splitters and mirrors with a size of $(50 \times 50 \times 50)$ mm^3 and (50×50) mm^2, to prevent disturbances (reflections, diffraction) in the interference fringes. Furthermore, the optical components should not change the polarisation of the laser, otherwise no interferences can be observed. The components are adjusted so that horizontal parallel interference bands are formed which is realised via a very small tilting angle in vertical direction. The distance of the interference bands to each other and their angle of inclination depends on the superposition angle of the two sub beams. The resulting interference image is recorded with a camera, in first measurements with a CCD camera (pco.pixelfly usb) and later with a CMOS camera (DALSA GENIE NANO-M2590).

A first assembly of the Mach-Zehnder interferometer was performed by C. Westphälinger [Wes16]. The interferometer was mounted on a vibration reducing table and the research object was a nitrogen gas jet at room temperature expanding into air. To produce the gas jet beam, a nozzle with a length of 4.5 mm, an inlet diameter of 4.5 mm, a narrowest inner diameter of 0.5 mm, and an outlet diameter of 1.0 mm was used. A recorded picture with a pressure of 10 bar of the nitrogen in front of the nozzle is shown in Figure 7.3. At the bottom the shadow of the nozzle is clearly visible. Above the nozzle the horizontal parallel interference bands are identifiable and a change in the brightness of the interference fringes over the middle of the nozzle where the gas jet beam is located.

Furthermore, C. Westphälinger [Wes16] compared the theoretical expected gas jet densities with the experimental obtained data. Therefore, a first method to determine the density of the jet beam was presented. The two sub beams, generating the interference fringes, have a fixed phase relationship to each other. This phase relationship changes by introducing a research object in one of the sub beams, which results in a change of the optical path length. This leads to a change in the brightness of the interference bands, which can also be interpreted as a shift of the interference maxima. The distance a between two interference bands corresponds to a shift of λ between the two sub beams. A shift of a of an interference maximum comply with a change of the optical path length ΔL of λ induced by the research object. This change of the optical path length ΔL can be described via

$$\Delta L = (Z(p + \Delta p) - Z(p)) \cdot \lambda = \Delta Z \cdot \lambda, \tag{7.9}$$

with $Z(p)$ a multiple of the distance a at a given pressure p. Furthermore, the optical path length L is defined as the product of the geometrical path length s, i.e. the path length of the light in the research object, and the refraction index depending on the pressure $n(p)$. Thus, ΔL can be additionally expressed by

$$\Delta L = n(p + \Delta p) \cdot s - n(p) \cdot s. \tag{7.10}$$

Both Equations combined lead to

$$(Z(p + \Delta p) - Z(p)) \cdot \frac{\lambda}{s} = n(p + \Delta p) - n(p). \tag{7.11}$$

The refraction index n of gases which is slightly above 1, for visible light, is proportional to the number of moles of the used gas n_{molar} in a volume V:

$$n - 1 \propto \frac{n_{\text{molar}}}{V}. \tag{7.12}$$

Using the ideal gas law $pV = n_{\text{molar}} RT$ leads to

$$n - 1 \propto \frac{n_{\text{molar}}}{V} = \frac{p}{TR} \tag{7.13}$$

with the pressure p, the temperature T, and the universal gas constant R. Introducing a constant of proportionality a results in

$$n = 1 + \frac{a}{TR} \cdot p. \tag{7.14}$$

The deviation Δn assuming a constant temperature leads to

$$\Delta n = \frac{a}{TR} \cdot \Delta p \iff \frac{\Delta n}{\Delta p} = \frac{a}{TR}. \tag{7.15}$$

Therefore, the refraction index in dependence of the gas pressure is described via:

$$n = 1 + \frac{\Delta n}{\Delta p} \cdot p. \tag{7.16}$$

The quotient $\frac{\Delta n}{\Delta p}$ is also given by

$$\frac{\Delta n}{\Delta p} = \frac{n\left(p + \Delta p\right) - n\left(p\right)}{\Delta p} \tag{7.17}$$

Using Equation (7.11) results in

$$\frac{\Delta n}{\Delta p} = \frac{\Delta Z}{\Delta p} \cdot \frac{\lambda}{s}. \tag{7.18}$$

The combination of Equation (7.16) and (7.18) allows for a determination of the refraction index of a gas through the shift of the interference bands ΔZ:

$$n = 1 + \frac{\Delta Z}{\Delta p} \cdot \frac{\lambda}{s} \cdot p. \tag{7.19}$$

The refection index of a gas jet is connected to its volume density ρ_{volume} by the Clausius-Mosotti relation:

$$\frac{n^2 - 1}{n^2 + 2} = \frac{\rho_{\mathrm{volume}}\alpha}{3}, \tag{7.20}$$

with α is the molecular polarizability of the used gas $\left(\alpha_{nitrogen} = 1.71 \cdot 10^{-30}\,\mathrm{m}^3\right)$. With the knowledge of the refraction index n of the gas jet determined by the shift of the interference pattern (Eq. (7.19)) Equation (7.20) allows for the calculation of the volume density ρ_{volume}:

$$\rho_{\mathrm{volume}} = \frac{n^2 - 1}{n^2 + 2}\frac{3}{\alpha}. \tag{7.21}$$

To determine the interference pattern shift, in a first step two projections on the ordinate of a small abscissa area of the interference fringes next to the jet beam were made. There, no shift due to the jet beam occurs and the average maximum positions of these two projections lead to the positions of the interference patterns unaffected from the jet beam. The projections show a periodic oscillation of the brightness due to the alternating minima and maxima of the interference pattern. Then, a projection on the ordinate in the abscissa area, where the jet beam is located were performed. Also there the periodic oscillation can be seen and the positions of the maxima of the interference pattern can be extracted. The comparison of the position of the maxima with and without jet beam allows now for the determination of the shift of the interference bands ΔZ. The detailed analysis and determination of the interference pattern shift and the resulting volume density can be found in [Wes16]. Figure 7.3 shows a shift of $\Delta Z = 0.232 \pm 0.066$ leading to a volume density $\rho_{N_{exp}} = (1.51 \pm 0.39) \cdot 10^{25}\,\mathrm{atoms/m}^3$. This is in good agreement with the calculated volume density $\rho_{N_{theo}} = 1.58 \cdot 10^{25}\,\mathrm{atoms/m}^3$ using Equation (5.2) [Wes16]. This previous work showed the possibility to arrange the interferometer around a jet target to investigate the jet beam properties.

The cluster-jet target for the MAGIX experiment was successfully assembled and set into operation. To allow for beam studies with respect to the target thickness and the shape of the cluster beam a Mach-Zehnder interferometer was built up and these investigations can be used to design an optimum catcher geometry to improve the vacuum conditions

in the later scattering chamber. Moreover, the impact of the stagnation conditions of the gas in front of the nozzle and different nozzle geometries can be studied. In addition, the time development of jet target can be observed by suddenly open the gas flow and thereby taking series of pictures. The Mach-Zehnder interferometer was established on its own aluminium frame around the target to decouple the interferometer from the target to avoid disturbances caused by the vibration of the cold head or the vacuum pumps.

The preliminary presented analysis allows only for the determination of the volume density directly behind the nozzle. To gain more information from the interference pattern, like an image from the gas jet including the target thickness distribution within the beam, an analysis program has been developed [Leß16]. There, a target thickness uncertainty for the analysis of 10 % was determined.

This program utilizes the relation, that the difference of the optical path length ΔL of the two sub beams, by inserting the research object in one of them, can be describes with a phase difference [Leß16, BL16]

$$\Delta \Phi = \frac{2\pi}{\lambda} \int \Delta n \, dz. \tag{7.22}$$

Next to the Clausius-Mosotti relation (Eq. (7.20)), the Gladstone-Dale relation describes the relation between the refraction index of the gas n and the volume density ρ_{volume} [BL16]

$$\frac{\Delta n}{\rho_{\text{volume}}} = \frac{n-1}{\rho_{\text{volume}}} = k_{GD}, \tag{7.23}$$

with k_{GD} being the Gladstone-Dale constant. This means, Equation (7.22) becomes

$$\Delta \Phi = \frac{2\pi k_{GD}}{\lambda} \int \rho_{\text{volume}} \, dz. \tag{7.24}$$

Determining the phase shift $\Delta \Phi$ now allows for a calculation of the volume density ρ_{volume}. According to Equation (5.1) this can be rewritten with the areal target thickness in beam direction

$$\rho_{\text{areal}} = \int \rho_{\text{volume}} (z) \, dz = \frac{\Delta \Phi \lambda}{2\pi k_{GD}} \tag{7.25}$$

This relation is used in the analysis program.

The program loads the recorded picture of the interference pattern and the settings of the Mach-Zehnder interferometer, namely the the laser wavelength $\lambda = 632.8\,\text{nm}$, the atomic mass of the gas to produce the jet beam m, and the Gladstone-Dale constant k_{GD}. Then the program calculates the phase shift out of a picture showing the interference pattern. Therefore, it made a two-dimensional fast Fourier transform (FFT) of a squared region (16×16) pixels around every pixel including three interference pattern.

To determine the phase shift the interference fringe pictures have to be transferred from the space domain to the frequency domain by using the FFT of the pictures

$$F(u,v) = \int\limits_{-\infty}^{+\infty} \int\limits_{-\infty}^{+\infty} f(x,y) \, e^{-i2\pi(ux+vy)} \, \mathrm{d}x\mathrm{d}y. \tag{7.26}$$
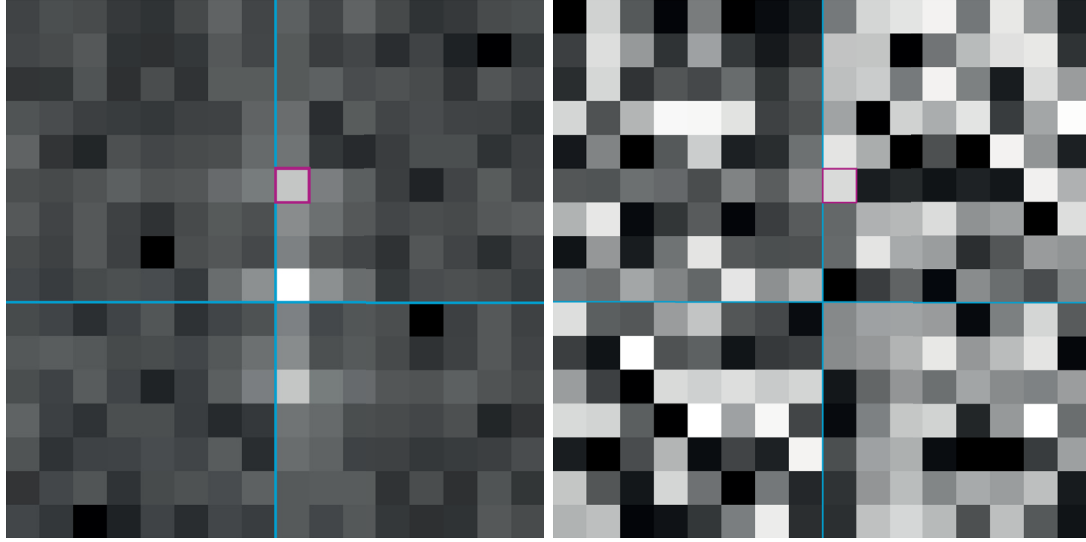
Figure 7.4: Magnitude (*left*) and phase (*right*) image exemplary for one pixel calculated from the FFT. The carrier frequency and the corresponding phase is marked with a violet square. The blue lines indicate the ordinate and the abscissa with the beam origin located at their intersection.

The magnitudes M_ω and phases Φ_ω can be determined using the Fourier Transformation $F(\omega)$

$$M_\omega = \sqrt{\text{Re}\left(F\left(\omega\right)\right)^2 + \text{Im}\left(F\left(\omega\right)\right)^2} \tag{7.27}$$

and

$$\Phi_\omega = \arctan\left(\frac{\text{Im}\left(F\left(\omega\right)\right)}{\text{Re}\left(F\left(\omega\right)\right)}\right). \tag{7.28}$$

Therein, $\text{Re}\left(F\left(\omega\right)\right)$ corresponds to the real part and $\text{Im}\left(F\left(\omega\right)\right)$ to the imaginary part of the Fourier Transformation $F(\omega)$. In the program, the magnitude and the phase are used. In the case of a discrete two-dimensional function $f(i,j)$ the Fourier Transformation $F(k,l)$ is used:

$$F(k,l) = \sum_{i=0}^{N-1}\sum_{j=0}^{N-1} f(i,j)\, e^{-i2\pi\left(\frac{ki}{N}+\frac{lj}{N}\right)}. \tag{7.29}$$

Utilizing this relation, the magnitudes and the phases of the squared regions of the interference picture are calculated, exemplarily shown for one pixel in Figure 7.4. In the magnitude picture, showing the effect of every frequency in two dimensions, the carrier frequency is determined (Fig. 7.4, left). This is the frequency of the interference pattern without the gas jet. The carrier frequency is found as the brightest spot in y direction ignoring the origin in the middle. Thereupon, the phase at the position of the carrier frequency (Fig. 7.4, right) is specified as the phase of the pixel in the center of the squared region. This is done for each pixel of the picture except the pixels at the edges, where is no possibility to realise the squared region around the pixel.

For each row the phase is plotted against the abscissa position. Due to the fact, that the phase can only be between 0 and 2π it shows a (approximately) sawtooth function (Fig. 7.5, left), so it has be transformed to a continuous course. Therefore, the section between
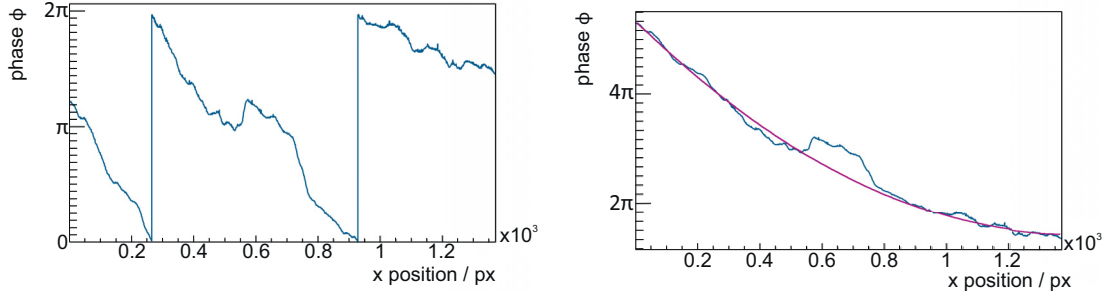
Figure 7.5: Example plot for a row where the phase shift is shown in dependence of the pixel position. The phase shift corresponding to the jet beam can be seen around pixel 600. *Left*: The course resembles a sawtooth function due to the fact, that the phase can only assume values ranging from 0 to 2π. *Right*: The continuous phases in dependence of the pixel position. The violet adaptation on the first 2/7 and the last 2/7 pixels represents the reference phase.

minimum and maximum is raised to the height of the maximum in front of the minimum (Fig. 7.5, right).

The phases without a gas jet beam have to be a constant value. However, because of a slightly not precise alignment of the horizontal interference pattern, it may has a polynomial course. Thus, an adaptation on the phase not showing the effect of the gas jet is performed to determine the reference phase. For this adaptation the first 2/7 and the last 2/7 of the pixels for a row are used, because the interferometer is aligned so that the jet beam is in the center of the picture. For each pixel the distance from the determined phase to the reference phase is calculated to be the phase difference $\Delta\Phi$. Thereof, the areal thickness can be determined with Equation (7.25).

A Mach-Zehnder interferometer was built up around the jet target MCT-M to investigate the jet beam characteristics. The information gained from these studies with respect to the target thickness, the shape of the jet beam, and the range of the target thickness allows for an optimised catcher system geometry to ensure good vacuum conditions in the scattering chamber.

The first studied Laval nozzle has a narrowest inner diameter of 0.5 mm and an outlet diameter of 2.0 mm with a permanently divergent outlet zone with a length of 9.0 mm and with an inlet zone of 1.0 mm (cf. section 3.3). This nozzle was mounted in the jet target MCT-M and measurements with nitrogen as target material were performed. The pressure of the nitrogen in front of the nozzle was increased from 1 bar to 20 bar in steps of 1 bar and the temperature was set to 288 K with the jet beam expanding into atmospheric pressure. A CMOS camera, Dalsa Genie Nano M2590, was used to record the Mach-Zehnder images with an exposure time of 87 μs. Figure 7.6 presents the resulting images, analysed with the program previously described, showing the target thickness profile. The not visible nozzle is located beneath the image and the jet beam is leaving the nozzle at the center. The beam direction is from bottom to top, as in every picture shown in the framework of the Mach-Zehnder interferometer pictures. The images with a nitrogen pressure below 9 bar show no significant signal, so the first presented picture was recorded at a pressure of 9 bar in front of the nozzle. The thickness increases with

increasing nitrogen pressure and decreases with increasing distance from the nozzle.

Moreover, the formation of the typically node structure occurs. This structure corresponds to parts of minimal and maximal thicknesses within the jet beam. This node structure is given as [Pau00a]

$$\frac{x_{\mathrm{M}}}{d^*} = 0.67 \cdot \sqrt{\frac{p_0}{p_a}} \tag{7.30}$$

with the distance between the thickness nodes x_{M}, the narrowest point of the nozzle d^*, the pressure of the nitrogen p_0, and the pressure in the vacuum chamber $p_a = 1.013\,\mathrm{mbar}$. The nodes are generated by the reflection of the jet beam at the free-jet boundary conditions and is compressed to a minimal cross-sectional, the Mach disk shock. The distances between the nodes decrease with increasing distance to the nozzle, because of the interaction between jet beam and residual gas. The first node is located within the nozzle and not visible in the Mach-Zehnder images. Therefore, as a good approximation, to compare the recorded data with the empirical description, the distance between the two first visible nodes was estimated. Figure 7.7 shows the calculated and estimated distances between the nodes. This analysis was performed for the measurements with a nitrogen pressure above 14 bar, because with lower pressure, no significantly node structure is visible within the Mach-Zehnder images. The uncertainties are given by the estimation of the position of the nodes and the conversion from pixels in millimetre. The data are in agreement with the empirical values. Therefore, the Mach-Zehnder interferometer is highly suited to investigate the jet beam properties.

Another measurement, performed with a CCD camera, pco.pixelfly usb, to record the images, shows the time evolution of the jet beam. A valve in the gas pipe in front of the nozzle was closed. The camera recording was started, then the valve was opened, and the jet beam develops. There, the nitrogen in front of the nozzle was at 20 bar and 288 K. The exposure time was adjusted to 10 µs and the time in between two measurement was roughly 150 µs, determined by the read out time of the camera. Figure 7.8 displays the time evolution of the jet beam, the first three recorded pictures show no signal. Therefore, the first picture taken 450 µs after opening the gas valve is shown, then every recorded picture is shown. After 2.1 ms the beam is completely developed and stays stable.

Further measurements were performed with an evacuated scattering chamber, thus the jet beam thickness profile changes significantly. The vacuum chamber was evacuated with a roots pumping system at highest nitrogen pressure of 20 bar to a pressure of 4 mbar. The nozzle, the target gas, the temperature, and pressure of the nitrogen in front of the nozzle were similar to the previous measurement. The resulting images in Figure 7.9 show the nitrogen jet beam expanding into vacuum. They were recorded with the CMOS camera with an exposure time of 87 µs. A gas jet beam is visible with increasing thickness, i.e., increasing pressure of the nitrogen in front of the nozzle, but the thickness decreases rapidly in lateral direction. This effect is typical for a gas jet beam expanding into vacuum and is caused by the interaction between the jet beam particles and the
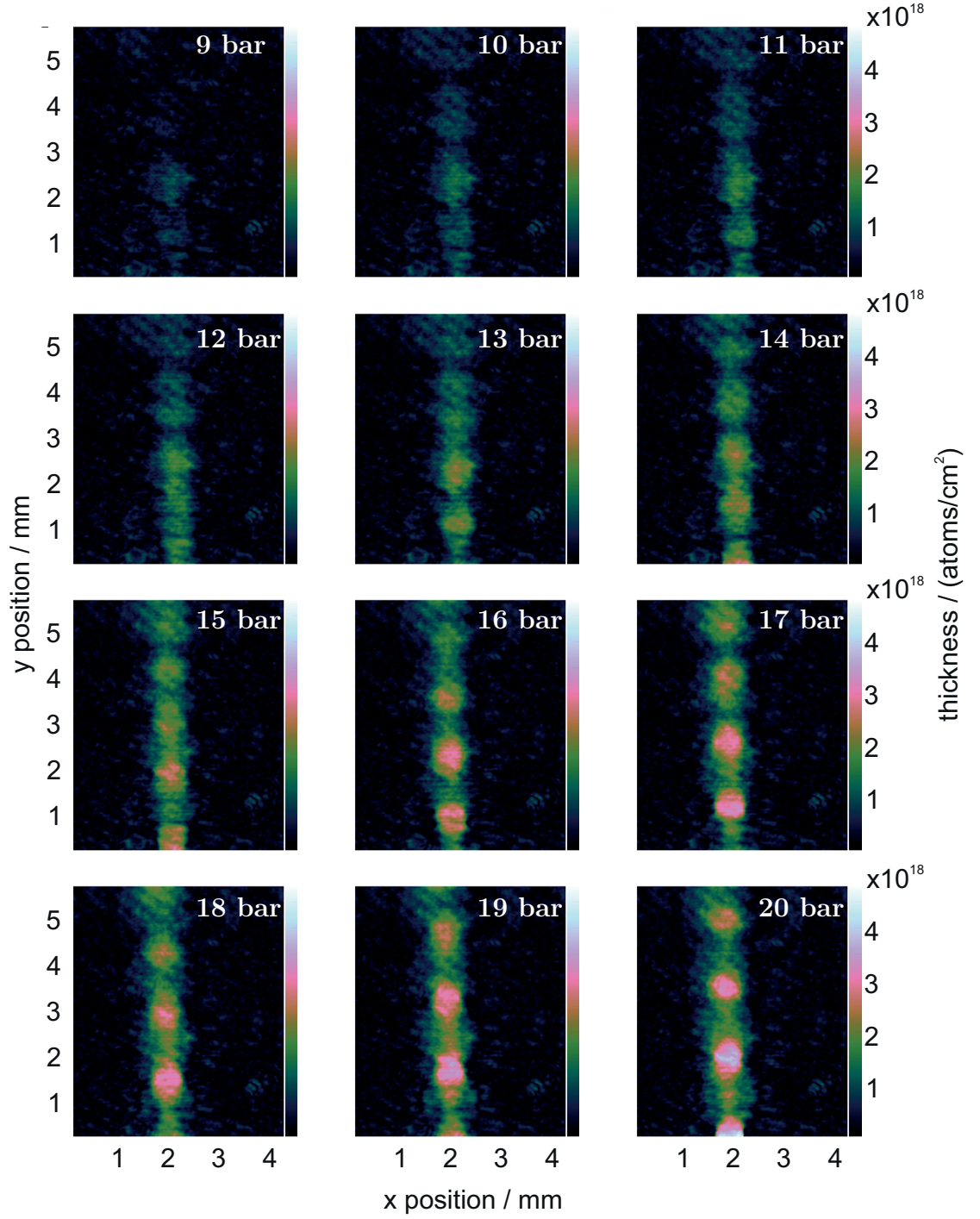
Figure 7.6: Nitrogen jet beam expanding into atmospheric pressure for different pressures in front of the nozzle. The first image was recorded with a nitrogen pressure of 9 bar in front of the nozzle, the following images show an increase of the pressure in 1 bar steps. The target thickness increases with increasing pressure and decreases with increasing distance to the nozzle. Moreover, a typical thickness node structure within the target beam occurs.
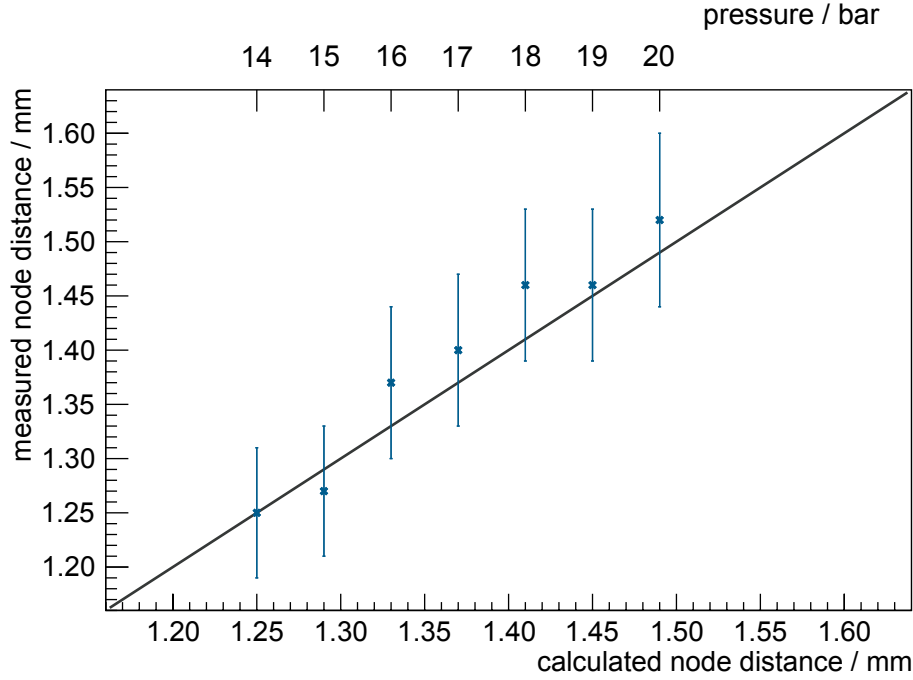
Figure 7.7: Calculated and measured node distances for a nitrogen jet beam with pressure above 14 bar expanding into atmospheric pressure. The line presents an excellent agreement of the data and the empirical description. A higher nitrogen pressure in front of the nozzle leads to a larger distance between the thickness nodes.

residual gas particles with same mass, and by the expansion due to the pressure within the beam. In case of 20 bar, the target thickness does not differ from the residual gas already after a distance of roughly 5 mm to the nozzle.

The maximum target thicknesses were calculated using Equations (5.2) - (5.4) and compared with the maximum thicknesses determined with the Mach-Zehnder images. The results are shown in Figure 7.10 and display a good agreement between data (blue dots) and theory (gray line). However, at higher pressures the data indicates thicknesses systematically above the calculated numbers, which might be caused by a non-uniform thickness distribution over the cross section at the nozzle exit. Such effects might be introduced by surface effects like friction at the inner nozzle wall.

The time evolution of a nitrogen jet beam with 20 bar expanding into vacuum was investigated using the CCD camera with the same settings as before. The first two pictures show no signal and the first picture was taken 300 µs after opening the gas valve. Every second image is shown in Figure 7.11, corresponding to a time of 300 µs between the displayed images. The thickness increases with increasing time and after 2.7 ms the beam is developed and stays stable.
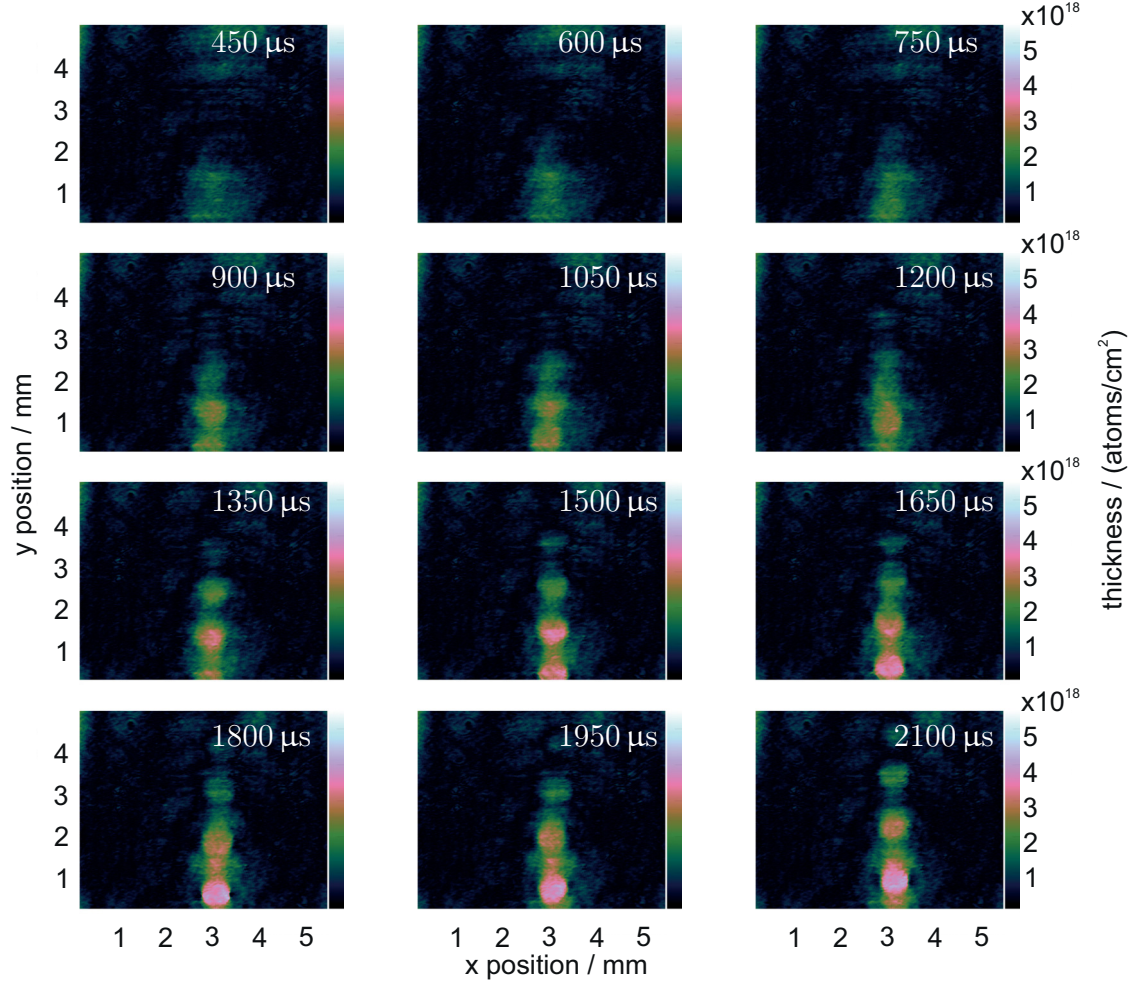
Figure 7.8: Time development of a nitrogen jet beam at 20 bar into atmospheric pressure. The first picture was taken 450 µs after opening the gas valve. The time difference between two pictures is 150 µs. The last picture shows the completely developed jet beam, which is then stable.

For the MAGIX experiment a jet beam whose thickness decreases such rapidly is not suitable. The jet beam will not reach the catcher system and remains in the scattering chamber leading to bad vacuum conditions and high background signals. Therefore, the gas in front of the nozzle is additionally cooled down to a temperature of 40 K resulting in the cluster formation process. A measurement with the previously determined design stagnation conditions with a hydrogen gas flow of $40\,\mathrm{l_n/min}$ and a temperature of 40 K was performed and is shown in Figure 7.12. This measurement and the following measurements were recorded with the CMOS camera with an exposure time of 87 µs. The nozzle is visible as a bright spot between $2.5\,\mathrm{mm} - 4.5\,\mathrm{mm}$. Due to the missing catcher system during the Mach-Zehnder interferometer measurements at the University of Münster and the roots pumping station with limited pumping speed compared to the later pumping system at MAGIX, only a vacuum of 6 mbar was achieved in the scattering chamber. The cluster beam with a diameter of roughly $2\,\mathrm{mm} - 3\,\mathrm{mm}$ is even at larger distances from

147
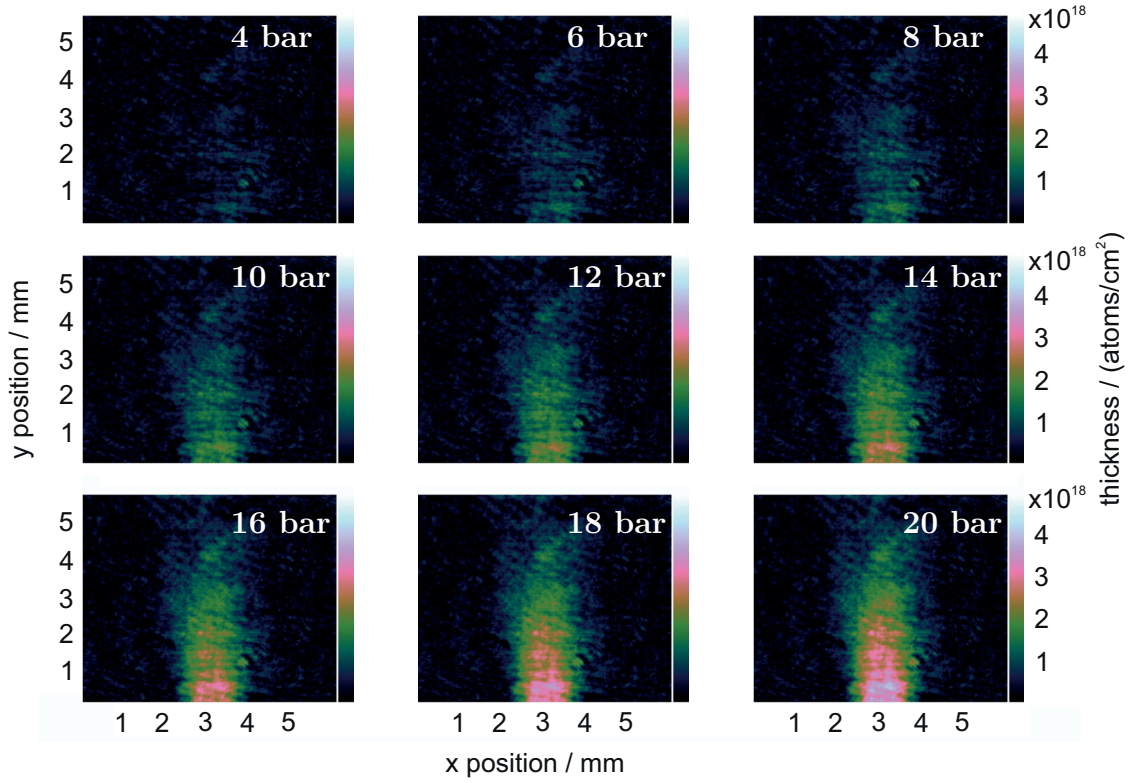
Figure 7.9: Images taken from a nitrogen jet beam expanding into vacuum. The pressure in front of the nozzle was adjusted to 4 bar in the first image and the pressure was increased in steps of 2 bar every picture. The thickness increases with increasing nitrogen pressure, but already after a short distance from the nozzle the thickness does not differ from the residual gas and the jet beam thickness decreases rapidly in lateral direction.

the nozzle of more than 30 mm well defined with high constant thickness, caused by the higher cluster mass compared to the residual gas particles. A maximum target thickness of $(1.6 \pm 0.2) \times 10^{18}$ atoms/cm^2 was achieved, which is in reasonable agreement with the calculated thickness for this nozzle of 2.5×10^{18} atoms/cm^2.

Next to the performed measurements using the Mach-Zehnder interferometer, another nozzle design was investigated. This nozzle has also a narrowest inner diameter of 0.5 mm and an outlet diameter of 2.0 mm, but with a first divergent and then parallel outlet zone at the same nozzle length, to suppress the divergence of the beam and thus increasing the effective target thickness (design idea from S. Aulenbacher, JGU). First measurements with nitrogen at a temperature of 288 K expanding into atmospheric pressure and vacuum were performed. Here, only the pictures recorded at a pressure of 20 bar are shown (Fig. cf. 7.13), the other images are presented in appendix A.3. The results show the same behaviour as recorded with the other nozzle. The expansion into atmospheric pressure results in the formation of a node structure with maximal and minimal thicknesses and the expansion into vacuum to a rapidly increasing jet beam.
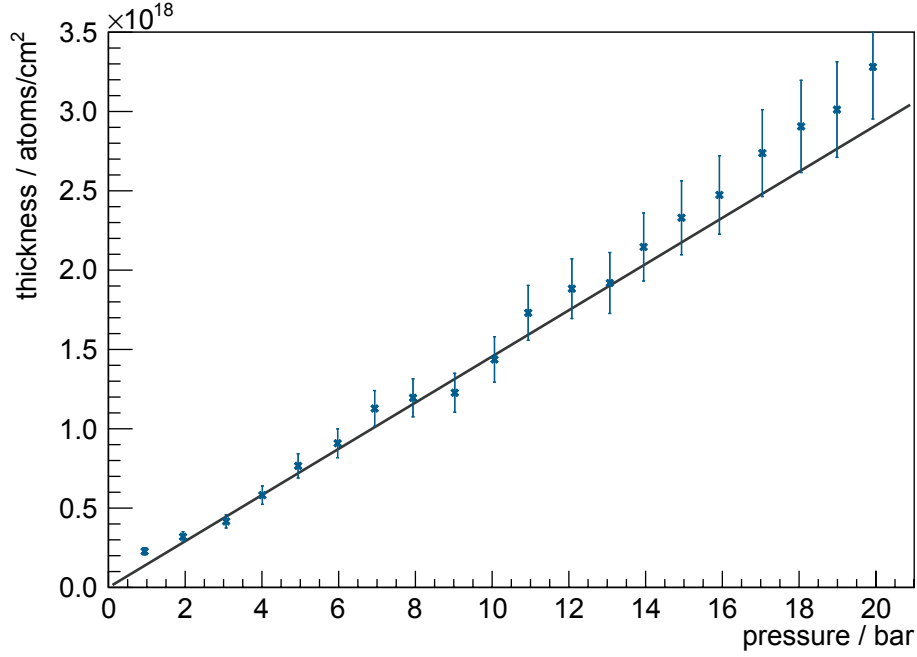
Figure 7.10: Calculated and measured maximum target thickness in dependency of the nitrogen pressure in front of the nozzle. The gray line shows the calculated target thickness and the blue dots presents the measured data which are in good agreement.

The maximum target thickness was also calculated using Equations (5.2) - (5.4) and compared with the previous result and the the maximum thickness determined with the Mach-Zehnder images. The result is shown in Figure 7.14 and even by the observation of a gas jet beam at a temperature of 288 K, the thickness with the parallel outlet zone nozzle (blue) is higher than with the divergent outlet zone nozzle (light blue). Thus, the goal of the idea of the collimation of the target beam due to the geometry of the nozzle is achieved.

Measurements at the design stagnation conditions with hydrogen gas in front of the nozzle are presented in Figure 7.15. There, a well defined cluster beam with a high range of the target thickness is clearly visible. The maximum target thickness was increased to $(2.1 \pm 0.2) \times 10^{18}$ atoms/cm^2, therefore, the idea of the changed nozzle geometry works and results in a higher target thickness, which is also in good agreement with the expected on of 2.5×10^{18} atoms/cm^2.

As calculated the nozzles achieve target thicknesses in the range of the design thickness. Due to the limitations of the final temperature by the used cooling system and the impossibility to increase the gas flow further with respect to the vacuum conditions, a nozzle with a narrowest inner diameter of 0.5 mm and a rectangular outlet of (0.5×2.0) mm^2 was manufactured, so that the electron beam sees the effective target thickness of 10^{19} atoms/cm^2. This and the previous nozzles were produced at the University of Münster, and studied with the Mach-Zehnder interferometer. The expansion
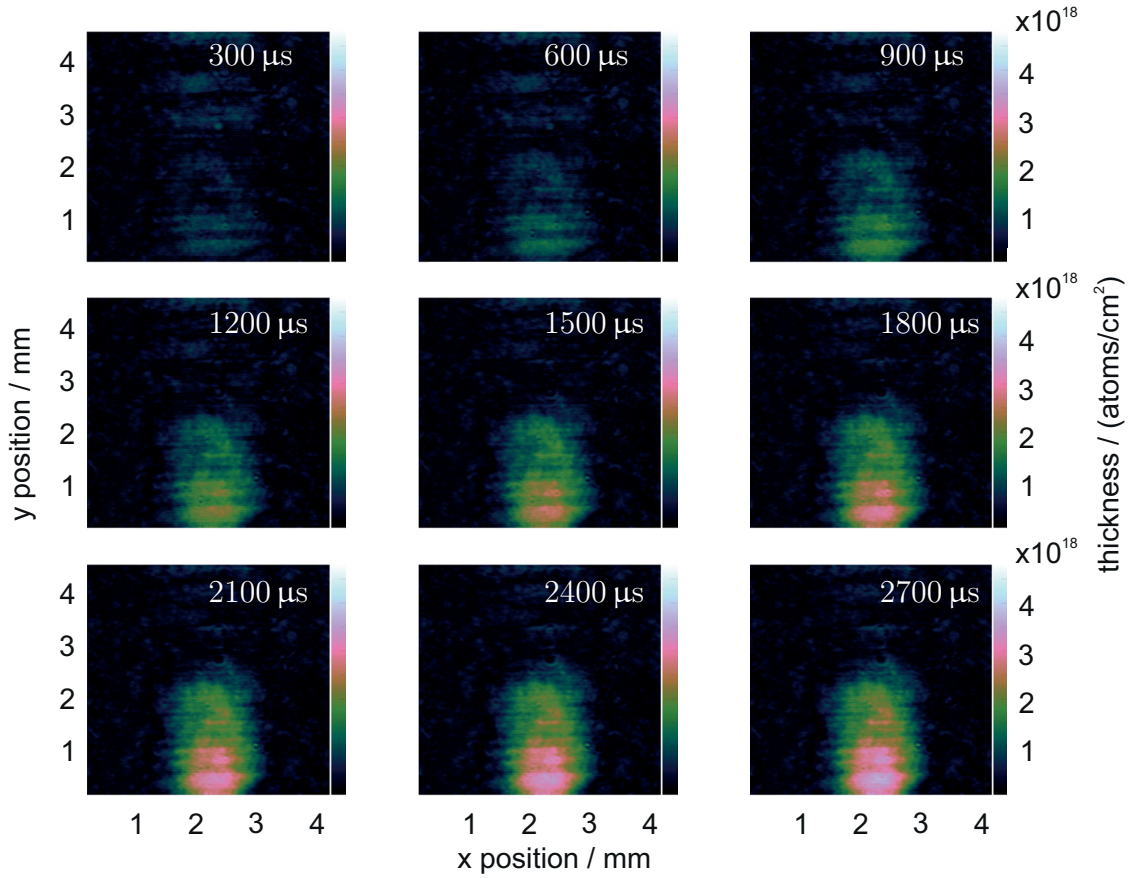
Figure 7.11: Time development of a nitrogen jet beam with 20 bar expanding into vacuum. The first picture was recorded 300 μs after opening the gas valve. Every second recorded picture is shown, because the signal shows only a slight change. The time difference between two presented pictures is 300 μs. The last picture shows the completely developed stable jet beam after 2.7 ms.

of a nitrogen jet beam at a pressure of 20 bar and a temperature of 288 K is shown in Figure 7.16. The measurement investigating the wide side are presented on the left and for the small side on the right. The expansion into atmospheric pressure is displayed on the top and the expansion into vacuum at the bottom. The expansion into atmospheric pressure shows the typical formation of the node structure within the beam. In case of the small side, the thickness within the nodes is extremely high and resulting in a partially defective reconstruction of the thickness. The expansions show a jet beam with decreasing thickness with distance from the nozzle, for the small side even closer to the nozzle. Additional images of the nitrogen jet expanding into atmospheric pressure and vacuum with pressures in between can be found in appendix A.3.

Measurements with the nozzle with rectangular outlet at the design stagnation conditions, i.e. $40\,l_n/min$ and 40 K, are shown in Figure 7.17. The wide side (left) shows a first wide cluster beam which shrinks with distance and then widens again. There, the maximum target thickness was determined to $(2.7 \times 0.3)\,atoms/cm^2$, expected was a thickness of $2.5 \times 10^{18}\,atoms/cm^2$. The small side (right) shows an extremely high intense cluster
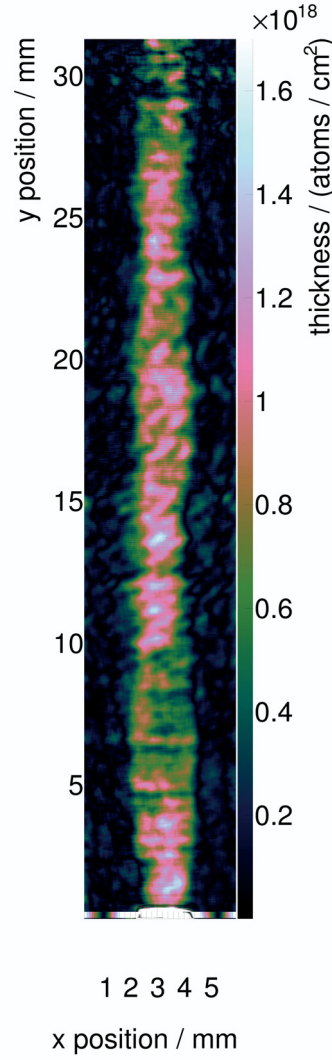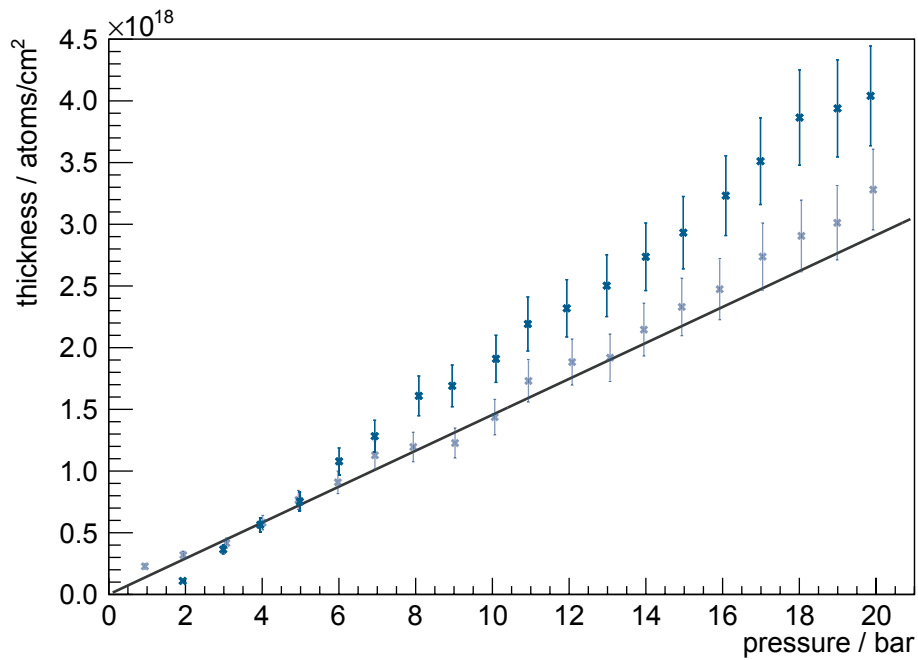
Figure 7.12: Expanding cluster jet beam with a hydrogen gas flow of $40\,\mathrm{l_n/min}$ and a temperature of $40\,\mathrm{K}$. A well defined cluster beam with a maximum target thickness of $(1.6 \pm 0.2) \times 10^{18}\,\mathrm{atoms/cm^2}$ and a diameter of roughly $2\,\mathrm{mm} - 3\,\mathrm{mm}$ is even at large distances of more than $30\,\mathrm{mm}$ clearly visible.

beam with a thickness of $(8.4 \times 0.8)\,\mathrm{atoms/cm^2}$ but which vanishes already after a few millimetre. There, a thickness of $10^{19}\,\mathrm{atoms/cm^2}$ was expected. The performed studies show that there are further investigations necessary on the design of the rectangular nozzle due to the difference in the expected and measured performance. Probably, the missing divergence from the narrowest inner diameter to the small outlet side results in the fast vanishing of the target thickness very recently. The results gained with the Mach-Zehnder interferometer using the different nozzles were also simulated by P. Brand [Bra18] and show a good agreement with the data.
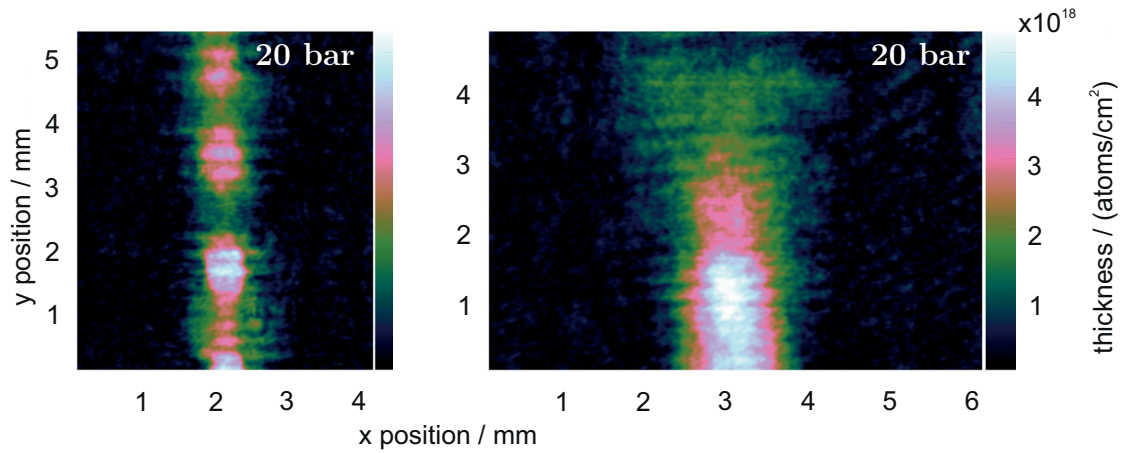
Figure 7.13: Expanding nitrogen jet beam at a pressure of 20 bar. *Left*: Expansion into atmospheric pressure with the formation of thickness nodes. *Right*: Expansion into vacuum with a rapidly decreasing thickness with distance from the nozzle.

Figure 7.14: Calculated and measured maximum target thickness in dependency of the nitrogen pressure in front of the nozzle for both used nozzles. The gray line shows the calculated target thickness. The blue dots display the measurements with the parallel outlet zone nozzle and for comparison the light blue dots show the previous measurement with the divergent outlet zone nozzle. A higher thickness using the parallel outlet zone nozzle can be achieved.
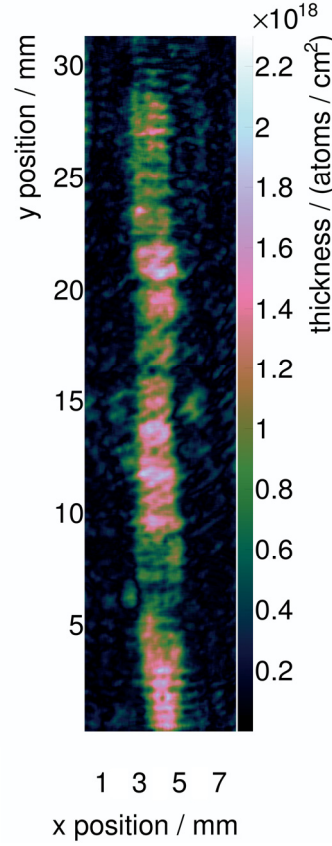
Figure 7.15: Cluster jet beam with a hydrogen gas flow of $40\,\mathrm{l_n/min}$ and a temperature of $40\,\mathrm{K}$ expanding into vacuum. A cluster beam with a maximum target thickness of $(2.1 \pm 0.2) \times 10^{18}\,\mathrm{atoms/cm^2}$ is clearly visible and well defined even at large distances from the nozzle.

7.3 Elastic Electron-Proton Scattering Cross Section Measurements at MAMI

The MESA accelerator with the future MAGIX experiment is currently under construction. Therefore, the already available Münster jet target MCT-M was installed at the electron accelerator MAMI in Mainz. The jet target MCT-M is mounted on the top of the scattering chamber, equipped with two turbomolecular pumps, installed in the MAMI beam line (see Fig. 7.18). The vacuum-tight flexible connection via a bellow between the target and the scattering chamber allows for an adjustment of the target beam with respect to the electron beam, which was in the first setup realised by the use of three thread rods. The catcher opposite to the nozzle is connected to a powerful pumping station with a pumping speed of $7000\,\mathrm{m^3/h}$ consisting of three roots pumps and a fore pump (details can be found in [Aul18]). The scattering chamber has a window made of mylar foil, so that the scattered electrons get almost unaffected into the spectrometers (Fig. 7.19).

After the successful installation and commissioning of the jet target MCT-M at the A1 hall at the MAMI electron accelerator, first beam times were performed. Thereby, first
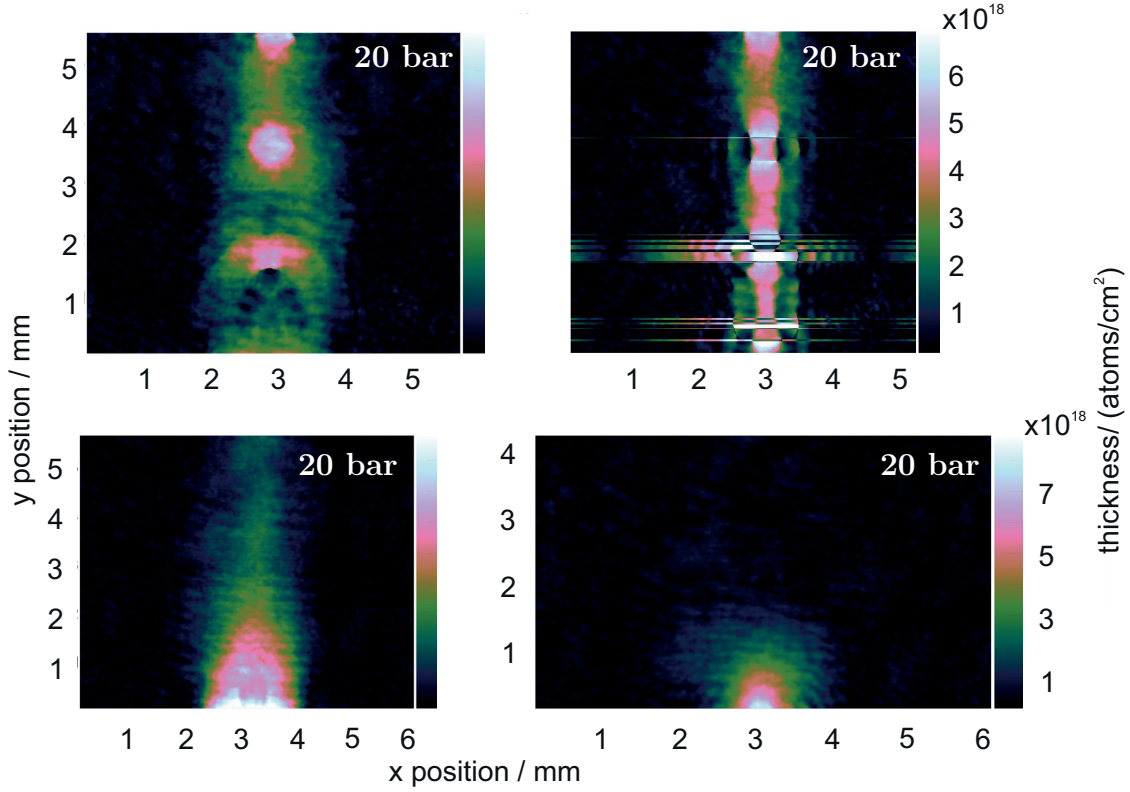
Figure 7.16: Nitrogen jet beams at pressures of 20 bar and temperatures of 288 K using a nozzle with rectangular outlet. *Top, left*: Investigation of the wide side by the expansion into atmospheric pressure. *Top, right*: Expansion into atmospheric pressure studied on the small side. Both pictures shows the typical node structure. The extremely high thickness leads to a partially defective reconstruction of the thickness. *Bottom, left*: Expansion into vacuum, studied is the wide side. *Bottom, right*: Expansion into vacuum with the small side. Jet beams with rapidly decreasing thickness with distance from the nozzle, even stronger for the small side, are visible.

cross sections of the elastic electron-proton scattering were measured and the quality of the data proved the capability of the new experimental setup using a jet target. During the measurements the electron beam had an energy of 450 MeV. Spectrometer B was used to measure the momentum of the scattered electrons and was adjusted between $20°$ and $32°$ in eight settings, with an acceptance of $\pm 1°$ (see Table 7.1). This corresponds to a momentum transfer Q^2 range of $0.022 \, \text{GeV}^2/c^2$ to $0.061 \, \text{GeV}^2/c^2$. Spectrometer A was set to $42°$ and served as a luminosity monitor.

The used jet nozzle had a narrowest inner diameter of 0.5 mm and an outlet diameter of 1.0 mm. A hydrogen flow through the nozzle of $25 \, \text{l}_\text{n}/\text{min}$ was realised leading to a theoretical areal target thickness of $2.8 \times 10^{18} \, \text{atoms/cm}^2$ directly behind the nozzle. The installed catcher opposite to the nozzle to pump the jet beam after the interaction with the electron beam away was designed by S. Aulenbacher [Aul18]. It had an opening circle of 15 mm and was mounted in a distance of roughly 7 mm from the nozzle. With this system, a vacuum of approximatly $3 \times 10^{-1} \, \text{mbar}$ was achieved in the scattering chamber at the flow of $25 \, \text{l}_\text{n}/\text{min}$ through the nozzle. The increase of the vacuum quality due to
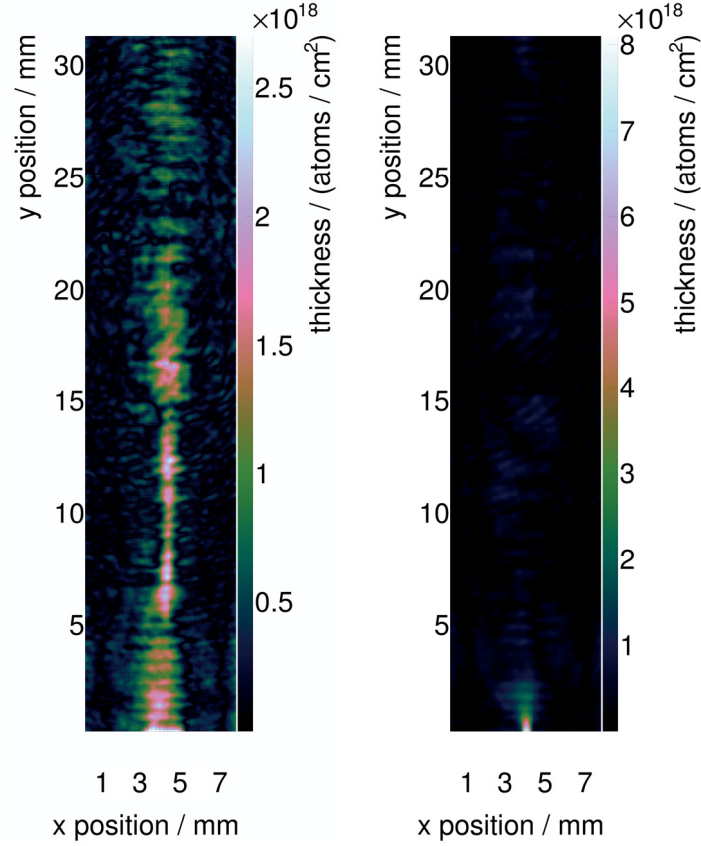
Figure 7.17: Hydrogen cluster beam at the design stagnation conditions expanding into vacuum. *Left*: The wide side leads to a first wide cluster beam, then a smaller beam, followed by an again wide beam. *Right*: The small side results in an extremely high target thickness, but the cluster beam thickness vanishes already after a few millimetre.

the use of an optimised catcher is currently under investigation by S. Aulenbacher [Aul18].

A schematic view of an elastic electron-proton scattering is shown in Fig. 7.20. The incoming electron is described by its four momentum $(E, \overrightarrow{p_1})$ using the natural unit system with $\hbar = 1$ and $c = 1$. After scattering it owns the four momentum $(E', \overrightarrow{p_2})$ in the direction $\Omega = (\theta, \phi)$. The proton of the jet target is at rest $\left(m_{\mathrm{p}}, \overrightarrow{0}\right)$. In case of the presented measurements, neither the target nor the electron beam were polarised. Thus, the elastic electron-proton scattering is isotropic with respect to the angle Φ and consecutively the cross section depends only on the angle Θ.

The energy of the elastically scattered electron $E'(\theta)$ is

$$E'(\theta) = \frac{E}{1 + \frac{E}{m_{\mathrm{p}}}(1 - \cos\theta)}. \tag{7.31}$$

155
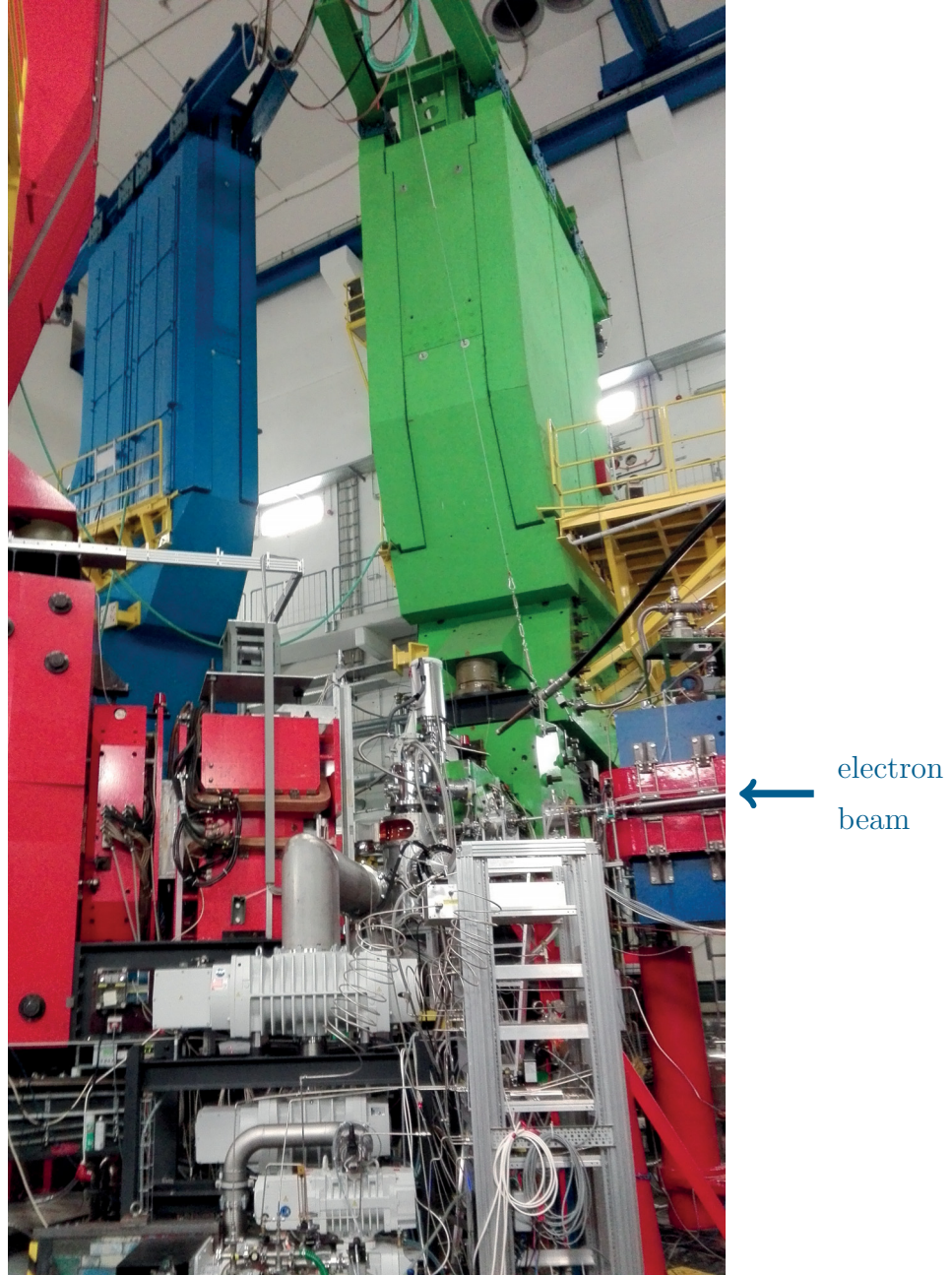
Figure 7.18: The jet target MCT-M installed at the scattering chamber inside the A1 hall at the MAMI electron accelerator. The jet beam direction is from top to bottom and the electron beam direction from right to left. Spectrometer B (blue) was used to measure the momentum of the scattered electrons in a range of $20\,°$ to $32\,°$. Spectrometer A (red) was adjusted to $42\,°$ and served as a luminosity monitor (only the lower part is visible at the left side). Spectrometer C (green) was not used in the presented measurements.

Therein, E is the initial electron energy, m_p the mass of the proton as the interaction partner, and θ the scattering angle. Thereby the momentum transfer Q^2 can be calculated

$$Q^2 = 4EE' \sin^2 \frac{\theta}{2}. \tag{7.32}$$
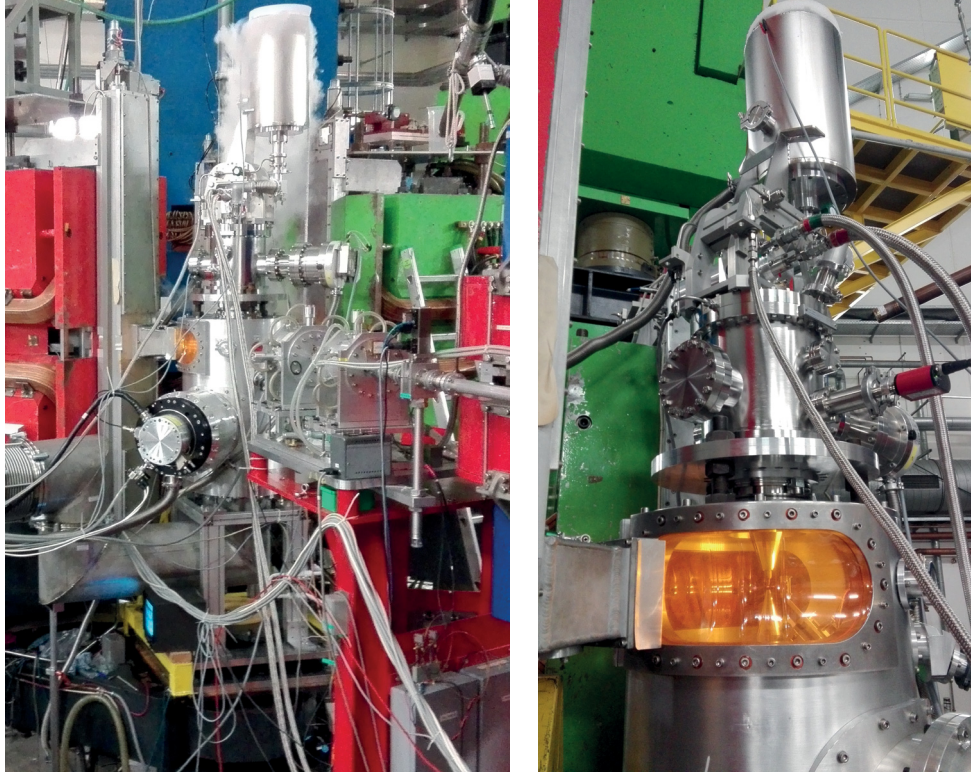
Figure 7.19: Detailed view of the jet target MCT-M installed inside the scattering chamber at the A1 hall of the MAMI electron accelerator. *Left*: The target in operation and the pre-cooling system filled with liquid nitrogen which leads to fog over the target. The mylar window allows for a passage of the scattered electrons into the spectrometer with nearly no energy loss. *Right*: The jet target MCT-M with a view through the window of mylar foil into the chamber. The Laval nozzle on the top is clearly visible and opposite to the nozzle the catcher system. The jet beam direction is from top to bottom. The interaction between jet and electron beam will be directly behind the nozzle.

Table 7.1: The eight settings for the measurements of the elastic scattering cross sections at the A1 hall at the MAMI accelerator. Spectrometer B was adjusted to eight different angles with an acceptance of $\pm 1°$. First the settings with even angles were performed. The angle region at $21°$ was measured to have an overlapping region at low angles where the slope of the cross section is stepper than at larger angles.

central angle of spectrometer B / name of setting	acceptance of spectrometer B
$20°$	$19° - 21°$
$21°$	$20° - 22°$
$22°$	$21° - 23°$
$24°$	$23° - 25°$
$26°$	$25° - 27°$
$28°$	$27° - 29°$
$30°$	$29° - 31°$
$32°$	$31° - 33°$
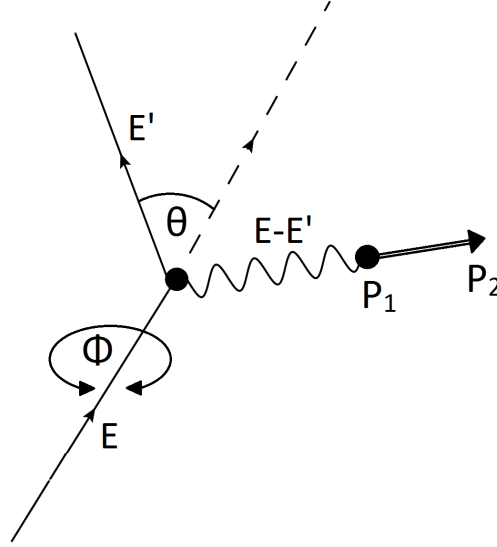
Figure 7.20: Sketch of an elastic electron scattering on a proton. The initial electron has a four momentum of $(E, \overrightarrow{p_1})$ and after the scattering of $(E', \overrightarrow{p_2})$ in the direction $\Omega = (\theta, \phi)$. The proton is at rest $\left(m_{\mathrm{p}}, \overrightarrow{0}\right)$. Based on [Ber10].

The cross section of the elastic electron-proton scattering assuming a one-photon approximation and an internal structure of the proton is given as [B$^+$14]

$$\left(\frac{d\sigma}{d\Omega}\right)_0 = \left(\frac{d\sigma}{d\Omega}\right)_{\mathrm{Mott}} \left(\frac{G_{\mathrm{E}}^2\left(Q^2\right) + \tau G_{\mathrm{M}}^2\left(Q^2\right)}{1 + \tau} + 2\tau G_{\mathrm{M}}^2\left(Q^2\right) \tan^2 \frac{\theta}{2}\right) \tag{7.33}$$

at the the limit of the four momentum transfer $Q^2 \to 0$. Therein, the Mott cross section is given by

$$\left(\frac{d\sigma}{d\Omega}\right)_{\mathrm{Mott}} = \frac{4Z^2\alpha^2 E'^2}{Q^4} \frac{E'}{E} \left(1 - \beta^2 \sin^2 \frac{\theta}{2}\right) \tag{7.34}$$

and the dimensionless value τ as

$$\tau = \frac{Q^2}{4m_{\mathrm{p}}^2}. \tag{7.35}$$

At the limit $Q^2 = 0$ the Fourier transformed of the spatial charge $G_{\mathrm{E}}\left(Q^2\right)$ and of the magnetization $G_{\mathrm{M}}\left(Q^2\right)$ distributions are normalized to the charge and magnetic moment of the proton. Thereby, units of the elementary charge e, the magnetic moment of the proton $\mu_{\mathrm{p}} = 2.7928\,\mu_{\mathrm{N}}$, and the nuclear magneton μ_{N} are used, leading to $G_{\mathrm{E}}\left(0\right) = Q_e/e = 1$ and $G_{\mathrm{M}}\left(0\right) = \mu_{\mathrm{p}}/\mu_{\mathrm{N}} = 2.7928$ [B$^+$14].

The cross section of the measured differential elastic electron-proton scattering is defined as

$$\frac{d\sigma}{d\Omega}\left(\theta\right) = \frac{\int\limits_T \dot{N}\left(\theta\right)\,\mathrm{d}t}{\int\limits_T L\left(T\right)\,\mathrm{d}t \cdot \int\limits_{\Delta\Omega} A\left(\Omega\right)\,\mathrm{d}\Omega}, \tag{7.36}$$

with the event rate $\dot{N}\left(\theta\right)$, the luminosity $L\left(T\right)$, and the acceptance of the spectrometer $A\left(\Omega\right)$.
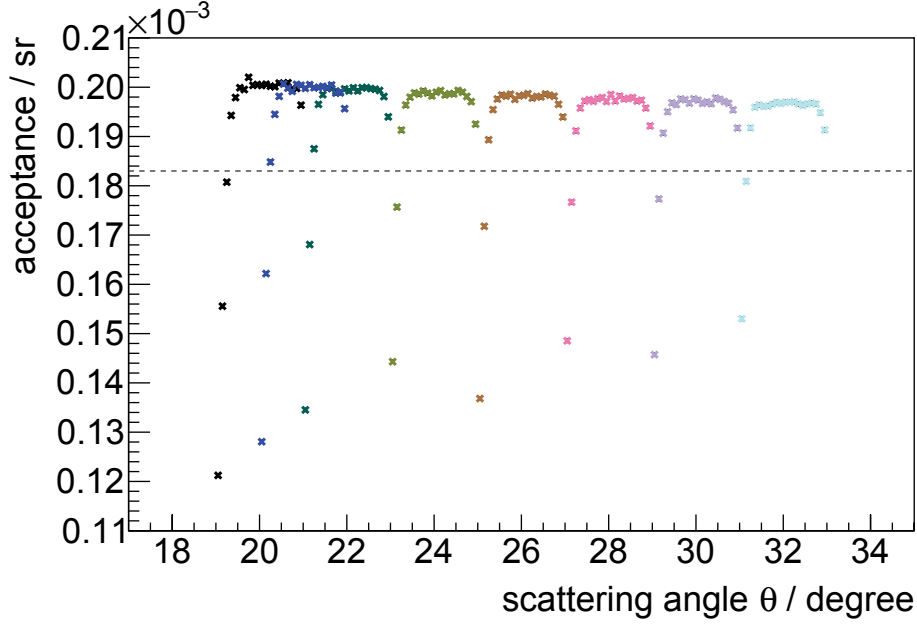
Figure 7.21: Acceptance of the spectrometer B for the eight settings measuring the elastic electron-proton scattering cross section. The acceptance decreases at the edges of low angles. Therefore, a limit of 5 % difference from point-to-point was set to distinguish between data which will be further analysed and data which will be ignored due to their low acceptance. The gray dashed line indicates this limit.

For the analysis of the taken data, the well established A1 collaboration analyse software Cola++ [Mer17b] was used. This program allows to calculate the event rate $\dot{N}(\theta)$, by processing the raw data. This data was extracted and further analysed with self coded C++ programs described in more detail in the following paragraph. The luminosity $L(T)$ was determined using the A1 collaboration software Lumi++ [Mer17b]. To determine the acceptance of the spectrometer $A(\Omega)$ Simul++ [Mer17b] was used to simulate 10 millions events for every of the eight settings including the spectrometer resolution.

The acceptance of the spectrometer B for the eight settings is shown in Fig. 7.21. At the edges to low angles the acceptance decreases and a limit of 5 % difference from point-to-point was set for the measurements which will be included. Data localised above the gray dashed line are further analysed and the data below the gray dashed line are ignored to avoid larger systematic uncertainties due to their low acceptance.

The integrated luminosity L_{int} is defined as

$$L_{\mathrm{int}} = \rho_{\mathrm{areal}} N_e, \tag{7.37}$$

wherein, ρ_{areal} is the areal thickness of the target and N_e the total number of electrons interacting with the target during the measurement time T. The electron number N_e itself is given by

$$N_e = \frac{Q}{e}\frac{1 - \frac{\mu}{100}}{s} \tag{7.38}$$

with e the elementary charge. A Förster probe in the third RTM measures the beam current I and thereof, the charge Q is determined by

$$Q = \int\limits_T I\,\mathrm{d}t\,. \tag{7.39}$$

This charge Q, the dead time μ of the detectors, and the scaling factor s which includes the fact, that not all events are saved, are extracted from the program Lumi++.

To calculate the event rate $\dot{N}(\theta)$ the data processed by Cola++ are extracted and further analysed. Figure 7.22 shows on top the measured scattering angles in dependency of the missing mass of the proton, calculated using the four-momentum of the scattered electron, for the setting at $20\,^\circ$. The scattering angle θ ranges from $16\,^\circ$ to $36\,^\circ$ in steps of $0.01\,^\circ$. For the missing mass, the range was set from $935\,\mathrm{MeV}/c^2$ to $942\,\mathrm{MeV}/c^2$ in steps of $0.01\,\mathrm{MeV}/c^2$. The acceptance for this special setting of the spectrometer B between $19\,^\circ$ - $21\,^\circ$ is clearly visible. The bottom picture depicts the simulation assuming the same setting with no background. Figure 7.23 shows the projection on the ordinate for data (top) and simulations (bottom) of the complete setting. In Fig 7.24 only the projection for the angles between $20.0\,^\circ$ and $20.1\,^\circ$ is shown. This binning was used for the following analysis. At the proton mass of $938.27\,\mathrm{MeV}/c^2$ a missing mass peak is clearly visible. Towards higher masses, a radiative tail in data as well as in simulations is visible due to the higher order radiative corrections. In Figure 7.24 an adaptation describing the background is additionally shown. The adaptation is a constant which was fitted to the data in the mass range below $937\,\mathrm{MeV}/c^2$ and above $941\,\mathrm{MeV}/c^2$. With respect to the radiative tail towards higher masses, the range was chosen unsymmetrical and the peak range was excluded. The adaptation was performed for data and simulations and subtracted from the signal. The event rate $\dot{N}(\theta)$ is calculated as the sum over the bin contents. The two-dimensional histograms and the missing mass plots for data and simulations for the seven other settings are shown in Appendix A.4.

These missing mass peaks show a low background compared to previous data taken with the use of a cell target filled with liquefied target gas [Ber10]. There, the walls of the cell target resulted in a higher background which was now prevented by the use of the new internal target eliminating the possible disturbances between the interaction of the walls and electron beam. The measurement demonstrates the advantages of internal targets and that they are highly suited for high precision experiments, i.e., MAGIX, due to their high background reaction suppression.

In this thesis, the aim was not to calculate the elastic electron-proton cross section, which would have used Spectrometer A to determine the absolute luminosity. The objective was to calculate the target thicknesses for every setting using the known elastic electron-proton
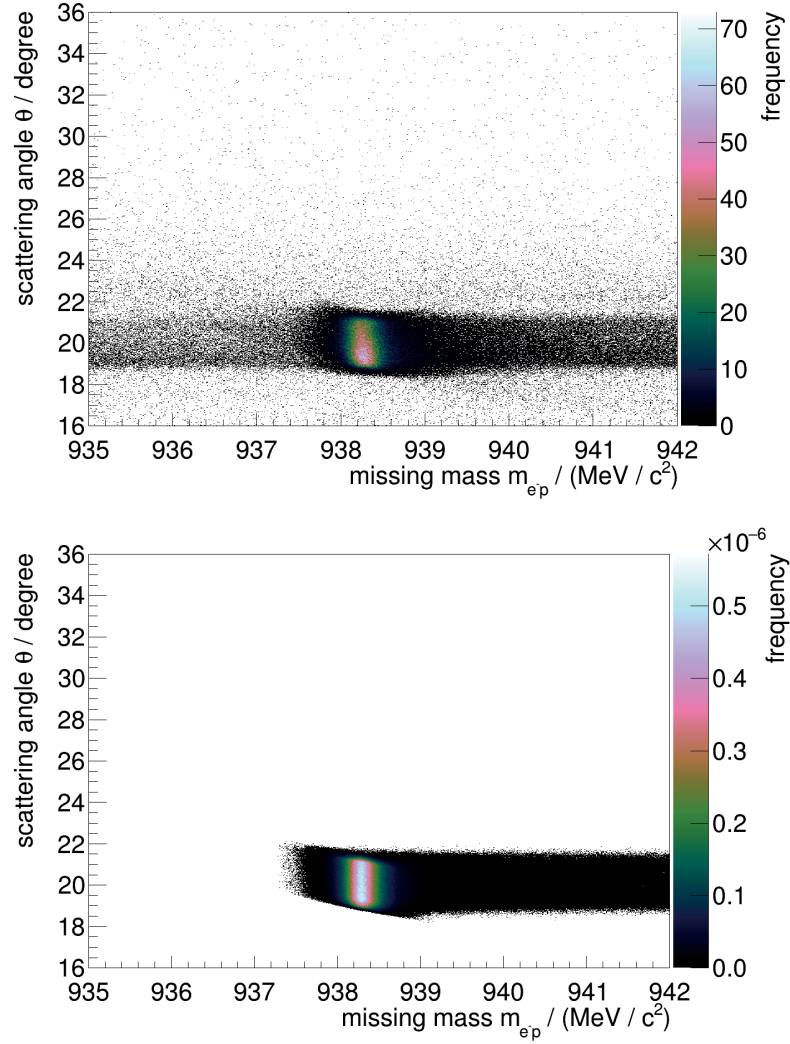
Figure 7.22: Scattering angle θ in dependency of the missing mass of the proton. A signal at the spectrometer B acceptance between $19\,°$ and $21\,°$ for the setting at $20\,°$ and at the proton mass of $938.27\,\mathrm{MeV}/c^2$ for data (*top*) and simulations (*bottom*) is clearly visible.

cross section values.

With Eq. (7.36), Eq. (7.37), the determined event rate, the acceptance, and the number of electrons interacting with the target, and in combination with the known elastic scattering cross sections, the resulting areal target thickness can be determined. The elastic scattering cross section and following analysis was calculated using the theoretical description of the data taken from J. Bernauer [Ber10]. In [Ber10] for a wide angle θ between $19\,°$ and $136\,°$ the cross section was measured and the data are best described using a plain uniform cubic spline function $S^{\mathrm{E,M}}$. The ansatz

$$G^{\mathrm{E,M}}_{\mathrm{spline}}\left(Q^2\right) = 1 + Q^2 S^{\mathrm{E,M}}\left(Q^2\right) \tag{7.40}$$
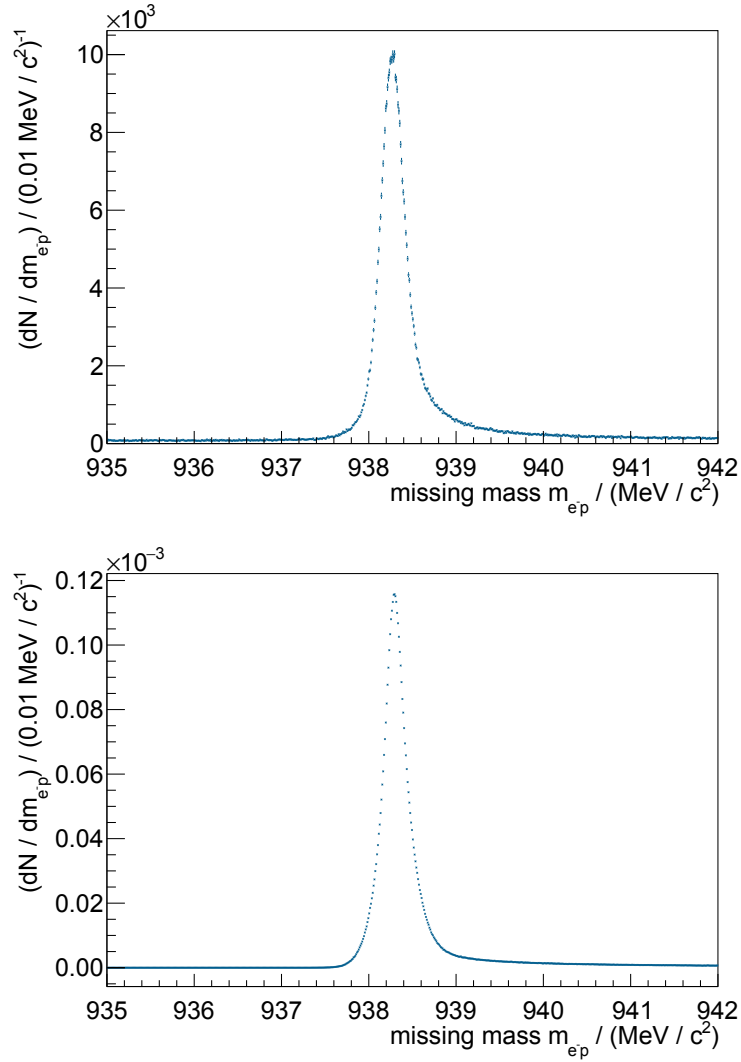
Figure 7.23: Projection on the ordinate of Fig. 7.22. The data (*top*) as well as the simulations (*bottom*) show a clearly visible peak at the proton mass of $938.27\,\mathrm{MeV}/c^2$. Moreover, a slope towards higher masses corresponding to the radiative tail is generated in data and simulations.

in Equation (7.33) is used to fulfil the normalisation constraint. These spline functions are composed of third order polynomials with continuity constraints. The range between two knots i and $i+1$ is given by

$$S_i\left(t\right) = \frac{1}{6}\begin{bmatrix} t^3 & t^2 & t & 1 \end{bmatrix} \begin{bmatrix} -1 & 3 & -3 & 1 \\ 3 & -6 & 3 & 0 \\ -3 & 0 & 3 & 0 \\ 1 & 4 & 1 & 0 \end{bmatrix} \begin{bmatrix} p_{i-1} \\ p_i \\ p_{i+1} \\ p_{i+2} \end{bmatrix}. \tag{7.41}$$
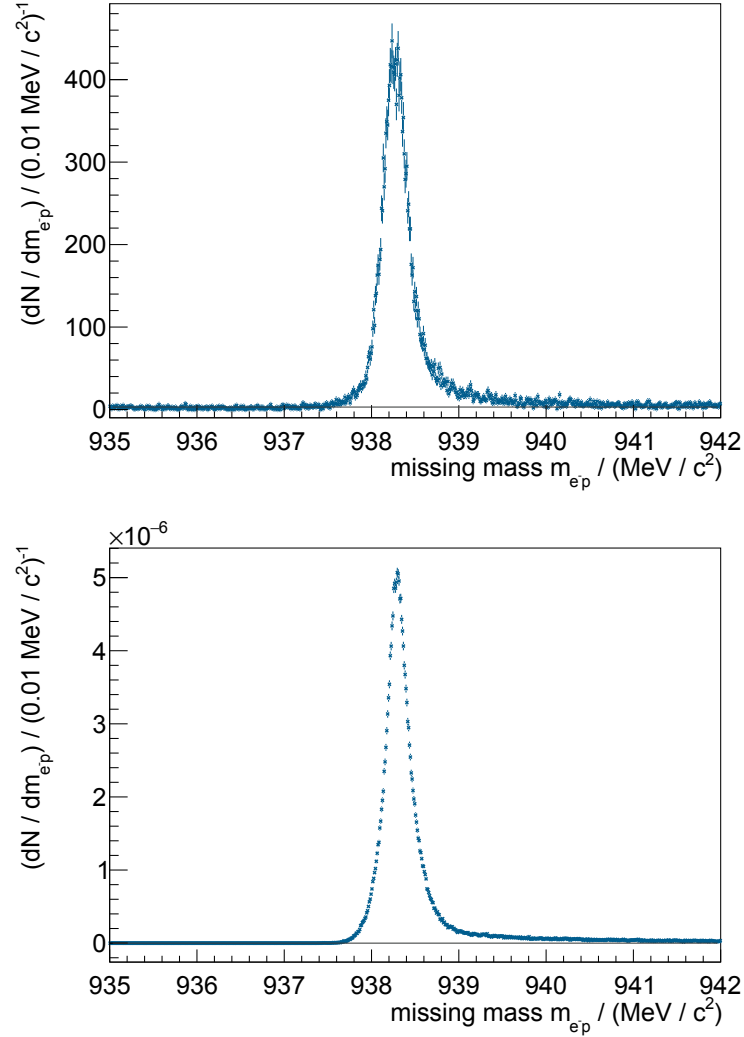
Figure 7.24: Projection on the ordinate of Fig. 7.22 only for the angles between $20.0\,°$ and $20.1\,°$ for data (*top*) and simulations (*bottom*). The background is described with a constant adaptation to the signal below $937\,\mathrm{MeV}/c^2$ and above $941\,\mathrm{MeV}/c^2$ with respect to the radiative tail towards higher masses. The adaptation was made for data and simulation and subtracted from the signal.

Therein, the positions between two knots Q_i^2 and Q_{i+1}^2 is determined by t between 0 and 1

$$t = \frac{Q^2 - Q_i^2}{Q_{i+1}^2 - Q_i^2}. \tag{7.42}$$

In the Q^2 range between $0\,\mathrm{GeV}/c^2$ and $1\,\mathrm{GeV}/c^2$ the spline model has knots at every $0.2\,\mathrm{GeV}/c^2$ resulting in 8 parameters. In the framework of this thesis for a Q^2 range of $0.022\,\mathrm{GeV}^2/c^2$ to $0.061\,\mathrm{GeV}^2/c^2$ measurements were performed, only 2 knots occur, resulting in 4 parameters for the spline model, because the number of parameters $k + 2$ are given by the number of knots k. Table 7.2 lists the relevant and used parameters.

Table 7.2: Spline parameters used for the eleastic electron-proton scattering cross section description [Ber10].

i	p_i^{E}	p_i^{M}
-1	-6.31651	-2.08450
0	-2.83182	-2.80421
1	-1.97181	-1.91391
2	-1.48803	-1.43427

Table 7.3: Target thickness based upon the scaling to the theoretical cross section. They are constant within the uncertainties for the different eight settings. Furthermore, they agree with the theoretical expected target thickness of 2.8×10^{18} atoms/cm^2 directly behind the nozzle.

setting / $^\circ$	areal target thickness / (atoms/cm^2)
20	$(1.15 \pm 0.01) \times 10^{18}$
21	$(1.19 \pm 0.01) \times 10^{18}$
22	$(1.11 \pm 0.01) \times 10^{18}$
24	$(1.10 \pm 0.01) \times 10^{18}$
26	$(1.20 \pm 0.01) \times 10^{18}$
28	$(1.08 \pm 0.01) \times 10^{18}$
30	$(1.13 \pm 0.01) \times 10^{18}$
32	$(1.08 \pm 0.01) \times 10^{18}$

The spline function describing the cross section was calculated and drawn for the presented measurements (Fig. 7.25, gray line). Every setting was individually adapted to the cross section using the target thickness as scaling parameter. The resulting target thicknesses are listed in Table 7.3. The calculated target thicknesses are within the uncertainties constant for the different eight settings. Moreover, the calculated target thickness of 2.8×10^{18} atoms/cm^2 directly behind the nozzle fits optimal to the measured thicknesses, assuming a decreasing thickness with increasing distance to the nozzle according to the divergence of the beam. Here, it was not appropriative to calculate an average target thickness over all eight settings, due to the fact, that the operation conditions of the target changed within the measurement. Due to the small fluctuations in the target thicknesses using the average target thickness would obvious result in a similar elastic electron-proton cross section scaling factor. Therefore, a jet target is highly suited for measurements on the elastic electron-proton scattering cross section and the further analysis for the proton radius puzzle.

Besides cross sections, the target beam thickness profile was measured using a wobbler. The wobbler consists of two coils which generate an alternating magnetic field to deflect the electron beam so, that it pivots over the jet beam in horizontal direction. The measured target beam profile is a convolution of the electron beam profile with the target beam profile. Therefore, a measurement using a tungsten wire with a diameter of $100\,\mu$m scanning the electron beam was performed to determine the properties of the electron beam. Moreover, the time profile of the wobbler has to be included. The position of the electron beam thereby follows an arcsine course which means, that the electron beam is most of the time beside the jet beam. The electron beam positions are calculated via the
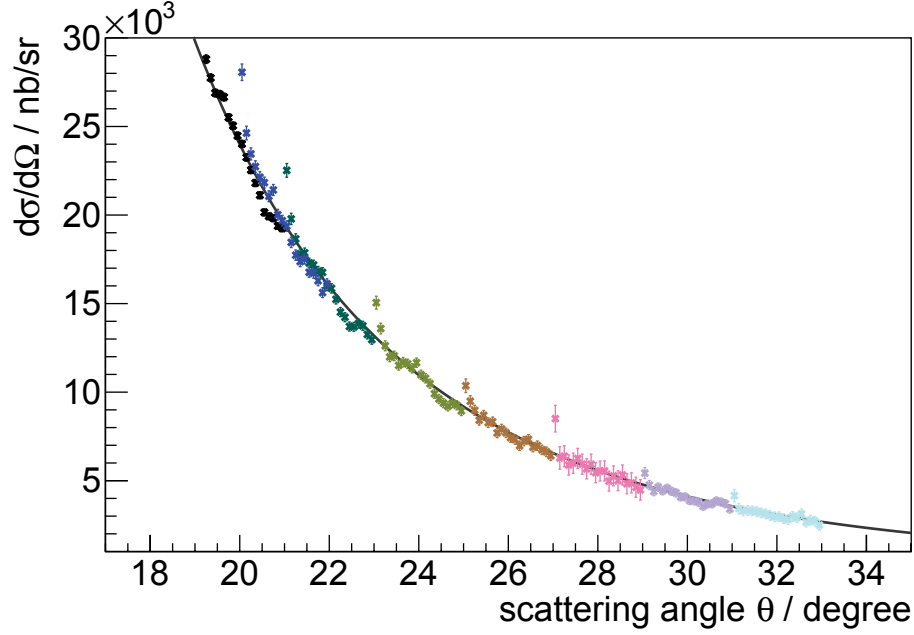
Figure 7.25: Measured elastic electron-proton scattering cross sections. The gray line shows the description of the cross section via a spline function performed by J. Bernauer [Ber10]. Every setting is drawn in a different colour and adapted to the expected cross section with the target thickness as scaling parameter. The measured data fit perfectly to the theoretical cross section.

currents for the deflection magnet coils.

This detailed analysis was performed in the framework of the master thesis of P. Brand [Bra18] and detailed information can be found there. The beam profile was recorded roughly $3\,\mathrm{mm}$ behind the nozzle where the cross section measurement was performed and is shown in Fig. 7.26 with a Gaussian fit to the data. The effect of the electron beam is neglectable due to its comparably vanishing diameter. There, the areal target thickness was determined to $(6.5 \pm 0.1) \times 10^{17}\,\mathrm{atoms/cm^2}$ with an additional background of $(2.9 \pm 0.1) \times 10^{17}\,\mathrm{atoms/cm^2}$ leading to a maximum target thickness of $(9.4 \pm 0.1) \times 10^{17}\,\mathrm{atoms/cm^2}$ in a distance of roughly $3\,\mathrm{mm}$ to the nozzle. The width of the beam was calculated using the sigma from the Gaussian fit to $\sigma = (1.19 \pm 0.03)$ mm. This preliminary result might be changing by a further calibration of the data by P. Brand within $10\,\%$ resulting in a smaller width of the target beam and a lower target thickness [Bra18]. These result will be discussed and compared with simulations within [Bra18]. During the measurement of the target thickness profile, the temperature of the hydrogen in front of the nozzle changed from $40\,\mathrm{K}$ to $50\,\mathrm{K}$ (from $2.8 \times 10^{18}\,\mathrm{atoms/cm^2}$ to $2.2 \times 10^{18}\,\mathrm{atoms/cm^2}$ directly behind the nozzle). Therefore, the target thickness is slightly lower compared to the target thickness determined using the cross section data. Nevertheless, the calculated target thickness is in reasonable agreement with the theoretical expected one of $2.2 \times 10^{18}\,\mathrm{atoms/cm^2}$ directly behind the nozzle, due to the

decreasing target thickness with increasing distance to the nozzle.
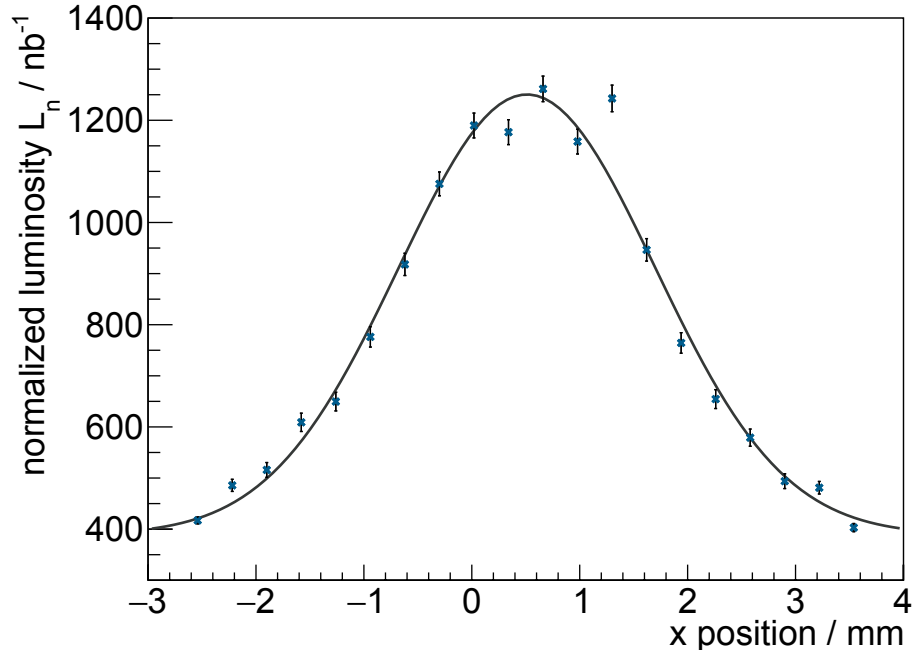
Figure 7.26: Target beam profile measured in a distance of roughly 3 mm where the cross section data was measured. A Gaussian fit on the data was performed. The areal target thickness was determined to $(6.5 \pm 0.1) \times 10^{17}$ atoms/cm^2 excluding the background of $(2.9 \pm 0.1) \times 10^{17}$ atoms/cm^2. The width of the beam was calculated to $\sigma = (1.19 \pm 0.03)$ mm [Bra18].

8 CryoFlash Experiment

Since the description of the stimulated emission as an inversion of the absorption by Albert Einstein in the year 1917 and the development of the first laser in the year 1960, the progress in peak intensity has made an extraordinary development [BT14]. Especially, the introduction of the principle of chirped pulse amplification (CPA) in 1985 generated a jump in this progress [Gib07]. The pulse duration dropped from picoseconds to femtoseconds and simultaneously, the focussed intensity raised by six orders of magnitude [Gib07]. For the CPA technique, the laser pulse is stretched in time by a factor of a thousand [F^+13, SM85, PMM87]. The pulse, now enlarged and therefore with lower peak power, can be amplified without destroying the power sensitive optics. After the amplification to a high energy, the laser pulse is re-compressed. This results in an ultra short high energy laser pulse.

Today, lasers with intensities of up to $10^{21}\,\mathrm{W/cm^2}$ are no longer a rarity [Gib07]. Due to this development, the interaction of high-intensity lasers with matter gains more and more interest at research institutes in various fields, e.g., laser physics, plasma physics, and elementary particle physics.

The CryoFlash experiment uses a Münster cluster-jet target in combination with the high intensity U2 laser system of the University of Düsseldorf to study the cluster-laser interaction.

8.1 Theory of Laser-Matter Interaction

During the interaction of an intense short pulsed laser with a target, the laser pulse impinges on the target with high intensities prior to the main pulse due to the rising edge of the laser pulse. This pre-pulse generates a pre-plasma and the following main pulse of the laser accelerates electrons out of the laser focus, which results in a positive space charged region of ions. The electric field through this charge separation allows the acceleration of ions up to energies in the range of MeV.

Important aspects are the generation of a plasma by the interaction of a pulsed intense laser with a target, the following electron acceleration and as a consequence the acceleration of ions.

Ionisation of Atoms and Plasma Origin

The interaction of a laser pulse with a plasma or rather the interaction of an electromagnetic wave with a single electron will be discussed to explain the processes of laser induced

electron or ion acceleration. The vector potential of light as an oscillating electromagnetic wave [Nü06]

$$\vec{A}(z,t) = A_0 \vec{e}_y \sin(k_L z - \omega_L t) \tag{8.1}$$

describes a laser with a direction of propagation in $\vec{e}_z$ and with a linear polarisation in $\vec{e}_y$ direction. Therein, $\omega_L/2\pi$ is the laser frequency, $k_L = 2\pi n_r/\lambda_L$ the wave number, and A_0 an amplitude. The refractive index n_r is equal to 1 in vacuum and the laser wavelength in vacuum is defined as $\lambda_L = 2\pi c/\omega_L$ with c being the speed of light.

Due to the absence of an electrostatic potential, the vector potential determines the electric field $\vec{E}_L$ [Mes06]

$$\vec{E}_L = -\frac{\partial \vec{A}}{\partial t} = \vec{E}_0 \cos(k_L z - \omega_L t) = \vec{e}_y \omega_L A_0 \cos(k_L z - \omega_L t), \tag{8.2}$$

the magnetic field $\vec{B}_L$

$$\vec{B}_L = \vec{\nabla} \times \vec{A} = \vec{B}_0 \cos(z,t) = \vec{e}_x k_L A_0 \cos(k_L z - \omega_L t) = \vec{e}_x \frac{n_r \vec{E}_0}{c} \cos(k_L z - \omega_L t), \tag{8.3}$$

and the intensity $\vec{I}_L$

$$\vec{I}_L = \langle | \vec{S} | \rangle = \frac{1}{\mu_0} \langle | \vec{E}_L \times \vec{B}_L | \rangle = \frac{\varepsilon_0 c E_0^2}{2}, \tag{8.4}$$

with the Poynting vector $\langle | \vec{S} | \rangle$ averaged over a laser period, the magnetic and dielectric constant μ_0 and ε_0 with $\mu_0 \varepsilon_0 c^2 = 1$. Therein, $\vec{E}_0$ and $\vec{B}_0$ are the amplitudes of the fields. The intensity of such an electromagnetic wave must be greater than the binding strength of the electron to an atom $I_L > I_a$ to create an ionisation for any target material (photoelectric effect with a single photon). The Bohr radius a_B [Gib07]

$$a_B = \frac{4\pi \varepsilon_0 \hbar^2}{m e^2} = 5.3 \times 10^{-9}\,\mathrm{cm} \tag{8.5}$$

and the electric field strength E_a

$$E_a = \frac{e}{4\pi \varepsilon_0 a_B^2} \simeq 5.1 \times 10^9\,\mathrm{V/m} \tag{8.6}$$

define the atomic intensity I_a, where the electric field strength is equal to the binding strength of the electron

$$I_a = \frac{\varepsilon_0 c E_a^2}{2} \simeq 3.51 \times 10^{16}\,\mathrm{W/cm}^2. \tag{8.7}$$

An excitation of the atom is also feasible, if the excitation energy matches the absorbed photon energy. Another possibility for ionisation of an atom is the multiphoton ionisation (MPI) [L$^+$16, RK$^+$95, Kul96, Gib07], where intensities in the order of $> 10^{10}\,\mathrm{W/cm}^2$ are appropriate to ionise the atom with several photons which are absorbed by already excited electrons. The above-threshold ionisation (ATI) [L$^+$16, RK$^+$95, Kul96, Gib07] describes the

phenomenon, that more photons are absorbed than necessary for the process of ionisation. The excess energy is converted to the kinetic energy E_e of the electron leaving the atom (Fig. 8.1)

$$E_e = (n + s) \hbar \omega - E_{\text{ion}} \tag{8.8}$$

with the number of photons needed n and exceeded s for the multiphoton ionisation and the ionization energy E_{ion} of the ion.

When the intensity is higher or the same as I_a, the laser field influences the atomic binding energy and distorts the Coulomb field of the atom. This effect known as tunneling ionisation (TI) [L$^+$16, Gib07] is distinguishable from MPI via the parameter γ

$$\gamma = \omega_L \sqrt{\frac{2E_{\text{ion}}}{I_L}}. \tag{8.9}$$

A value of $\gamma > 1$ leads to multiphoton and $\gamma < 1$ to tunneling ionisation. The Coulomb potential interference with a homogeneous electric field is decribed by the atomic potential [Gib07]

$$V(x) = -\frac{Ze^2}{x} - e\varepsilon x \tag{8.10}$$

with ε representing the absolute permittivity. There is the possibility, that the external field suppresses the atomic potential. In this case, it is quantum mechanically feasible, with a finite probability, that the electron tunnels through the barrier: tunneling ionisation or barrier suppression ionisation (BSI). Furthermore, a barrier lower than E_{ion} leads to a spontaneous emission of the electron named over-the-barrier ionisation (OBTI) (Fig. 8.1). These processes result in quasi-free electrons and ions forming a plasma [Gib07].

The Coulomb potential of a charge Ze in the plasma decreases with the inverse distance $1/r$, and additionally the plasma particle attracts a cloud of oppositely charged particles, resulting in an effective shielding of the electric field [Jä09]

$$\phi_{el} = \frac{1}{4\pi\epsilon_0} \frac{Ze}{r} \exp\left(\frac{-r}{\lambda_D}\right). \tag{8.11}$$

The Debye length λ_D is the characteristic shielding length defined as

$$\lambda_D = \sqrt{\frac{k_B T_e}{4\pi n_e e^2}}, \tag{8.12}$$

wherein $k_B T_e$ is the effective temperature with the Boltzmann constant k_B and n_e the electron density where the electric field decreases by a factor of $1/e$.
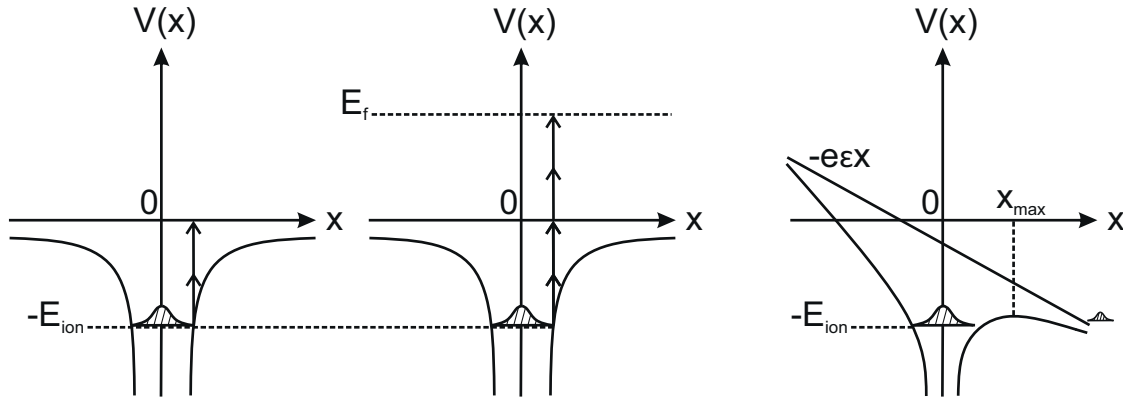
Figure 8.1: *Left*: Principle of the multiphoton ionisation (MPI). Due to the absorption of n photons with energy $\hbar\omega$ an electron with the binding energy E_{ion} leaves the atom with a minimal kinetic energy. *Center*: Schematic view of the above-threshold ionisation (ATI). An electron leaves the atom with high kinetic energy caused by the absorbtion of more photons than necessary for the ionisation. *Right*: Sketch of the tunneling or barrier suppression ionisation (TI, BSI). The presence of a high external electric field leads to an ionisation of the atom. Based on [Gib07].

Interaction between a Single Electron and a Laser Field

In case of the cluster-laser interaction, the laser interacts first with the electrons of the clusters. Therefore, the interaction of a laser with a single electron is described to understand the processes during the cluster-laser interaction.

The Lorentz equation describes the motion of an electron in presence of an electromagnetic wave [Gib07]

$$\vec{F}_L = \frac{d\vec{p}}{dt} = \frac{d}{dt}\left(\gamma m \vec{v}\right) = e\left(\vec{E}_L + \vec{v} \times \vec{B}_L\right), \tag{8.13}$$

therein $\gamma = \left(1 - v^2/c^2\right)^{-1/2}$ is the relativistic factor and $\vec{v}$ the electron velocity. Considering only a transverse electromagnetic field ($y = 0$) leads to an oscillation of the electrons in the form of [Jä09]

$$x = -\frac{a_0 c}{\omega_L}\left(1 - \cos\phi\right) \tag{8.14}$$

$$z = \frac{a_0^2 c}{4\omega_L}\left(\phi + \frac{1}{2}\sin 2\phi\right) \tag{8.15}$$

including the phase of a linearly polarized wave $\phi\left(t, z\right) = \omega_L t - k_L z$ and the relativistic amplitude of the laser pulse $a_0 = E_L e/\omega_L m_e c$. This amplitude, also known as normalized vector potential differentiates the laser plasma interaction into non relativistic ($a_0 \ll 1$) and relativistic ($a_0 \geq 1$) electron movement [Bra17].

From the perspective of the average rest frame of the electron the trajectories of the electron results in the figure-of-eight motion (trajectory in the form of the number eight) induced by the oscillation in x-direction with the laser frequency and in z-direction with the double laser frequency (see Fig. 8.2) [Gib07].
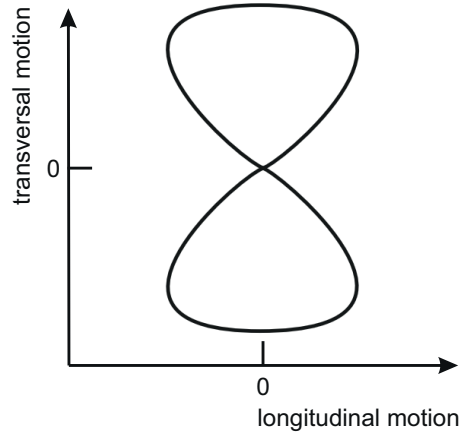
Figure 8.2: Motion of the electron in a laser field in the reference frame which moves with the average drift velocity and results in the figure-of-eight motion. Based on [Bra17, Gib07].

These Equations only hold true under the assumption of a plane wave, realistically the applied lasers own a short pulse duration and an intensity distribution. The intensity shows a strong radial gradient and the resulting force [B$^+$96a, SM97, QM98]

$$\vec{F}_{\text{pond}} = -\frac{e^2}{4m_e\omega_L^2\overline{\gamma}}\vec{\nabla}\left(\vec{E}_L^2\left(x\right)\right) \tag{8.16}$$

is named ponderomotive force with the relativistic factor $\overline{\gamma} \approx \left(1 + a_0^2\right)^{1/2}$ averaged over the time. The electrons experience an acceleration out of the laser focus in the decreasing direction of the intensity gradient of the laser by this force. Additionally, the drifting electrons oscillation amplitude is reduced due to the decreasing intensity resulting in a lower restoring force.

Ion Acceleration

The direct ion acceleration requires laser intensities in the range of $I = 10^{24}\,\text{W/cm}^2$ as a result of the higher inertia of ions than for electrons [Bra17]. Up to now, there are no such lasers available. Therefore, the laser induced ion acceleration up to energies on the MeV scale occur as a secondary process. The preceding step is the immediate acceleration of a great number of electrons out of the laser focus due to the presence of high electric fields ($\sim$ GeV/m) caused by high laser intensities [K$^+$16]. In a nutshell, the laser field induces a motion of the electron and this charge separation results in an acceleration of the ions [K$^+$01].

The CryoFlash experiment will focus on the interaction of a high intensity laser with a cryogenic cluster-jet beam (see chapter 8.2) resulting in two different effects of ion acceleration: Target Normal Sheath Acceleration (TNSA) [S$^+$00, H$^+$00, W$^+$00] and Coulomb explosion [S$^+$04, T$^+$03, K$^+$99]. In the case of the TNSA, electrons, produced at the front of the clusters, propagate through them with nearly no energy loss and the

fastest electrons leave them at the opposite site (see Fig. 8.3). Inside of the clusters, the charge separation leads to an electric field and the electrons produce a shielding in the range of the Debye length. The thus generated field strength (up to 10^{12} V/m) is high enough to ionise the clusters, generate ions and accelerate them in normal direction, which means that the electric field is perpendicular to the front side of the cluster.
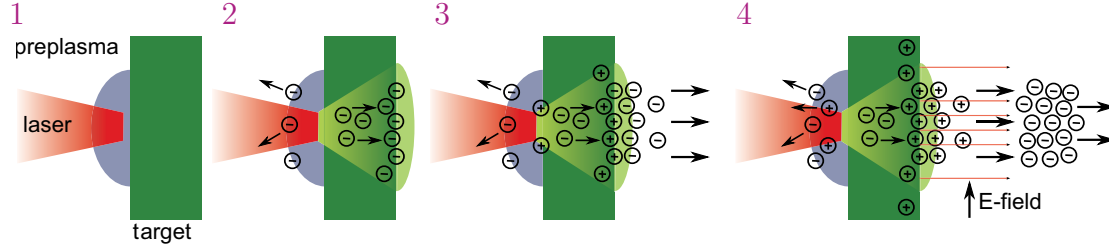
Figure 8.3: Sketch of the Target Normal Sheath Acceleration (TNSA) ion acceleration process. 1) The pre-pulse of the laser generates a pre-plasma at the surface of the target. 2) The following main pulse of the laser accelerates relativistic electrons due to the ponderomotive force. 3) The plurality of electrons leaving the target at the rear side. 4) The thereby generated electric field strength is strong enough to accelerate the ions from the target. The accelerated ions are highly collimated and leave the target in normal direction to the target. Based on [Sch18, Gri14].

In case of a Coulomb explosion, the ions of the cluster drift apart, due to the charge separation in the cluster because of the high energy of the hot electrons (see Fig. 8.4). Thereupon, the positive highly charged state inside the cluster leads to an explosion of the cluster. The elemental ions leaves the cluster homogeneous in all directions and acquire a high kinetic energy.
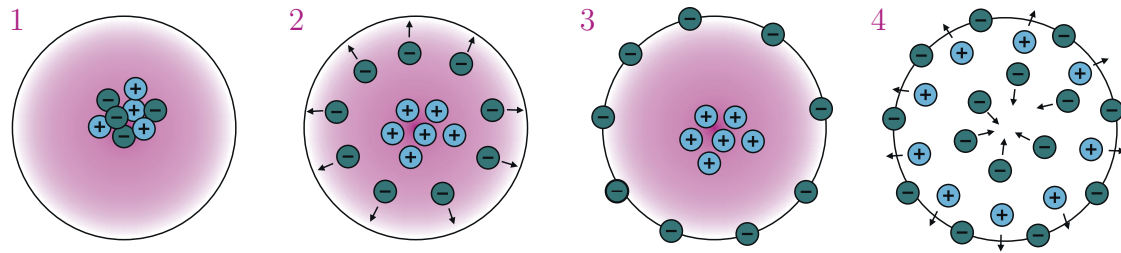
Figure 8.4: Sketch of the Coulomb explosion. The laser pulse (red) interacting with a cluster (1) results in an radial acceleration of the electrons due to the ponderomotive force (2) until this force is equal the attractive electric field (3). Consequently, the ions are accelerated out of the cluster homogeneously in all directions whereas the plurality of electrons return to their initial position (4). Based on [Sch18].

X-ray Generation

The underlying reason why the interaction of a cluster with a laser pulse generates X-rays, is the fact, that accelerated charged particles are sources of radiation. The origin of X-rays from the cluster-laser interactions can be described by two different phenomena. After the laser pulse, the electrons experience an oscillation due to the plasma generated

by the cluster-laser interaction. This oscillation is called betatron oscillation [R$^+$04, P$^+$05, P$^+$06, K$^+$08b, A$^+$08] and leads to a collimated X-ray beam as in a conventional synchrotron. The frequency of the betatron oscillation is given by

$$\omega_b = \frac{\omega_P}{\sqrt{2\gamma}},$$ (8.17)

wherein, ω_P is the plasma frequency and γ the Lorentz factor.

The high harmonic generation (HHG) [Kul96, Mar16, L$^+$09b, Kje15, D$^+$15] occurs when a high intensity short laser pulse is focussed in matter, like a cluster. Thereby, new frequencies which are integer multiples of the origin laser frequency are generated. The maximal energy which an ionized electron gains from the electric field of the laser can be used to determine the maximal energy $E_{\max}$ (cut-off energy) of the generated photons [L$^+$09b, Kje15]:

$$E_{\max} = I_P + 3.17 U_P,$$ (8.18)

wherein, U_P is the ponderomotive potential and I_P the ionization potential of the particle. The photons are generated in a three step model (see Fig. 8.5).
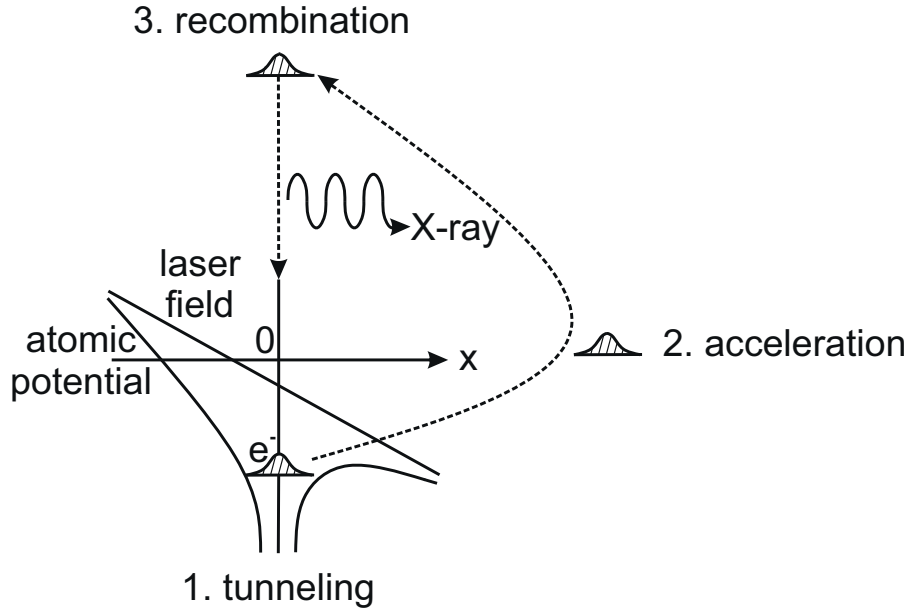
Figure 8.5: Principle of the high harmonic generation (HHG) via the three step model. In the first step, an electron leaves the atom by tunnel ionisation (1). Then, the electron experiences an acceleration in the electromagnetic field of the laser (2). Last, the electron recombines with the ion and emitts harmonics up to the X-ray range (3). Based on [D$^+$15].

The electron quantum mechanically tunnels out of the potential of the atom but then the dynamics of the electrons are considered classically. Therefore, classically the electron is generated in vacuum with no initial velocity. Due to the electric field of the laser, the electron experiences an acceleration. The electron will change the direction due to the change of the direction of the electric field. Therefore, the electron will be accelerated back to the parent atom. The electron reaches the atom and this leads to a recombination

process wherein the atom returns to its ground state and radiation (X-rays) will be emitted, known as the high harmonic generation [P$^+$05].

8.2 CryoFlash Experiment

The CryoFlash experiment uses a high intensity laser in combination with a cryogenic cluster-jet beam to realise and analyse an ultrashort laser driven X-ray pulse source [Wil17b]. Therefore, the ARCTURUS laser system of the University of Düsseldorf (see chapter 8.4) interacts with a cluster-jet beam generated by a cluster-jet target designed, built up, and set into operation at the University of Münster (see chapter 8.3).
The processes to generate an X-ray source from this interaction are described in chapter 8.1. The main advantage of a cluster-jet beam interacting with a laser in comparison to the typically used foil targets, is the continuous flow of target material with high target thickness which allows for an utilisation of the high repetition rate provided by the laser. Results gained by this experiment will lead to an ultrashort laser driven X-ray pulse source with adjustable energies. These kind of sources find their application in the research fields of condensed matter physics, materials sciences, processes of information technology, and dynamics of chemistry and biochemistry. Thereby, the focus will be on investigations and manipulations of ultrafast processes in the range of femtoseconds to attoseconds. To study these processes, the well known pump probe method in spectroscopy and microscopy is used. First, the test object will be excited (pump) and later observed (probe). Therefore, photons in the X-ray regime are from special interest ($\sim 5\,\text{keV}$ - $1\,\text{MeV}$) due to their ability to penetrate through the material under investigation. The use of ultrashort pulses results in the opportunity to receive snapshots of the fast processes.
Significant for the qualities of the X-ray sources are the characteristics of the used laser and cluster beam. Therefore, investigations with different cluster beam properties, like density, cluster size, and used gas type, and with various laser settings, for example repetition rate or energy, will take place to optimise the interaction of these with respect to an ultrashort tunable X-ray source.
In a first step the cluster-jet target MCT1S was built up and characterized in a previous master thesis at Münster [Gri14] (cf. chapter 8.3) and was assembled at the U1 laser system at the University at Düsseldorf (cf. chapter 8.4) to do preliminary studies on the interaction. Following the proof of a successful interaction between these two devices, this cluster-jet target is now already integrated at the final U2 ARCTURUS laser system (cf. chapter 8.4). Due to the higher energy and the high repetition rate, the ARCTURUS laser perfectly fits the requirements on the laser system to generate a X-ray source. At the ARCTURUS laser system a variety of different diagnostic systems exist to characterize and optimise the experimental setup (see chapter 9.1). Based on these results a complete new cluster-jet target MCT-D will be designed and built up at the University of Münster to fulfil all the requirements worked out in the experiments with the cluster-jet target MCT1S (cf. chapter 9.2.6). The final combination of the ARCTURUS laser system with

the new cluster-jet target, both state-of-the-art devices, will allow for intensive studies on X-ray generation.

8.3 Cluster-Jet Target MCT1S

The cluster-jet target MCT1S (Münsteraner Cluster-jet Target 1 Silke) was built up, set into operation, and examined in a recent master thesis at the University of Münster [Gri14]. There, a complete but at the same time compact cluster-jet target, including the cluster source, an interaction chamber, and a beam dump were assembled to characterise and optimise the cluster beam with different diagnostic tools with respect to the requirements of the interaction with a laser. In Düsseldorf, the cluster source is directly integrated in the laser system. Therefore, this thesis will focus on the used cluster source.

The core structure of the cluster source of the MCT1S target is a predecessor of the already presented structure (chapter 2.2) of the Münster cluster-jet targets. The main difference is the collimator chamber enclosing the skimmer chamber, which in this case act at the same time as an insulation vacuum chamber for an optimised cooling of the target gas.

The cluster-jet target MCT1S uses a Laval nozzle with a narrowest inner diameter of 28 μm to generate a cluster beam (chapter 2.2.1). The expansion of hydrogen gas cooled down to 22 K with high pressure up to 16 bar leads to cluster formation. This corresponds to a flow of $1.3\,l_n$/min through the nozzle resulting in a target density of up to 3×10^{15} atoms/cm^3 in a distance of 33 cm from the nozzle. At this distance, 33 cm from the nozzle, measurements determining the target density were performed at the University of Münster [Gri14]. The skimmer chamber is pumped with two roots pumps in combination with a fore pump. The used pumps at the U1 laser system are presented in Table 8.1.

After the production of the cluster beam, an orifice, the skimmer separates the cluster beam from the residual gas which remains in the skimmer chamber and is pumped away. The cluster-jet target MCT1S uses a skimmer with an opening diameter of 0.7 mm. In contrast to the $\overline{\text{P}}$ANDA cluster-jet targets (chapter 4.3 and chapter 4.17) the skimmer is fixed. The skimmer chamber is equipped with a nozzle shutter, consisting of a linear motor (LinMot P02-23Sx80F/20x80-HP) and a metal sheet, which allows for a blocking of the cluster beam in the skimmer chamber (Fig. 8.6). This feature enables the possibility to switch between cluster beam with high density to no cluster beam during the experiment which is necessary for background studies on the interaction with a laser. Furthermore, the linear motor can be used to pulse the cluster beam due to its possible high velocity $v = 7.3$ m/s and acceleration $a = 750$ m/s^2. In the bachelor thesis of S. Bölsker [Bö15] the linear motor was programmed to use the same trigger as the laser to synchronise the pulsed cluster beam with the laser pulse. More details are given in chapter 9.1.

Passing the skimmer, the cluster beam enters the collimator chamber, which is pumped via two turbomolecular pumps. The cluster beam leaves the collimator chamber through a second orifice, the collimator (diameter of 0.7 mm).
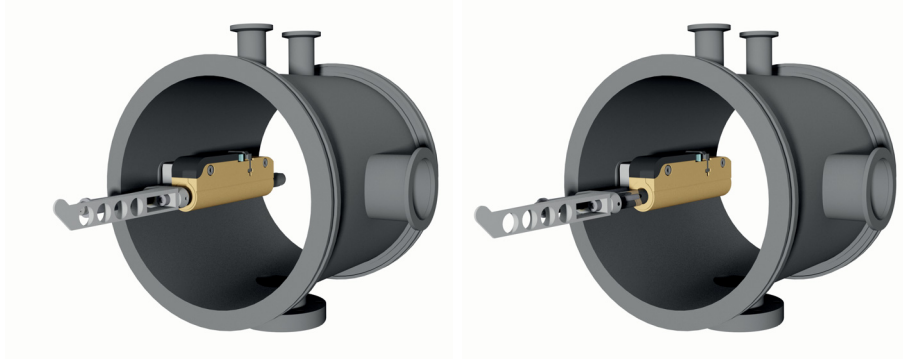
Figure 8.6: The nozzle shutter mounted in the skimmer chamber of the cluster-jet target MCT1S which consists of a linear motor and a metal sheet. Left: Linear motor is entrenched and the nozzle shutter is open. Right. Linear motor is extended and the nozzle shutter is closed. Thereby, the cluster beam impinges on the massive round tip of the metal sheet and no longer enters in the following chambers. The holes in the metal sheet lead to a weight loss which is necessary to reach high accelerations and velocities without fluctuations of the nozzle shutter. Generated by D. Bonaventura.

Table 8.1: Characteristics of the different pumps used at the cluster-jet target MCT1S. FP_{no} represents fore pumps, RP_{no} roots pumps, and TP_{no} turbomolecular pumps.

$pump_{no}$	manufactures and designation	hydrogen pumping speed
FP_1	Leybold Sogevac SV300	$240\,m^3/h$
RP_1	Leybold RUVAC WSU 1001	$1000\,m^3/h$
RP_2	Leybold RUVAC RA 5001	$5550\,m^3/h$
TP_1	Pfeiffer TPU 2200	$2800\,l/s$
TP_2	Leybold Turbovac 1000	$900\,l/s$

This cluster source was assembled at the U1 laser system at the University of Düsseldorf. Therefore, the cluster source was built up on an aluminium frame and connected to the interaction chamber of the U1 laser system (see Figure 8.7). The aluminium frame allows for a precise adjustment of the cluster beam to the laser focus. This was achieved through the use of four height-adjustable feet under the aluminium frame. Additionally, the source is connected with a slip band on the frame, to move the target perpendicular to the laser beam. A vacuum valve allows for a separation of these two devices. The cluster beam interacts with the laser beam in a distance of roughly $90\,cm$ from the nozzle. With this setup target densities of roughly $5 \times 10^{13}\,atoms/cm^3 - 5 \times 10^{14}\,atoms/cm^3$ are available. Due to this relatively low density and the low laser energy of the U1 laser system no successful laser-cluster interaction was recorded.

Therefore, in a first step the cluster-jet target MCT1S was optimised. The collimator and skimmer chamber including the skimmer and collimator were removed. The cold head with the Laval nozzle was directly mounted on a removable wall of the interaction chamber. In the case of the U1 laser, the laser beam is directed directly in front of the nozzle. Thus, the interaction between cluster and laser beam is not in the center of the interaction chamber. After this modification the laser beam directly interacts with the cluster beam behind the nozzle, where the highest densities of roughly $7.5 \times 10^{16}\,atoms/cm^3$ can be

cluster-jet target MCT1S   interaction chamber

optical
monitor
system

interaction point between
cluster and laser beam
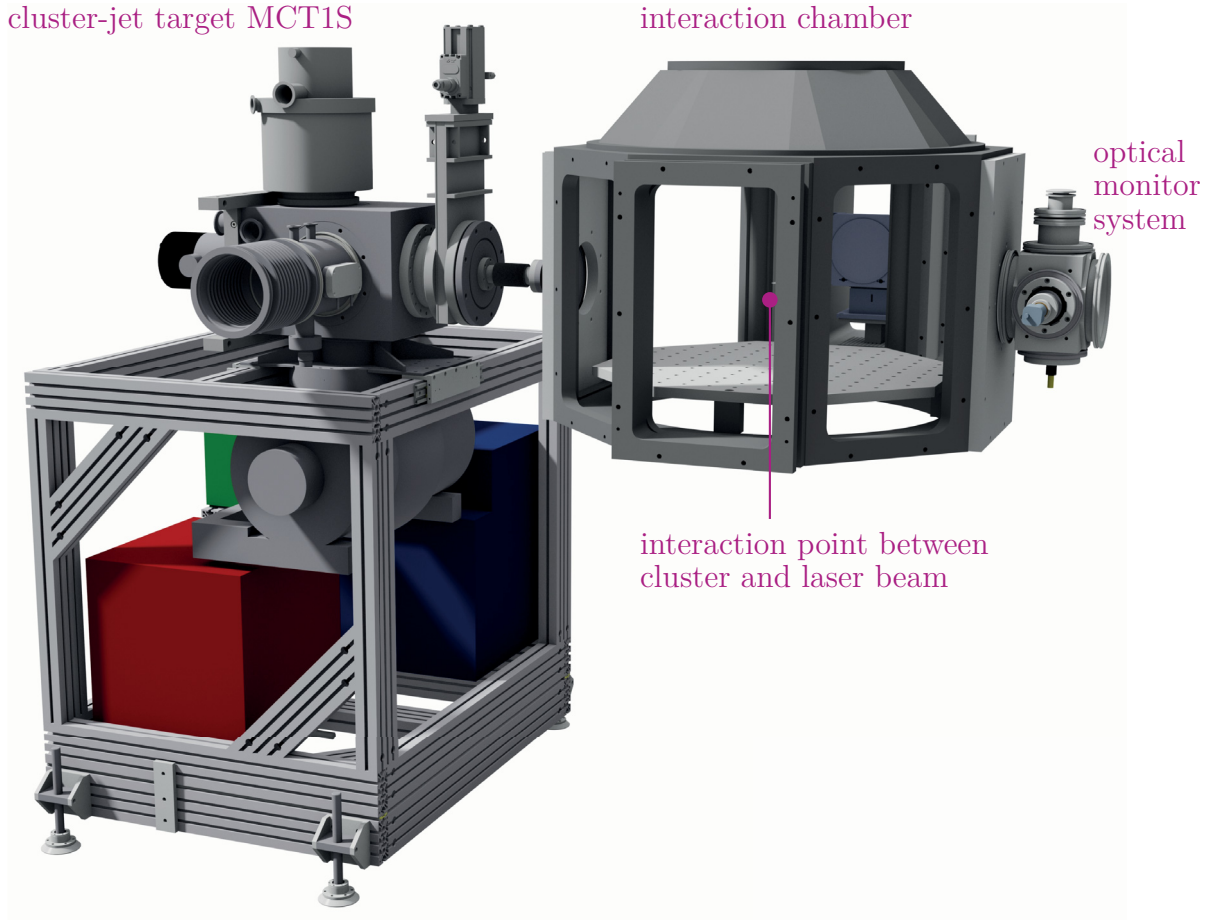
Figure 8.7: The cluster-jet target MCT1S assembled at the U1 laser system in Düsseldorf. On the left side the cluster-jet target with its devices mounted on an aluminium frame which allows for a complete adjustment of the cluster beam to the laser focus is shown. A vacuum shutter allows for a separation of the cluster target from the interaction chamber (right) of the laser system. The laser enters the chamber on the top and is then guided via optics horizontally from the back to the front of the chamber. The cluster beam direction is from left to right and the interaction of the cluster beam with the horizontal laser beam is in the middle of the interaction chamber. The chamber mounted on the right side of the interaction chamber, was used to align the cluster beam to the laser beam (see chapter 9.1). Generated by D. Bonaventura, edited.

achieved, because the thickness decreases with the inverse of the distance ($\rho \sim 1/r$). Furthermore, the pumping system was also adapted. The two turbomolecular pumps at the collimator chamber are no longer necessary and the two roots pumps with the fore pump are now pumping the interaction chamber. On the basis of this modification a first successful interaction of the laser beam with the cluster beam was identified (cf. chapter 9.1).

In a second step, the modified cluster-jet target MCT1S was mounted at the ARCTURUS laser system. The movable interaction chamber wall with the target was dismounted from the U1 interaction chamber and installed in the same way at the U2 interaction chamber (cf. Fig. 8.8). There the interaction between cluster and laser beam has to be in the center of the chamber with respect to the diagnostic tools. Therefore, a cold finger between cold
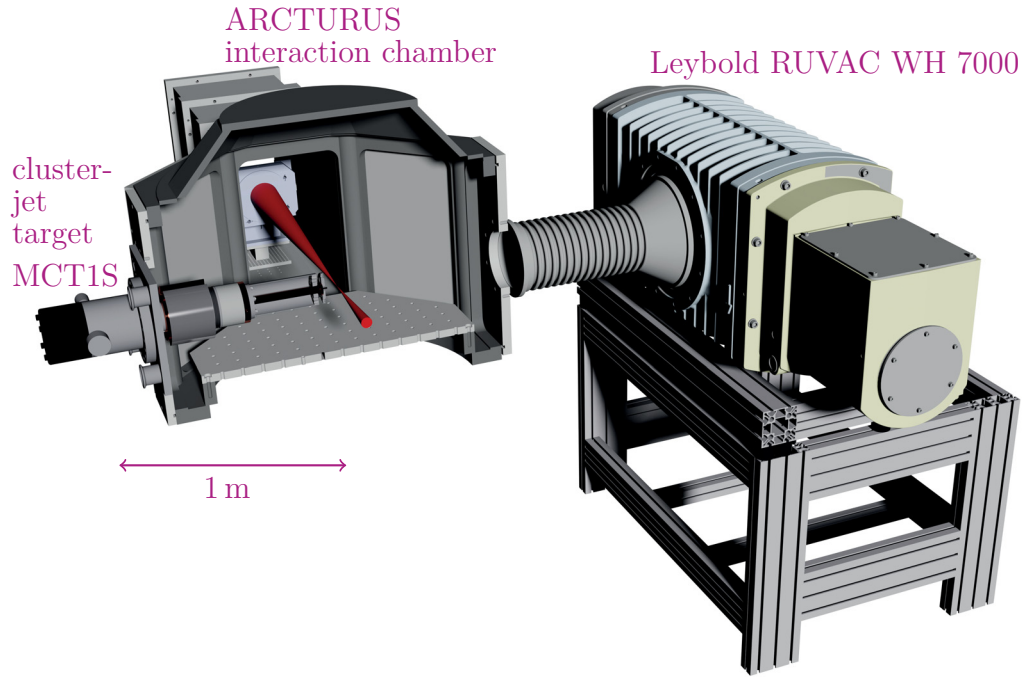
Figure 8.8: The cluster-jet target MCT1S is directly mounted on the wall of the interaction chamber. The cluster beam direction is from left to right. The U2 laser beam is focussed via optics directly in front of the nozzle, where the highest densities can be achieved. The laser beam (red) direction is from back to the front. The roots pump Leybold RUVAC WH 7000 opposite to the cluster nozzle pumps the clusters directly after the interaction with the laser beam away. Generated by D. Bonaventura, edited.
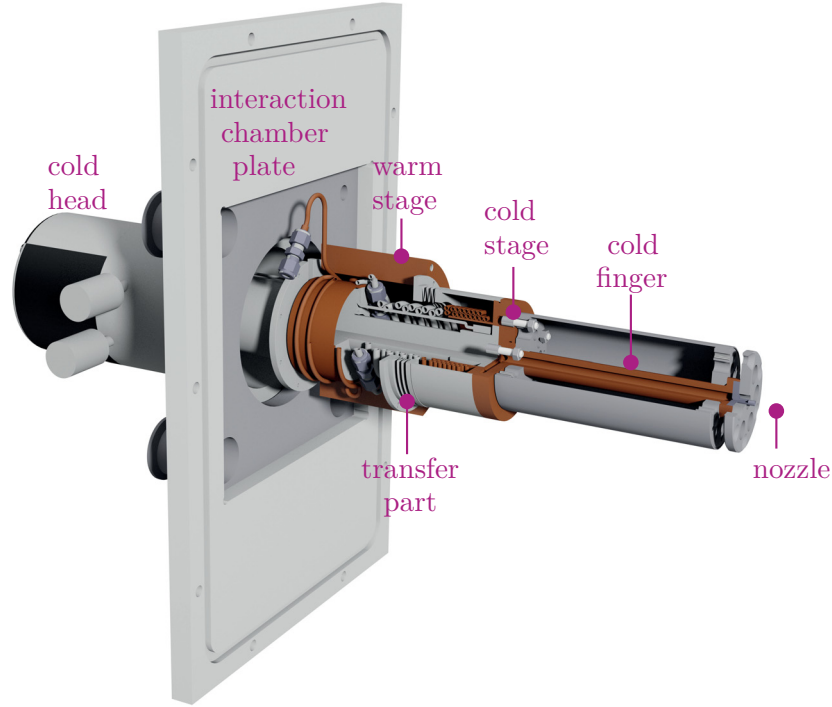
head and nozzle was designed and installed at the cluster-jet target to place the exit of the nozzle in the center of the interaction chamber (see Fig. 8.9). Additionally, the roots pump Leybold RUVAC RA 5001 was exchanged by a roots pump Leybold RUVAC WH 7000 ($7800 \, \mathrm{m}^3/\mathrm{h}$) which is installed directly at the interaction chamber opposite of the cluster-jet target as a beam dump pump to pump the clusters away directly after the interaction (cf. Fig. 8.10).

8.4 U1 and ARCTURUS Laser System (U2)

The institute of laser and plasma physics of the University of Düsseldorf provides two different laser systems with various characteristics, the U1 and the U2 (ARCTURUS system), for the investigation on cluster-laser interactions in the framework of the CryoFlash experiment.

U1 Laser System

The U1 laser system consist of a Titanium:Sapphire laser with a central wavelength of $\lambda = 800 \, \mathrm{nm}$. The required pump energy is provided via a frequency-doubled Nd:YAG laser with a wavelength of $532 \, \mathrm{nm}$, which in turn is pumped by a diode laser. Due to CPA

Figure 8.9: The cluster-jet target MCT1S directly mounted on the wall of the interaction chamber. A cold finger between cold head and nozzle was designed and installed to place the interaction between cluster and laser beam in the center of the chamber. Generated by D. Bonaventura, edited.

the laser pulse leaves the system with a power of 400 mW, a pulse length of 7.5 fs, a central wavelength of $\lambda = 800$ nm, and a repetition rate of 1 kHz, 10 Hz or 1 Hz. Moreover, the operation in a continuous mode is also possible. The laser pulse passes a vacuum tube and arrives at one of the three possible vacuum chambers equipped with diagnostic systems. The cluster-jet target MCT1S is installed in such a chamber perpendicular to the laser beam. This laser system reaches pulse energies up to 100 µJ, features a high stability and is therefore ideally suited for preliminary studies on the cluster-laser interaction.

ARCTURUS Laser System (U2)

The U2 laser system, or ARCTURUS laser system is the more powerful system of the institute of laser and plasma physics. The ARCTURUS laser was built up in 2008 and has been running continuously since then. Additionally, upgrades to its present performance were performed.

The Titanium:Sapphire laser provides a high energy laser pulse with various features due to the multiple amplification supplied via the CPA method (cf. Fig. 8.11). A cross-polarized wave system (XPW) is installed in the preamplifier system to enhance the contrast (ratio between intensity of the laser peak and background) of the laser pulse and to suppress the pre-pulse of the laser, so that only the main pulse interacts with the target material. Afterwards, the laser pulse is guided through two additional amplification
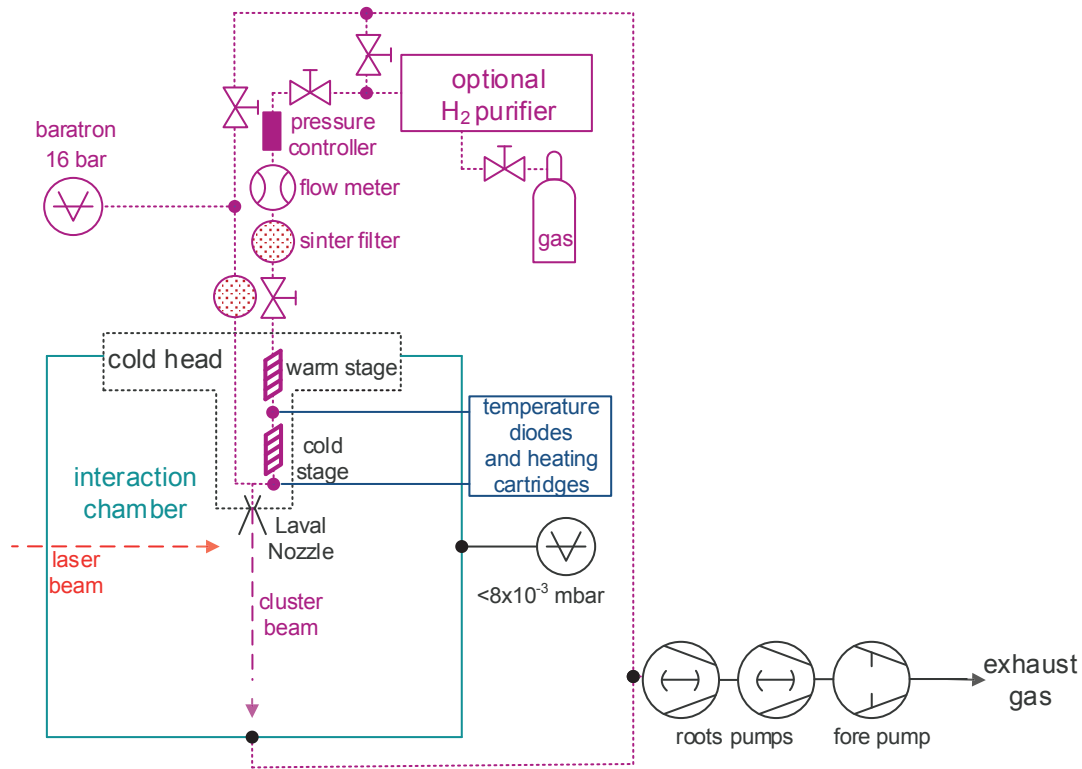
Figure 8.10: Sketch of the gas and vacuum system of the cluster-jet target MCT1S installed at the U2 laser system.

systems and then divided into three sub beams. The probe beam is guided directly into the experimental hall. The other two main beams are once more amplified, compressed, and then directed into the experimental hall.

Therefore, three beams are available in the experimental hall. Two of them are equally, but independently amplified up to 5 J and led through vacuum pipes into two available vacuum chambers equipped with diagnostics. Moreover, the two beams can be temporally varied and directed into the same chamber, interacting one after the other or simultaneously with the target material. The third pulse is used as a diagnostic beam which can also be varied in space and time. The characteristics of these three beams are listed in Table 8.2 and Figure 8.12 shows the experimental hall and the three beam lines. The ARCTURUS high-performance laser allows for an intense study on the cluster-laser interaction with respect to generating X-ray sources or acceleration of ions in the framework of the CryoFlash experiment.
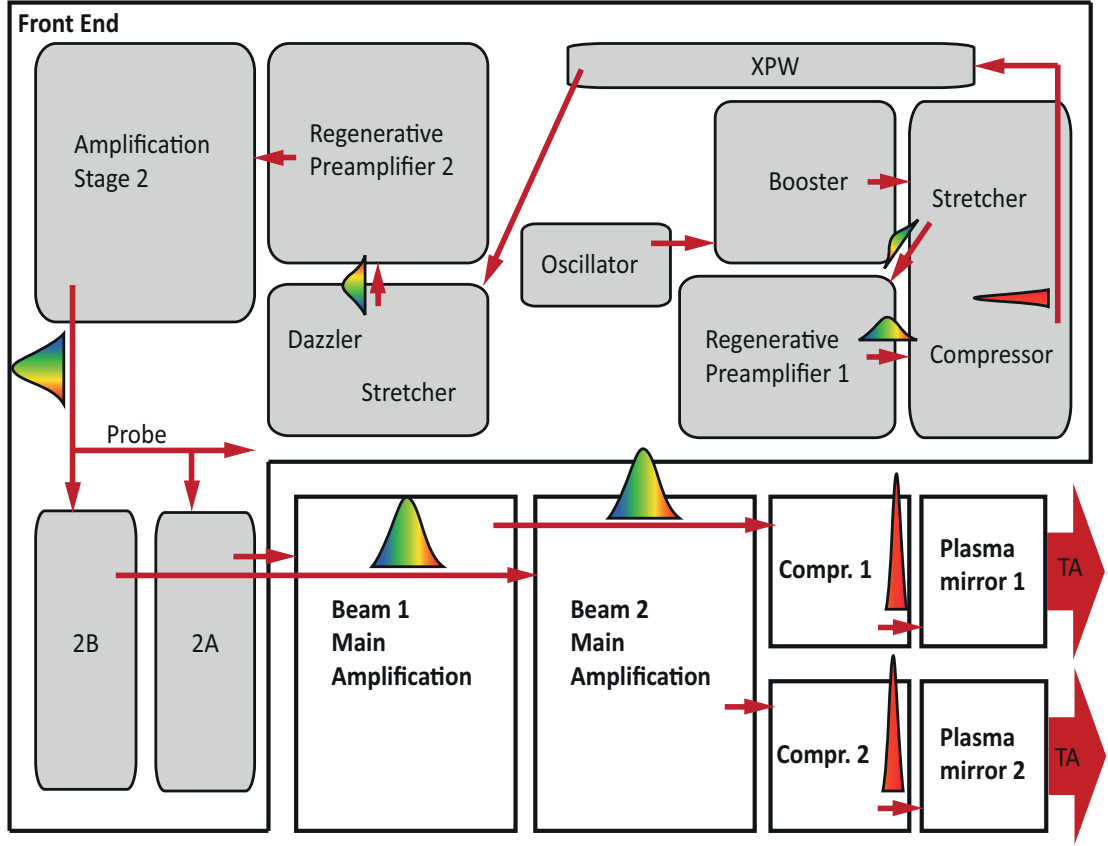
Figure 8.11: Overview of the U2 laser system (ARCTURUS) at the University of Düsseldorf. The oscillator generates the laser pulse which is then preamplified and guided through a XPW module to enhance the contrast. Afterwards the laser pulse passes through two additional amplifer systems and is then divided into three sub beams. One beam, the probe beam, is directly guided into the experimental hall. The two main beams are once more amplified and compressed before entering the experimental hall, taken from [Bra17]. Thanks to S. Brauckmann (HHUD).

Table 8.2: Characteristics of the three usable laser beams of the U2 laser system of the University of Düsseldorf. For the studies of the cluster-laser interaction the high intensly B1 beam was used. The number in brackets demonstrates the achievable contrast with the use of a plasma mirror in the laser beam line [K$^+$16, Aur17].

	beam 1	beam 2	diagnostic beam
diameter	8 cm	8 cm	2 cm
energy	5 J	5 J	< 100 mJ
power	200 TW	200 TW	3 TW
contrast	$< 10^{-10}$ (10^{-12})	$< 10^{-10}$ (10^{-12})	$< 10^{-10}$
focus size	$10 \, \mu m^2$	$10 \, \mu m^2$	$35 \, \mu m^2$
repetition rate	10 Hz	10 Hz	10 Hz
pulse length	30 fs	30 fs	30 fs
maximal intensity	$> 10^{20} \, W/cm^2$	$> 10^{20} \, W/cm^2$	$10^{16} \, W/cm^2$
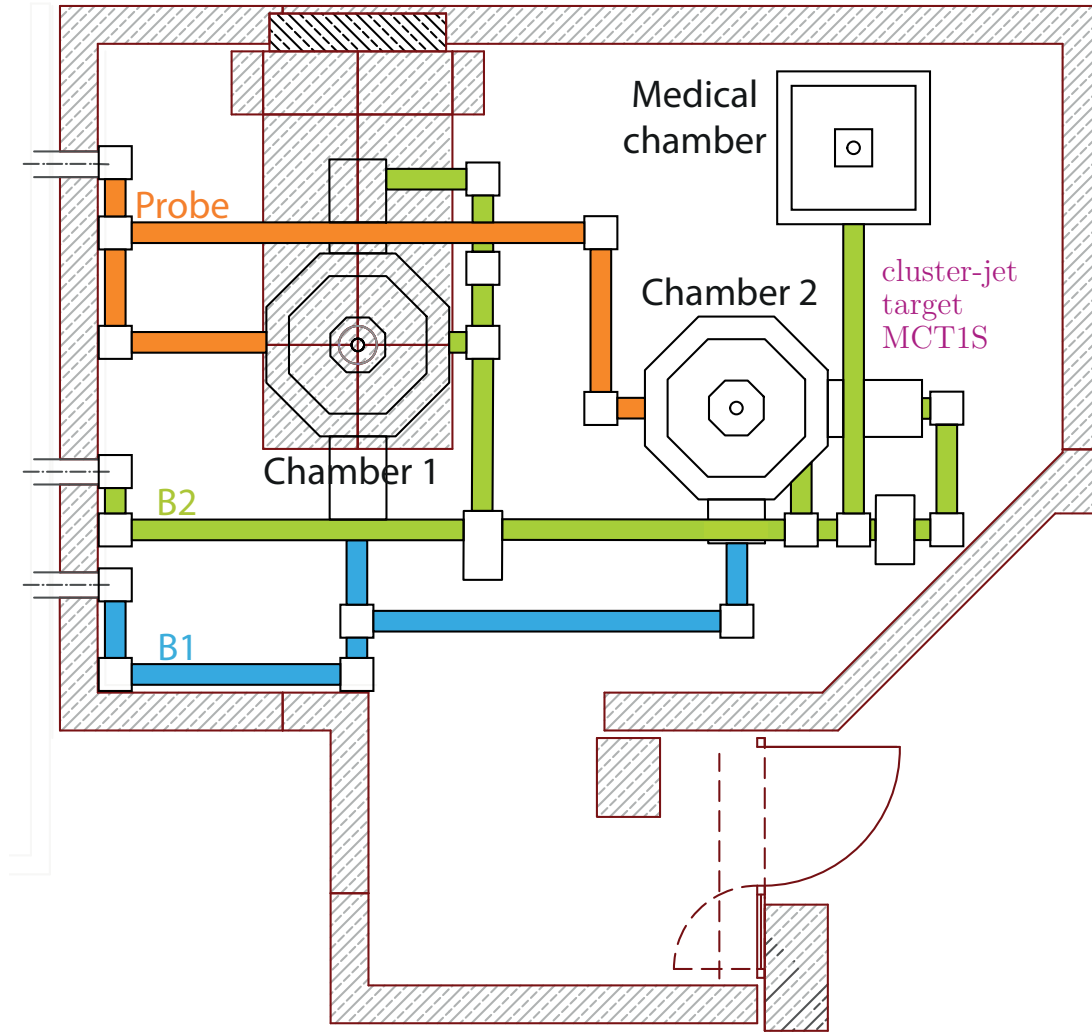
Figure 8.12: Experimental hall and the three beam lines of the laser beams (cf. Table 8.2). The cluster-jet target MCT1S is installed on the right wall of chamber 2. The cluster beam direction is from right to left. The laser beam B1 (blue) was used to investigate the cluster-laser interaction. Both, the cluster beam as well as the laser beam are parallel to the ground. The interaction between the cluster and laser beam is placed in the center of chamber 2. For radiation shielding and protection from high energy particles the experimental hall is enclosed with special concrete walls (gray), taken from [Sch18]. Thanks to A.-M. Schroer (HHUD).

9 Investigations on Cluster-Laser Interaction

The interaction of high intensity lasers with clusters allows for the acceleration of electrons, ions, and for the generation of X-rays (see chapter 8.1) [K$^+$01,R$^+$04]. First measurements with respect to the cluster-laser interaction and their results will be presented in this chapter. To investigate these effects and the underlying physical processes, a cluster-jet target was installed at the U1 and at the U2 laser system of the University of Düsseldorf.

9.1 Studies on Cluster-Laser Interaction using the U1 Laser System

The cluster-jet target MCT1S (see chapter 8.3) was built up and set successfully into operation in the framework of a previous master thesis [Gri14]. Additionally, systematic studies on the target performance and on the cluster beam for the cluster-laser interaction were performed. Therefore, an optical, non-destructive, relative thickness monitor system was investigated. A laser diode ($\lambda = 650$ nm, $P = 1$ mW, $\varnothing = 6$ mm (expanded)) illuminates the cluster beam and a CCD camera (pco.pixelfly usb) mounted in an angle of 90 ° with respect to the laser diode obtains a picture of the interaction zone (see Figure 5.5). Opposite of the laser a blackened conical beam dump is installed to reduce the scattering light of the laser. Additionally, previous studies showed a minimised background of scattered light due to the application of black cardboard in front of the reflecting parts. In the master thesis the system was installed at a distance of 33 cm from the nozzle and the feasibility of this system and first pictures were successfully performed. The principle and analysis steps are described in detail in chapter 5.1.2.

For investigations on the cluster-laser interaction, the source of the cluster-jet target MCT1S was mounted on a special aluminium frame which allows for a precise alignment of the cluster beam with respect to the laser focus. Therefore, the aluminium frame out of KANYA modules was built up on four height-adjustable feet. Furthermore, between the source and the frame a slip band was installed to move the target source perpendicularly to the laser beam. These possibilities for a precise adjustment were very important, because the U1 laser focus of roughly $10\,\mu m - 40\,\mu m$ had to overlap with the cluster beam. To adjust and control the cluster beam position with respect to the laser beam, the optical monitor system was used (cf. Fig. 8.7).

The cluster-laser interaction at the U1 laser system took place in a distance of roughly 90 cm from the nozzle. Since there was no opportunity to install the optical monitor
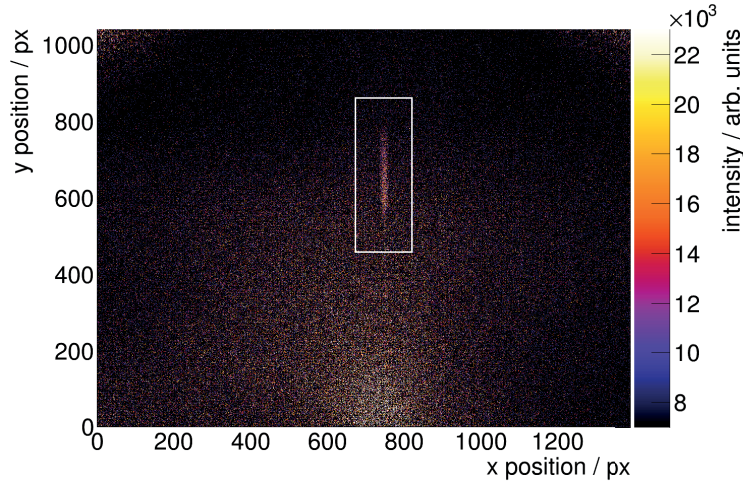
Figure 9.1: Image of the cluster beam recorded with the optical monitor system at the beam dump of the $\overline{\text{P}}$ANDA cluster-jet target prototype. 20 pictures with exposure times of 1 min of the cluster beam were made and added up and background corrected. The cluster beam was produced with the glass nozzle with the second extension at 17 bar and 25 K. The cluster beam direction is from left to right. The laser beam direction is from top to bottom. The small vertical bright line within the white box (x position of roughly 750 pixels) represents the cluster beam. The width in horizontal direction is defined by the laser beam diameter. The vertical length represents the cluster beam diameter. Data obtained together with C. Hargens [Har16].

system directly inside the interaction chamber, the system had to be installed outside at the opposite wall of the interaction chamber in relation to the cluster source (cf. Fig. 8.7). The distance from the nozzle was therefore enlarged to 160 cm, due to the straight expansion of the cluster the distance for the cluster position determination is not significant. To examine the performance of the optical monitor system at larger distances than 33 cm, the system was installed at the end of the beam dump of the $\overline{\text{P}}$ANDA cluster-jet target prototype (chapter 4.3) at a distance of more than 5 m. There, the cluster beam was larger than the field of view of the camera. Therefore, an orifice with an opening of $\varnothing = 3$ mm was installed at the interaction chamber to reduce the cluster beam size at the monitor system to obtain a cluster beam part of well defined size. A cluster beam diameter of roughly (7.5 ± 0.2) mm was expected at the monitor system and due to the relatively low thickness in this distance from the nozzle, 20 pictures with exposure times of 1 min of the cluster beam were taken and added up. To reduce the background, a picture with an exposure time of 1 min without cluster beam, thus showing the scattered light, was subtracted 20 times. Figure 9.1 shows the result of the optical monitor system. The corresponding projection on the ordinate (736 px - 765 px) where the cluster beam is located, is depicted in Figure 9.2 and indicates a cluster beam diameter of (250 ± 5) px which is equivalent to (7.5 ± 0.2) mm $((1)\,\text{px} \equiv (0.033 \pm 0.001)\,\text{mm}$ [Gri14]). It therefore demonstrates that the optical monitor system is applicable for the alignment of the cluster-jet target MCT1S to the laser focus.
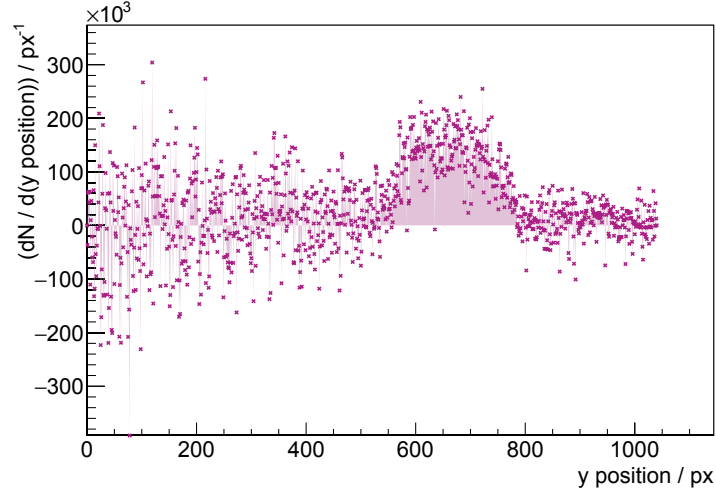
Figure 9.2: Resulting projection on the ordinate (736 px - 765 px) where the cluster beam is located of Fig. 9.1. The projection presents the properties of the cluster beam. A peak in the intensity between the y position of roughly 550 pixels and 800 pixels is clearly visible. This corresponds to a cluster beam diameter of (7.5 ± 0.2) mm using the conversion from pixels to millimetre.

## Alignment of the Cluster-Jet Target MCT1S to the U1 Lase

The cluster-jet target MCT1S was installed at the U1 laser system in spring 2016. C. Hargens [Har16] determined the centre of the vacuum chamber used for the optical monitor system to (507 ± 10) px to have a reference point for the adjustment. At the U1 laser system a cluster beam diameter of 10.90 mm or 363 px was expected in a distance of 160 cm, the distance of the optical monitor system, from the nozzle. Thereupon, following the adjustment of the cluster source was performed. For a horizontal as well as vertical adjustment the vacuum chamber of the monitor system could be used, due to its rotationally symmetric construction. Thereby, the chamber had only to be rotated by 90°. For this analysis system the hydrogen in front of the nozzle has to be liquid and therefore, the hydrogen was cooled down to a temperature of 26 K and the pressure was increased to 14 bar. Figure 9.3 shows the picture of the cluster beam (background subtracted) and the corresponding projection after the horizontal alignment. The centre of the cluster beam is now located at (517 ± 10) px and has a diameter of 342 px $\cong$ 10.25 mm which matches the expected value of 363 px $\cong$ 10.90 mm considering the smearing parameter of $s = 29$ px $\cong$ 0.85 mm.

During the analyse of the projection the automatic background subtraction routine did not work perfectly. However, for determination of the cluster beam position and width, this is from no relevance here.

The alignment in vertical direction included an increase of the height of the complete cluster source by 8 mm. Therefore, the set point of the cluster beam center changed to (240 ± 5) px. Figure 9.4 represents the cluster beam and its projection after the alignment.
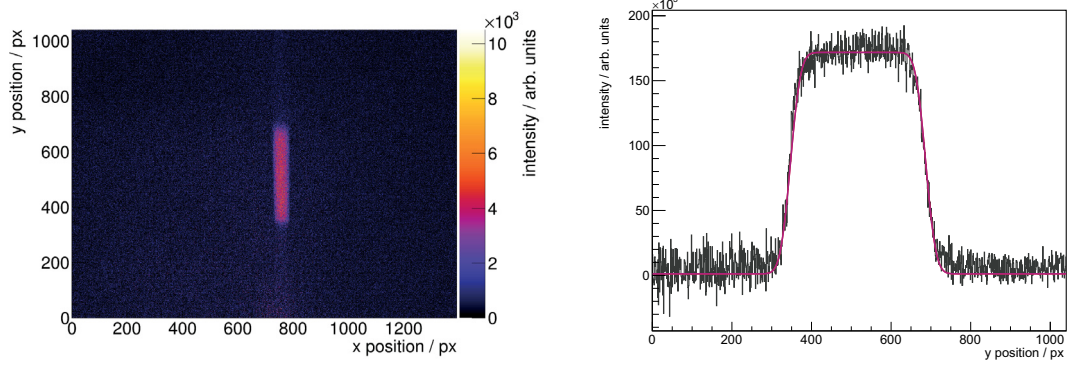
Figure 9.3: *Left.* Picture recorded with the optical monitor system after the alignment of the cluster-jet target MCT1S to the U1 laser beam with respect to the horizontal direction. The cluster beam direction is from left to right and the laser beam goes from top to bottom. The cluster-jet target was adjusted to 14 bar and 26 K. *Right*: The projection on the ordinate shows a clearly visible cluster beam.
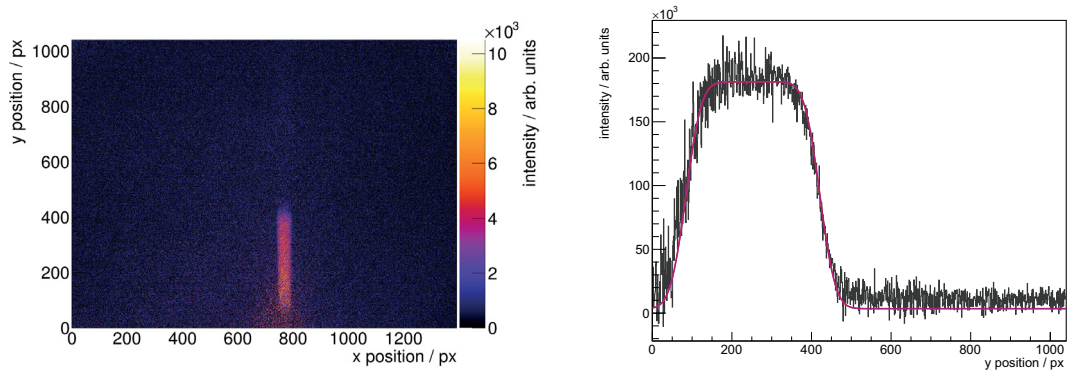

Figure 9.4: Image (*left*) and projection (*right*) showing the cluster beam after the alignment with respect to the vertical direction recorded with the optical monitor system. The cluster beam direction if from left to right and the laser beam goes from top to bottom. The cluster-jet target was adjusted to 14 bar and 26 K.

The center of the cluster beam is located at (253 ± 5) px and the diameter is determined to 338 px $\cong$ 10.13 mm with the smearing parameter of $s = 44$ px $\cong$ 1.32 mm.

The results gained with the optical monitor system at the U1 laser system showed that the system was ideally suited to adjust the cluster source to the laser beam. The center of the cluster beam now matched the laser focus with a very low uncertainty and the cluster beam diameter was as wide as expected.

Nozzle Shutter

The installed nozzle shutter allowed for a high repetition on/off switch of the cluster beam to reduce the gas flow of the cluster beam into the interaction chamber. A CAD drawing of the nozzle shutter is depicted in Figure 8.6. The shutter of the nozzle shutter can be
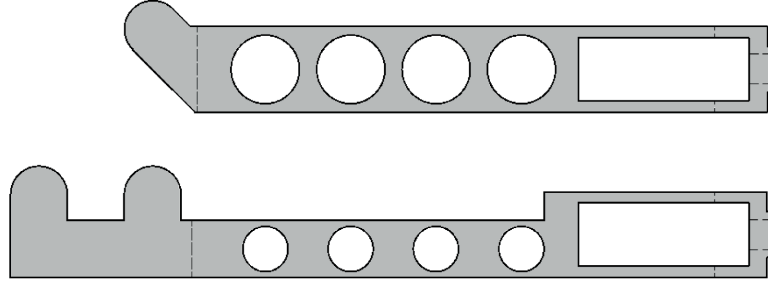
Figure 9.5: Two different designed and studied shutters for the nozzle shutter. *Top*: Single aperture. *Bottom*: The double aperture allows the blocking of the cluster beam in two different positions. The holes reduce the weight and the inertia of the shutter. Generated by D. Bonaventura, edited.

exchanged. Two designed and studied apertures are shown in Fig. 9.5.

Investigations performed in the framework of the bachelor thesis of S. Bölsker [Bö15] showed that the double aperture is ideally suited for the desired application. In this case the shutter is closed, when the aperture is at the position 36 mm or 56 mm (Fig. 9.6). The shutter remains on a closed position till a rising trigger edge is registered. Then the shutter moves with an acceleration of $300 \, \text{m/s}^2$ and a velocity of $7 \, \text{m/s}$ to the other position corresponding to a pulsed cluster beam with 10 Hz which matches the repetition rate of the U2 laser (cf. Fig. 9.6). This motion sequence is repeatable to ensure measurements with this high repetition rate. This motion profile was programmed on the hardware of the device to run automatically.

The nozzle shutter was successfully tested in vacuum with the desired high repetition rate of 10 Hz. Moreover, the shutter in combination with a cluster beam at 14 bar and 28 K was studied. Thereby, the vacuum conditions in the three chambers, collimator chamber, interaction chamber, and beam dump, of the cluster-jet target in dependence of the nozzle shutter were measured (cf. Fig. 9.6). An open shutter and a cluster beam entering the chambers leads to a high vacuum pressure, whereas, a blocked cluster beam results in low vacuum pressures. The impact of the nozzle shutter on the vacuum pressures in all three chambers is clearly visible. In addition, the positions of the shutter where the cluster beam is blocked, can be extracted from Figure 9.6. More details can be found in [Bö15].

First measurements on the cluster-laser interaction using a spectrometer show no results, as expected, due to the relatively low thicknesses of $\sim (10^{13} - 10^{14})$ atoms/cm^2 at the laser focus in a distance of roughly 90 cm from the nozzle. Therefore, the cluster-jet target was modified to higher thicknesses via a lower distance between interaction point and nozzle. The details of the modification are described in chapter 8.3. Henceforward, the interaction took place directly behind the nozzle, where the highest thicknesses of up to 2.5×10^{16} atoms/cm^2 can be achieved.
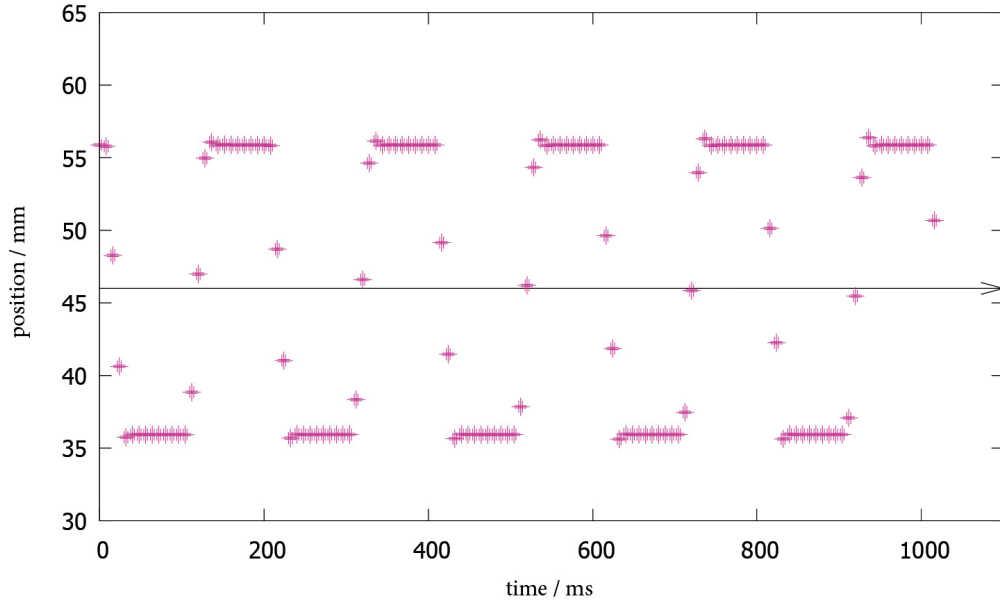
Figure 9.6: Position of the aperture with a repetirion rate of 10 Hz. In time distances of 100 ms the aperture switches between the positions 38 mm and 58 mm. The positions were adjusted to the setup of the cluster-jet target. A passing of the horizontal line indicates the time for one single motion [Bö15].
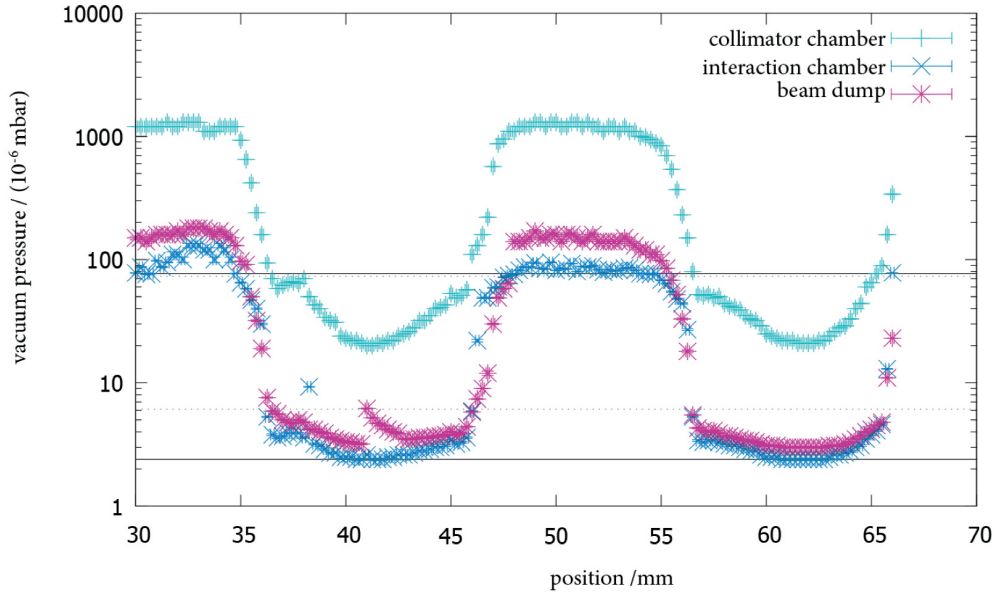
Figure 9.7: Influence of the nuzzle shutter position on the vacuum pressure in the cluster-jet target chambers. An open shutter leads to a high vacuum pressure and a blocked cluster beam to a low vacuum pressure. Clearly visible are the positions corresponding to an open or closed nozzle shutter (indicated with the horiziontal lines). The jump at roughly 37 mm in the vacuum of the collimator chamber and at roughly 41 mm of the vacuum in the beam dump is induced by artefacts of the used vacuum gauge [Bö15].

Table 9.1: Characteristics of the Balmer lines [Dem15] [K$^+$18].

name	transition of n	wavelength / nm	energy difference / eV	color
Hα	3	656.279	1.89	red
Hβ	4	486.133	2.55	aqua
Hγ	5	434.046	2.86	blue
Hδ	6	410.173	3.03	violet
Hε	7	397.007	3.13	ultraviolet

Observation of Balmer Lines

To study the cluster-laser interaction, a grating spectrometer (Andor, Shamrock 303i) in combination with a 14 bit camera was mounted in $15°$ with respect to the laser beam direction. Grating spectrometers use the optical diffraction of light on a grid to generate interference, which produces a wavelength spectrum. If the laser interacts with the clusters, a plasma is generated and a typical spectrum is emitted. The measurement was performed with hydrogen as target material. Therefore, the spectrum of the plasma will show the spectral lines of the hydrogen atom. The measurement was performed with various stagnation conditions of the hydrogen in front of the nozzle. Figure 9.9 shows such a measurement with a pressure of 18.2 bar and a temperature of 38 K of the hydrogen in front of the nozzle. Figure 9.10 presents the corresponding projection on the abscissa. Due to the wide range of wavelengths in the spectrum, two different pictures had to be recorded to cover the whole observable spectrum. The top picture illustrates four visible peaks at the wavelengths 397.007 nm, 410.173 nm, 434.046 nm and 486.133 nm (see Table 9.1). It was recorded with an exposure time of 60 s. The bottom picture, recorded with a exposure time of 20 s shows a peak at a wavelength of 656.279 nm. These spectral lines corresponds to the beginning of the Balmer lines. The emission takes place, when an electron of a hydrogen atom transits from a shell $n \geqslant 3$ to $n = 2$, wherein n is the number of the shell or the principal quantum number (see Fig. 9.8, Table 9.1). The bright spot on Figure 9.9 (top) corresponds to the second-harmonic generation of the laser at a wavelength of roughly 400 nm.

Figure 9.10 shows the projections on the abscissa of Fig. 9.9. There are five peaks visible (four in the left and one in the right) at the pixel positions of roughly 1100, 1375, 1880, 3000, and 2360. Additionally, a large background occurs caused by the second-harmonic generation of the laser (left). To calculate the intensities of the individual Balmer lines, every peak was analysed individually. Therefore, each peak was considered within a pixel intervall width of roughly $(300 - 1000)$ pixels with only one individual peak in the center. To get rid of the background, an adaptation using a polynomial of second order was subtracted. The resulting peak was adapted with a Gaussian distribution, the integral was calculated and at the same time, the bin contents were summed up. Both analysis methods lead to the same value, so consequently the summation of the bin contents was made for all five peaks for all performed measurements.
The resulting intensity of the Balmer lines depending on the temperature of the cluster-jet
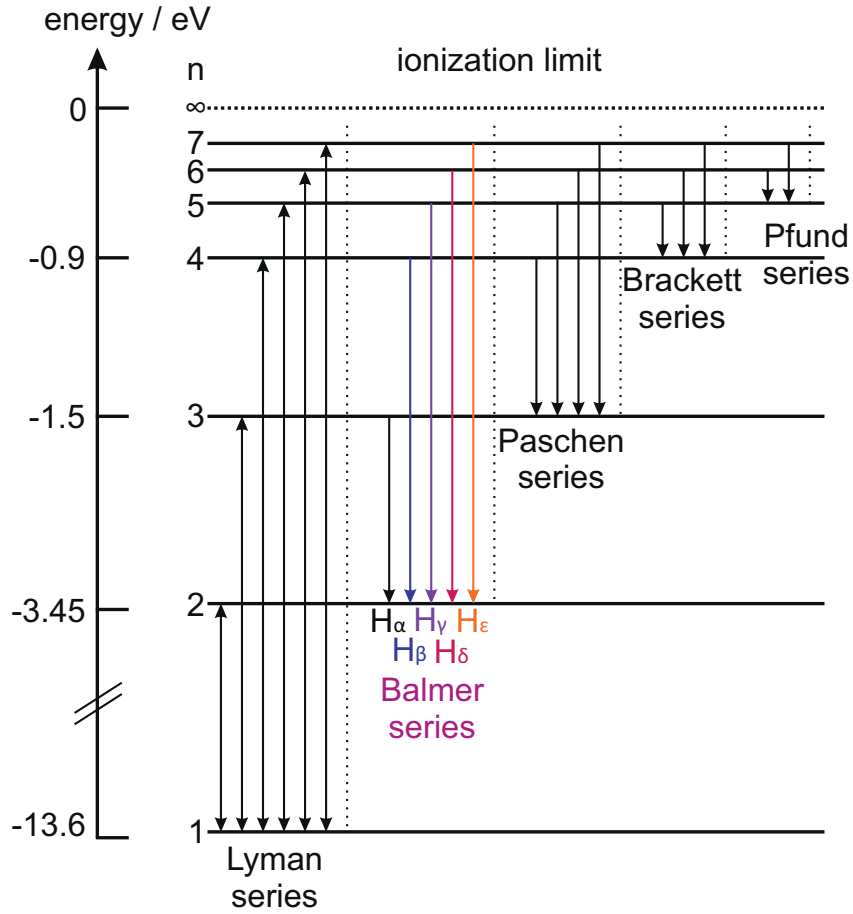
Figure 9.8: Sketch of the energy lebels of hydrogen with different emission- and absorption-lines. The Balmer serie corresponds to the transition from $n > 2$ to $n = 2$. Based on [Dem15].

target are shown in Fig. 9.11 (top) and for the pressure in Fig. 9.11 (bottom). The lines through the data are discussed later in this section. The intensity increases with increasing pressure and decreasing temperature. This specific change of the stagnation conditions leads to an increase of the gas flow through the nozzle and therefore, a higher volume density. Moreover, the mass and size of the clusters increases. The increase of the intensity of the Balmer lines in dependency of the target volume density in logarithmic scale is presented in Fig. 9.12.

A clear rise in intensity for each Balmer line with increasing density is visible. The intensities of the Hε (yellow stars) line fluctuate a bit, this is caused by the relatively low signal-to-background ratio. The Hα (black crosses) shows a less strong rise compared to the other lines. This line is the most pronounced line with the highest intensities, therefore, a saturation of the camera occured which leads to a constant intensity. For this reasons, the Hε and Hα lines are no longer included in the following analysis.
At the three remaining lines (Hβ, Hγ, and Hδ), an adaptation of the form

$$I(x) = \exp^{a + b \cdot x + c \cdot x^2}, \tag{9.1}$$
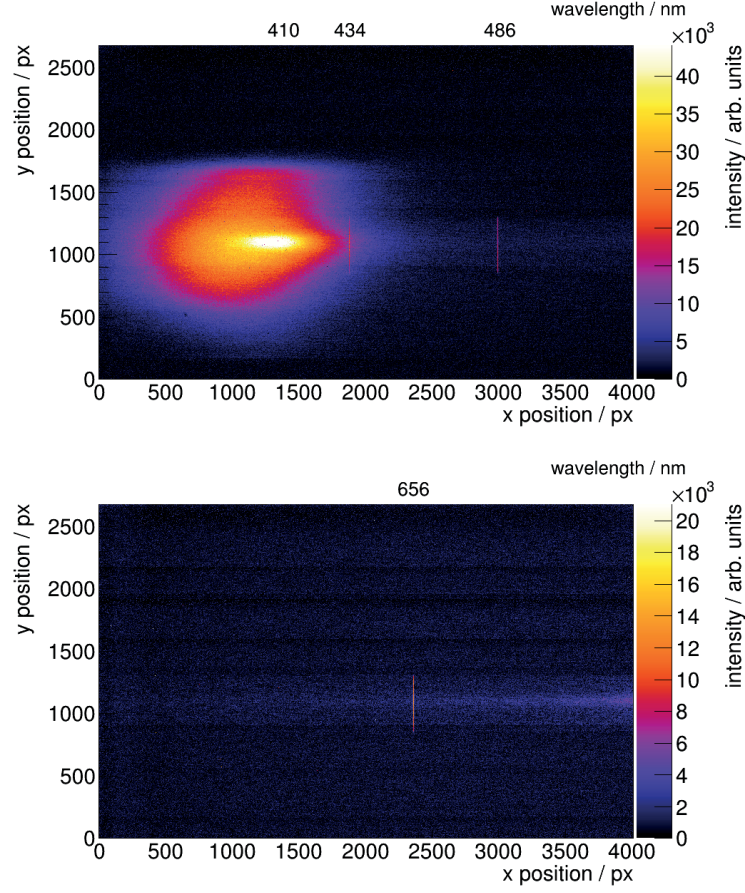
Figure 9.9: Balmer lines measured with a spectrometer resulting from cluster-laser interaction. The cluster beam was adjusted to a pressure of 18.2 bar and a temperature of 38 K. The top image was recorded with an exposure time of 60 s, the bottom one with 20 s. The wavelength increase from left to right. Five spectral lines are visible. The bright spot corresponds to the second-harmonic generation of the laser.

was performed, wherein I is the intensity and x the density. The gained three specific functions with the calculated parameters a_i, b_i, and c_i are also displayed in Figures 9.11. There, the fit function is also in good agreement with the data points.

The observation of the Balmer line intensities allow for the determination of the plasma temperature during the cluster-laser interaction. The occupation numbers $N_1, N_2, N_3, ...$ of the energy states with the corresponding energies $E_1, E_2, E_3, ...$ are defined by the Boltzmann distribution. As long as the system is in thermal equilibrium their ratio is [EE10]

$$\frac{N_2}{N_1} = \exp\left(-\frac{E_2 - E_1}{k_\text{B} T}\right) . \tag{9.2}$$

Therein, $k_\text{B} = 8.6173303(50) \cdot 10^{-5}$ eV/K [EE10] is the Boltzmann constant and T the absolute temperature. The ratio of the occupation N_2/N_1 can be interpreted as the ratio
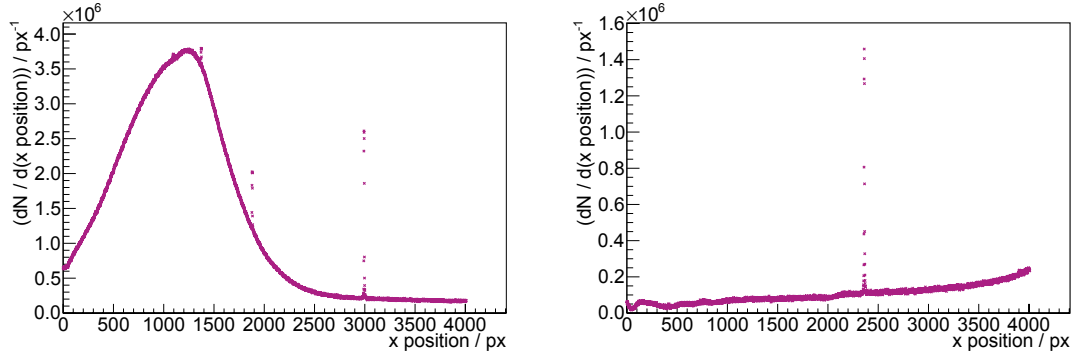
Figure 9.10: Projections on the abscissa from the two pictures of Fig. 9.9. Clearly visible are the four peaks in the left projection and one peak in the right projection in the intensity corresponding to the Balmer lines. The upper projection shows a large background under the peaks of the Balmer lines caused by the second-harmonic generation of the laser. Therefore, a background subtraction has to be performed.
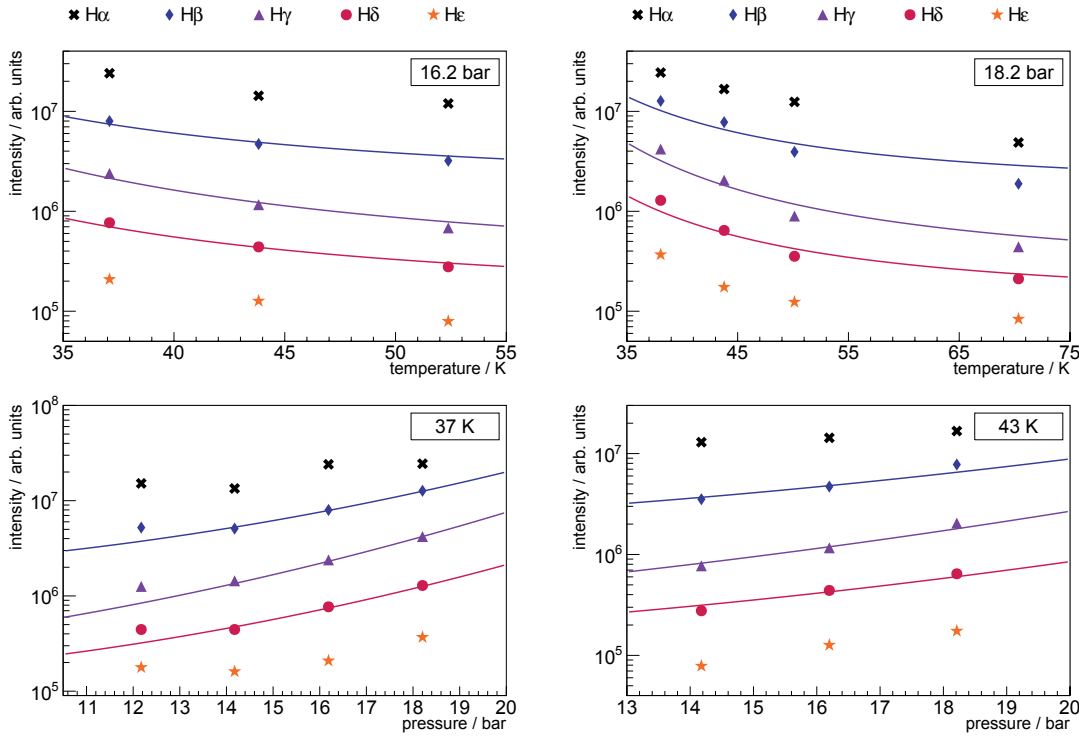
Figure 9.11: *Top*: Balmer line intensities in dependence of the hydrogen temperature in front of the nozzle for two different pressures: 16.2 bar and 18.2 bar. *Bottom*: Intensities of the Balmer lines in dependency of the cluster beam pressure for two different temperatures: 37 K and 43 K.

of the intensities of the Balmer lines I_2/I_1. Consequently, out of this relation, the plasma temperature can be calculated

$$T = \frac{E_1 - E_2}{\ln\left(\frac{I_2}{I_1}\right) \cdot k_\mathrm{B}}. \tag{9.3}$$
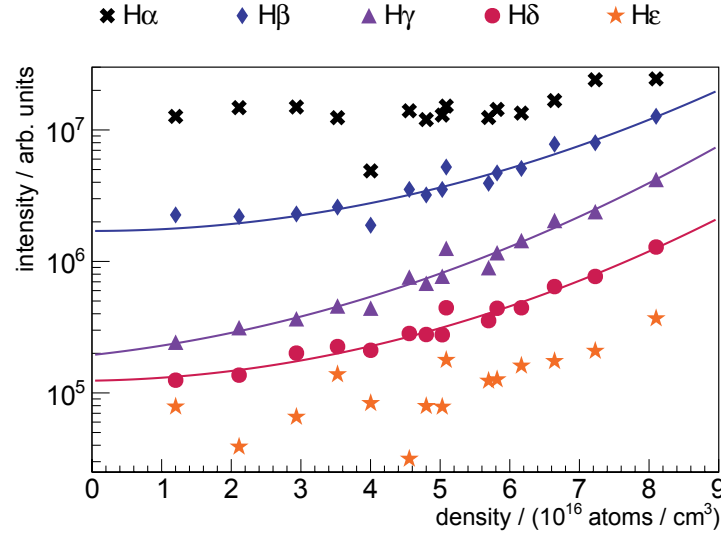
Figure 9.12: Intensity of the Balmer lines in dependence of the calculated cluster beam density. Additionally, fits on the course of Hβ, Hγ, and Hδ are performed with Eq. (9.1).

The relation of the intensities I_2/I_1 were calculated using the fits out of Fig. 9.12. The energies E_1 and E_2 for each individual Balmer line can be found in Table 9.1. The calculated plasma temperatures are shown in Fig. 9.13. The plasma temperatures determined with the Hβ-Hγ and Hβ-Hδ show in comparison to Hγ-Hδ an increase with increasing density. This behaviour was expected, because a higher density leads to a stronger interaction resulting in a higher plasma temperature. The curve with a negative gradient is not in agreement with the expectations, thus, further investigations of systematic uncertainties due to camera, spectrometer, and other experimental effects are necessary. Nevertheless, during the observed cluster-laser interaction, plasma temperatures between 1600 K and 4500 K were calculated. Within a certain target density, the plasma temperatures agree within a factor less than three. This is a first important result concerning the cluster-laser interaction. It has not only been demonstrated that the interaction takes place, but also that the interaction is quantifiable via the Plasma temperatures gained from the performed measurements. For future more quantitative studies on this topic, the wave length dependent spectrometer efficiencies for the detection of photons have to be determined, which was not possible for the pilot measurements presented here.

9.2 Studies on Cluster-Laser Interaction using the U2 Laser System

After these first successful results with the cluster-jet target MCT1S at the U1 laser system, the target was mounted at the U2 laser system to study the cluster-laser interaction with even higher laser energies (cf. Figure 8.8). Due to the complex optics inside the interaction
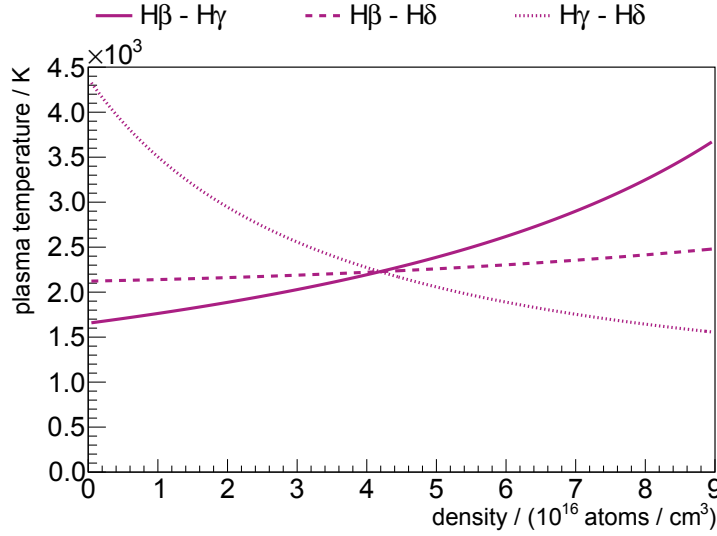
Figure 9.13: Plasma temperature calculated using the Balmer line intensity relations resulting from cluster-laser interaction. As expected, Hβ-Hγ and Hβ-Hδ show an increase of the plasma temperature with increasing density. The plasma temperatures achieve values between 1600 K and 4500 K.

chamber for the laser, the interaction of the cluster beam with the laser has to take place in the centre of the chamber. To achieve a high target thickness in that position, a cold finger between the cold head and the nozzle was established. Therefore, the interaction takes place in a distance of 2.85 cm from the nozzle to the center of the chamber. Most of the measurements were performed with hydrogen gas as target material, measurements with different gases, like argon and nitrogen, are especially mentioned. The given laser energy is measured not directly in the interaction chamber, but in the laser room. Due to the optics used to guide the laser beam to the interaction point and a thin optical window (pellicle) to separate the vacuum of the interaction chamber from the vacuum in the laser beam line, only roughly 27 % of the laser energy is available at the interaction point.

At the time of the measurements performed and presented within this thesis, the laser achieved a maximum energy of 4.8 J in the laser room, with a wavelength of (800 ± 50) nm and a pulse length of 35 fs at the interaction point [Aur17].

The cluster-jet target density in case of hydrogen was varied between 3.8×10^{16} atoms/cm^3 at 16 bar and 50 K and 5.2×10^{16} atoms/cm^3 at 16 bar and 36.7 K (using Eq. (5.2)). A decrease in the pressure leads to an even lower target density of 7.2×10^{15} atoms/cm^3 at 3 bar and 50 K.

9.2.1 Spectroscopy of Emission Lines

After the successfully observed Balmer lines within the interaction of the clusters with the U1 laser, a spectrometer was set up at the U2 laser system. The spectrometer was installed at 45° with respect to the laser beam in forward direction. First measurements performed with hydrogen at the maximum achievable density at 16 bar and a readily
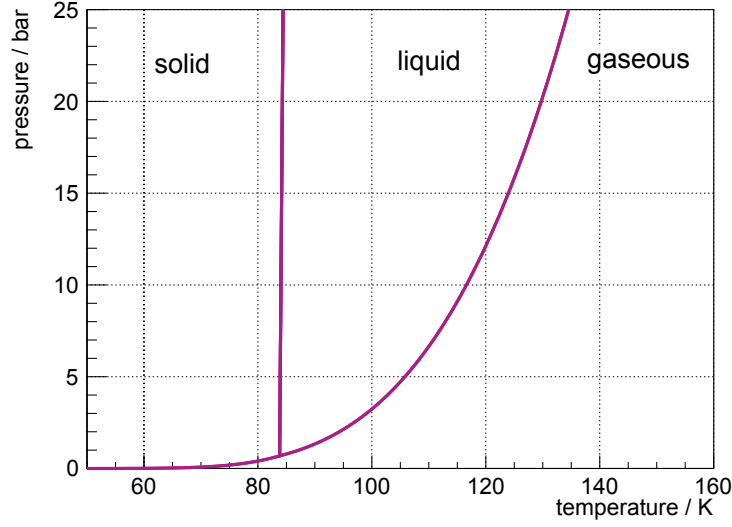
Figure 9.14: Vapour pressure curve for argon. Liquid argon in front of the nozzle is realisable at higher temperatures, i.e. below 125 K compared to hydrogen at 16 bar [Liq].

accessible temperature of 45 K, due to the missing insulation vacuum chamber, showed no signal, neither by a single pulse of the laser nor by an integration over 60 laser pulses. An additional moveable gas jet nozzle below the interaction point allowed for investigations on gas jet-laser interactions. Using the gas jet target for the measurement with the spectrometer, the camera was oversaturated by the supercontinuum of the laser.

The measurements performed with the hydrogen cluster beam used gaseous hydrogen in front of the nozzle. The modification of the MCT1S resulted in the removal of the insulation vacuum chamber. Therefore, the cooling power of the cold head was limited and was not sufficient to cool the hydrogen down to temperatures where its liquid. Liquid hydrogen in front of the nozzle leads to a higher target thickness and larger cluster sizes. For this reason, it is possible that only liquid hydrogen in front of the nozzle results in spectral lines observable with this setup.

The transition from the gaseous to the liquid phase of argon occurs at higher temperatures in the pressure range where a cluster-jet target operates (cf. Fig. 9.14). Therefore, the cluster-jet target was modified to operate with argon. The Laval nozzle had to be changed due to the higher mass of argon in comparison to hydrogen to ensure a similar gas flow through the nozzle resulting in a similar target thickness. The nozzle geometry stayed the same, only the narrowest inner diameter was enlarged to roughly $\varnothing = 83\,\mu$m. Additionally, a temperature diode and a heating cartridge were installed at the warm stage of the cold head to ensure that the argon did not solidify at this stage and block the gas pipes.

The resulting images of 60 laser pulses are shown in Fig. 9.15. During the measurement series, the laser energy was set to 2.8 J. The first measurement was performed in the liquid state of argon at 16 bar and 110 K (top). There, a target density of 1.5×10^{17} atoms/cm^3 was realised. The spectrometer was adjusted to a central wavelength of roghly 700 nm. At the same stagnation conditions the spectrometer was additionally adjusted to a central
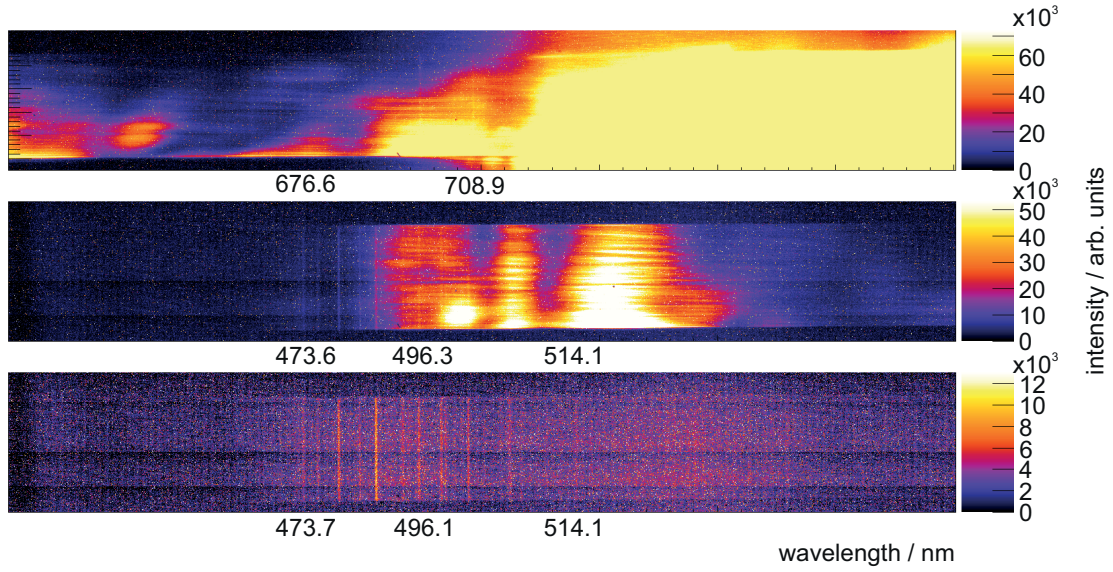
Figure 9.15: Images resulting from spectroscopy measurements. *Top*: Argon clusters at 16 bar and 110 K (liquid) with a central wavelength of 700 nm. *Center*: The same stagnation conditions as before, but the central wavelength was adjusted to 500 nm. *Bottom*: Measurement with gaseous argon in front of the nozzle (15 bar and 126 K) with a central wavelength of 500 nm. In all cases the emission lines of argon are clearly visible. The corresponding positions and wavelengths are shown in Table 9.2. The measurements performed in the liquid state additionally show bright areas corresponding to the supercontinuum of the laser.

wavelength of roughly 500 nm to see a different wavelength range (center). The third measurement was done in the gaseous phase of argon at 15 bar and 126 K (bottom) with a target density of 1.2×10^{17} atoms/cm^3. For comparison here, the central wavelength of the spectrometer was also set to 500 nm.

In all cases vertical lines corresponding to the emission lines of argon are clearly visible. Especially, both measurements at the same central wavelength show the same emission lines. Additionally, the image recorded with liquid argon compared to gaseous argon shows a bright area in the wavelength range above 710 nm. This spot corresponds to the supercontinuum of the laser. Consequently, the different interactions of the laser with the clusters produced in the liquid or gaseous phase are explained by the differences in density and mass.

Table 9.2 summarises the pixel positions of the emission lines, the corresponding wavelengths and for comparison literature values. The determination of the pixel positions, as well as the calibration, and conversion to the wavelengths were done by B. Aurand (HHUD). Due to the high backgrounds underneath the data, no further analysis, like in section 9.1, can be done.

9.2.2 Energy Absorption of Clusters

The absorption of the laser energy by clusters can be measured. To this end, a calorimeter measures the energy of the laser pulse after the interaction with the clusters. The absorbed

Table 9.2: Spectroscopy result using an argon cluster-jet target. The wavelength is labelled with λ. The first block was recorded with a central wavelength of $700\,\text{nm}$, the other two at $500\,\text{nm}$. The arrangement is the same as in Fig. 9.15. The analysis was done by B. Aurand (HHUD).

pressure	temp.	physical state	location	calculated λ	literature λ
bar	K	of argon	px	nm	nm
16	110	liquid	1032	665.5	664.3
			1120	669.6	668.4
			1272	676.6	675.3
			1743	698.4	696.5
			1968	708.9	706.7
16	110	liquid	1250	473.6	473.5
			1311	476.4	476.4
			1396	480.3	480.6
			1561	488.0	487.9
			1673	493.2	493.3
			1740	496.3	496.5
			1833	500.6	500.9
			1855	501.6	501.7
			1947	505.9	506.2
			2124	514.1	514.1
15	126	gaseous	1252	473.7	473.5
			1308	476.3	476.4
			1400	480.5	480.6
			1484	484.4	484.7
			1556	487.8	487.9
			1736	496.1	496.5
			1828	500.4	500.9
			1852	501.5	501.7
			1944	505.7	506.2
			2124	514.1	514.1

energy is a measure for the strength of the interaction between clusters and the laser. First measurements performed with a gas jet target are shown in Fig. 9.16. There, a gas jet nozzle with a narrowest inner diameter of $\varnothing = 1\,\text{mm}$ and an outlet diameter of $\varnothing = 2\,\text{mm}$ was directly placed beneath the focus of the laser beam. The gas in front of the nozzle was at room temperature and the gas pressure was varied to see the dependency of the absorption. The measurement presented in Fig. 9.16 at the top used hydrogen as target material. The laser energy was determined to $2.17\,\text{J}$ in the U2 laser room. Due to the optics in the laser beam line its efficiency was determined to roughly $27\,\%$. Additionally, the laser energy was measured with a calorimeter placed directly behind the interaction point of the gas jet with the laser pulse ($0°$ in forward direction with respect to the laser beam direction). This calorimeter showed a laser energy of $0.64\,\text{J}$ and will later be used for calculating the absorption of the gas jet. The pressure of the hydrogen gas jet was varied between $5\,\text{bar}$ and $40\,\text{bar}$. For every data point, at the already mentioned laser energies, 5 single laser pulses were used. The uncertainties are given by
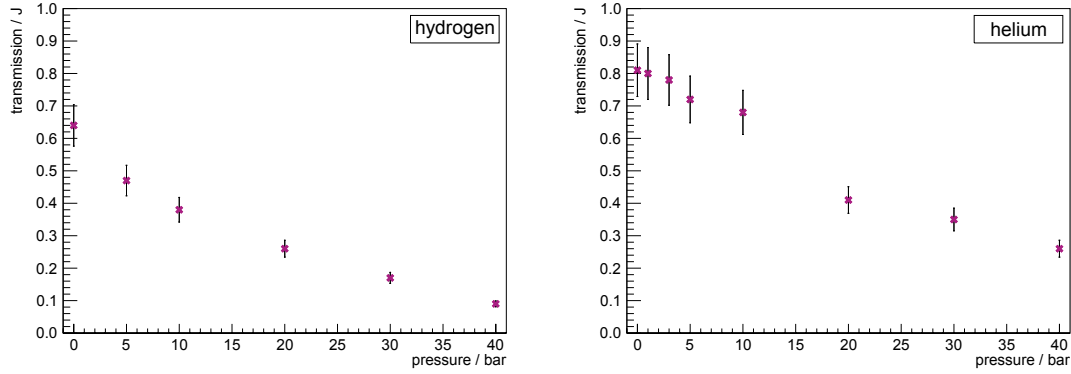
Figure 9.16: Transmission measurements for a hydrogen (*left*) and helium (*right*) gas jet. A strong dependency of the pressure can be seen. A high gas jet pressure (high target density) leads to a lower transmission of the laser energy.

the standard deviation of the five measurements performed within same conditions and were determined to 10 %.

The same measurement performed with helium gas as target material is shown in Fig. 9.16 on the right. There, the laser energy was determined to 2.78 J in the laser room and 0.81 J at the experiment location. These energies were measured several times in-between the measurements with the gas jet to ensure a stable operation of the laser. For every data point, 10 single laser pulses were used.

Both measurements show a strong dependency of the transmission from the gas pressure. The higher the pressure and therefore the density, the lower the transmission, corresponding to a higher absorption of the laser energy within the gas jet. Thus, a high density of the gas jet beam results in a higher absorption of the laser energy and a stronger interaction between them.

Figure 9.17 shows measurements using the cluster-jet target MCT1S. The dependency of the transmission of the laser energy from the pressure of the hydrogen in front of the nozzle was measured (left). The temperature was adjusted to 50 K. The laser energy was 2.48 J in the laser room and 0.70 J directly at the interaction point. For every data point, 10 single laser pulses were used and the laser energy was measured in-between every measurement to ensure a stable laser energy. The uncertainties are given by the standard deviation of the five measurements performed within same conditions and determined to 10 %.

Figure 9.17 (right) shows the temperature dependency of the laser energy transmission. There, the pressure of the cluster jet beam was adjusted to 16 bar. The laser energy was measured to 2.62 J or rather 0.77 J.

The two performed studies show no significant dependency from the transmission with respect to the cluster beam parameters. Due to the cluster-laser interaction, it is expected that the transmission of the laser energy decreases with increasing pressure of hydrogen gas in front of the nozzle, resulting in a higher target thickness and larger cluster size, like it was shown for a gas jet target. The reason for that, lies in the different hydrogen
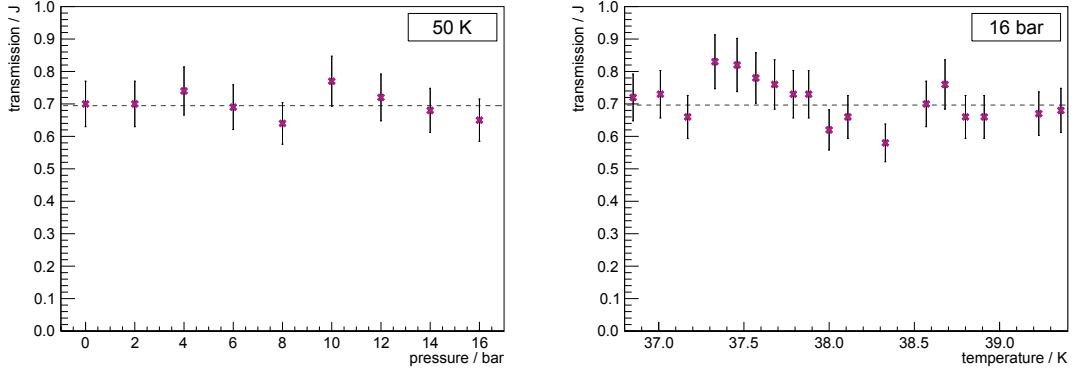
Figure 9.17: *Left*: Transmission spectra for a hydrogen cluster jet target at 50 K in dependency of the pressure in front of the nozzle. *Right*: Transmission spectra using a hydrogen cluster beam at 16 bar with temperature variations in front of the nozzle. No significantly dependency can be seen. It is expected, that the transmission of the laser energy decreases with increasing pressure of hydrogen gas in front of the nozzle resulting in a higher target thickness and larger cluster size, like it was demonstrated for a gas jet target.

thicknesses. The measurements with the gas jet target were performed with hydrogen pressures between 5 bar and 40 bar at room temperature in front of the nozzle resulting in target densities of 2.0×10^{19} atoms/cm^3 to 1.6×10^{20} atoms/cm^3. In the case of the cluster-jet target a hydrogen pressure of 16 bar at 37 K resulting in 5.2×10^{16} atoms/cm^3. Due to the much smaller narrowest nozzle of the cluster beam compared to the gas jet beam, the thickness of the gas jet beam is approximately three orders of magnitude higher. The much higher thickness yields measurable energy absorption spectra in case of the gas jet. The measurements performed with the hydrogen jet beam showed a decrease of the energy absorption of approximately 86 % within the thickness range. The cluster beam with a thickness of three orders of magnitude lower than the gas jet beam will show a decrease of the energy absorption by 0.086 %. Furthermore, the thickness of the cluster beam varied in the measured temperature range only by 4 %. Due to these facts, there will be no significantly visible signal within the uncertainties.

The idea of a combined cluster and gas jet beam to increase the absorbed energy was also tested to study the influence of a gas background on the cluster-laser interaction. There, a hydrogen cluster beam at 16 bar and 50 K was used. The helium gas jet was set to 1 bar. The influence of these two components without the other was already obtained (Fig. 9.16 and 9.17). The energy of the laser was determined to $2.71 - 2.81$ J or rather 0.81 J. The results are presented in Table 9.3. The combination of these two different target kinds does not lead to an increase of the absorbed energy.

An additional measurement was performed with argon as target material. As already mentioned (cf. section 9.2.1), using argon leads to measurements in the liquid state. There, the gas flow through the nozzle and consequently the density and cluster size is higher than in the gaseous phase.
During the measurement the laser energy was 2.62 J in the laser room and 0.81 J at the

Table 9.3: Transmission measurement with hydrogen cluster beam combined with helium gas jet beam.

target	pressure / bar	temperature / K	transmission / J
			0.81 ± 0.08
cluster jet	16	50	0.85 ± 0.09
gas jet	1	293	0.80 ± 0.08
cluster and gas jet	16/1	50/293	0.83 ± 0.08

Table 9.4: Transmission measurements with an argon cluster beam.

pressure / bar	temperature / K	phase state of argon	transmission / J
			0.81 ± 0.08
16	109.8	liquid	0.69 ± 0.07
10	112.3	liquid	0.76 ± 0.08
16	124.4	liquid / gaseous	0.68 ± 0.07
15	128.5	gaseous	0.63 ± 0.06

interaction point. This energy was measured between every individual setting of the argon cluster beam, to ensure stability. For each laser energy, 10 single pulses were used. The results show a possible slight energy absorption in dependency of the phase state of argon. To clarify this evidence, more detailed studies have to be performed (Table 9.4).

The absorption of laser energy by clusters could not be sufficiently shown in the framework of this thesis. More detailed studies, like measurements with liquid hydrogen in front of the nozzle, had to be performed. This is planned using the newly designed MCT-D cluster-jet target which is expected to provide the required target thicknesses (cf. section 9.2.6).

9.2.3 X-ray Generation

To investigate the X-rays generated by the cluster-laser interaction a X-ray camera from the company Andor was used as a diagnostic tool [AND]. The camera was mounted in forward direction with respect to the laser beam direction. In front of the camera two filters consisting of a 50 µm thick mylar foil and a 200 nm thick aluminium foil, were installed to protect the sensor of the camera from the direct laser light. These filters block photons with energies below 2.5 keV.

To figure out the relation between the cluster-laser interaction and the resulting X-rays, two different measurement series were performed. In the first series, the laser energy was adjusted to 3.2 J and the temperature of the hydrogen in front of the nozzle of the cluster-jet target was fixed to 50 K. The pressure was adjusted to three different values: 3 bar, 12 bar, and 16 bar. In the second series the cluster-jet target was adjusted to 16 bar and 50 K and the laser energy was varied: 3.2 J, 2 J, and 1.3 J.

Figure 9.18 shows an example for the pictures recorded with the Andor camera. A background image was recorded and subtracted from all images with signal. In the images, the laser energy was 3.2 J and the cluster-jet target was at 16 bar and 50 K. Figure 9.18 additionally demonstrates the analysis steps and highlights the important
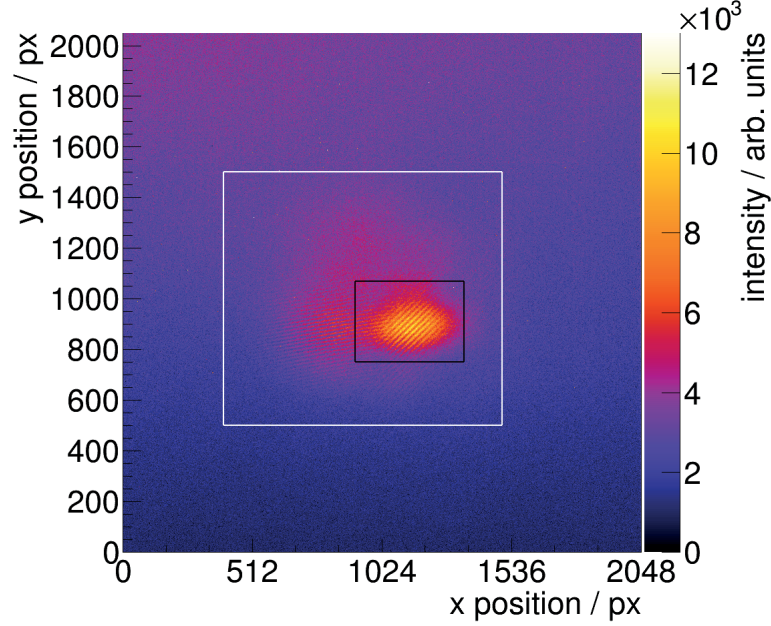
Figure 9.18: Recorded background subtracted image of X-rays with an Andor camera. The laser energy was set to 3.2 J and the cluster-jet target was adjusted to 16 bar and 50 K. The white box shows the signal, whereas the black box displays the direct laser light induced by a leak in the filter in front of the camera.

sections in the image. The big white box (abscissa: 400 pixel - 1500 pixel and ordinate: 500 pixel- 1500 pixel) displays the signal. The smaller black box (abscissa: 920 pixel - 1350 pixel and ordinate: 750 pixel- 1070 pixel) shows a very high signal, this corresponds to a leak in the filters, and the direct laser light is visible. Therefore, the intensity in the white box, subtracted by the intensity of the black box, is used as the intensity for the X-ray signal. The intensity displayed by the camera does not correspond to a count rate and is therefore given in arbitrary units with no uncertainties. The leak signal remains after the background subtraction due to photons produced by the cluster-laser interaction.

The intensity clearly increases with increasing laser energy. This is demonstrated in Figure 9.19 (left). The bright point is specially marked, because it seems that an error occured during the recording and saving of the corresponding image. It is the first picture assumed to be recorded with the lower laser energy but perhaps there the energy was as high as in the picture before, which then corresponds to a laser energy of 2 J. Afterwards, it is difficult to find out if the notation to the picture is wrong or not, therefore, the measurement is shown, but has to be handled with care. The dependency of the X-ray signal from the pressure of the hydrogen gas as target material is shown in Figure 9.19 (right). The intensity, as expected, increases with the gas pressure.

In the framework of this thesis, the main focus is on the qualitative description of the results gained on X-rays. Therefore, a detailed study on this topic with significant more
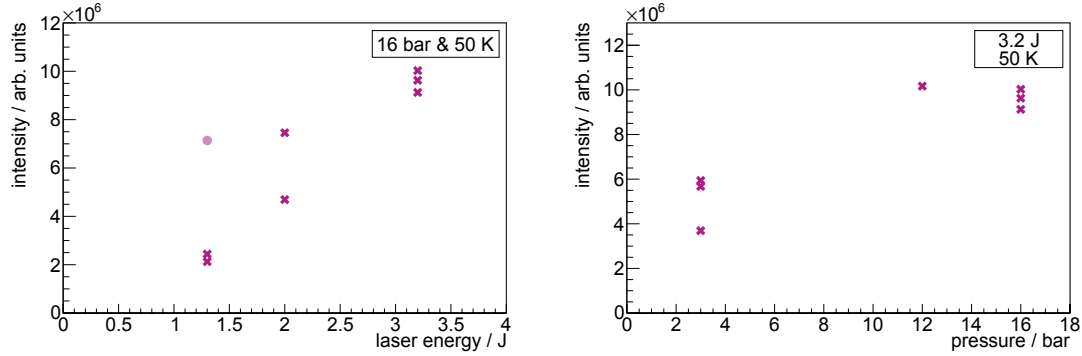
Figure 9.19: *Left*: X-ray intensity in dependency of the laser energies. The cluster-jet target parameters are fixed to 16 bar and 50 K. The intensity increases with increasing energy. The bright point is marked specially, due to the fact that it is not clear if the data point belongs to 1.3 J or 2 J. *Right*: An increase of the pressure of the hydrogen gas in front of the nozzle at stable temperature 50 K and stable laser energy 3.2 J, leads to an increase of the X-ray signal.

measurements and an intact filter in front of the camera will follow with the newly designed cluster-jet target (cf. section 9.2.6) [Leß18]. Nevertheless, the relatively few measurements show a X-ray signal generated by the cluster-laser interaction and a dependency from the cluster-jet target parameters and the laser energy as expected. Furthermore, these first measurements show the feasibility of this measurement principle and demonstrate important facts with respect to following measurements.

9.2.4 Measurements of Accelerated Protons using a Thomson Parabola

In laser plasma physics a Thomson parabola spectrometer is a well established tool to investigate the energy spectrum with high energy resolution and a separation of accelerated particles by their charge-to-mass ratio [Tho13, Sch18]. The setup is shown in Figure 9.20. A pinhole separates the detector from the interaction chamber. The application of a pinhole within the spectrometers allows for an observation of only a small part of the particles, to improve the resolution. Moreover, the photons, generated from X-rays or the laser itself would oversaturate the detector. The installation of a pinhole leaves only a small oversaturated spot at the position of the pinhole, called the zero point (cf. Fig. 9.21).

After the pinhole, a magnetic and an electric field were installed. The magnetic field deflects the charged particles vertically due to their electric charge and momentum. In the used setup, the positively charge particles are deflected to the top and negatively charged particles to the bottom. Moreover, the strength of deflection depends on the momentum of the particles. Within the magnetic field, the particle is affected by the Lorentz force F_L. The Larmor radius r_L of the particle motion can be expressed by equating the Lorentz force F_L and the centrifugal force F_Z

$$r_\mathrm{L} = \frac{mv_0}{qB_0},\qquad(9.4)$$
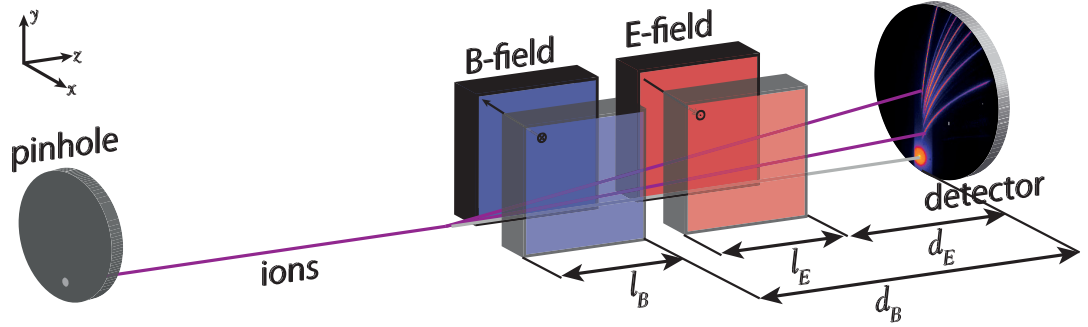
Figure 9.20: Sketch of a Thomson parabola spectrometer consisting of a pinhole, a magnetic field, an electric field, and a detector system to investigate accelerated ions. At the left side of the sketch, a feasible resulting picture on the detector is shown. Taken from [Sch18]. Thanks to A.-M. Schroer (HHUD).
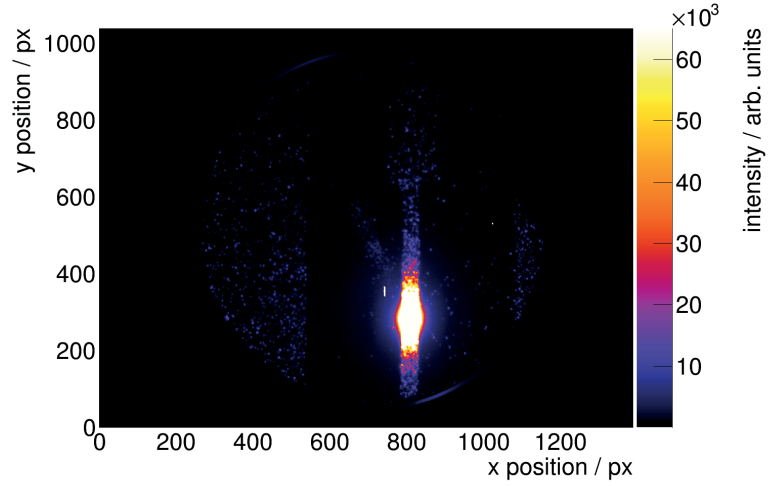
Figure 9.21: Image recorded with a Thomson parabola spectrometer. Only a bright spot is visible, the zero point. It is generated by the photons of the laser, reflections or X-rays. The laser energy was adjusted to 3.3 J. The higher the energy, the brighter the spot.

with m, v_0, and q being the mass, velocity, and charge of the particle and B_0 the magnetic field. The position in the y-direction can be calculated as

$$y = \frac{q}{mv_0} B_0 l_{\mathrm{B}} \left(d_{\mathrm{B}} + \frac{l_{\mathrm{E}}}{2} \right). \tag{9.5}$$

Therein, l_{B} and d_{B} are the length and the distance of the magnetic field to the detector (cf. Fig. 9.20). Particles with higher momentum are less deflected in vertical direction than particles with low momentum.

The following electric field separates the particles due to their mass and charge state perpendicular to the first deflection. The performed measurements used hydrogen as target material with only ions of one defined mass and charge state. Therefore, the electric
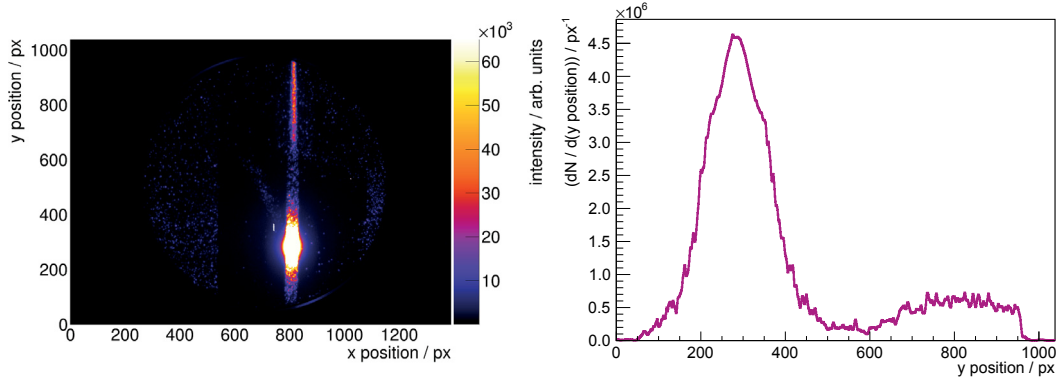
Figure 9.22: *Left*: Image resulting from the Thomson parabola spectrometer. The zero point is visible as a bright spot in the lower third of the image, and above it a vertical trace of protons is visible. The position of the protons depends on their kinetic energy and the intensity is proportional to the number of protons. The laser energy was at 3.3 J and the hydrogen of the cluster beam was adjusted to 16 bar and 60 K. *Right*: Projection on the ordinate of the x positions between 774 pixel and 848 pixel. The high intensity peak at position 300 pixel corresponds to the zero point. Between position 600 pixel and 950 pixel the signal of the protons is visible. The sharp edge at the end of the protons is caused by the edge of the MCP.

field was removed during the measurements. In the former case, the two fields lead to a deflection of the ions in parabolic traces, giving the spectrometer its name. The signals of the deflected ions are amplified with a MCP, the produced electrons impinge on a phosphor screen (cf. chapter 5.1.2), and a CCD camera records the resulting image.

The Thomson parabola spectrometer was installed under $0\,°$ with respect to the direction of the laser beam. A resulting image of the accelerated ions from the interaction of the laser pulse with the cluster-jet target is shown in Figure 9.22 (left). The zero point is clearly visible as a bright spot in the lower third of the image. Moreover, a vertical trace of protons above the zero point is visible. A projection on the ordinate of this image is presented in Figure 9.22 (right). The high peak in the intensity at roughly 300 pixel corresponds to the zero point. A second smaller distribution between 600 pixel and 950 pixel is caused by the accelerated protons. During this measurement, the laser energy was adjusted to 3.3 J and the cluster-jet target to 16 bar and 60 K with hydrogen in front of the nozzle.

To ensure that the signal is induced by protons and not caused by reflections of photons, an electric field was applied, leading to a deflections in horizontal direction. The resulting image is displayed in Figure 9.23. There, the proton trace is not only deflected vertically but additionally horizontally, confirming that the trace is generated by protons.

The analysis of the accelerated protons due to their kinetic energy and intensity was done using the analysis program from A. Alejo from the Queen's University in Belfast. A picture of the program interface is shown in Figure 9.24. The recorded image is loaded into the program. Afterwards, the experimental setup has to be defined. The resolution of the picture can be calculated by using the diameter of the MCP $d = 77\,\text{mm}$. The zero point (ZP) is selectable as the bright spot. Additionally, the magnetic field $B_0 = 0.18\,\text{T}$, the magnetic field length $l_B = 50\,\text{mm}$, and the distance to the MCP system $d_B = 128\,\text{mm}$
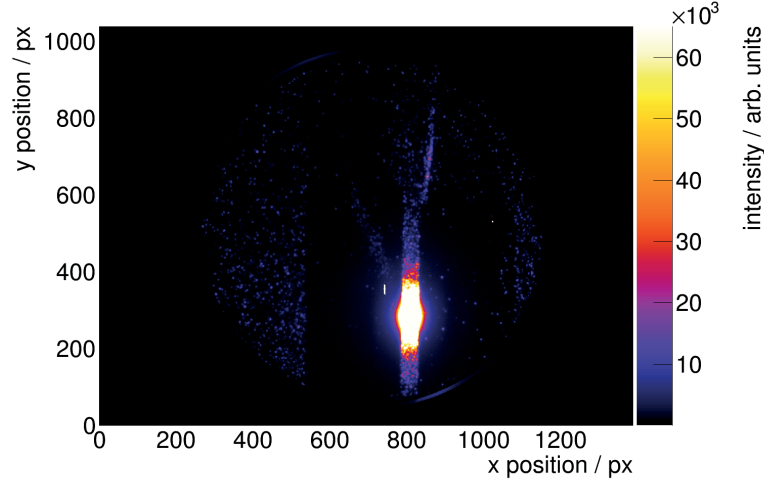
Figure 9.23: The additionally applied voltage of 200 V leads to an additional deflection in the horizontal direction. Therefore, the trace is induced by accelerated protons.

have to be filled in. The theoretical proton trace based on these values are now calculated and drawn in the image (magenta). The three solid lines show the signal area, the width can be varied. The two dash-dotted lines of same width shows the area used for the background determination. By changing the minimum and maximum energy of the protons the trace enlarges on the top or bottom, respectively. Furthermore, this program allows for an extraction of the proton spectrum. Such a spectrum is shown in Figure 9.25 corresponding to the data shown in Figure 9.22. The spectrum shows the flux of protons in arbitrary units depending on the kinetic energy of the protons. The flux decreases with increasing energy. The gray line indicates the maximum proton energy. Up to this energy, the flux decreases and then remains approximately the same. Therefore, the maximum proton energy is determined as the intersection of the solid line at a flux of 10^{10} arb. units with the spectrum. In this case the maximum energy is (53.1 ± 8.8) keV. The flux, determining the maximum kinetic energy, also called cut-off energy, varies from measurement to measurement.

Measurements were performed, investigating the maximum proton energy in dependency of the laser energy. For this measurement, the cluster-jet target was adjusted to 16 bar and 45 K. The laser energy was varied between 0.1 J and 4.8 J, and for every laser energy, ten measurements were taken, except for the maximum energy. The results (Fig. 9.26) show a clear increase in maximum proton energy with increasing laser energy, but a saturation at an energy of roughly 2.15 J. The fluctuations within one defined laser energy are induced by the uncertainties during the analysis and the fluctuations of the laser energy. At a laser energy of 0.1 J no proton signal was visible, only at the energy of 0.22 J and above a proton signal occurs. Therefore, from the picture at a laser energy of 0.1 J, as a description of the background signal, the flux determining the maximum energy was calculated to 10^{10} arb. units. Since there are no uncertainties inaccessible, no uncertainties are drawn within the resulting pictures, but multiple measurements were
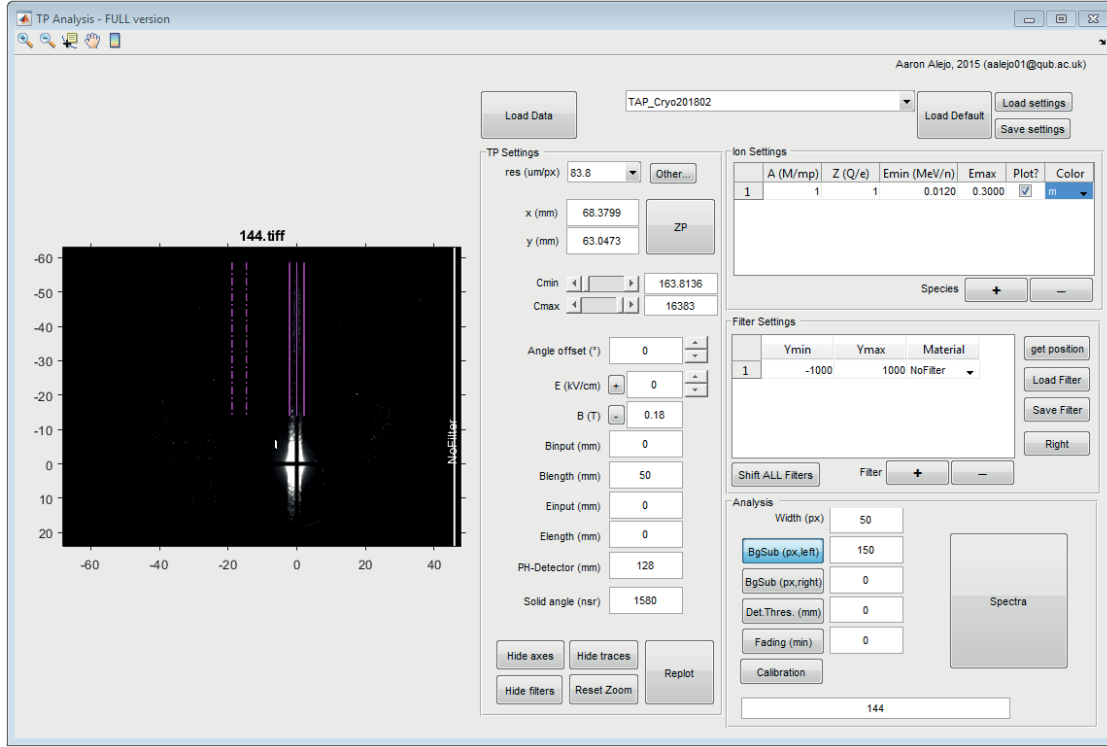
Figure 9.24: Picture of the analysis program from A. Alejo from the Queen's University in Belfast. Filling in the important data with respect to the experimental setup, the program allows for the determination of the proton spectrum using the recorded image with the Thomson parabola spectrometer.

performed at a given setup. Nevertheless, an estimation of the uncertainties was made. Uncertainties are estimated by the use of the analysis program. The variation of the magnetic field length, magnetic field, the distance to the detector, the zero point position, the resolution (μm/pixel), the width of the proton signal, and the area of the background signal result in an uncertainty of $\pm11.2\,\%$. Moreover, the determination of the flux limit (cf. gray line in Fig. 9.25) which determines the maximum energy holds an uncertainty of $\pm12.0\,\%$. The determination of the maximum energy where the proton energy spectrum falls below the flux limit results in an uncertainty of $\pm2.0\,\%$ at high maximum proton energies of more than $45\,$keV and for lower maximum energies in $\pm15.0\,\%$. Consequently, the calculated maximum proton energy has a total uncertainty of $\pm16.5\,\%$ for energies larger than $45\,$keV and $\pm22.2\,\%$ for lower energies.

A measurement series was performed with different temperatures of the hydrogen in front of the nozzle. The laser energy was adjusted to $2.35\,$J and the pressure of the hydrogen to $16\,$bar. The recorded images are shown in Figure 9.27 and display a strong dependency from the cluster beam temperature. Figure 9.28 shows the spectra for all 31 measurements at different temperatures. The temperature starts at $36.69\,$K and ends at $47.10\,$K. The structure at roughly $20\,$keV is due to some reflections also visible in the pictures recorded with the MCP system. The proton flux at a certain proton energy decreases with increasing temperature. Therefore, the maximum kinetic energy of the
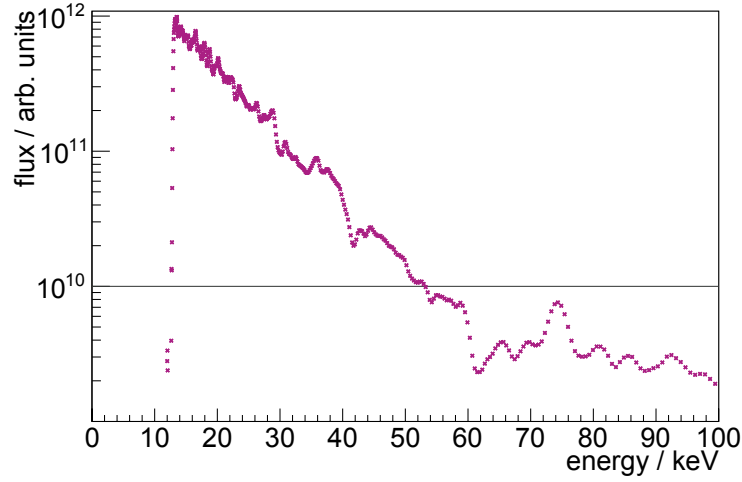
Figure 9.25: Proton spectrum of Figure 9.22. This spectrum was generated with the analysis program from A. Alejo (cf. Fig. 9.24). The flux decreases with increasing intensity. The strong rising edge on the left is induced by the edge of the MCP. At a flux of roughly 10^{10} arb. units (solid gray line) no significantly proton signal is visible. Therefore, the maximum proton energy was determined to (53.1 ± 8.8) keV, where the spectrum intersects with the solid gray line.
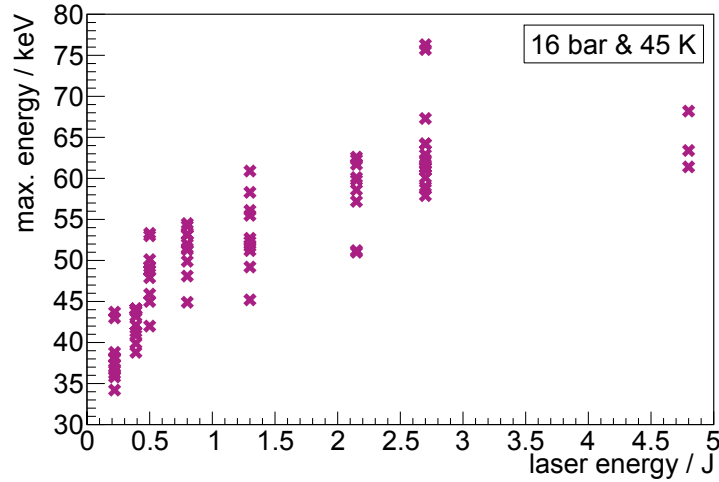

Figure 9.26: Maximum proton energy in dependency of the laser energy. At an energy of 0.1 J no proton signal was visible. A clear increase of the maximum proton energy with increasing laser energy is visible. At a laser energy of 2.15 J a saturation occurs.

protons decreases with increasing cluster-jet temperature (Fig. 9.29).

Between the temperatures 36.69 K and 40.36 K the maximum proton energy shows a strong dependency (see Fig. 9.29). Above 40.36 K the signal flattens and only a slightly decrease of the maximum proton energy is visible. The new designed and currently under construction cluster-jet target MCT-D for studies on cluster-laser interactions will allow for even lower temperature of 20 K. Thus, a strong increase in the maximum proton
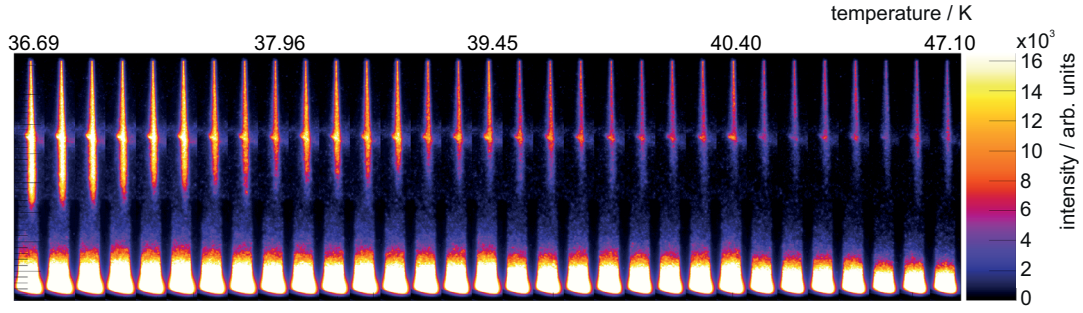
Figure 9.27: All 31 recorded images during the variation of the temperature of the hydrogen gas in front of the nozzle. The laser energy was adjusted to 2.35 J and the pressure of the hydrogen to 16 bar. A strong dependency on the temperature is visible. The measurements start at 36.69 K (*left*) and end at 47.10 K (*right*).
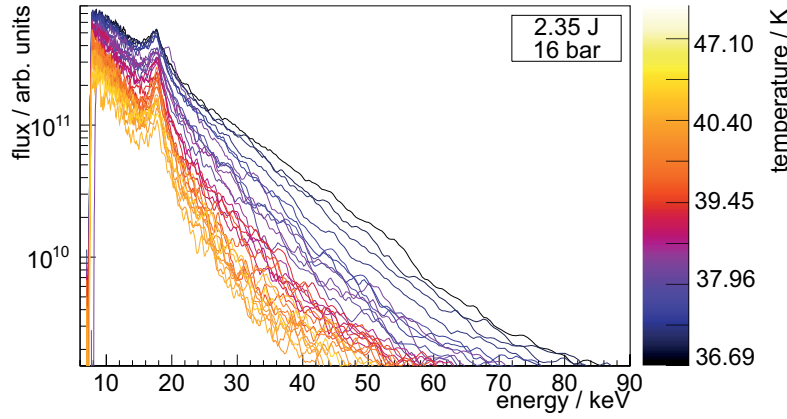
Figure 9.28: Proton spectra from the images shown in Fig. 9.27. The measurements start at 36.69 K and end at 47.10 K. The proton flux at a certain proton energy decreases with increasing temperature. The abscissa (10^9 arb. units) corresponds to the flux determining the maximum proton energy.

energy is expected. This is discussed in more detail in section 9.2.6.

A new and innovative application is the use of a cluster-jet target to generate laser induced ion acceleration, because a cluster-jet target delivers a continuous flow of target material [S$^+$04, D$^+$10]. Therefore, the high repetition rate of the laser of 5 Hz could be utilised in a measurement. The cluster-jet target was adjusted to 16 bar and 50 K. The laser energy was determined to 2.5 J. The laser was set into high repetition mode and 51 images with a frequency of 5 Hz were recorded. The resulting pictures are displayed in Figure 9.30. All 51 pictures show the proton trace above the zero point with equal intensities. The calculated spectra of these images are presented in 9.31. Due to the fact that all 51 spectra have the same shape and the same flux per proton kinetic energy, they superimpose. Every laser pulse leads to the same spectrum and therefore, the same maximum proton energy (Fig. 9.32). The maximum energy was determined to 41.8 keV with a stability better than 10 %. Such stable and reproducible results are novel in the
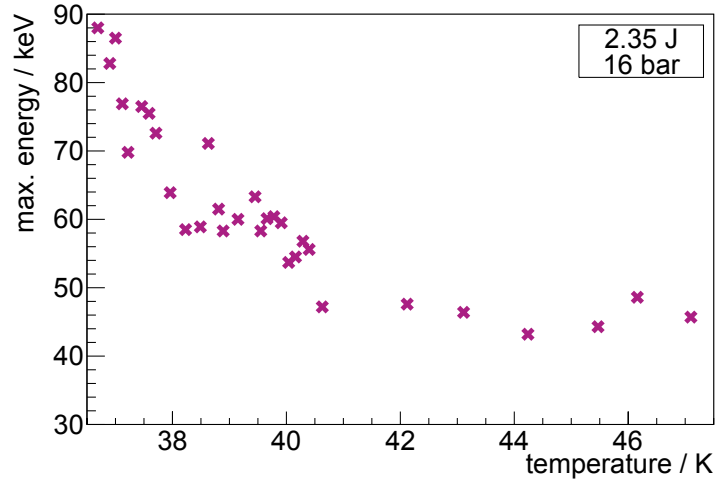
Figure 9.29: Determined maximum proton energy in dependency of the temperature. An increase of the temperature leads to an decrease of the maximum proton energy. Between the temperatures 36.69 K and 40.36 K the maximum proton energy shows a strong dependency.

field of ion acceleration in laser plasma physics. The interaction with a foil target typically results in different spectra for each laser shot. Therefore, a cluster-jet target is highly suited to produce stable and high repetition results with the interaction of a laser. As consequence of these surprising and important results, more detailed measurements with the new high performance cluster-jet target are scheduled (section 9.2.6) [Leß18].

Furthermore, the influence of using a plasma mirror was studied. A plasma mirror allows for an enhancement of the laser contrast (ratio between intensity of the laser peak and background) from 10^9 to 10^{11} and can be placed within the laser beam line via stepper motors. The results of the proton energy spectra show no differences between the measurements within the fluctuations.

Additional measurements performed with a gas jet target were performed. The interaction between a laser pulse and a gas jet target does not result in the acceleration of protons. The images only display the zero point and no proton signal above. This is caused by the different acceleration effects depending on the target material and phase. In case of clusters, the Coulomb explosion results in the acceleration of protons.

Further measurements using the cluster-jet target MCT1S performed under 45° and 135° [Leß18] show the same results like the measurements done under 0°. Therefore, the protons are accelerated due to the effect of the Coulomb explosion (cf. chapter 8.1). The Coulomb explosion leads to a homogeneous proton acceleration in all spatial directions. Moreover, the strong dependency on the cluster nozzle temperature was additionally measured at 45° and 135°. The other ion acceleration process, TNSA, would result in a collimated ion beam in normal direction to the target which was not observed here. Therefore, this acceleration process is of negligible relevance.

Concerning a constant hydrogen pressure in front of the nozzle, a lower temperature
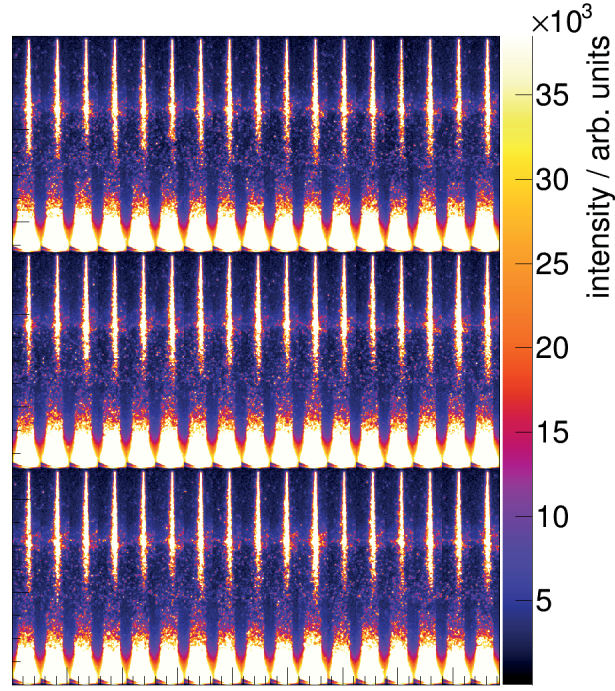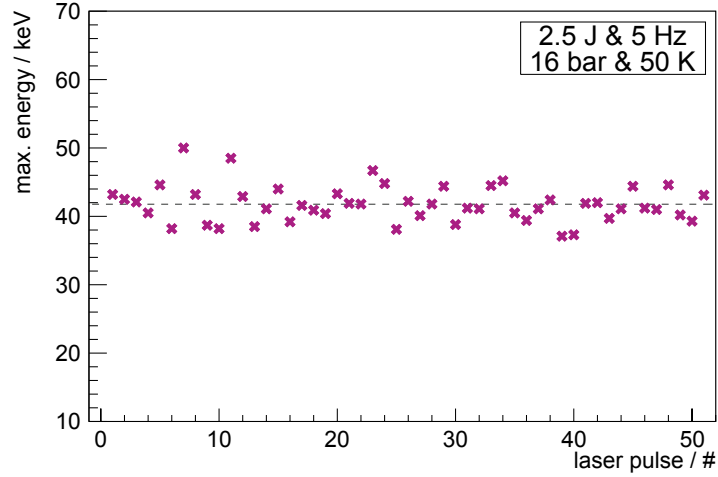
Figure 9.30: Reproducibility measurements of the proton spectra with a high laser pulse repetition of 5 Hz. All distributions of the 51 taken pictures show a similar signal.
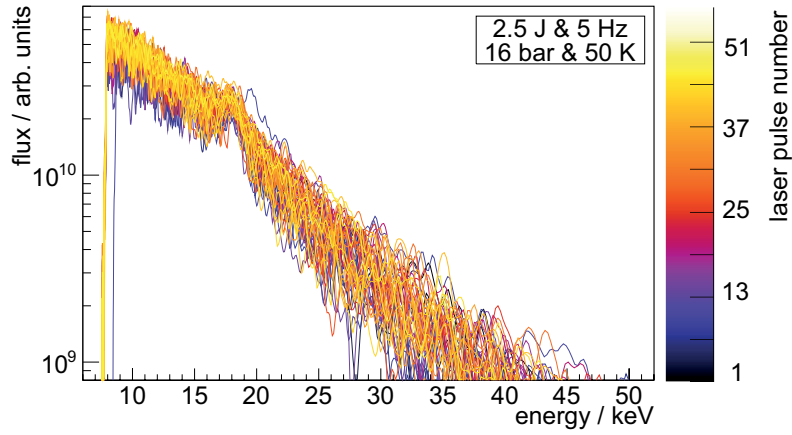
Figure 9.31: Proton spectra of the reproducibility measurements with a high laser pulse repetition of 5 Hz. All 51 spectra are shown, but they overlay each other due to their similarity. This reproducibility of the results is novel and highly suited for further investigations.

results in larger cluster. Assuming a Coulomb explosion, the maximum kinetic proton energy can be calculated and only depends on the cluster diameter and not on the laser energy, but the energy has to be sufficiently large (cf. Eq. (9.10)).

Figure 9.32: Calculated maximum proton energy of the reproducibility measurements of the proton spectra with high repetition of 5 Hz of the laser. The average maximum proton energy was determined to 41.8 keV with a stability better than 10 %.

Therefore, the laser parameters and the cluster size is of relevance. The diameter of a cluster d_{Cluster} can be estimated via

$$d_{\mathrm{Cluster}} = 2 \left(\frac{3mN}{4\pi \rho_{\mathrm{Cluster}}} \right)^{\frac{1}{3}}.$$
(9.6)

Therein, m is the mass of the used gas molecule and N the average cluster size calculable with Hagena's scaling law (cf. Eq. (2.9)). The cluster are comparable to solid hydrogen, therefore, the cluster density can be estimated to $\rho_{\mathrm{Cluster}} = 70.6 \, \mathrm{kg/m^3}$ [Zü03]. The cluster diameters within the measurement at 16 bar with changing temperature are calculated and shown in Table 9.5 including the underestimation factor of 2.6. measured at the University of Münster [Kö15].

The Coulomb explosion of a cluster results in an increase of the proton kinetic energies. Their energy depends on their initial position within the cluster. The maximum proton energy E_{max} of a cluster is [S$^+$04]

$$E_{\mathrm{max}} = \frac{4}{3}\pi Z^2 e^2 n R^2 \approx 300 Z^2 \left(\frac{n}{5 \cdot 10^{22} \, \mathrm{cm^{-3}}} \right) \cdot \left(\frac{R}{1 \, \mathrm{\mu m}} \right)^2 \, \mathrm{MeV}.$$
(9.7)

With the charge state $Z = 1$ in case of hydrogen, e the electron charge, n the cluster density, and R the cluster radius. Thereby, a homogeneous distribution of the cluster density is assumed. The predicted maximum proton energies are listed in Table 9.5. The predicted and measured maximum proton energies only differ by a factor of three. The assumption of an average cluster size (Equation (9.6)) in comparison the realistic log normal distributed cluster sizes within a cluster beam leads to differing results. Further measurements with even lower hydrogen temperatures of 20 K resulting in even larger maximum proton energies will be performed [Leß18]. Moreover, measurements using

Mie scattering were performed to determine the log normal distribution of the cluster size [Leß18, Man18].

The Coulomb explosion occurs if the laser intensity is high enough to expel all electrons from the cluster. Therefore, a normalized laser electric field amplitude a [S$^+$04]

$$a = \frac{eE}{m\omega c},\tag{9.8}$$

with the electric field E, the mass of a electron m, the laser frequency ω, and the speed of light c is introduced. This amplitude is defined for a certain laser with an intensity I and a wavelength of λ as [S$^+$04]

$$a = 0.85\sqrt{\left(\frac{I}{10^{18}\,\text{W/cm}^2}\right)}\frac{\lambda}{\mu\text{m}}.\tag{9.9}$$

This amplitude a has to be [S$^+$04]

$$a > \sqrt{\frac{8\pi Z e^2 n}{3mc^2}} \equiv 34\sqrt{\left(\frac{Zn}{5 \cdot 10^{22}\,\text{cm}^{-3}}\right) \cdot \left(\frac{R}{1\,\mu\text{m}}\right)}\tag{9.10}$$

to immediately emit all electrons out of the cluster and assuming a cluster smaller than the Debye length synonymous to a plasma that is transparent for the laser.

In the case of the performed measurements, the largest cluster size was calculated to $d_{\text{Cluster}} = 77.8\,\text{nm}$ (Eq. (9.6)). A Coulomb explosion appears by an amplitude a larger than 0.86. The normalized amplitude a for the U2 laser assuming an intensity of $10^{20}\,\text{W/cm}^2$ (corresponding to 5 J) is

$$a = 0.85\sqrt{\left(\frac{10^{20}\,\text{W/cm}^2}{10^{18}\,\text{W/cm}^2}\right)}\frac{800\,\text{nm}}{\mu\text{m}} \approx 6.8.\tag{9.11}$$

Thus, the laser intensity is high enough to let the clusters explode and accelerate protons, like it was presented in the results. Moreover, an amplitude $a \geq 1$ represents a relativistic electron motion and $a \ll 1$ a non-relativistic motion of the electron.

The cluster-jet target MCT1S allows for measurements with different gases as target material. Thus, argon as a noble gas was used as target material for measurements on accelerated ions. With respect to the vapour pressure curve (Fig. 9.14) argon was adjusted to 16 bar and 107 K (liquid) and 16 bar and 124 K (gaseous) in front of the nozzle. These measurements lead to no detectable ion signals with the Thomson parabola spectrometer. Calculations of the argon cluster diameters lead to roughly 70.2 nm in case of 124 K and to roughly 91.4 nm at 107 K. Thus, the value of the amplitude (Eq. (9.10)) results in $22.2 - 29.0$, which is larger than the U2 laser system provides (Eq. (9.11)). Therefore, the U2 laser system cannot accelerate protons of these argon clusters. Nevertheless, an alignment laser was used to visualise the argon cluster beam within the liquid phase. A picture is shown in Fig. 9.33. There, the nozzle outlet is visible and the vertical green line corresponds to the scattered laser light within the cluster beam.

Table 9.5: Calculated cluster diameters for the measurement at 16 bar with changing temperature. Additionally the predicted and the measured maximum proton energies are shown.

temperature / K with an overall $\Delta T = \pm 1\,\text{K}$	calculated mean cluster diameter / nm	maximum proton energy / keV calculated	measured
36.69	77.8 ± 3.8	193.0 ± 18.9	88.0 ± 14.5
36.90	77.0 ± 3.7	189.1 ± 18.2	82.8 ± 13.7
37.00	76.6 ± 3.7	187.1 ± 18.1	86.5 ± 14.3
37.12	76.2 ± 3.7	185.1 ± 18.0	76.9 ± 12.7
37.22	75.8 ± 3.6	183.2 ± 17.4	69.8 ± 11.5
37.46	74.9 ± 3.6	178.9 ± 17.2	76.5 ± 12.7
37.59	74.5 ± 3.5	177.0 ± 16.3	75.5 ± 12.5
37.71	74.1 ± 3.5	175.1 ± 16.5	72.6 ± 12.0
37.96	73.2 ± 3.4	170.9 ± 15.9	63.9 ± 10.5
38.23	72.3 ± 3.4	166.7 ± 15.7	58.5 ± 9.7
38.49	71.4 ± 3.3	162.6 ± 15.0	58.9 ± 9.7
38.63	70.9 ± 3.3	160.3 ± 14.9	71.1 ± 11.7
38.81	70.3 ± 3.2	157.6 ± 14.4	61.5 ± 10.1
38.89	70.1 ± 3.2	156.7 ± 14.3	58.3 ± 9.6
39.15	69.2 ± 3.2	152.7 ± 14.1	60.0 ± 9.9
39.45	68.3 ± 3.1	148.7 ± 13.5	63.3 ± 10.4
39.55	68.0 ± 3.1	147.4 ± 13.4	58.3 ± 9.6
39.66	67.7 ± 3.1	146.1 ± 13.4	60.1 ± 9.9
39.78	67.3 ± 3.0	144.4 ± 12.9	60.4 ± 10.0
39.91	66.9 ± 3.0	142.7 ± 12.8	59.5 ± 9.8
40.04	66.5 ± 3.0	141.0 ± 12.7	53.7 ± 8.9
40.16	66.2 ± 3.0	139.7 ± 12.7	54.5 ± 9.0
40.29	65.8 ± 2.9	138.1 ± 12.2	56.8 ± 9.4
40.40	65.4 ± 2.9	136.4 ± 12.1	55.6 ± 9.1
40.63	64.8 ± 2.9	133.9 ± 12.0	47.2 ± 7.8
42.12	60.7 ± 2.6	117.5 ± 10.1	47.6 ± 7.9
43.11	58.3 ± 2.4	108.4 ± 8.9	46.4 ± 7.7
44.24	55.6 ± 2.3	98.6 ± 8.2	43.2 ± 9.6
45.47	52.9 ± 2.1	89.2 ± 7.1	44.3 ± 9.8
46.16	51.5 ± 2.0	84.6 ± 6.6	48.6 ± 8.0
47.10	49.7 ± 1.9	78.8 ± 6.0	45.7 ± 7.5
50.00	44.6 ± 1.6	63.4 ± 4.6	41.8 ± 9.3

9.2.5 Measurements of Accelerated Electrons using a Thomson Parabola

After the successful measurements of accelerated protons, analyses of their kinetic energy, and dependency on the cluster and laser parameters, the orientation of the magnetic field of the Thomson parabola (cf. section 9.2.4) was rotated by 180°. As a result, now electrons are detectable due to their acceleration to the top of the MCP above the zero point. The protons are accelerated to the bottom, not visible any more. The aim of this measurement was to verify the generation of accelerated electrons and not to determine the exact energy and flux as it was done before with respect to the protons.
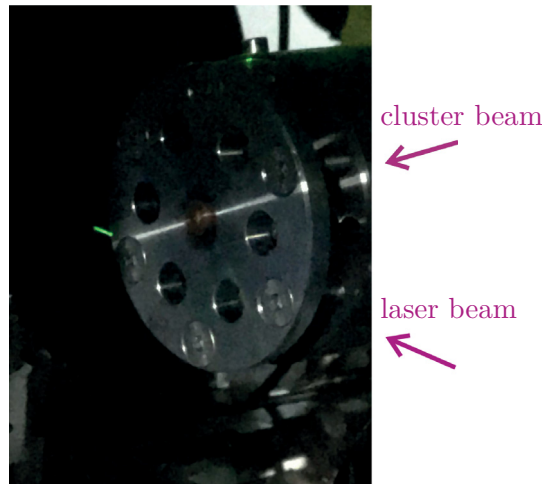
Figure 9.33: The overlapping of the alignment laser (green) and the cluster beam is visible as a vertical small line in front of the nozzle outlet of the cluster-jet target. Taken by A. Khoukaz.

The Thomson parabola was placed in forward direction under $0\,°$ with respect to the laser beam. As described before and with the same distances, a pinhole was installed between cluster-laser interaction point and the parabola to ensure that only electrons generated in the cluster-laser interaction are verified with the MCP placed behind the parabola to visualise the electrons.

Figure 9.34 shows the result gained with a laser energy of 2.4 J and a cluster-jet target with a pressure of 16 bar and a temperature of 50 K of the hydrogen in front of the nozzle. The image depicts a circle, the MCP. The bright spot at x-position 700 pixel and y-position 200 pixel corresponds to the zero point. There, all uncharged particles generate a signal. Due to their missing charge, the particles not affected by the magnetic field and propagate straightforward. The zero point is at exactly the same position as the pinhole. Therefore, the direct laser light induces a signal at the zero point. The higher the energy of the laser the brighter the zero point. Above the zero point, marked with two white boxes, the accelerated electron signal is clearly visible, excluding a background signal due to scattered light in-between. The closer the electron is with respect to the zero point, the higher is the kinetic energy of the electrons and vice versa.

The projection on the ordinate of the complete image (cf. Fig. 9.35, left) shows the zero point as a high peak in the intensity at a y-position of 200 pixel. Furthermore, a second peak at a y-position of 660 pixel is visible, corresponding to a background signal due to scattered light in-between the electron signal. An enlargement of the projection within the two white boxes results in Figure 9.35 (right), showing the electron signal. The two gray vertical lines mark the area of the background signal.

The electron signal was calculated by determining the intensity of the area in the two white boxes. Using the program for calculating the proton flux and energy, the electrons cover a range of 0.48 keV to 58 keV, if they were protons (cf. section 9.2.4). This kinetic energy
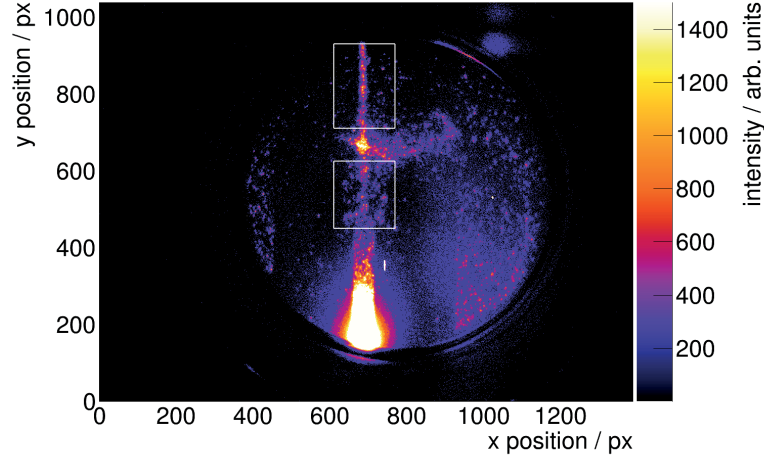
Figure 9.34: Resulting MCP picture showing the zero point generated by uncharged particles propagating through the pinhole and unaffected by the magnetic field. Above the zero point the signal from the accelerated electrons is visible and marked with two white boxes, excluding a background signal due to scattered light in-between. Electrons with high kinetic energy are closer to the zero point than low kinetic energy electrons.
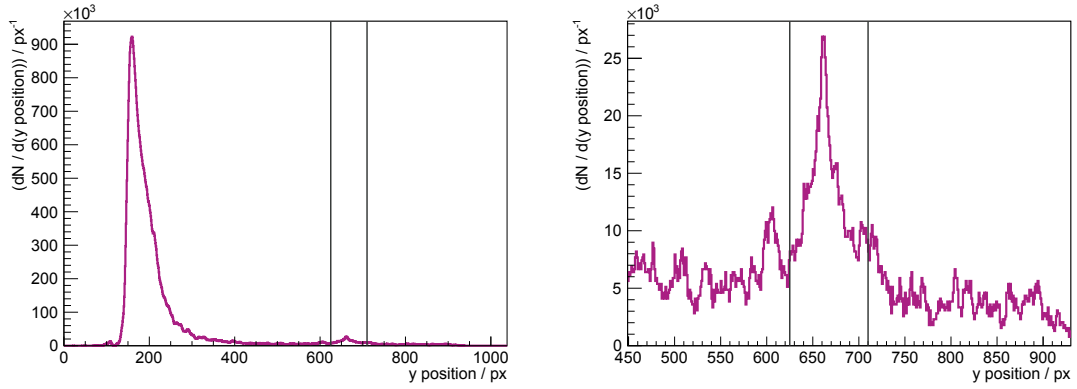

Figure 9.35: Projections on the ordinate of Figure 9.34. The two gray vertical lines mark the area of the background signal. *Left*: Projection of the full abscissa. A high intensity peak at y-position 200 pixel is visible, corresponding to the zero point. A smaller peak at y-position 660 pixel shows a background signal due to scattered light in-between the electron signal. *Right*: Enlarged view of the ordinate within the white boxes showing the electron signal.

$E_{\text{kin, p}}$ of the protons leads to a momentum of $p_{\text{p}} = 0.95\,\text{MeV}/c$ to $p_{\text{p}} = 10.43\,\text{MeV}/c$ using

$$\left(E_{\text{kin, p}} + m_{\text{p}}c^2\right)^2 = m_{\text{p}}^2 c^4 + p_{\text{p}}^2 c^2, \tag{9.12}$$

with $m_{\text{p}} = 938.27\,\text{MeV}/c^2$ being the proton mass and c the speed of light. Assuming that the momentum of the electrons $p_{\text{e}} = p_{\text{p}}$ are the same as for the protons, the kinetic energies of the electrons can be calculated

$$\left(E_{\text{kin, e}} + m_{\text{e}}c^2\right)^2 = m_{\text{e}}^2 c^4 + p_{\text{e}}^2 c^2, \tag{9.13}$$
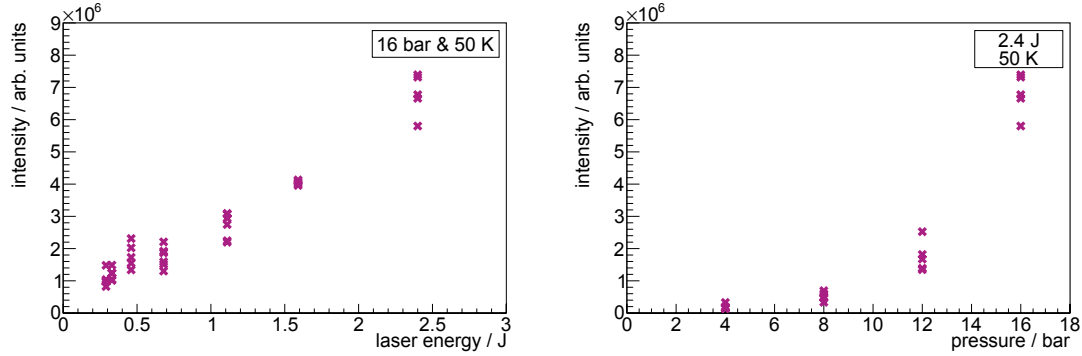
Figure 9.36: The cluster-jet target was adjusted to 50 K. *Left*: The laser energy was varied between 0.3 J and 2.4 J at a pressure of 16 bar of the hydrogen in front of the nozzle. The electron signal increases with increasing laser energy. *Right*: The laser energy was 2.4 J. The pressure of the hydrogen in front of the nozzle was varied between 4 bar and 16 bar in steps of 4 bar. A higher pressure leads to a higher electron signal.

with $m_e = 0.511 \, \text{MeV}/c^2$ the mass of an electron. Thus, the visible electrons within this measurements own an kinetic energy between $E_{\text{kin, e}} = 0.572 \, \text{MeV}$ and $E_{\text{kin, e}} = 9.936 \, \text{MeV}$.

Figure 9.36 presents the electron intensity depending on the laser energy and the hydrogen pressure of the cluster-jet target, respectively. The temperature of the cluster beam was adjusted to 50 K. An increase of the laser energy and the pressure leads to an increase in the electron intensity. Unfortunately, it was not possible to differentiate if the number of electrons in the measurable energy range increases or if the number of electrons stays constant and their energy increases. Probably, a combination of both effects occurs.

Consecutive measurements under $45\,°$ show only a slight and under $135\,°$ no electron signal [Leß18].

Due to the anisotropic acceleration of the electrons, they are most likely generated by the laser wakefield acceleration (LWFA). The electron acceleration due to the laser wakefield acceleration was first proposed in 1979 by Tajima and Dawson [TD79]. There, a short and intense laser pulse generates a plasma wave due the wake of the laser pulse [Bra17, E+09]. These waves are comparable to the waves occurring in the wake behind a ship. The non-linear ponderomotive force of the laser results in plasma oscillations, leading to an acceleration of the electrons away from the areas with high laser intensity gradients. Thereby, behind the laser pulse, a gap of positive charge is generated surrounded by the accelerated electrons. Furthermore, the electrons experience an additional opposite potential backwards to the laser axis caused by the plasma. Electrons falling into the wake are captured there and gain a strong energy in the direction of the laser pulse. Therefore, only the measurement in the direction of the laser beam shows the accelerated electrons due to the LWFA.
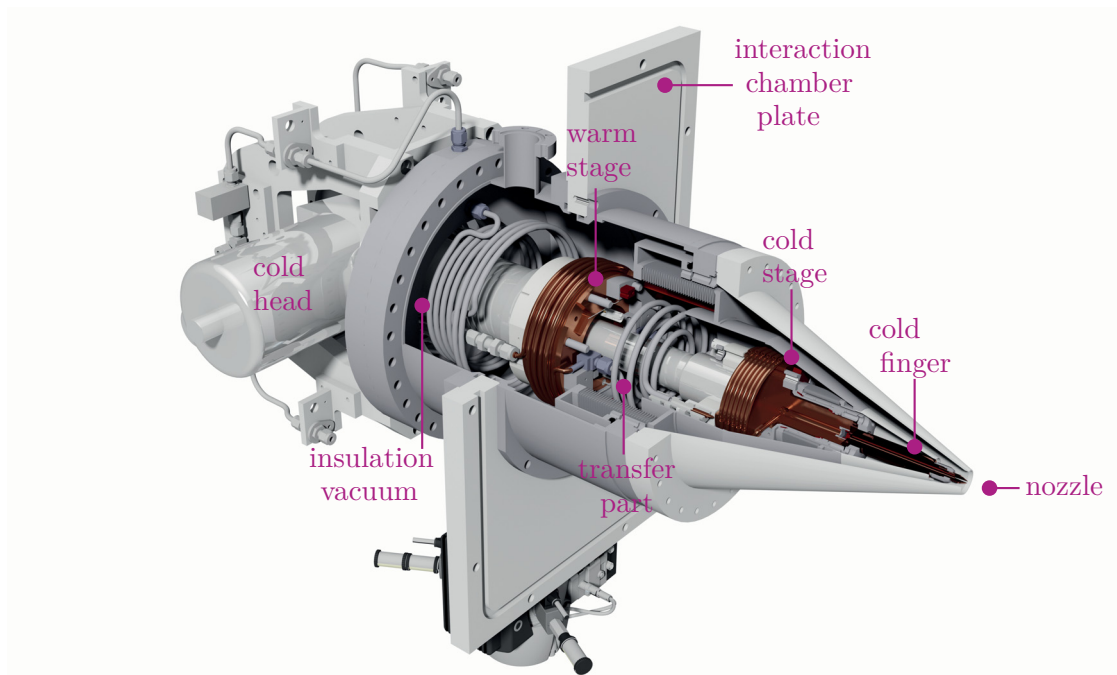
9.2.6 Cluster-Jet Target MCT-D for Cluster-Laser Interaction Studies

Based on the experience gained with the cluster-jet target MCT1S, a new target was designed to further investigate the cluster-laser interaction. The design of the new cluster-jet target MCT-D (Fig. 9.37) is based upon the jet target MCT-M for the MAGIX experiment (cf. chapter 6.4). The cluster-jet target MCT-D is currently under construction and will be assembled at the end of this year. The powerful coldhead 10MD (Leybold) in combination with an insulation vacuum chamber around the cooling parts will allow for a cooling of the gas down to temperatures of $20\,\text{K}$ in front of the nozzle. The measurements on the accelerated protons show a strong increase of the maximum kinetic proton energy with decreasing temperature (cf. Fig. 9.29). The lower temperature leads to an increase of the target density as well as of the cluster size. At a temperature of $20\,\text{K}$ with a pressure of $16\,\text{bar}$, a target density of more than $8.4 \times 10^{17}\,\text{atoms/cm}^3$ and a cluster diameter of more than $231\,\text{nm}$ (Eq. (9.6)) or both even larger is expected. Furthermore, the physical state of hydrogen changes from gaseous to liquid. Thus, a jump in the density and cluster size is expected, but cannot be predicted qualitatively, leading to a strong increase of the proton energies.

The laser intensity is high enough to accelerate protons from a cluster with a diameter of roughly $610\,\text{nm}$ (Eq. (9.10)) due to the Coulomb explosion. This could lead to maximum proton energies of roughly $12\,\text{MeV}$.

This target, like the cluster-jet target MCT1S, will be installed directly on a chamber plate of the ARCTURUS interaction chamber to ensure the exact positioning of the nozzle despite an optional reassembly. Furthermore, a cold finger as extension of the cold heads cold stage will give the opportunity to align the nozzle tip at the center of the interaction chamber. Another important development is the tip of the target. The target is very conical at the top, and the copper nozzle is surrounded with stainless steal which will be anodized black. Thus, the surface of the target near the laser focus reflects less and there is more space around the tip for optics and diagnostic tools.

Figure 9.37: The cluster-jet target MCT-D for further investigation on the cluster-laser interaction. The design is based on the jet target for the MAGIX experiment. This target will be directly installed on an interaction chamber plate and owns a cold finger to realise the interaction between clusters and laser directly behind the nozzle in the center of the chamber. A supportive insulation vacuum around the cooling parts of the target will allow for even lower temperatures of 20 K of the gas in front of the nozzle. Generated by D. Bonaventura, edited.

10 Conclusion

This thesis presented that cluster-jet targets are highly suited for hadron, lepton, and laser beam experiments. It focussed on the $\overline{\text{P}}$ANDA cluster-jet target prototype for the future $\overline{\text{P}}$ANDA experiment at FAIR, the jet target MCT-M for the MAGIX at MESA experiment, and the cluster-jet target MCT1S for the CryoFlash experiment at the University of Düsseldorf. These targets share nearly the same requirements which were discussed within this thesis in cooperation of supervised bachelor and master students.

- High target thickness directly behind the nozzle of 10^{19} atoms/cm^2 for MAGIX and 4.5×10^{15} atoms/cm^2 in a distance of $2.25\,\text{m}$ from the nozzle for $\overline{\text{P}}$ANDA to achieve the desired luminosities.

- The target thickness should be constant in time without time structures, but at the same time adjustable. The $\overline{\text{P}}$ANDA experiment is aiming for a thickness ramp adjusted to the antiproton beam current to ensure a constant luminosity and event rate. The CryoFlash experiment studies the cluster-laser interaction for different stagnation conditions to gain a deeper insight into this interaction.

- The possibility to use different target materials of highest purity, i.e., hydrogen, nitrogen, argon, oxygen, to match the experimental objective.

- The adaptation of the targets to the experimental setup. In case of the $\overline{\text{P}}$ANDA experiment, the cluster source, as well as the beam dump have to be installed in a distance of roughly $2.25\,\text{m}$ from the interaction point to realise a $4\,\pi$ acceptance of the detector. For MAGIX and CryoFlash, where the interaction takes place directly behind the nozzle, the targets have to be very conical at the nozzle tip to ensure a high detector acceptance and space for the laser beam and the various used diagnostics tools.

- $\overline{\text{P}}$ANDA and MAGIX are aiming for a low intrinsic background rate to perform high precision measurements. Therefore, the $\overline{\text{P}}$ANDA cluster-jet target uses two special shaped orifices to size and shape the beam in order to reduce the gas flow in the interaction chamber. MAGIX will use a catcher system opposite to the nozzle to directly pump the clusters after the interaction out of the scattering chamber. Moreover, a rectangular beam shape leads to a high target thickness with a maximal overlap region of the cluster and the accelerator beam leading to a low background rate. The $\overline{\text{P}}$ANDA cluster-jet target prototype therefore uses a rectangular shaped orifice and MAGIX will use a rectangular shaped nozzle.

- The continuous flow of target material is an advantage in laser plasma physics. In case of the CryoFlash experiment it allows to use the available high laser pulse repetition rate which is not applicable for solid targets and shows stable interaction rates in contrast to solid state targets.

The main component of every Münster cluster source is the fine Laval nozzle. These nozzles, especially their geometry, is essential for the cluster formation process and the performances of the targets. Therefore, production processes at the University of Münster were developed and established to face the different requirements on the nozzles.

$\overline{\text{P}}$ANDA Cluster-Jet Target Prototype

The $\overline{\text{P}}$ANDA cluster-jet target prototype is built up in next to $\overline{\text{P}}$ANDA geometry and is successfully in operation since years [Kö15]. In the framework of this thesis, a new record thickness of $(4.85 \pm 0.24) \times 10^{15}$ atoms/cm^2 at a distance of 2.1 m from the nozzle was achieved matching the $\overline{\text{P}}$ANDA design conditions (chapter 5.3.1). Moreover, the possibility to adjust the thickness during a beam time to the numbers of antiprotons was demonstrated to ensure a constant luminosity and event rate at the $\overline{\text{P}}$ANDA experiment (chapter 5.1.1).

An optical monitor system to visualise and extract a relative target thickness information, the size, and shape of the cluster beam was installed at the $\overline{\text{P}}$ANDA cluster-jet target prototype in a distance of more than 5 m and the cluster beam was visualised for the first time at such distance using this system (chapter 5.1.2). Moreover, the system was used to analyse and adjust the cluster beam within the preliminary interaction chamber center of the KOALA target to ensure optimal adjustments for the planned Mie measurements and at the MCT1S cluster-jet target to adjust the cluster beam to the laser focus at the U1 laser system of the University of Düsseldorf (chapter 5.1.2 and 9.1).

Another visualisation system, the MCP detection system [K$^+$14b], was used to visualise the interaction zone between a cluster-jet target and the COSY accelerator beam (chapter 5.1.2). Moreover, this system installed at the end of the $\overline{\text{P}}$ANDA cluster-jet target prototype proved the propagation of the cluster beam over a distance of more than 5 m without disturbances. A MCP system is discussed to be installed at the later beam dump of the final $\overline{\text{P}}$ANDA cluster-jet target to analyse the cluster beam during the running experiment (cf. chapter 5.1.2) [Kho18].

The different Laval nozzles, originating from the production processes of the University of Münster (cf. chapter 3), were installed at the $\overline{\text{P}}$ANDA cluster jet target prototype and characterised with respect to their performance and influence on the cluster properties (chapter 5.3). Velocity measurements in combination with simulations were performed yielding two different production processes within the nozzle depending on the hydrogen phase in front of the nozzle: cluster formation and fragmentation. Moreover, the positions within the nozzle, where the clusters decouple from the surrounding gas, were measured and resulted in values depending on each specific nozzle of 0.5 mm to more than 17.0 mm from the narrowest diameter.

The optical system in the skimmer chamber allows for the observation of core beams within the cluster beam resulting in higher target thicknesses. These structures, especially their thicknesses and velocities, were measured using the nozzle tilting system resulting in velocity differences of more than $200\,\mathrm{m/s}$ within one cluster beam at certain stagnation conditions (chapter 5.3.2). Thus, the thickness, as well as the velocity and the decoupling of clusters changes within the cluster beam. The complex inner geometry of the Laval nozzles determines these characteristics within the beam. These properties are essential and have to be studied to calculate the achievable target thickness.

The necessary length of a Laval nozzle was studied by shortening the outlet zone. A reduction by $3\,\mathrm{mm}$ shows no influence on the performance of the nozzle, but further measurements with even shorter nozzles have to be performed.

The GSI nozzle, nozzles for an internal target experiment at the ESR at GSI, demonstrated the possibility to manufacture a nozzle with a small narrowest inner diameter of $\varnothing_{\mathrm{GSI19}} = 12\,\mathrm{\mu m}$ with a high and stable target thickness of $(1.09 \pm 0.10) \times 10^{14}\,\mathrm{atoms/cm^2}$ at a distance of $2.1\,\mathrm{m}$ from the nozzle (chapter 5.3.3).

The production process resulting in a glass nozzle showed that the nozzle has to be larger than $3\,\mathrm{mm}$ to produce a well defined cluster beam. Nevertheless, a developed composite design even allows for investigation with the glass nozzle resulting in a thickness of $(1.22 \pm 0.27) \cdot 10^{14}\,\mathrm{atoms/cm^2}$ at a distance of $2.1\,\mathrm{m}$ from the nozzle (chapter 5.3.4).

The measurements performed within this thesis allow for a characterisation and valuation of the produced nozzles. Moreover, the experiences achieved are used to optimise the nozzle geometry and the nozzle production process towards high performance cluster-jet targets.

Jet Target MCT-M

The state-of-the-art jet target MCT-M for MAGIX at MESA was designed, built up, and set into operation. Calculations assuming the design target thickness were performed to design a target adjusted to these requirements. As a result, a booster stage to pre-cool the target gas before entering the target source was developed and Laval nozzles with different geometries were produced (chapter 7.1). The operation and the cluster beams produced with this nozzles were investigated by the use of a Mach-Zehnder interferometer (chapter 7.2). This system allows for a non-destructive absolute target beam thickness profile reconstruction with different stagnation conditions of the gas in front of the nozzle and vacuum conditions in the vacuum chamber and the suitability for this application was demonstrated. The typical node structures were observed caused by the expansion of nitrogen into atmospheric pressure which is in good agreement with the theoretical description. Furthermore, the thicknesses of the nitrogen jet beams expanding into vacuum matched the calculated thicknesses. The measurements of the cluster beams at the previous determined design stagnation conditions results in the expected thicknesses in the design range. Moreover, the results offer the possibility to design an optimised catcher geometry to minimise the gas flow in the scattering chamber. A novel nozzle design with a rectangular shaped outlet was investigated, but further studies are necessary

due to the differences between the calculations and measurements. These results are published in [G$^+$18].

Moreover, the target was installed at the electron microtron accelerator MAMI in MAINZ to investigate electron-proton interactions (chapter 7.3). With the use of deflecting magnets within the MAMI acccelerator beam line, the beam profile of the cluster beam was observed and analysed by scanning the cluster beam with the electron beam. Elastic electron-proton cross sections were measured with an electron energy of 450 MeV in the angular range of 20° to 32° corresponding to a momentum transfer $Q^2(\theta)$ range of $0.022\,\mathrm{GeV}^2/c^2$ to $0.061\,\mathrm{GeV}^2/c^2$. On basis of known electron-proton cross section data, the gained data were described and the target thickness was determined as a scaling factor between the taken and previously determined data yielding a maximum target thickness of $(1.20 \pm 0.01) \times 10^{18}\,\mathrm{atoms/cm}^2$.

Cluster-Jet Target MCT1S

The installation of the cluster-jet target at the U1 and U2 laser systems of the University of Düsseldorf allows for investigations with respect to cluster-laser interaction. Measurements performed with the U1 laser system results in the observation of the Balmer spectral lines yielding to plasma temperatures between 1600 K and 4500 K (chapter 9.1).

The highly intense U2 laser system allows for further studies on the cluster-laser interaction (chapter 9.2). There, various diagnostic systems were used to perform entirety measurements. The generation of X-rays in dependency of the target stagnation conditions and the laser energy was observed (chapter 9.2.3). Moreover, energy spectra of accelerated protons were measured and analysed yielding a maximum proton energy of (88.0 ± 14.5) keV. The measurement of accelerated protons with similar energies isotropivally distributed in three different angles confirmed that the protons are accelerated by Coulomb explosion. Absolutely novel in the field of plasma physics is the shown stability and reproducibility of the results on accelerated protons using the cluster-jet target (chapter 9.2.4). A corresponding further publication is in progress. Moreover, the continuous flow of target material allows for the use of the high laser pulse repetition of 5 Hz. Additionally, accelerated electrons for different stagnation conditions of the target and the laser energy were recorded (chapter 9.2.5). Based on these experiences a new cluster-jet target, MCT-D, is designed and currently under construction.

A Appendix

A.1 Adaptation of the Recorded Circular Shaped Beam Profile

As introduced in section 5.1.1 the recorded beam profiles are best described by a convolution of a step function and a normalised Gaussian distribution. Hence, for the adaptation follows [Kö15, Tä12]

$$\tilde{\rho}_{\text{circ}}(x) = f(x) * g(x) = \int\limits_{-\infty}^{+\infty} f(\tau)g(x-\tau)\,\mathrm{d}\tau. \tag{A.1}$$

Within the beam limits

$$\tilde{\rho}_{\text{circ}}(x) = \int\limits_{-R_c}^{+R_c} f(\tau)g(x-\tau)\,\mathrm{d}\tau, \tag{A.2}$$

where the step function is equal 1

$$\tilde{\rho}_{\text{circ}}(x) = \int\limits_{-R_c}^{+R_c} 1 \cdot g(x-\tau)\,\mathrm{d}\tau. \tag{A.3}$$

$$\tilde{\rho}_{\text{circ}}(x) = a \int\limits_{-R_c}^{+R_c} \exp\left(\frac{-b\,(x-\tau)^2}{2}\right)\,\mathrm{d}\tau. \tag{A.4}$$

The substitution $\Theta^2 = \frac{b(x-\tau)^2}{2}$ yields to the expression

$$\tilde{\rho}_{\text{circ}}(x) = -a\sqrt{\frac{2}{b}} \int\limits_{\sqrt{\frac{b}{2}}(x-R_c)}^{\sqrt{\frac{b}{2}}(x+R_c)} \exp\left(-\Theta^2\right)\,\mathrm{d}\Theta. \tag{A.5}$$

$$\tilde{\rho}_{\text{circ}}(x) = -a\sqrt{\frac{2}{b}} \left(\int\limits_{0}^{\sqrt{\frac{b}{2}}(x-R_c)} \exp\left(-\Theta^2\right)\,\mathrm{d}\Theta - \int\limits_{0}^{\sqrt{\frac{b}{2}}(x+R_c)} \exp\left(-\Theta^2\right)\,\mathrm{d}\Theta \right), \tag{A.6}$$

wherein, the error function

$$\text{erf}(\hat{x}) = \frac{2}{\sqrt{\pi}} \int\limits_{0}^{\hat{x}} \exp\left(-\vartheta^2\right)\,\mathrm{d}\vartheta \tag{A.7}$$

can be used to express the function as

$$\tilde{\rho}_{\text{circ}}(x) = -a\sqrt{\frac{2}{b}}\frac{\sqrt{\pi}}{2}\left(\text{erf}\left(\sqrt{\frac{b}{2}}\,(x - R_c)\right) - \text{erf}\left(\sqrt{\frac{b}{2}}\,(x + R_c)\right)\right). \tag{A.8}$$

Introduction of the smearing parameter $\tilde{s} = \sqrt{\frac{2}{b}}$ and from the Gaussian distribution $a = \sqrt{b/2\pi}$ results in

$$\tilde{\rho}_{\text{circ}}(x) = \frac{1}{2}\left(\text{erf}\left(\frac{x + R_c}{\tilde{s}}\right) - \text{erf}\left(\frac{x - R_c}{\tilde{s}}\right)\right). \tag{A.9}$$

For the rectangular shaped adaptation follows analogously (details see [Kö15])

$$\tilde{\rho}_{\text{rect}}(x, y) = \frac{1}{4}\left(\text{erf}\left(\frac{x + R_c}{\tilde{s}}\right) - \text{erf}\left(\frac{x - R_c}{\tilde{s}}\right)\right) \cdot \left(\text{erf}\left(\frac{y + R_c}{\tilde{s}}\right) - \text{erf}\left(\frac{y - R_c}{\tilde{s}}\right)\right). \tag{A.10}$$

Nevertheless, using the separation ansatz $\rho(x', y') = \rho_0 \cdot \tilde{\rho}(x', y')$ Eq. (5.13) can be written as

$$q_m(x) = v \int_{x-d/2}^{x+d/2} \text{d}x' \int_{-\infty}^{+\infty} \text{d}y' \int \rho_0 \tilde{\rho}(x', y'). \tag{A.11}$$

$$q_m(x) = \rho_0 v \int_{x-d/2}^{x+d/2} \text{d}x' \int_{-\infty}^{+\infty} \text{d}y' \int \tilde{\rho}(x', y'). \tag{A.12}$$

This definition applied in the modified ideal gas law (Eq. (5.10)) leads to

$$q_{pV} = \rho_0 \frac{vRT}{M} \int_{x-d/2}^{x+d/2} \text{d}x' \int_{-\infty}^{+\infty} \text{d}y' \tilde{\rho}(x', y'). \tag{A.13}$$

The volume density ρ_{volume} of the cluster beam measured with the scanning rod system mainly depends on the maximal pressure increase in the chamber. The combination of Eq. (A.13) and (5.6) shows this relation. Furthermore, the residual gas background p_{back} in the chamber has to be take into account [Kö15, Tä12]

$$p(x) = \rho_0 \frac{vRT}{SM} \int_{x-d/2}^{x+d/2} \text{d}x' \int_{-\infty}^{+\infty} \text{d}y' \tilde{\rho}(x', y') + p_{\text{back}}. \tag{A.14}$$

A.2 Velocity Measurements of the A19 Nozzle

Measurement series with the A19 nozzle with a pressure of 8 bar with temperatures between 26 K and 32 K in steps of 2 K shows the dependency of the velocity distribution from the stagnation conditions (Fig. A.1). This series starts in the liquid phase of hydrogen and ends in the gaseous phase. The first two measurements show a wide velocity distribution with standard derivations of $(43 - 46)$ m/s and the last two a sharp velocity distribution with standard derivations of $(10 - 15)$ m/s. The change in-between, where typically a double peak structure occurs, is not visible. For every measurement setting, more than 20000 individual time-of-flight data were recorded. The corresponding mean velocities are shown in Table A.1.
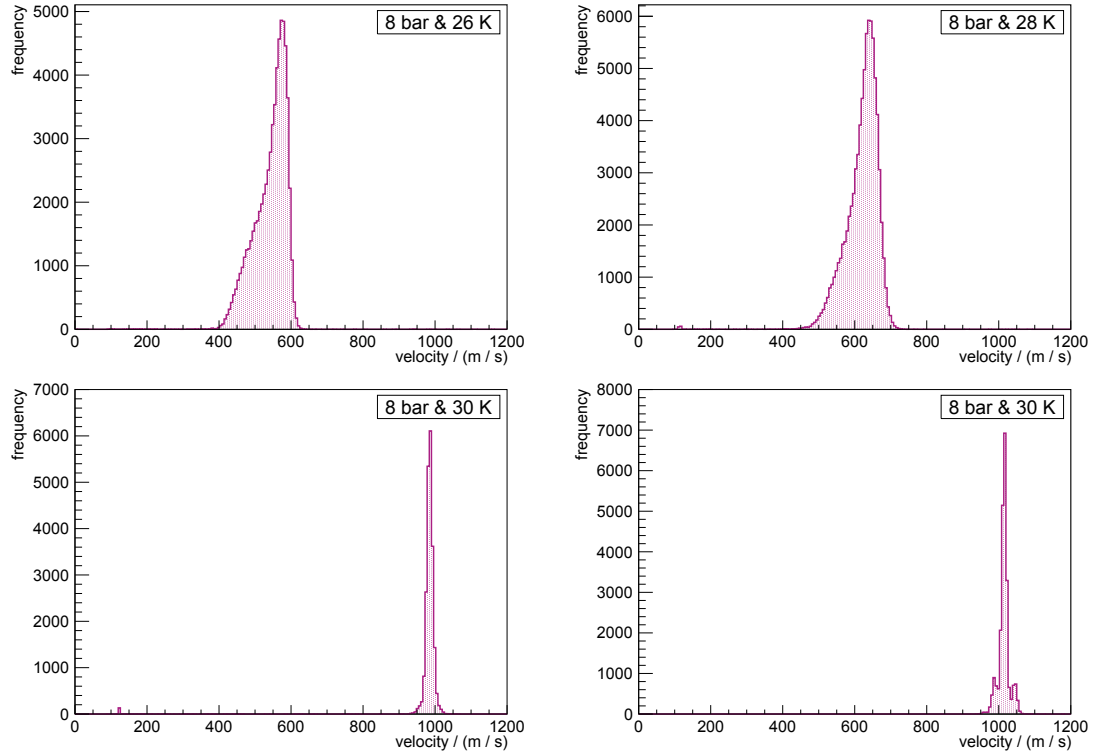
Figure A.1: Measurements series performed with the A19 nozzle with a pressure of 8 bar with temperatures between 26 K and 32 K in steps of 2 K. In case of liquid hydrogen, a wide velocity distribution is visible (*top*). Gaseous hydrogen results in a single sharp peak (*bottom*). A double peak structure in between is not visible. For every setting, more than 20000 individual time-of-flight data were recorded. The corresponding mean velocities are shown in Table A.1.

Table A.1: Mean velocities for the measurement series performed with a pressure of 8 bar with temperatures between 26 K and 32 K in steps of 2 K (Fig. A.1). The mean velocities developed as expected. The mean velocities are higher than measured with the A21 nozzle.

nozzle	pressure	temperature	velocity	standard deviation
	bar	K	(m/s)	(m/s)
A19	8	26	539 ± 2	46
	8	28	618 ± 3	43
	8	30	983 ± 5	10
	8	32	1013 ± 5	15

A.3 Mach-Zehnder Interferometer

Nozzle with Parallel Outlet Zone

Measurements using the Mach Zehnder Interferometer to investigate the nozzle with parallel outlet zone. Additional, to the shown images, measurements with nitrogen pressures in-between were measured. The images (Fig. A.2) on the top present the expansion into atmospheric pressure and the images in the center and bottom, the expansion into vacuum.
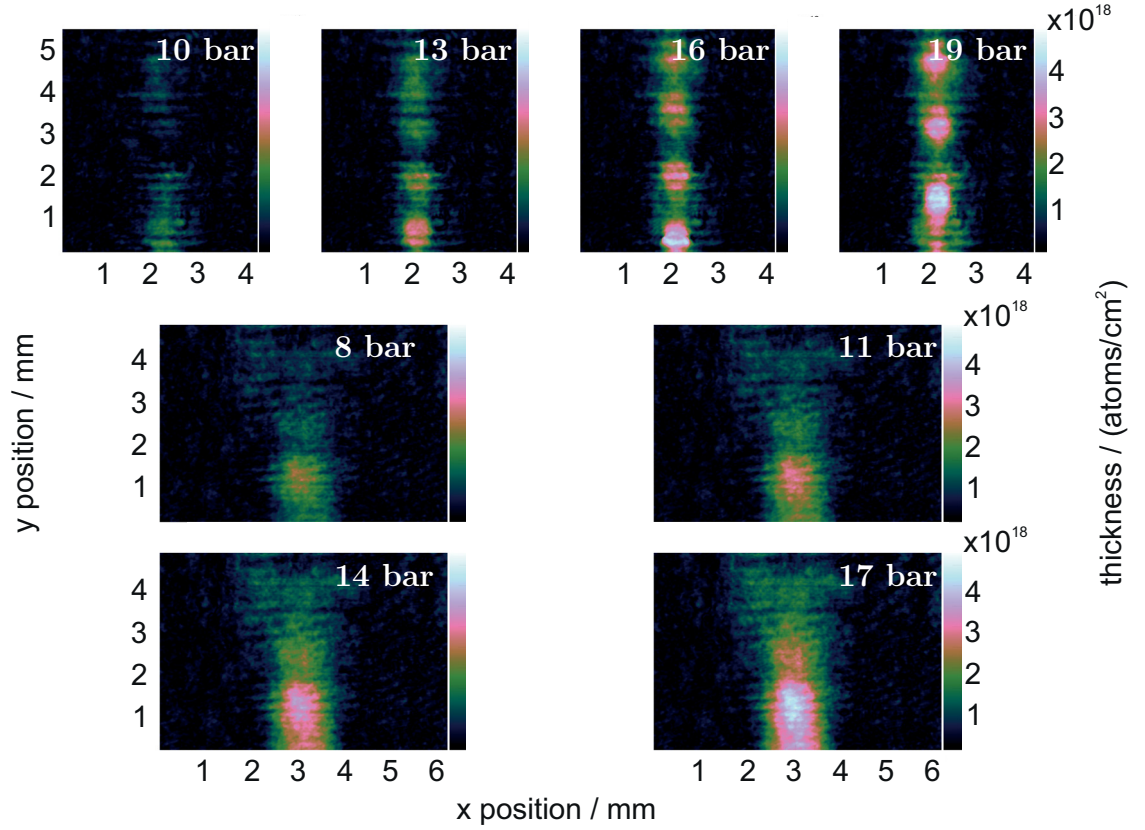
Figure A.2: Expansion of a nitrogen jet with different pressures in front of the nozzle into atmospheric pressure (*top*) and vacuum (*center* and *bottom*).

Nozzle with Rectangular Shaped Outlet

Resulting images of the expansion of nitrogen through the nozzle with a rectangular shaped outlet in atmospheric pressure (Fig A.3) and vacuum (in Fig. A.4) are shown for the wide side (first four pictures) and for the small side (last four pictures).
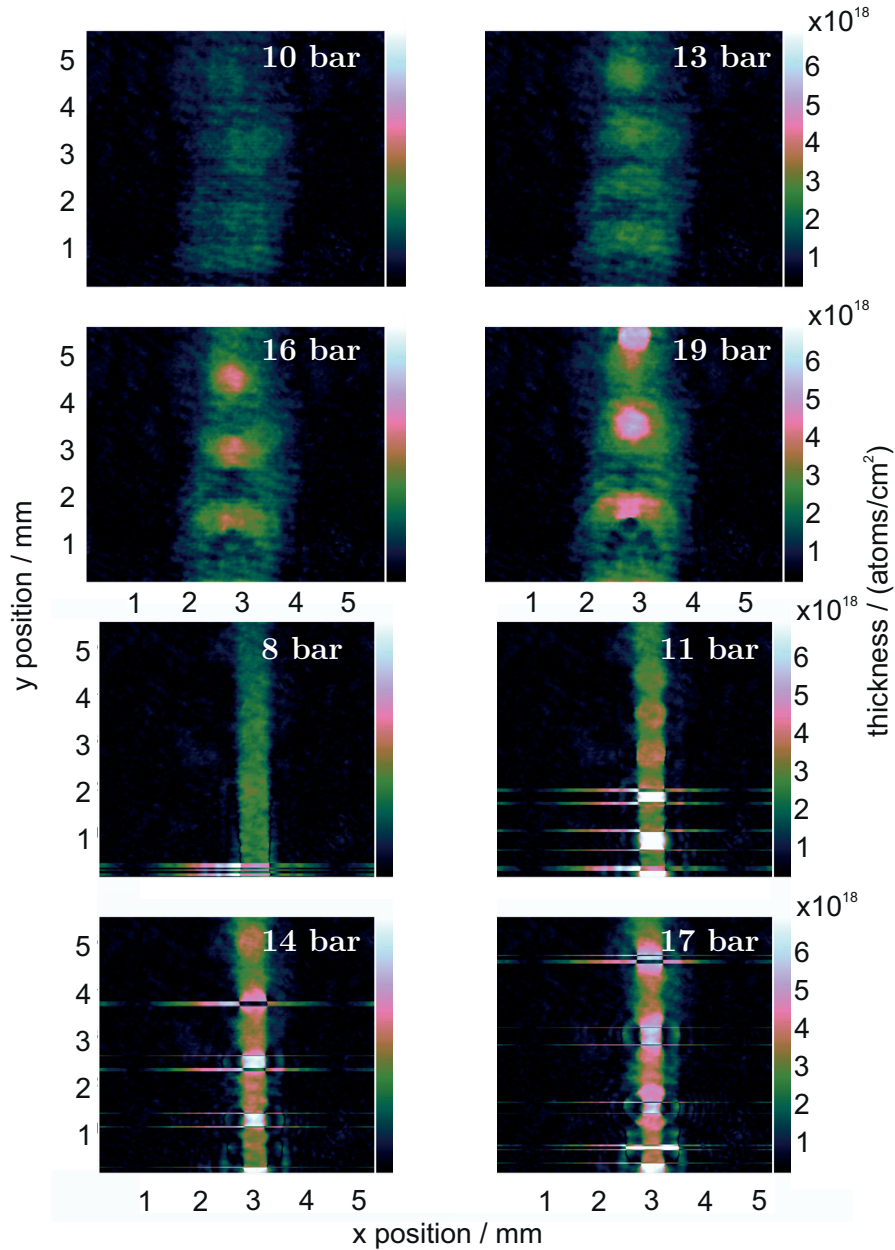
Figure A.3: Images of a nitrogen jet with different pressures expanding into atmospheric pressure. The nozzle with the rectangular shapes outlet was used and the first four pictures show the wide side and the last four pictures the small side.
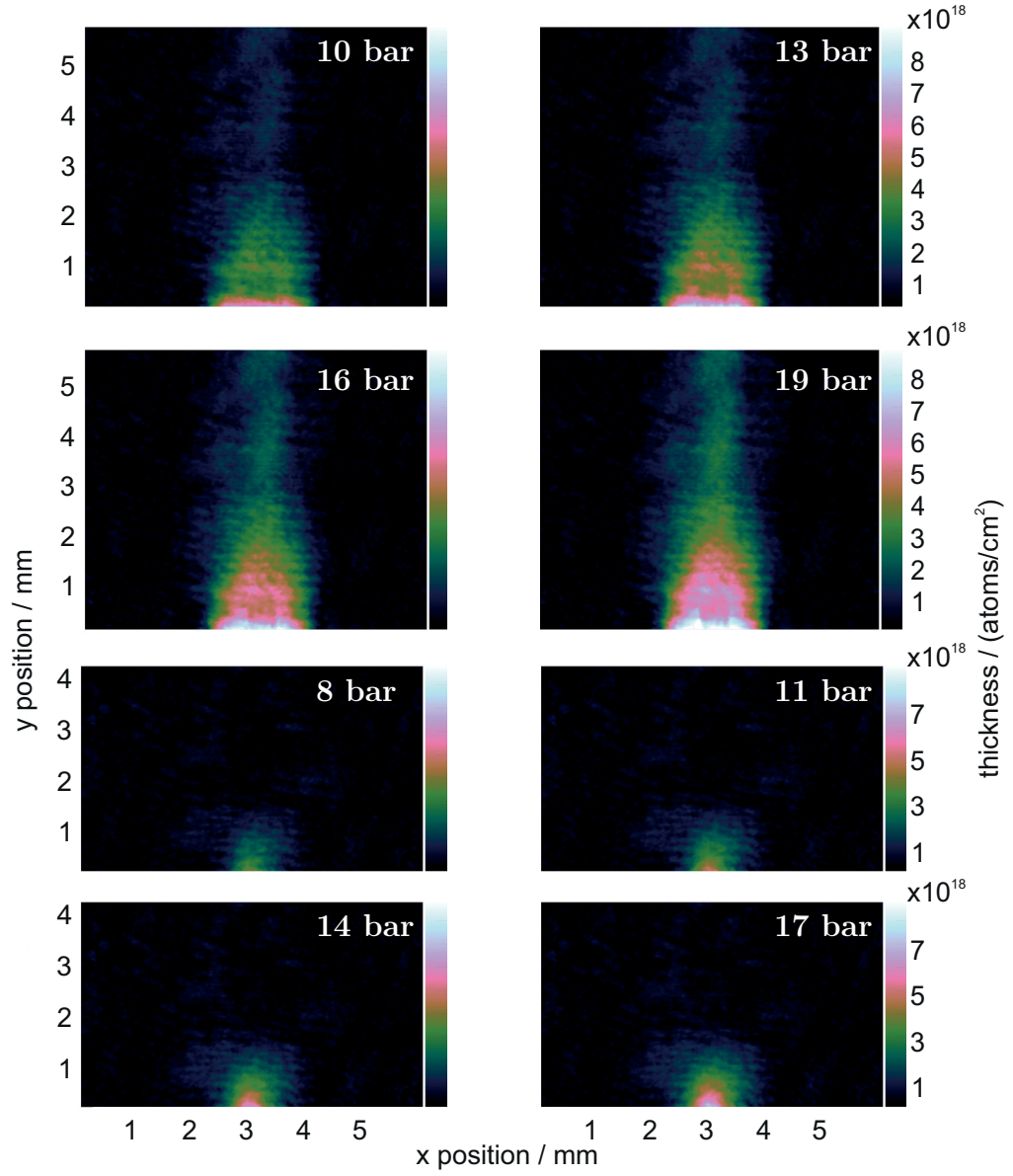
Figure A.4: Expansion of a nitrogen jet with different pressures into vacuum . The wide side (first four pictures) and the small side (last four pictures) of the nozzle with rectangular shaped outlet zone is studied.

A.4 Missing Mass Plots of MAMI Data

For the determination of the elastic electron-proton cross section, the two-dimensional histograms of the measured scattered angles in dependency of the missing mass of the electron and proton for data and simulations are used. Here these histogramms for all eight settings are shown for data in Fig. A.5 and simulations in Fig. A.6. The order is given by: $20°$, $21°$, $22°$, $24°$, $26°$, $28°$, $30°$, and $32°$. The projections on the abscissa to calculate the event rate are shown in Fig. A.7 for data and Fig. A.8 for simulations.
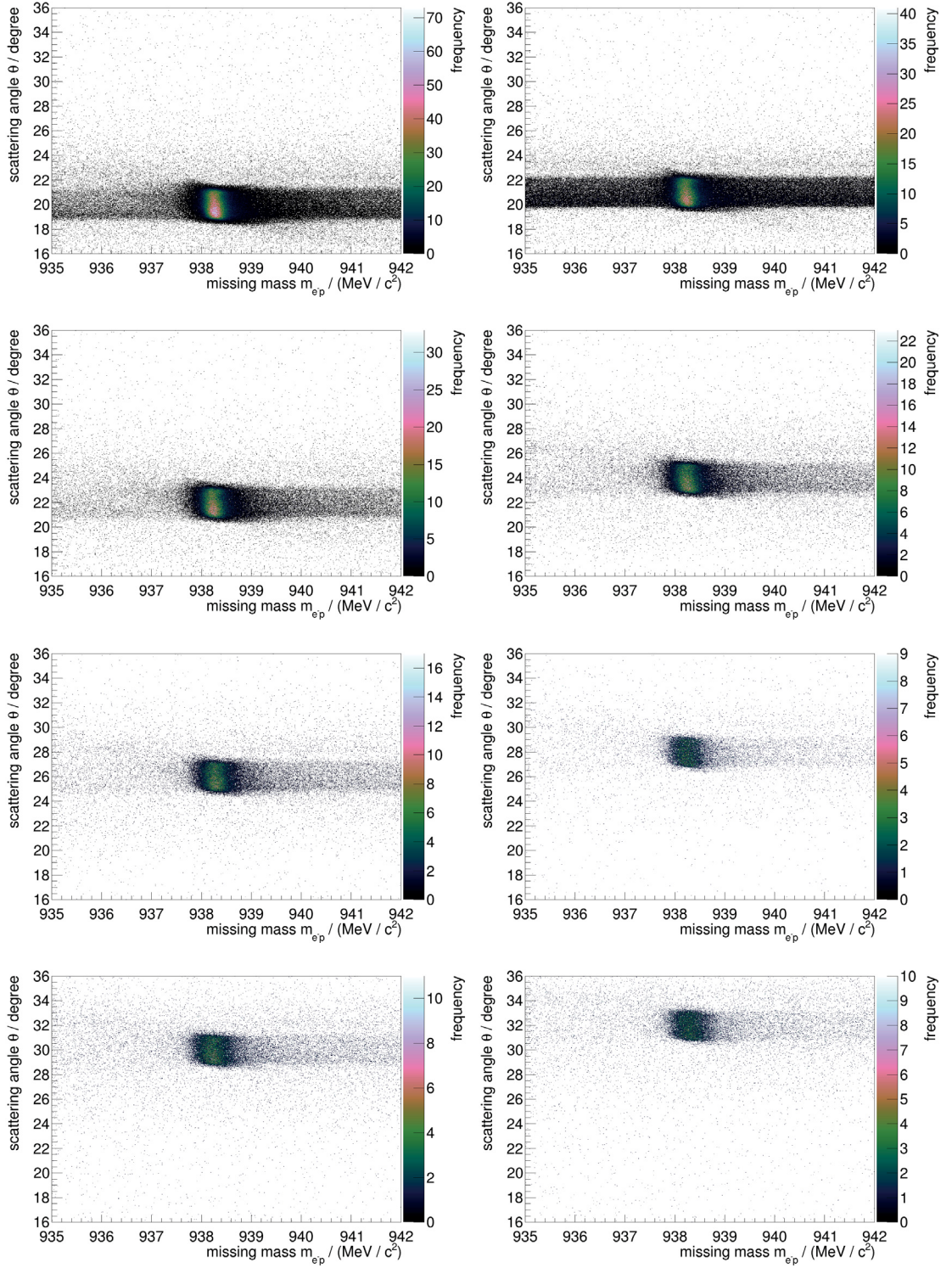
Figure A.5: Scattered angle θ in dependency of the missing mass of the proton for data. A signal at the spectrometer B acceptance for every individual setting at the proton mass of $938.27\,\mathrm{MeV}/c^2$ for data is clearly visible.
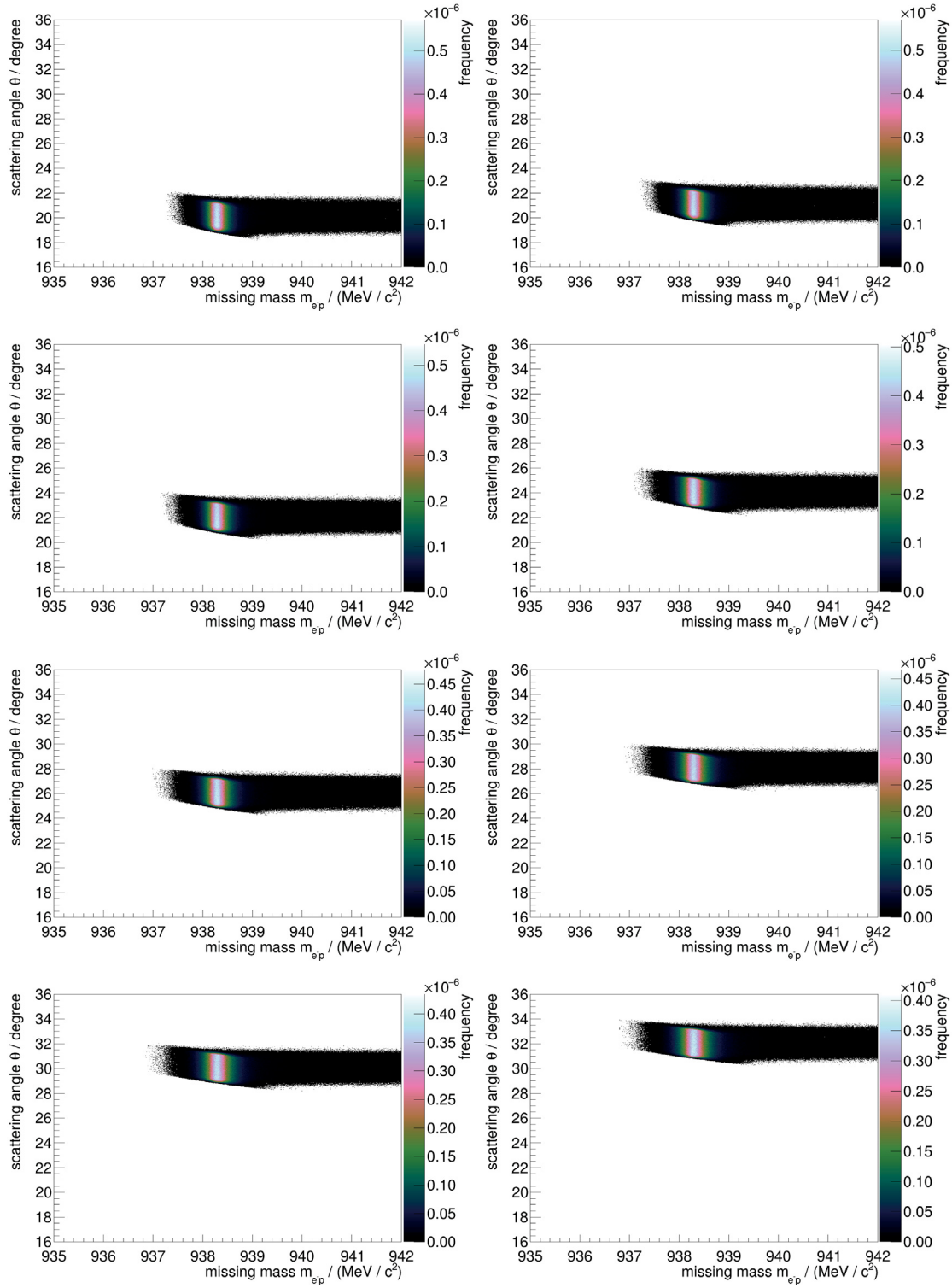
Figure A.6: Scattered angle θ in dependency of the missing mass of the proton for simulations. A signal at the spectrometer B acceptance for every individual setting at the proton mass of $938.27\,\mathrm{MeV}/c^2$ next to the radiative tail towards higher masses is clearly visible.
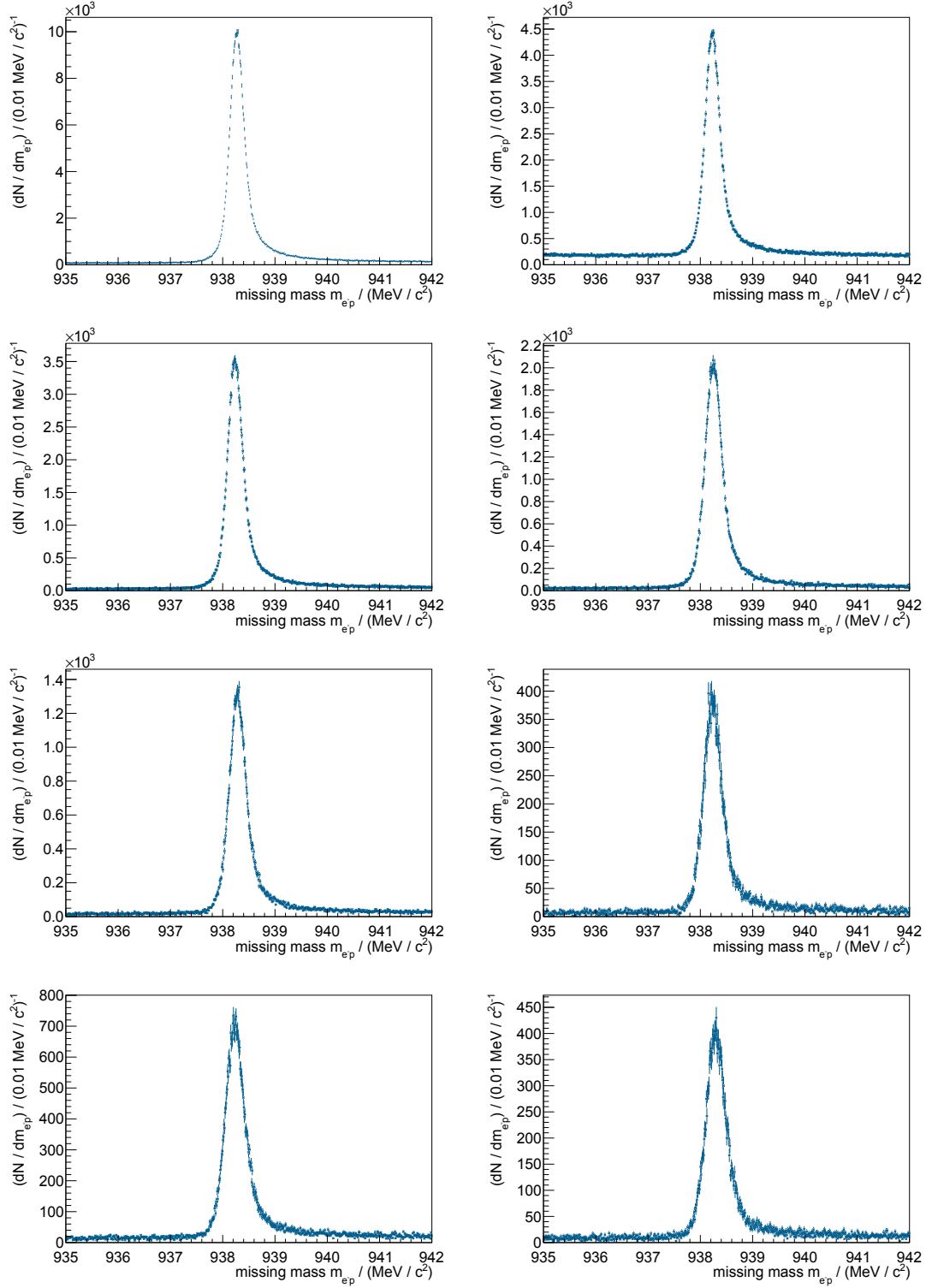
Figure A.7: Projection of the scattered angle in dependency of the missing mass of the proton. The data show a clearly visible peak at the proton mass of $938.27\,\mathrm{MeV}/c^2$ with nearly no background. Moreover, the radiative tail towards higher masses is visible.
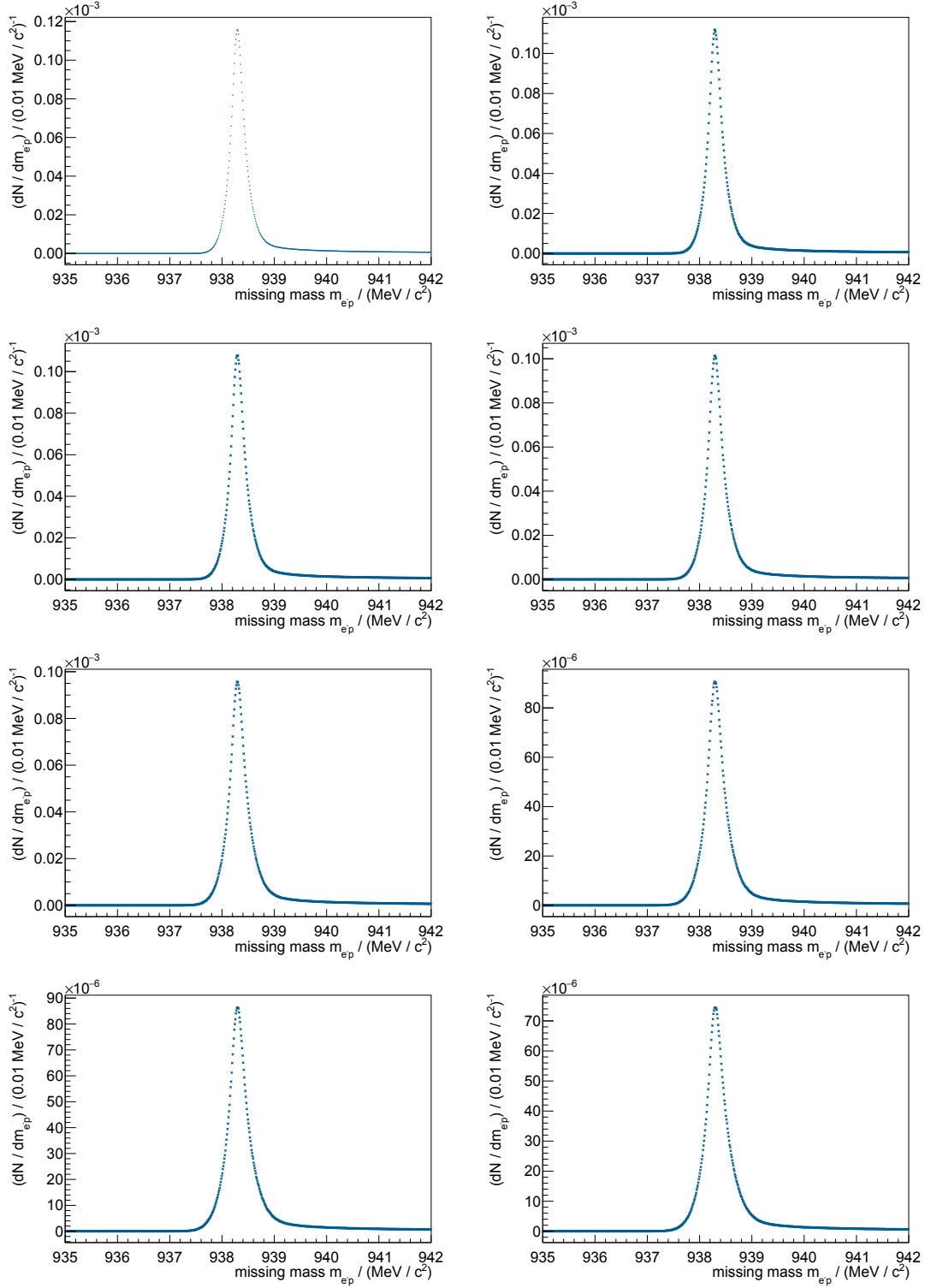
Figure A.8: Projection on the ordinate of the two-dimensional histograms of the scattered angle in dependency of the missing mass of the proton. The simulations show a clearly visible peak at the proton mass of $938.27\,\mathrm{MeV}/c^2$ and a slope towards higher mass corresponding to the radiative tail.

Bibliography

[A⁺97]   K. Aulenbacher et al. The MAMI source of polarized electrons. *Nucl. Instrum. Meth.*, 391(3):498 – 506, 1997.

[A⁺98]   G. S. Adams et al. Observation of a New $J^{PC} = 1^{-+}$ Exotic State in the Reaction $\pi^- p \to \pi^+ \pi^- \pi^- p$ at $18\,\text{GeV/c}$. *Phys. Rev. Lett.*, 81:5760–5763, 1998.

[A⁺04]   H.-H. Adam et al. Proposal for the Wide Angle Shower Apparatus (WASA) at COSY-Jülich. Technical report, Forschungszentrum Jülich, 2004.

[A⁺05]   B. Aubert et al. Observation of a Broad Structure in the $\pi^+ \pi_- J/\Psi$ Mass Spectrum around $4.26\,\text{GeV/c}^2$. *Phys. Rev. Lett.*, 95:142001, 2005.

[A⁺08]   F. Albert et al. Betatron oscillations of electrons accelerated in laser wakefields characterized by spectral X-ray analysis. *Phys. Rev. E*, 77:056402, 2008.

[A⁺11]   A. Antognini et al. The Lamb shift in muonic hydrogen and the proton radius. *Physics Procedia*, 17:10–19, 2011.

[A⁺12]   G. Aad et al. Observation of a new particle in the search for the Standard Model Higgs boson with the ATLAS detector at the LHC. *Phys. Lett.*, B716:1–29, 2012.

[A⁺15]   R. Aaij et al. Observation of $J/\psi p$ Resonances Consistent with Pentaquark States in $\Lambda_b^0 \to J/\psi K^- p$ Decays. *Phys. Rev. Lett.*, 115:072001, 2015.

[Ams98]   C. Amsler. Proton-antiproton annihilation and meson spectroscopy with the Crystal Barrel. *Rev. Mod. Phys.*, 70:1293–1339, 1998.

[AND]   ANDOR. *Oxford Instruments.* https://www.andor.oxinst.com, last visited September 2018.

[And89]   Anderson, H. L. and American Institute of Physics. *A Physicist's desk reference.* American Institute of Physics, 1989.

[Aug]   I. Augustin. FAIR Status Report. talk, PANDA LVI. Collaboration Meeting. Ruhr-Universität Bochum, 2016.

[Aul14]   S. Aulenbacher. *Design and Simulation of the Internal Gas-Target for MAGIX.* Diploma thesis, Johannes Gutenberg-Universität Mainz, 2014.

[Aul18]   S. Aulenbacher. doctoral thesis, Johannes Gutenberg-Universität Mainz, 2018. in preparation.

[Aur17]   B. Aurand. private communication. 2017.

[B$^+$]   D. Becker et al. The P2 Experiment - A future high-precision measurement of the electroweak mixing angle at low momentum transfer. arXiv:1802.04759, 2018.

[B$^+$96a]   D. Bauer et al. Relativistic Ponderomotive Force, Uphill Acceleration, and Transition to Chaos. *Phys. Rev. Lett.*, 75, 1996.

[B$^+$96b]   S. Brauksiepe et al. COSY-11, an internal experimental facility for threshold measurements. *Nucl. Instrum. Meth.*, A376:397–410, 1996.

[B$^+$99]   D. Barberis et al.   A coupled channel analysis of the centrally produced K^+K^- and $\pi^+\pi^-$ final states in pp interactions at $450\,\mathrm{GeV/c}$. *Phys. Lett. B*, 462:462–470, 1999.

[B$^+$01]   S. Barsov et al. ANKE, a new facility for medium energy hadron physics at COSY-Juelich. *Nucl. Instrum. Meth.*, A462:364–381, 2001.

[B$^+$10]   J. C. Bernauer et al. High-precision determination of the electric and magnetic form factors of the proton. *Phys. Rev. Lett.*, 105:242001, 2010.

[B$^+$14]   J. C. Bernauer et al. Electric and magnetic form factors of the proton. *Phys. Rev.*, C90(1):015206, 2014.

[Bö15]   S. Bölsker.   *Inbetriebnahme und Analyse einer mikrocontrollergesteuerten Hochgeschwindigkeitsblende für gepulste Cluster-Jet-Targets.* Bachelor's thesis, Westfälische Wilhelms-Universität Münster, 2015.

[Bal17]   R. Balske.   *Charakterisierung des Kaltkopfystems für das MAGIX@MESA Gas-Jet Target.* Bachelor's thesis, Westfälische Wilhelms-Universität Münster, 2017.

[BD]   INC. BEAM DYNAMICS. *Molecular Beam Skimmers.* https://www.beam-dynamicsinc.com, last visited September 2018.

[Ber06]   Schäfer Bergmann. *Lehrbuch der Experimentalphysik, Gase, Nanosysteme, Flüssigkeiten*, volume 5. Walter de Gruyter, 2006.

[Ber09]   F. Bergmann. *Studien zum seltenen Zerfall des η-Mesons $\eta \to \pi^0 + e^+ + e^-$ am Experimentaufbau WASA-at-COSY.* Diploma thesis, Westfälische Wilhelms-Universität Münster, 2009.

[Ber10]   J. C. Bernauer. *Measurement of the elastic electron-proton cross section and separaton of the electric and magnetic form factor in the Q^2 range from 0.004 to 1 $(GeV/c)^2$.* doctoral thesis, Johannes Gutenberg-Universität Mainz, 2010.

[Ber17]   F. Bergmann.   *Studies on the reaction $p + d \to {}^3He + \eta$ and search for C violation in the decay $\eta \to \pi^0 + e^+ + e^-$ with WASA-at-COSY.* doctoral thesis, Westfälische Wilhelms-Universität Münster, 2017.

[BL16]   D. Benyahia and M. Lemerini. Interferometer method using abel inversion to deduce a mapping of helium gas density and temperature. *Microwave and Optical Technology Letters*, 58(2):393–397, 2016.

[Bom14]   R. R. Bommareddi. Applications of Optical Interferometer Techniques for Precision Measurements of Changes in Temperature, Growth and Refractive Index of Materials. *Technologies*, 2(2):54–75, 2014.

[Bra17]   S. K. Brauckmann. *X-ray generation by high intensity laser pulses.* doctoral thesis, Heinrich-Heine-Universität Düsseldorf, 2017.

[Bra18]   P. Brand. Master's thesis, Westfälische Wilhelms-Universität Münster, 2018. in preparation.

[BT14]   F. Bretenaker and N. Treps. *Laser: 50 Years Of Discoveries.* World Scientific, 2014.

[B$^+$on]   J. Beringer et al. Review of Particle Physics. *Phys. Rev. D 86, 010001*, 2012 and 2013 partial update for the 2014 edition. (Particle Data Group).

[C$^+$06]   Y. Chen et al. Glueball spectrum and matrix elements on anisotropic lattices. *Phys. Rev. D*, 73:014516, 2006.

[Cai18]   S. Caiazza. Thin gem detectors developments for the magix experiment. RD51 Mini-Week, 2018.

[CER83]   CERN. By a hairsbreadth. *bulletin*, 45, 1983. http://cds.cern.ch/record/-1720922/files/45-1983.pdf, last visited September 2018.

[Chr17]   M. Christmann. Construction and characterization of a GEM prototype detector for MAGIX. MAGIX Collaboration Meeting 2017, Mainz, Germany, 2017.

[COD]   CODATA. *Committee on Data of the International Council for Science.* https://www.codata.org, last visited September 2018.

[D$^+$97]   H. Dombrowski et al. The Muenster cluster target for the COSY-11 experiment. *Nucl. Phys.*, A626:427C–433C, 1997.

[D$^+$10]   H. Du et al. Interaction of intense laser pulses with hydrogen atomic clusters. *Chinese Physics B*, 19:035202, 2010.

[D$^+$11a]   M. Dehn et al. The MAMI C accelerator. *The European Physical Journal Special Topics*, 198(1):19, 2011.

[D$^+$11b]   J. Dietrich et al. Status of 2 MeV electron cooler for COSY-Jülich/HESR. In *Sources and Medium Energy Accelerators.* Proceedings of 2011 Particle Accelerator Conference, New York, NY, USA, 2011.

[D+15]   M. Dell'Angela et al.   Time resolved X-ray absorption spectroscopy in condensed matter: A road map to the future. *J. Electron. Spectrosc. Relat. Phenom.*, 2015.

[d+17]   R. J. deBoer et al. The ^{12}C$(\alpha, \gamma)^{16}$O reaction and its implications for stellar helium burning. *Rev. Mod. Phys.*, 89, 2017.

[DBT13]   A. Khoukaz D. Bonaventura and A. Täschner.   Verfahren zur Herstellung monolithischer Lavaldüsen, 2013. Grant DE102013003644B4.

[Dem13]   K. Demmich. *Energiekalibrierung des Vorwärtsdetektors an WASA-at-COSY unter besonderer Berücksichtigung der Reaktion $p + d \rightarrow {}^3He + \eta'$*. Master's thesis, Westfälische Wilhelms-Universität Münster, 2013.

[Dem15]   W. Demtröder.   *Experimentalphysik 3, Atome, Molekühle und Festkörper*. Springer, 2015.

[Den16]   A. Denig. Dark Photon Searches at MAMI and MESA / Mainz. Dark Sectors Workshop, SLAC, USA, 2016.

[E+09]   E. Esarey et al. Physics of laser-driven plasma-based electron accelerators. *Rev. Mod. Phys.*, 81:1229–1285, 2009.

[EE10]   H. J. Eichler and J. Eichler. *Laser, Bauformen, Strahlführung, Anwendungen*. Springer, 2010.

[Eks95]   C. Ekström. Internal targets - a review. *Nucl. Instr. Meth.*, 362(1):1–15, 1995.

[F+05]   U. Fischer et al. *Tabellenbuch Metall*. Verlag Europa Lehrmittel, 2005.

[F+13]   C. Feng et al. Chirped pulse amplification in a seeded free-electron laser for generating high-power ultra-short radiation. *Nucl. Instrum. Meth.*, 712:113 – 119, 2013.

[FA15]   S. Friederich and K. Aulenbacher. Test electron source for increased brightness emission by near band gap photoemission. In *Proceedings, 6th International Particle Accelerator Conference (IPAC 2015): Richmond, Virginia, USA, May 3-8, 2015*, pages 1512–1514, 2015.

[Fri14]   C. Fritzsch.   *Untersuchung verschiedener Normierungsreaktionen für dp-Kollisionen am ANKE-Experiment*. Master's thesis, Westfälische Wilhelms-Universität Münster, 2014.

[Fri18]   C. Fritzsch. doctoral thesis, Westfälische Wilhelms-Universität Münster, 2018. in preparation.

[G+18]   S. Grieser et al. A Cryogenic Supersonic Jet Target for Electron Scattering Experiments at MAGIX@MESA and MAMI. *Nucl. Instrum. Meth.*, 2018.

[Gag18]   S. Gagneur. *Strahlprofilmessung des Gas-Jet-Targets für das MAGIX-Experiment.* Bachelor's thesis, Johannes Gutenberg-Universität Mainz, 2018.

[Gel74]   E. Gelfort. Das Separationsvermögen des Wien-filters. *International Journal of Mass Spectrometry and Ion Physics*, 14(4):349 – 361, 1974.

[Gen08]   S. General. *Massenspektroskopische Untersuchung von Wasserstoffclustern am Münsteraner Cluster-Jet Targets.* Diploma thesis, Westfälische Wilhelms-Universität Münster, 2008.

[GF06a]   GSI Helmholtzzentrum für Schwerionenforschung and Facility for Antiproton and Ion Research FAIR. An International Accelerator Facility for Beams of Ions and Antiprotons, Conceptual Design Report. Technical report, 2006.

[GF06b]   GSI Helmholtzzentrum für Schwerionenforschung and Facility for Antiproton and Ion Research FAIR. FAIR Baseline Technical Report, Executive Summary. Technical report, 2006.

[Gib07]   P. Gibbon. *Short Pulse Laser Interactions with Matter, An Introduction.* Imperial College Press, 2007.

[Gos09]   P. Goslawski. *Hochpräzise Impulsbestimmung des COSY-Beschleunigerstrahls im Rahmen der Messung zur Bestimmung der η-Masse am Experimentaufbau ANKE.* Diploma thesis, Westfälische Wilhelms-Universität Münster, 2009.

[Gos13]   P. Goslawski. *High precision measurement of the η meson mass at COSY-ANKE.* doctoral thesis, Westfälische Wilhelms-Universität Münster, 2013.

[Gri]   S. Grieser. *Development of the Internal Jet Target for MAGIX at MESA.* 650. WE-Heraeus-Seminar Physics of Energy-Recovering Linacs, Bad Honnef, Germany, 2017.

[Gri14]   S. Grieser. *Das Cluster-Jet Target MCT1S und die Analyse von Clusterstrahlen.* Master's thesis, Westfälische Wilhelms-Universität Münster, 2014.

[GSI06]   GSI Helmholtzzentrum für Scherionenforschung and Facility for Antiproton and Ion Research FAIR. FAIR Baseline Technical Report. 2006.

[H+00]   S. P. Hatchett et al. Electron, photon, and ion beams from the relativistic interaction of petawatt laser pulses with solid targets. *Physics of Plasmas*, 7(5):2076–2082, 2000.

[Hü14]   N. Hüsken. *Untersuchung der Reaktion $p+d \rightarrow {}^3He + \eta$' am Experimentaufbau WASA-at-COSY.* Master's thesis, Westfälische Wilhelms-Universität Münster, 2014.

[Hü17a]   N. Hüsken. *η and π^0 production in proton-deuteron fusion to ${}^3HeX$ with WASA-at-COSY.* doctoral thesis, Westfälische Wilhelms-Universität Münster, 2017.

[H⁺17b]   F. Hug et al.   MESA - an ERL Project for Particle Physics Experiments. In *Proceedings, 28th International Linear Accelerator Conference (LINAC16): East Lansing, Michigan, September 25-30, 2016*, page MOP106012, 2017.

[H⁺18]   Q. Hu et al. Simulation of proton–proton elastic scattering for the KOALA recoil detector. *Nucl. Instrum. Meth.*, 898:133 – 138, 2018.

[Hag87]   O. F. Hagena. Condensation in free jets: Comparison of rare gases and metals. *Z. Phys. D Atoms, Molecules and Clusters*, 4(3):291–299, 1987.

[Hag92]   O. F. Hagena. Cluster ion sources (invited). *Rev. Sci. Instrum.*, 63(4):2374–2379, 1992.

[Ham06]   Hamamatsu. *MCP Assembly*, 2006. Technical Information.

[Har16]   C. Hargens. *Aufbau und Inbetriebnahme eines Gas-Jet Targets für MAGIX @ MESA sowie die Justage eines Cluster-Jet Targets für Laserstreuexperimente.* Bachelor's thesis, Westfälische Wilhelms-Universität Münster, 2016.

[Har18]   C. Hargens. Master's thesis, Westfälische Wilhelms-Universität Münster, 2018. in preparation.

[Hei15]   R. Heine. Current Status of the MESA Project. In *Proceedings, 6th ICFA Advanced Beam Dynamics Workshop on Energy Recovery Linacs (ERL 2015): Stony Brook, NY, USA, June 7-12, 2015*, page WEIBLH1049, 2015.

[Her13]   A.-K. Hergemöller. *Präparation von Clusterstrahlen und der Aufbau der finalen Clusterquelle für das $\overline{P}ANDA$-Experiment.* Master's thesis, Westfälische Wilhelms-Universität Münster, 2013.

[Her18]   A.-K. Hergemöller.   doctoral thesis, Westfälische Wilhelms-Universität Münster, 2018. in preparation.

[Het17]   B. Hetz. *Construction, implementation, and first beam analysis using the newly developed slow control system of the $\overline{P}ANDA$ cluster-jet target in Münster.* Master's thesis, Westfälische Wilhelms-Universität Münster, 2017.

[Het18]   B. Hetz. doctoral thesis, Westfälische Wilhelms-Universität Münster, 2018. in preparation.

[HFK⁺76] H. Herminghaus, A. Feder, K.H. Kaiser, W. Manz, and H.v.d. Schmitt. The design of a cascaded 800 MeV normal conducting C.W. race track microtron. *Nucl. Instrum. Meth.*, 138(1):1 – 12, 1976.

[Hin08]   F. Hinterberger. *Physik der Teilchenbeschleuniger und Ionenoptik.* Springer, 2008.

[HO72]   O. F. Hagena and W. Obert. Cluster Formation in Expanding Supersonic Jets: Effect of Pressure, Temperature, Nozzle Size, and Test Gas. *J. Chem. Phys.*, 56(5):1793–1802, 1972.

[Hor15]   F. Hordt. *Dynamische Regelung der Dichte von Cluster-Jet Targets für Speicherringexperimente.* Bachelor's thesis, Westfälische Wilhelms-Universität Münster, 2015.

[Hos14]   J. P. Hosemann. *Auf dem Weg zur Erklärung der Welt: Meilensteiner der Physik und Astrophysik.* LOGOS Berlin, 2014.

[Hus12]   C. Husmann. *Untersuchungen zur Optimierung der Dropleterzeugung innerhalb des Pellettargets des Experimentaufbaus WASA-at-COSY.* Diploma thesis, Westfälische Wilhelms-Universität Münster, 2012.

[Jä09]   O. Jäckel. *Characterization of ion acceleration with relativistic laser-plasma.* doctoral thesis, Friedrich-Schiller-Universität Jena, 2009.

[Jan06]   A. Jankowiak. The Mainz Microtron MAMI –Past and future. *The European Physical Journal A - Hadrons and Nuclei*, 28(1):149–160, 2006.

[Joh98]   Johnson Matthey. *Technical Manual HE 20 Hydrogen purifier*, 1998. Gas Processing Technology.

[K$^+$99]   K. Krushelnick et al. Multi-MeV Ion Production from High-Intensity Laser Interactions with Underdense Plasmas. *Phys. Rev. Lett.*, 83:737–740, 1999.

[K$^+$01]   A. V. Kuznetsov et al. Efficiency of ion acceleration by a relativistically strong laser pulse in an underdense plasma. *Plasma Phys. Rep.*, 27:211–220, 2001.

[K$^+$08a]   K. H. Kaiser et al. The 1.5-GeV harmonic double-sided microtron at Mainz University. *Nucl. Instrum. Meth.*, A593:159–170, 2008.

[K$^+$08b]   S. Kneip et al. Observation of Synchrotron Radiation from Electrons Accelerated in a Petawatt-Laser-Generated Plasma Cavity. *Phys. Rev. Lett.*, 100:105006, 2008.

[Kö10]   E. Köhler. *Das Münsteraner Cluster-Jet Target MCT2, ein Prototyp für das $\overline{P}ANDA$-Experiment, & die Analyse der Eigenschaften des Clusterstrahls.* Diploma thesis, Westfälische Wilhelms-Universität Münster, 2010.

[K$^+$12]   K. Knie et al. Concept for the Antiproton Production Target at Fair. In *Proceedings of IPAC2012*, 2012. New Orleans, USA, 2012.

[K$^+$14a]   V. Kamerdzhiev et al. 2 MeV electron cooler for COSY and HESR- first results. Proceedings of IPAC2014, Dresden, Germany, 2014.

[K$^+$14b]   A. Khoukaz et al. Two-dimensional visualization of cluster beams by microchannel plates. *Nucl. Instrum. Meth.*, A735:12–18, 2014.

[Kö15]   E. Köhler. *Mass spectroscopy of hydrogen cluster-jets and beam density optimisation studies.* doctoral thesis, Westfälische Wilhelms-Universität Münster, 2015.

[K+16]   S. Kar et al.   Guided post-acceleration of laser-driven ions by a miniature modular structure. *Nature Communications*, 7(10792), 2016.

[K+18]   A. Kramida et al. NIST Atomic Spectra Database (ver. 5.5.6). *National Institute of Standards and Technology*, 2018.

[Kho96]   A. Khoukaz. *Messungen zur schwellennahen Produktion geladener Pionenpaare in der Proton-Proton-Streuung.*   doctoral thesis, Westfälische Wilhelms-Universität Münster, 1996.

[Kho16]   A. Khoukaz. PANDA Cluster-Jet Target: Target and Beam Tests at COSY. *COSY Beam Time Advisory Committee (CBAC), June 27–28, 2016, Location: Institut für Kernphysik, Forschungszentrum Jülich GmbH, 52428 Jülich*, 2016.

[Kho18]   A. Khoukaz. private communication. 2018.

[Kje15]   S. E. E. Kjeld. Nonlinear optics: Twisted high-harmonic generation. *Nature Photonics*, 9:710–712, 2015.

[Kle00]   E. Klempt. Meson Spectroscopy: Glueballs, Hybrids and Q$\overline{\text{Q}}$ Mesons. *PSI Zuoz Summer School, Phenomenology of Gauge Interactions*, 2000.

[Kul96]   K. C. Kulander. Dynamics of laser excitation, ionization and harmonic conversion in inert gas atoms. *Prog Crystal Growth and Charact*, 33:193–199, 1996.

[L+09a]   J. W. Leachman et al. Fundamental Equations of State for Parahydrogen, Normal Hydrogen, and Orthohydrogen. *J. Phys. Chem. Ref. Data*, 38(3):721–748, 2009.

[L+09b]   O. Link et al. Ultrafast electronic spectroscopy for chemical analysis near liquid water interfaces: Concepts and applications. *Applied Physics A*, 96:117–135, 2009.

[L+16]   S. H. Lin et al. *Advances in multi-photon processes and spectroscopy.* World Scientific, 1984-2016.

[Leß16]   L. Leßmann. *Investigations on gas jet beam profiles with a Mach-Zehnder interferometer.* Master's thesis, Westfälische Wilhelms-Universität Münster, 2016.

[Leß18]   L. Leßmann. doctoral thesis, Westfälische Wilhelms-Universität Münster, 2018. in preparation.

[Lig]   LightFab. *SLE with LightFab 3D Printer.* https://www.lightfab.de/files/-Downloads/SLE_3D_printed_glass.pdf, last visited September 2018.

[Liq]   Air Liquide. *Gas Encyclopedia.* https://industrie.airliquide.de/, last visited September 2018.

242

[Loh05]   E. Lohrmann. *Hochenergiephysik*. Teubner, 5th edition, 2005.

[Lun17]   S. Lunkenheimer. Nucleosynthesis C12-16. MAGIX Collaboration Meeting 2017, Mainz, Germany, 2017.

[M$^+$74]   J. J. Murphy et al. Proton form factor from 0.15 to 0.79 fm^{-2}. *Phys. Rev.*, C9:2125–2129, 1974. [Erratum: Phys. Rev.C10,2111(1974)].

[M$^+$14a]   H. Merkel et al. Search at the Mainz Microtron for Light Massive Gauge Bosons Relevant for the Muon g-2 Anomaly. *Phys. Rev. Lett.*, 112(22):221802, 2014.

[M$^+$14b]   M. Mihovilovic et al. Initial state radiation experiment at MAMI. *EPJ Web Conf.*, 72:00017, 2014.

[M$^+$16]   P. J. Mohr et al. CODATA Recommended Values of the Fundamental Physical Constants: 2014. *Rev. Mod. Phys.*, 88(3):035009, 2016.

[M$^+$17]   M. Mihovilovic et al. First measurement of proton's charge form factor at very low Q^2 with initial state radiation. *Phys. Lett.*, B771:194–198, 2017.

[Man18]   C. Mannweiler. Master's thesis, Westfälische Wilhelms-Universität Münster, 2018. in preparation.

[Mar16]   J. P. Marangos. Development of high harmonic generation spectroscopy of organic molecules and biomolecules. *J. Phys. B*, 49(13):132001, 2016.

[Mer16a]   H. Merkel. Experiments with internal targets at the mainz energy-recovering superconducting accelerator. 54th International Winter Meeting on Nuclear Physics, Bormio, Italy, 2016.

[Mer16b]   H. Merkel. Internal Target Experiments at the MESA accelerator. *PoS*, BORMIO2016:037, 2016.

[Mer17a]   H. Merkel. Experiments with internal targets at the mainz energy-recovering superconducting accelerator. International Workshop on (e, e' p) Processes, Bled, Slowenia, 2017.

[Mer17b]   H. Merkel. private communication. 2017.

[Mes06]   D. Meschede. *Gerthsen Physik*. Springer Verlag, 2006.

[Mic]   Micreon. *Laser Micro Machining*. https://www.micreon.de, last visited September 2018.

[Mih17]   M. Mihovilovic. ISR @ A1. MAGIX Collaboration Meeting 2017, Mainz, Germany, 2017.

[MP99]   C. J. Morningstar and M. Peardon. Glueball spectrum from an anisotropic lattice study. *Phys. Rev. D*, 60:034509, 1999.

[Nü06]   F. Nürnberg. *Vollständige Rekonstruktion und Transportsimulation eines laserbeschleunigten Protonenstrahls unter Verwendung von mikrostrukturierten Targetfolien und radiochromatischen Filmdetektoren.*   Diploma thesis, Technische Universität Darmstadt, 2006.

[Noba]   Nobelprize.org. The nobel prize in physics 1976. http://www.nobelprize.org/nobel_prizes/physics/laureates/1976/, last visited December 2016.

[Nobb]   Nobelprize.org. The nobel prize in physics 2013. http://www.nobelprize.org/nobel_ qprizes/physics/laureates/2013/, last visited December 2016.

[Ott07]   J. Otte. *Messung der Clustergeschwindigkeit und der Teilchendichte am Münsteraner Cluster-Jet-Target.*   Diploma thesis, Westfälische Wilhelms-Universität Münster, 2007.

[P+05]   K. T. Phuoc et al. Laser based synchrotron radiation. *Physics of Plasmas*, 12(2):023101, 2005.

[P+06]   K. T. Phuoc et al. Imaging Electron Trajectories in a Laser-Wakefield Cavity Using Betatron X-Ray Radiation. *Phys. Rev. Lett.*, 97:225002, 2006.

[P+08]   B. Povh et al. *Teilchen und Kerne.* Springer, 8th edition, 2008.

[P+10]   R. Pohl et al. The size of the proton. *Nature*, 466:213–216, 2010.

[P+15]   N. Petridis et al. Prototype internal target design for storage ring experiments. *Physica Scripta*, 2015(T166):014051, 2015.

[P+16]   C. Patrignani et al. Review of Particle Physics. *Chin. Phys.*, C40(10):100001, 2016.

[PAN08a]   PANDA Collaboration. Technical Design Report for: PANDA Electromagnetic Calorimeter (EMC). Technical report, FAIR, 2008.

[PAN08b]   PANDA Collaboration. Technical Design Report for the PANDA Muon Detectors. Technical report, FAIR, 2008.

[PAN09]   PANDA Collaboration. Physics Performance Report for: $\overline{\text{P}}$ANDA, Strong Interaction Studis with Antiprotons, 2009.

[PAN12a]   PANDA Collaboration. Technical Design Report for the PANDA Internal Targets. Technical report, FAIR, 2012.

[PAN12b]   PANDA Collaboration. Technical Design Report for the PANDA Micro Vertex Detector. Technical report, FAIR, 2012.

[PAN12c]   PANDA Collaboration. Technical Design Report for the PANDA Straw Tube Tracker. Technical report, FAIR, 2012.

[PAN12d]   PANDA Collaboration. The Cluster-Jet Target and Developments for the Pellet Target. *Technical Design Report for the PANDA Internal Targets*, 2012.

[Pau00a] H. Pauly. *Atom, Molecule, and Cluster Beams I.* Springer, 2000.

[Pau00b] H. Pauly. *Atom, Molecule, and Cluster Beams II.* Springer, 2000.

[PCO] PCO AG. https://www.pco.de/fileadmin/user_upload/db/download/-kb_smear_20100723.pdf, last visited September 2018.

[Pel15] M. Pelizäus. Charmonium Physics at PANDA. Talk at young PANDA session, collaboration meeting (Bochum), 2015.

[Pet15] N. Petridis. Novel internal target source for future storage ring experiments. TSR@ISOLDE Workshop, Zurich, Switzerland, 2015.

[PMM87] M. Pessot, P. Maine, and G. Mourou. 1000 times expansion/compression of optical pulses for chirped pulse amplification. *Optics Communications*, 62(6):419 – 421, 1987.

[QM98] B. Quesnel and P. Mora. Theory and simulation of the interaction of ultraintense laser pulses with electrons in vacuum. *Phys. Rev.*, E58:3719–3732, 1998.

[R+] H. Reich et al. The ESR internal target. *Nuclear Physics A*, 626(1-2):417–425. Proceedings of the Third International Conference on Nuclear Physics at Storage Rings, 1997.

[R+04] A. Rousse et al. Production of a keV X-Ray Beam from Synchrotron Radiation in Relativistic Laser-Plasma Interaction. *Phys. Rev. Lett.*, 93:135005, 2004.

[RK+95] G. Ravindra Kumar et al. Study of the Interactions of Intense Laser Beams and of Fast-ion Beams with Molecules. *Rapid Communications in Mass Spectrometry*, 9:329–335, 1995.

[S+] R. Stassen et al. The HESR RF-System and Tests in COSY. In *Proceedings of EPAC08.* Genoa, Italy, 2008.

[S+80] G. G. Simon et al. Absolute electron Proton Cross-Sections at Low Momentum Transfer Measured with a High Pressure Gas Target System. *Nucl. Phys.*, A333:381–391, 1980.

[S+98] R. A. Smith et al. Characterization of a cryogenically cooled high-pressure gas jet for laser/cluster interaction experiments. *Rev. Sci. Instrum.*, 69(11):3798–3804, 1998.

[S+00] R. A. Snavely et al. Intense High-Energy Proton Beams from Petawatt-Laser Irradiation of Solids. *Phys. Rev. Lett.*, 85:2945–2948, 2000.

[S+04] S. Sakabe et al. Generation of high-energy protons from the coulomb explosion of hydrogen clusters by intense femtosecond laser pulses. *Phys. Rev. A*, 69:023203, 2004.

[S⁺15] T. Stengler et al. Modified ELBE Type Cryomodules for the Mainz Energy-Recovering Superconducting Accelerator MESA. In *Proceedings, 17th International Conference on RF Superconductivity (SRF2015): Whistler, Canada, September 13-18, 2015*, 2015.

[Sch12a] B. S. Schlimme. *Messung des elektrischen Neutron-Formfaktors in der Reaktion $^3\overrightarrow{He}(\overrightarrow{e}, e', n)pp$ bei $Q^2 = 1.58 \ (GeV/c)^2$*. doctoral thesis, Johannes Gutenberg-Universität, Mainz, 2012.

[Sch12b] D. Schröer. *Strahlzeitvorbereitungen zur Untersuchung der schwellennahen Produktion von η-Mesonen in der quasifreien Reaktion $p+d{\rightarrow}d+\eta+p_{spec}$ bei ANKE*. Diploma thesis, Westfälische Wilhelms-Universität Münster, 2012.

[Sch18] A.-M. Schroer. *Investigation of ion acceleration from underdense targets using a high intensoty short pulse laser*. doctoral thesis, Heinrich-Heine-Universität Düsseldorf, 2018.

[SM85] D. Strickland and G. Mourou. Compression of amplified chirped optical pulses. *Optics Communications*, 55(6):447 – 449, 1985.

[SM97] E.A. Startsev and C. McKinstrie. Multiple scale derivation of the relativistic ponderomotive force. *Phys. Rev. E*, 55:7527–7535, 1997.

[T⁺] R. Toelle et al. HESR at FAIR: Status of Technical Planning. In *Proceedings of PAC07*. Albuquerque, New Mexico, USA, 2007.

[T⁺03] J. W. G. Tisch et al. Interaction of intense laser pulses with atomic clusters: Measurements of ion emission, simulations and applications. *Nucl. Instrum. Meth.*, 205:310 – 323, 2003. 11th International Conference on the Physics of Highly Charged Ions.

[Tä12] A. Täschner. *Entwicklung und Untersuchung von Cluster-Jet-Targets höchster Dichte*. doctoral thesis, Westfälische Wilhelms-Universität Münster, 2012.

[TD79] T. Tajima and J. M. Dawson. Laser Electron Accelerator. *Phys. Rev. Lett.*, 43:267–270, 1979.

[Tho13] Bakerian Lecture: Rays of positive electricity. *Proceedings of the Royal Society of London A: Mathematical, Physical and Engineering Sciences*, 89(607):1–20, 1913.

[Umr97] D.W. Umrath. *Grundlagen der Vakuumtechnik*. 1997.

[V⁺05] V. L. Varentsov et al. ASACUSA Gas-Jet Target: Present Status And Future Development. *AIP Conference Proceedings*, 793(1):328–340, 2005.

[Ves18] S. Vestrick. Bachelor's thesis, Westfälische Wilhelms-Universität Münster, 2018. in preparation.

[W⁺88] M. Wutz et al. *Theorie und Praxis der Vakuumtechnik.* Friedr. Vieweg & Sohn, 4 edition, 1988.

[W⁺00] S. C. Wilks et al. Energetic Proton Generation in Ultra-Intense Laser-solid Interactions. 2000.

[W⁺07] A. Winnemöller et al. The WASA-at-COSY pellet target. Technical report, Forschungszentrum Jülich, 2007. Annual Report JUEL-4262.

[Wei03] M. Weis. *Elektroproduktion neutraler Pionen und Entwicklung eines Steuerungssystems für die Drei-Spektrometer-Anlage am Mainzer Mikrotron.* doctoral thesis, Johannes Gutenberg-Universität Mainz, 2003.

[Wes16] C. Westphälinger. *Mach-Zehnder-Interferometer zur Dichtebestimmung eines Gas-Jet Targets.* Bachelor's thesis, Westfälische Wilhelms-Universität Münster, 2016.

[Wil96] K. Wille. *Physik der Teilchenbeschleuniger und Synchrotronstrahlungsquellen*, volume 2. Teubner, 1996.

[Wil17a] C. Wilkin. The legacy of the experimental hadron physics programme at COSY. *Eur. Phys. J.*, A53(6):114, 2017.

[Wil17b] O. Willi. Time–resolved ionization dynamics in solid density plasmas. Workshop: High Intensity Laser Matter Science at the HED Instrument at the European XFEL Hamburg, 5–6 April 2017 European XFEL, Schenefeld, 2017.

[Y⁺] W.-M. Yao et al. Note on Non $q\bar{q}$ Mesons. *J. Phys. G*, 33(1). (Particle Data Group), 2006.

[Y⁺07] C. Z. Yuan et al. Measurement of the $e^+e^- \to \pi^+\pi^- J/\psi$ Cross Section Via Initial-State Radiation at Belle. *Phys. Rev. Lett.*, 99:182004, 2007.

[Zü03] A. Züttel. Materials for hydrogen storage. *Materials Today*, 6(9):24 – 33, 2003.

[Zan12] A. Zannotti. *Inbetriebnahme und Test wesentlicher Produktions-, Justage- und Detektionskomponenten des $\overline{P}ANDA$ Cluster-Jet Targets.* Bachelor's thesis, Westfälische Wilhelms-Universität Münster, 2012.

Acknowledgement